Solving the two-interface problem in vibrational sum frequency generation spectroscopy applied to multilayer thin film systems

A DISSERTATION
SUBMITTED TO THE FACULTY OF THE GRADUATE SCHOOL
OF THE UNIVERSITY OF MINNESOTA
BY

Daniel Bruce O'Brien

IN PARTIAL FULFILLMENT OF THE REQUIREMENTS
FOR THE DEGREE OF
DOCTOR OF PHILOSOPHY

Aaron M. Massari, advisor

March 2014

Acknowledgements

A significant portion of my time as a graduate student was spent on technical ventures: building instruments, coding them to run in LabVIEW, and learning about computer system administration. To those ends, I acknowledge support staff in the department. In the electronics shop I thank Bruce Moe, Mike Cassey, and Eric Shultz for helpful discussions and feedback. My venture into the area of high vacuum instrument design was facilitated by the Chemistry Department's mantra to redistribute hardware to the newest research groups first, and so I am grateful for the opportunities I had to ransack the lab space of former groups, which resulted directly in my hefty education in vacuum science. I thank Sean Murray in the mass spectrometry lab and the Kass group for further support in those efforts. Chuck Tomlinson was indispensably helpful for department-level problem solving.

I acknowledge my undergraduate professor Don Poe for engaging me in research and for his encouragement to attend graduate school at UMN. Thanks to Tom Tiwald at J.A. Woollam for ardently answering all my questions. I thank those who I interacted with the most in my time at UMN, the Massari Group members past and present, for providing an enjoyable and stimulating lab environment. I acknowledge both the Massari and Blank Groups for constructive feedback while preparing for milestone presentations, as well as for our biweekly joint group meetings. I thank Tim Anglin for our collaborations and all of our discussions and at every intensity level – and for rounds of squash and excellent home-brew. I give my sincerest regards to my advisor Aaron, who gave me the freedom to make my own choices and his confidence in those choices, and for his semi-infinite positivity that countered my critical tendencies. My graduate school experience and ultimate contribution are a direct result of that relation.

Finally, I thank my in-laws Gary and Grace Ann for support and showing genuine interest, my parents Bruce and Nancy for raising me to be self-confident and motivated, my wife Kate for her endless support throughout my time at UMN, and sliding doors for all of my blessings.

Dedication

For Kate and our boys, Owen and Carter

Abstract

This dissertation describes advances made in applying sum frequency generation spectroscopy (SFG, in particular *vibrational* SFG or VSFG) to multilayer thin film systems. Application of VSFG to thin film systems is motivated by the challenge of characterizing molecular structure at the active boundary in organic field-effect transistors, these are inherently *buried* interfaces. VSFG is a surface-selective probe of molecular structure; however, when VSFG is applied to an organic thin film, the detected signal has contributions from two potential sources – the two interfaces of the organic – which must be separated. The problem is further confounded by optical interferences inherent in multilayer thin film systems. An intuitive mathematical model is developed; postulating a solution to the two-interface problem of SFG applied to planar and stratified multilayer structures. The model system for this dissertation is thin films of the small molecule N,N'-dioctyl-3,4,9,10-perylenedicarboximide (PTCDI-C_8) vapor deposited on silica thin film substrates, consistent with an oFET thin film geometry. The interference model is used for an extensive simulation analysis that reveals intricacies contained in the intensity data of VSFG applied to that system. VSFG experiments performed on samples with PTCDI-C_8 deposited as gradient thicknesses provide compelling evidence that the model gives an accurate description of optical interference effects and that it can be used to separate contributions to the total VSFG signal intensity. The supplementary materials contain a collection of Mathematica notebooks that can be used to investigate optical interference effects on SFG data collected from systems composed of an arbitrary number of thin film layers.

Table of Contents

List of Tables

List of Figures

1 Background

"If I have seen further it is by standing on ye sholders of Giants."

- Sir Isaac Newton

CHAPTER SUMMARY

This chapter provides the background information necessary to articulate the primary emphasis of this dissertation. The principal interest is in exploiting the unique interfacial sensitivity of vibrational sum frequency generation spectroscopy (VSFG) to characterize molecular structure at the buried interface of organic field-effect transistors (oFETs). The problem is motivated in the second section by detailing the potential advantages of organic semiconductors in terms of cost and performance that is undercut by their transitory functional behavior. While many processes contribute to overall oFET performance, there is a clear connection to molecular structure at the active interface; however, its buried nature makes it difficult to characterize experimentally. The discussion on VSFG gives a detailed historical background and theoretical account including a summary of the dipole approximation, which leads to the interfacial specificity of VSFG making it an ideal tool for studying the active interface of oFETs. However, it is emphasized that coherent spectroscopies applied to thin film systems are subject to optical interference effects. In addition, there are always two interfaces contributing to the detected VSFG response. From the historical account it is made clear that the two-interface problem combined with optical interference effects is a current limitation for the application of VSFG and that there is a need for an optical

interference model to describe the effects from multilayer thin film systems on VSFG signals. This is the fundamental provocation of this dissertation and motivates the remaining chapters.

1.1 MOLECULAR STRUCTURE AT A BURIED INTERFACE

The distinctive processes that occur at the boundary of condensed-phase materials (i.e. solid-solid, solid-liquid, solid-gas, liquid-gas) is the impetus for the extensive efforts to characterize and tune the material properties at those boundaries, broadly encompassed in the discipline known as surface science. Within this comprehensive field one major subject area is in characterizing the boundaries of organic molecule thin films. Historically, organic thin film systems have been important for applications such as adhesion,[1,2] adsorption,[3–5] reactivity,[6,7] and wettability.[8–10] Elucidating the mechanisms involved in each system's function is a complex problem, but there is a clear connection to the structure of the molecules immediately adjacent to the boundary. For many applications, the interface of interest is at the outermost exposed surface, allowing the surface scientist direct experimental access to probe the properties of the molecules there.

While external material surfaces present their own challenges in terms of structural characterization, with the advent of organic semiconductor materials, there has been a dramatic escalation of interest in characterizing the molecules at *buried* interfaces. Making *in situ* measurements is essential because in most cases, processes that have a direct effect on overall device performance occur at internal material interfaces and it is the nature of the boundary during operation that drives these processes. For example, charge separation and recombination at the boundary of electron donor and acceptor phases are crucial interfacial phenomena for organic

photovoltaics (oPVs) and light emitting diodes (oLEDs).[11,12] Likewise, electron injection from metal electrodes into electrochromic thin films and carrier trapping are processes that can be dominated by interfacial structure.[13,14] A particularly salient example in which the device behavior is almost exclusively controlled by molecular structure at a buried interface is the organic field-effect transistor (oFET). For oFETs, although the charge transfer mechanisms that occur within the active region are complex, it is effectively only the first monolayer or two at the buried interface of the organic thin film and the dielectric material that participate in overall device performance.[15–20]

Characterizing interfacial molecular structure in organic thin film systems presents several challenges and when the active interface is internal (i.e. buried) the problem of characterizing molecular structure poses unique difficulties. First, the number of molecules at the interfaces can be far fewer than the total number of molecules through the bulk of the film so that any measurement must have high interfacial sensitivity. Most linear optical measurements are contaminated by response from the bulk of the film, complicating data interpretation. However, nonlinear optical spectroscopies have unique selection rules that can be exploited to gain new information about the system under study. In this context, it is the symmetry rule for all even order spectroscopies that, within the electric dipole approximation, they are forbidden in the bulk of centrosymmetric media. Only at interfaces where inversion symmetry is broken do they produce a response, making them inherently surface selective. It is for this reason that the second order spectroscopy sum frequency generation (SFG) can be used to deduce molecular orientation at any interface accessible by light.[21–26]

SFG is a coherent technique, and when measurements are performed on thin film systems the detected response is subject to thin film optical interference effects. For films thicker than a monolayer there are always two interfaces that contribute to the detected signal and typically only one is of primary interest. The local input fields present at the active interfaces depend on the geometry of the entire system as do the fields emitted from those interfaces. Thus, all detected SFG peaks potentially have contributions from *both* interfaces. Separating those contributions is a complex problem, especially in systems composed of more than a single thin film, which is the case for most organic semiconductor devices. However, the two-interface problem must be overcome in order to accurately deduce molecular structure at a specific interface in an organic thin film system.

The ideas presented in this dissertation relate equally well to any even order spectroscopy applied to any planar and stratified multilayer thin film system with material layers that lack inversion symmetry; however, the introductory discussion and all experimental work has focused on oFETs. Throughout my graduate work oFETs have been the principal emphasis. They embody the primary issue at hand: the interface that dictates device performance is buried and the devices are inherently multilayer structures. And so, while the majority of this project is focused on a solution to the two-interface problem in SFG, the inspiration for these efforts come from the unique challenge of characterizing the structure of molecules at buried interfaces in organic thin film systems, specifically oFETs, utilizing nonlinear optical spectroscopy.

1.2 ORGANIC SEMICONDUCTING THIN FILMS

The technological relevance of organic semiconducting thin film systems is a result of an amalgamation of their inherent physical and chemical properties, relative ease of processing, and cost when compared to traditional inorganic materials. As "plastic" electronics, organic semiconductors often do not require a clean room to be processed, can be deposited on flexible substrates, and are relatively easy to mass produce (e.g. high throughput printing techniques). In many cases, they are stable at ambient conditions and have been shown to exhibit tunable conductivities through self-doping and redox chemistry.[27,28]

Advances in performance have yielded devices that are increasingly effective and efficient and present day commercial successes of organic semiconductor thin film devices benchmark these developments. For instance, oLEDs sold as large area panels for modern day aesthetic lighting are available. Perhaps more impressively, organic semiconductors are being used in video displays, both as oLEDs that make up the individual pixels as well as oFETs that make up the active matrix (AM) for addressing those pixels. Organic semiconductor technology offers faster display refresh rates, brighter pictures, and a wider range of viewing angles relative to older technologies. Few people realize that some smartphones such as the Samsung Galaxy S II and III already employ oLEDs in the pixel arrays. Realizing fully organic portable video displays (both in the AM as well as the pixels) is a goal for the near future for fully "plastic" displays that are lightweight, shatter-proof, and flexible. In the television industry organic semiconducting technology has just recently resulted in the commercial release of the world's first *curved* panel television displays (the curve is

said to give a more immersed viewing experience).[29,30] Other devices in development include organic circuits used for potential low-cost radio frequency identification tags (RFIDs),[31] photovoltaics used in organic solar cells (oSCs) and a broad spectrum of organic thin film transistors (oTFTs) for use in electronic circuits, as well as pressure and temperature sensors.[32–34]

There have been tremendous strides towards consumer applications; however, organic semiconductors are generally plagued by short shelf lives and transitory functional lifetimes. For instance, commercial video displays include technology that has been developed to compensate for material degradation in order to expand the apparent lifetime of otherwise degraded pixels[35] and special circuits have been developed to compensate for threshold voltage shifts in oFETs for potential use in the AM.[36] They are at present generally not robust enough for most commercial applications without these types of extraneous compensation techniques. Nevertheless, development of these secondary technologies is an indication of the difficulty presented by the functionality of organic semiconductors transcended by their potential benefits.

This section reviews advances leading up to the present day field of organic semiconductors followed by a discussion on oFETs which invariably relates charge transport to molecular structure at a buried interface. Then a brief account is given of some of the standard tools used to measure structure at buried interfaces in organic semiconductor thin film systems. The conclusion is that there is a need for a technique that is interface-specific, highly sensitive, and able to measure structure at buried interfaces and on a wide variety of systems. This leads naturally to the next section on the nonlinear optical spectroscopy called sum frequency generation (SFG).

1.2.1 *A Brief History of Organic Semiconductors*

The study of the electrical properties of organic materials with conjugated and aromatic π-electron systems began with scattered reports of a few noteworthy substances but has escalated over the past 35 years to a cutting edge research field that has resulted in the commercialization of some of these technologies in the last decade. Conducting properties in small molecule organics that form crystalline solids have been studied for over 100 years. Some of the earliest work includes the report of anthracene as a photoconductive substance in 1906[37] and 1913[38] and an investigation of its dark conductivity in 1910.[39] The report of a perylene-bromine complex in the solid state with a remarkably low resistivity in 1954 was another intriguing discovery that touched on an ongoing problem in organic semiconductors: they often do not maintain optimal conductivity over time.[40] The synthesis of polyacetylene was first reported in 1958 and was shown to be a semiconductor in the solid state with variable conductivity.[41] Its conductivity remained mostly a curiosity for nearly 20 years. In the early 1970's, a report of the crystalline inorganic polymer polysulfur nitride with metallic conducting properties[42,43] rekindled interest in the electronic properties of the organic polymer.[44,45] Groundbreaking work in the late 1970's by Shirakawa, MacDiarmid, Heeger and coworkers on thin films of crystalline polyacetylene showed the possibility of an eleven order-of-magnitude increase in conductivity utilizing optimal stereochemistry and introduction of both p-type and n-type dopants.[46–49] The work on doped polyacetylene is considered the beginning of the modern age of organic electronics and is the basis for their award of the Nobel Prize in Chemistry in 2000. Following this work, the field of conducting organic polymers and molecules including their synthesis, characterization

and potential uses has exploded. There have been thousands of papers, reviews, and books published that focus on identifying organic semiconductor compounds, characterizing their physical and chemical properties, and developing applications for their use in semiconductor devices.

1.2.2 *The Organic Field-Effect Transistor*

An organic field-effect transistor is shown in Figure 1-1. The oFET configuration shown is for a bottom-gate/bottom-contact geometry used in this work (the gate electrode is separated from the source and drain electrodes by a dielectric layer).

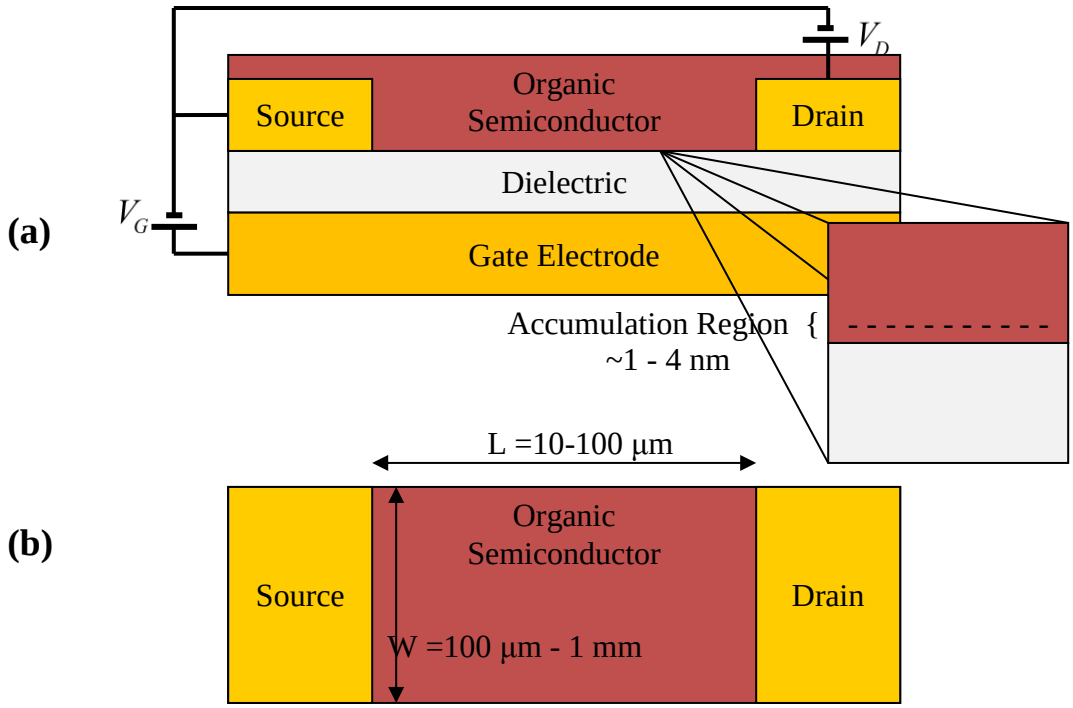

Figure 1-1. (a) Side view of the geometry of a bottom gate/bottom contact organic field-effect transistor with a look at the accumulation region. (b) Top view with dimensions of the conduction channel (not to scale).

The gate and dielectric typically consist of a doped semiconductor with an oxide insulating layer 200 - 400 nm thick (commonly silicon/silicon dioxide). The source and

drain electrodes are a metal with a work function close to the highest occupied molecular orbital (HOMO) or lowest unoccupied molecular orbital (LUMO) (depending on charge carrier type). They can be deposited directly on the insulating substrate using clean room techniques such as a photolithographic mask with electron beam vapor-deposition. The organic thin film is typically 30 – 50 nm thick and is normally deposited by vacuum sublimation or solution processing. Characteristic conduction channel dimensions are included in Figure 1-1 (b).[50,51]

An oFET is a switching device: when a suitable potential is applied at the gate electrode, V_G, charge carriers collect in a thin layer of the organic semiconductor (~1 – 4 nm) at the interface of the organic and dielectric. This interface is referred to as the accumulation layer.[50–52] Current flows in this conduction channel when a potential difference is applied between the source and drain electrodes, V_D. Charge carriers can be either holes (p-type) or electrons (n-type). The more common p-type organic semiconductors turn on with negative gate voltages whereas n-type are activated by positive gate voltages.

1.2.2.1 Electrical Characterization

There are several terms used in the literature to quantify the useful properties of oFETs. The most common measure is the field-effect mobility, μ (referred to as the mobility throughout this dissertation). The mobility is a parameter that relates the electron drift velocity, v_d, to the applied electric field E.

$$v_d = E\mu \tag{1.1}$$

It is directly proportional to conductivity, σ, through the volume number density of charge carriers, N, and the fundamental charge, e.

$$\sigma = Ne\mu \tag{1.2}$$

Mobility units are usually given in $cm^2/V*s$ and typical values for oFETs range from 10^{-7} $cm^2/V*s$ for amorphous organic films to 1 – 10 $cm^2/V*s$ for highly crystalline films.[50,53] Other important parameters include the threshold voltage V_T, defined as the limit of the gate voltage for which conduction does not occur between the source and drain electrodes, and the current on/off ratio I_{on}/I_{off} is an important measure when any small leakage in the off state is an issue.

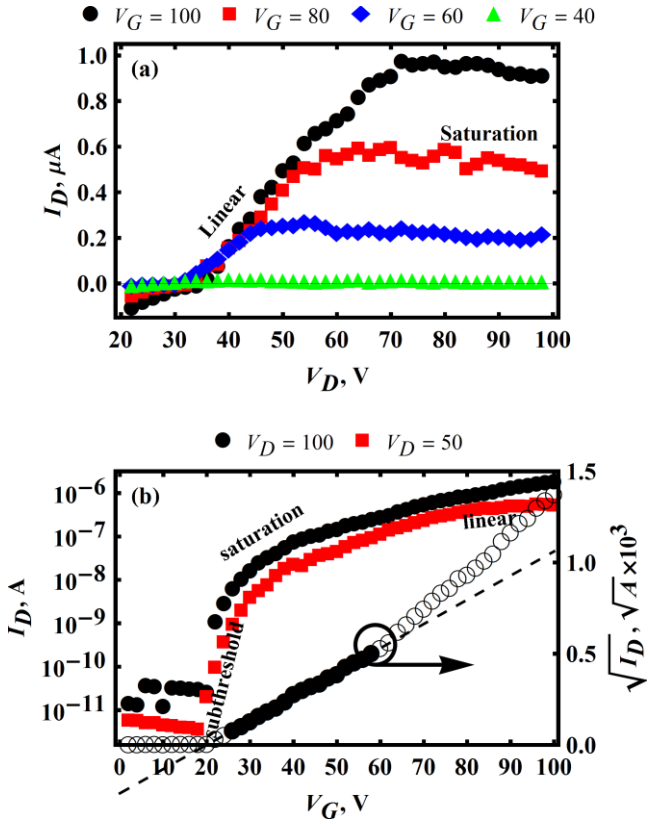

Figure 1-2. Typical output (a) and transfer (b) characteristics of PTCDI-C_8 oFETs fabricated for this project. Also, scaled on the right in (b) are data for $V_D = 100$ V shown with a typical fit to the saturation regime of the curve.

The conducting properties of oFETs are usually characterized by holding either V_D or V_G constant while sweeping over the other to obtain $I_D - V_D$ (output characteristics) and $I_D - V_G$ (transfer characteristics) curves. Figure 1-2 shows exemplary transfer and output curves taken on devices fabricated in our lab. The organic material for these scans is N,N'-dioctyl-3,4,9,10-perylenedicarboximide (PTCDI-C_8), an n-type organic semiconductor used exclusively in this work. The electrical curves were obtained under high vacuum in order to minimize effects from atmospheric oxygen and water. The curve features are discussed in what follows.

Several equations have been derived that make it convenient to characterize the mobility of oFETs experimentally.[51,52] Mobility is a consequence of the charge carrier profile in the conduction channel. The areal charge density q_{ind} (number of carriers/area) is proportional to the volume number density through the fundamental charge and the channel depth t. It is also proportional to the voltage difference between the gate voltage and the voltage along the conduction channel $V(x)$ due to the bias applied between the source and drain electrodes and through the capacitance of the dielectric material C_{ox}. Here x denotes the lateral position within the channel between the source and drain electrodes.

$$q_{ind}(x) = N(x)et = C_{ox}\left(V_G - V(x)\right) \tag{1.3}$$

Eq. (1.3) is not quite correct since the point at which charge carriers are injected into the conduction channel most often does not correspond to $V_G = 0$. Factors that shift the point of injection include barriers at the source and drain electrode/organic interfaces, impurities within the semiconductor film, deep traps that must be filled

before conduction will occur, and any other non-idealities. To compensate for all these effects the threshold voltage V_T is defined and the equation is rewritten.

$$q_{ind}(x) = N(x)et = C_{ox}\left(V_G - V_T - V(x)\right) \tag{1.4}$$

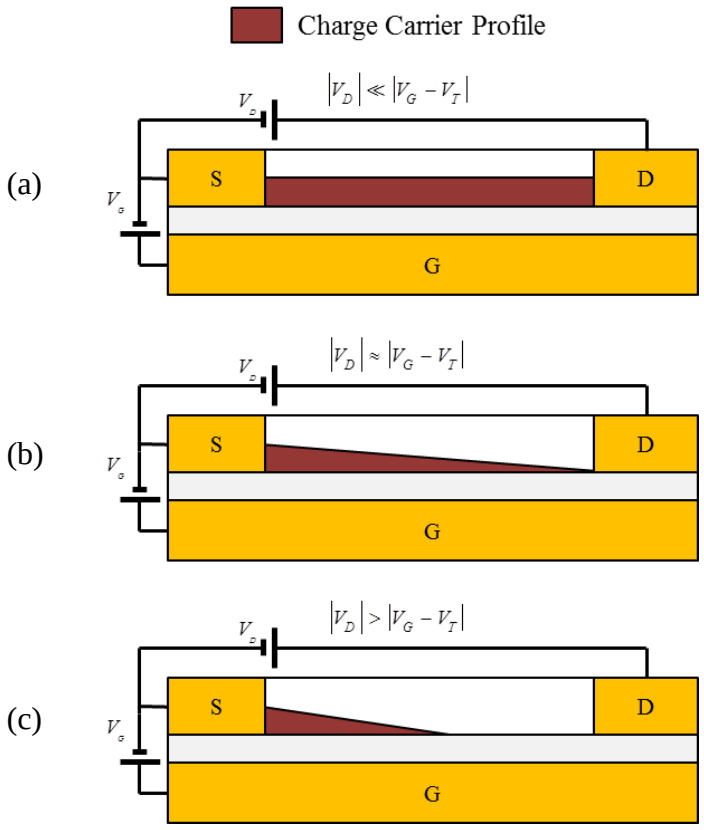

Figure 1-3. Carrier concentration profiles across the conduction channel when (a) $|V_D| \ll |V_G - V_T|$ the linear regime, (b) $|V_D| \approx |V_G - V_T|$, and (c) $|V_D| > |V_G - V_T|$ the saturation regime.

With the source electrode voltage set to ground and assuming $V(x)$ is due only to V_D, which has a linear gradient profile across the channel, the charge carrier profile takes on the spatial characteristics of V_D. When $|V_D|$ is small compared to $|V_G - V_T|$ the carrier concentration is approximately constant across the channel. As long as

$|V_D| < |V_G - V_T|$ the average value of q_{ind} can be expressed as Eq. (1.5) since the average value of a linear function is half its maximum value plus its intercept.

$$\langle q_{ind}(x) \rangle = \langle N(x) \rangle et = C_{ox}\left(V_g - V_T - \frac{V_D}{2} \right) \tag{1.5}$$

Figure 1-3 shows qualitative representations of the carrier concentration in the accumulation region for the cases that $|V_D| \ll |V_G - V_T|$, $|V_D| \approx |V_G - V_T|$, and $|V_D| > |V_G - V_T|$.

In order to obtain the $I-V$ relationships, the derivation begins with Ohm's law and substitutes in the results from Eqs. (1.2) and (1.5).

$$\begin{aligned} \frac{I_D}{A} = \sigma \frac{V_D}{L} &\rightarrow \frac{I_D}{tW} = \langle n(x) \rangle e\mu \frac{V_D}{L} \\ I_D &= \frac{W}{L} C_{ox}\mu \left(V_G - V_T - \frac{V_D}{2} \right) V_D \\ &= \frac{W}{L} C_{ox}\mu \left[(V_G - V_T) V_D - \frac{V_D^2}{2} \right] \end{aligned} \tag{1.6}$$

The final result of Eq. (1.6) gives the I-V equation in the linear regime, that is, the current is linear in V_G at small V_D. At higher V_D the carrier density can become clipped which makes the linear gradient approximation invalid.

There are three regions defined for $I-V$ curves: the subthreshold, saturation, and linear regimes (refer to Figure 1-2). In the subthreshold part of the $I_D - V_{G/D}$ curves $|V_G| < |V_T|$, the oFET has no connected carrier accumulation and Eq. (1.6) is invalid. With $|V_G| > |V_T|$ there are two regimes of operation. When $|V_D| \approx |V_G - V_T|$ the curves are approaching saturation, the point at which the carrier concentration becomes pinched at

the drain electrode, and when $|V_D| \gg |V_G - V_T|$ the curves are in the saturation regime and the carrier profile is clipped. In the saturation regime any increase in V_D leads to no increase in current since the integrated resistance remains constant in the channel. When $|V_D| \ll |V_G - V_T|$ the quadratic V_D term in Eq. (1.6) can be dropped and is referred to as the linear regime of the curves.

Two derivatives are useful for calculating the mobility, the transconductance g_m and conductance g_d.

$$\begin{aligned} g_m &= \left.\frac{\partial I_D}{\partial V_G}\right|_{V_D} = \frac{W}{L} C_{ox} \mu_{lin} V_D \\ g_d &= \left.\frac{\partial I_D}{\partial V_D}\right|_{V_G} \approx \frac{W}{L} C_{ox} \mu_{lin} \left(V_G - V_T\right) \end{aligned} \tag{1.7}$$

Eq. (1.7) shows results for calculating the mobility in the linear regime (μ_{lin}). In the saturation regime V_D can be approximated by setting it equal to $V_G - V_T$.

$$I_{D,sat} = \frac{W}{2L} C_{ox} \mu_{sat} \left(V_G - V_T\right)^2 \tag{1.8}$$

The mobility can then be calculated from the $I_D - V_G$ curves in the saturation regime most easily by fitting $\sqrt{I_{D,sat}}$ curves (see Figure 1-2 (b), the right side axis).

The simple equations derived and commonly used are based on sweeping approximations; thus, they do not fully account for characteristic $I - V$ curves. As a result, experimentally determined mobilities in the linear and saturation regimes often do not agree.[50–52,54,55] Experiments have shown that other effects are important such as injection barrier effects from the source and drain electrodes and mobility dependence

on V_G and V_D.[51,54,56,57] It is for these reasons that mobilities are usually calculated in the linear regime where the approximations are considered to be more valid.

1.2.2.2 Charge Mobility Theories

Charge mobility theories account for the microscopic static and dynamic processes that are responsible for the macroscopic conducting properties of oFETs. There are numerous sophisticated models that have been developed for the mechanism of charge transport on the many different classes of oFETs;[58–63] however, the nature of charge mobility is still not well understood.[50,64,65] At present, it is thought that these devices operate by some mix of a charge hopping and polaronic mechanisms. The dependent variable to test mobility models is usually temperature since it is the easiest "knob to turn," experimentally. The charge hopping regime is temperature-assisted and is usually used to describe mobility in highly amorphous films. The polaron model is temperature-limited and usually applied to crystalline films.

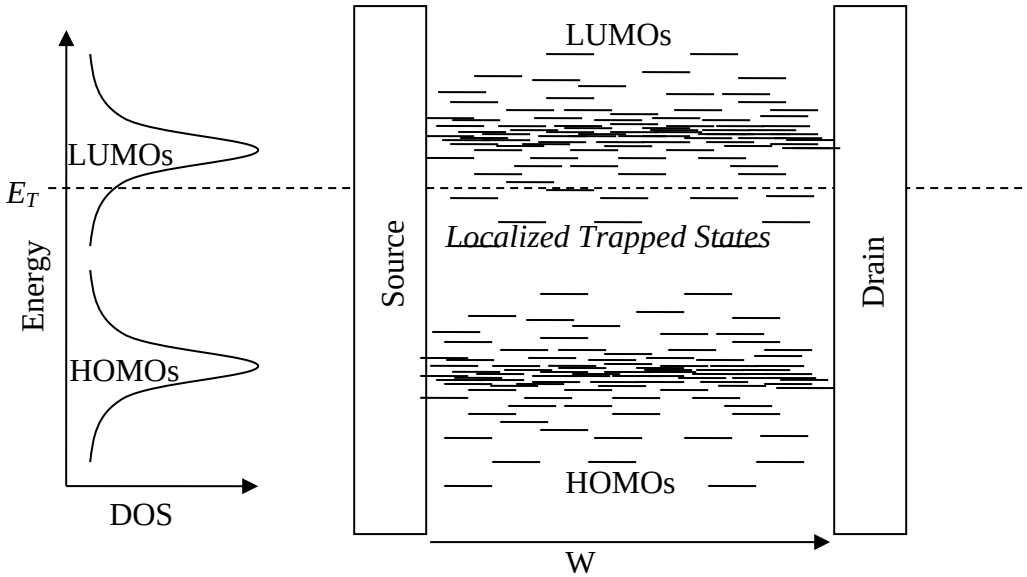

Figure 1-4. Graphical representation of the charge hopping theory in amorphous organic films for a negative (electron) charge carrier.

Charge hopping theory treats molecular groups as forming spatially discrete states within the conduction channel and contributing to a distribution in the density of states (DOS) occupiable by charge carriers. [59] In the simplest approximation, these may be thought of as the molecular HOMOs for holes or LUMOs for electrons. Figure 1-4 depicts the theory graphically for a normally distributed DOS and a negative (electron) charge carrier. When charge carriers are injected they must hop between these localized states along the width of the conduction channel (in one dimension for simplicity) while staying above some defined temperature dependent trap energy, E_T. Carriers that fall into states below the trap energy are said to be trapped. This mechanism is temperature assisted: higher thermal energy allows carriers to overcome energetic barriers between adjacent states due to disorder. Thermally induced waves (phonons) in the film rapidly change the interactions of molecular orbitals (MOs) on adjacent molecules on the time scale of hopping events. This renders states that are at one instant a trap in another instant a conducting state. Increased thermal energy also raises the probability for carriers to hop out of deeper tr $\mu \propto \exp\left(-\frac{\Delta}{k_B T}\right)$ apped states. Experimental data and hopping models have indicated mobility has an Arrhenius-like dependence on temperature T.[51,66]

(1.9)

Here Δ is the activation energy for the barrier and k_B is the Boltzmann constant. Experimental evidence for trap states has been obtained using the method of thermally stimulated currents (TSC) as well as thermally stimulated luminescence (TSL) on amorphous organic films.[67–69]

The distribution in the DOS (and therefore the density of trapped and conducting states) is strongly dependent on film morphology. Highly amorphous films lead to wider distributions with more electronic trap states, which in turn lead to lower mobilities. Defects in the film (i.e. impurities) can cause additional local trap sites in the HOMO-LUMO gap.[51,64–66,69] Specific systems can have widely varying DOS characteristics which has a direct effect on overall device performance.

For highly ordered crystalline films, charge hopping theory does not account for the inverse-power law dependence of mobility on temperature.[51,70] At very low temperatures, measured mobilities are high and reflect the band theory of inorganic semiconductors. With the exception of a few highly pure crystals that demonstrate high mobility and anisotropy at ambient temperatures (e.g. rubrene >5 $cm^2/V*s$),[53,71,72] measured mobilities at elevated temperatures of most organic crystals correspond to mean free paths that are less than the intermolecular distances.[51] These results exclude the delocalization assumed in the band theory of semiconductors.

Polaron models have been developed to account for the temperature dependence of mobility in highly ordered organic films. A polaron is thought of as a quasi-particle that travels through the lattice. It consists of a charged particle (electron or hole) and the accompanying distortions in the lattice associated with a reorganization energy. Figure 1-5 illustrates a simple physical description of the polaron in one dimension.

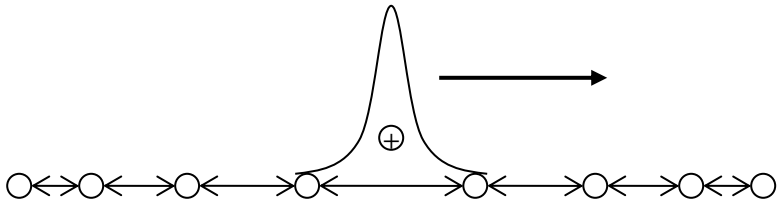

Figure 1-5. Illustration of a hole-polaron moving in a one dimensional lattice, the circles are nuclei.

Eq. (1.10) is the result for one derivation of the theory that relates the mobility to temperature in the high temperature limit. E_b is the polaron binding energy, defined as the energy gain of an infinitely slow carrier due to the polarization and deformation of the lattice.[17]

$$\mu \propto \frac{1}{\sqrt{E_b}\left(k_B T\right)^{3/2}} \exp\left(-\frac{E_b}{2k_B T}\right) \tag{1.10}$$

The interactions of the polaron with thermally induced phonons predict restricted charge flow with temperature ($T^{-3/2}$ dependence) when $k_B T \gg E_b$. The polaron model also accounts for self-trapping that occurs due to the reorganizational energy of the lattice. In molecular crystals the polaron model is a limit on the charge hopping model where the DOS of conducting states is very narrow.

Another model commonly encountered in the literature is known as the multiple trapping and release mechanism (MTR). It was originally developed for amorphous silicon semiconductor (α-Si) devices but has since been applied to organics.[17,65,73] The model assumes delocalized band transport with a high concentration of localized electronic trapped states near the band edge. MTR has been applied primarily to organic devices consisting of small molecule crystalline films; however, meaningful

results are obtained over limited temperature ranges.[51,65,74] MTR is generally not considered a complete description of charge transport in oFETs.

Charge mobility in organic semiconductors is thus described as some mixture of three basic mechanisms: carriers hopping between localized states with some states defined as traps, carriers described as polaronic quasi-particles moving through lattice sites defined with some polaron binding energy, and carriers moving in delocalized states comparable to the semiconductor band model, which may include localized traps below the band edge. The dominant mobility limiting mechanisms in the majority of oFETs are thought to be hopping versus polaronic. Amorphous films are typically modeled well by the hopping mechanism whereas crystalline films are better modeled with polarons. The switch between these two mechanisms is believed to occur with mobilities around 0.1-1.0 $cm^2/V*s$, the region in which many oFETs are found.[64]

Considerations for modeling specific systems must factor in film morphology. This includes the extent of disorder, defects, and impurities, as well as the degree of molecular orbital overlap, anisotropy in any crystalline regimes, and effects from grain boundaries in films that form amorphous as well as crystalline regions (i.e. poly(3-hexylthiophene-2,5-diyl, P3HT)).[75] The dielectric layer has also been shown to play an important role in charge transport.[76–78] While a unified theory on charge mobility remains unresolved, there is a clear connection to molecular packing that is inextricable connected to molecular structure.[79] Better understanding will come with experiments that elucidate structural information.

1.2.2.3 Charge Transfer Theory

The mobility theories as presented mask the connection to the microscopic processes that occur in order to move charges through the system. The fundamental process is that of charge transfer from an initial localized quantum state ψ_i to a final state ψ_f coupled to a density of final states $\rho(E_f)$. The process can be viewed as a nonradiative decay of an electronic state. The chemical equation can be written in terms of charge donor and acceptor species.

$$D^{-\psi_i} + A \underset{k_{fi}}{\overset{k_{if}}{\rightleftarrows}} D + A^{-\psi_f} \tag{1.11}$$

Using first order perturbation theory one writes a transition rate constant k_{if} at long times as[52]

$$k_{if} = \frac{2\pi}{\hbar}\left|\langle \psi_f | V | \psi_i \rangle\right|^2 \rho(E_f) \tag{1.12}$$

The electronic coupling matrix element between initial and final states depends on the molecular orbital overlap and the interaction energy V. The functional form of $\rho(E_f)$ includes temperature effects, reorganization energy, free energy (including effects from applied bias), and effects from vibrational coupling. For instance, in the high temperature regime, that is, for vibrational modes satisfying $\hbar\omega \ll k_B T$ the rate expression takes the form of semiclassical Marcus theory[80,81]

$$k_{if} = \frac{2\pi}{\hbar}\left|\langle \psi_f | V | \psi_i \rangle\right|^2 \sqrt{\frac{1}{4\pi\lambda k_B T}} \exp\left[-\frac{(\Delta G^0 + \lambda)^2}{4\lambda k_B T}\right] \tag{1.13}$$

where ΔG^0 is the Gibbs free energy of the reaction and λ is the reorganization energy.

The transition rate describes the static and dynamic effects that influence mobility on a microscopic scale. From the electronic coupling matrix element it is clear that molecular alignment and molecular structure are important parameters to consider. On a macroscopic scale, orbital overlap varies in amorphous regions or in films with distinct domains (e.g. grain boundaries vs. polycrystalline domains). It is the macroscopic scale that directly influences overall device performance so that average molecular structure through the device channel is an important parameter when assessing contributions to overall device mobility.

1.2.3 *Survey of Structural Characterization at Buried Interfaces*

For oFETs, the active interface is internal to the thin film system (i.e. buried), so that the problem of characterizing molecular structure poses particular challenges. There are numerous approaches to characterizing the structure of interfacial molecules, each possessing its own strengths and weaknesses. X-ray techniques that measure specular reflectivity or diffraction in grazing incidence to wide angle operation can be used to sample film structure on many different length scales.[82–85] These techniques typically sample the entire thin film system and extracting information on the interfaces is a matter of setting up an appropriate model and beam geometry. The models and theory behind X-ray scattering are well-established and the data interpretation is often clear. On the other hand, these approaches sample only the most ordered (crystalline) regions of the thin film, while the amorphous fraction may contribute significantly to device success. Furthermore, the grazing incidence beam geometries that can be utilized to access interfacial information are limited to total external reflection, generally probing the outer interface or a combination of bulk and interfacial

contributions.[86–89] X-ray spectroscopic techniques have also been demonstrated as surface sensitive probes. For example, near edge x-ray absorption fine structure (NEXAFS)[90–92] or X-ray photoelectron emission microscopy (X-PEEM)[93] can be used to deduce structure at an interface. However, they are generally limited to sampling exposed interfaces.

Scanning probe microscopy (SPM) techniques like atomic force microscopy (AFM) or kelvin probe microscopy (KFM) offer mesoscopic spatial resolution of topography and surface potential.[18,94–100] Microscopic structure can sometimes be inferred by these measurements;[95,101] however, they are inherently biased to probe the external surface. Buried interfaces are sometimes studied by SPM by fabricating extremely thin films (< 1 monolayer) and assuming that what is learned about this layer also applies to the buried interface of a thicker film.[102,103]

Optical spectroscopies offer the advantage of non-destructive characterization but their signals are generally overwhelmed by bulk response. Surface-enhanced spectroscopic techniques like surface enhanced Raman spectroscopy (SERS) may offer very high surface sensitivity but have extremely restrictive requirements for the substrate. In other instances, buried interfaces have been studied by physically removing the film from the substrate at low temperatures and carrying out X-ray or SPM measurements on the newly exposed surface.[104,105] Of course, this destructive approach renders the device unviable for further testing and likely perturbs the (formerly) buried interface.

Many of these techniques are complementary, and a common strategy is to use some combination of experiments to impart some confidence in data interpretation.

With this in mind, a broad implication of this work is to contribute to the viability of adding nonlinear spectroscopy as an additional tool for the surface scientist studying buried interfaces in thin film systems.

1.2.4 *Conclusion*

Developing organic semiconducting devices with stable mobilities and threshold voltages, high I_{on}/I_{off}, and having long functional lifetimes is of paramount importance for applications involving oFETs. While there have been some noteworthy breakthroughs in terms of device performance;[106–109] deep physical understanding of primary factors affecting device functionality is generally either elusive, or is obtainable only for specific systems. Organic semiconductors have now been studied for over 30 years with many elegant physical discoveries, but there remain many fundamental questions.

In terms of understanding factors that are relevant to device performance and degradation there are still considerable challenges. These include low charge carrier mobilities, high threshold voltages, threshold voltage drifts, current leaks, bias-stress effects, deep traps, environmental instability, and variable switching rates.[65,110] Bias-stress effects are important because applied voltages can induce permanent changes in oFET functionality. Deep traps contribute to decreased mobility over time and current leaks. Environmental instability is very important especially for n-type devices because of susceptibility to oxidation from atmospheric oxygen. Stable switching rates are important for applications that involve high speed on/off switching such as graphical displays.[111] All of these affect or are affected by the microscopic geometric and

electronic structure in the active interfacial region of these devices. This region is the focus of this project.

Characterizing the structure of molecules in the active region of oFETs is a particularly challenging problem. The two most basic requirements of an ideal experiment for studying molecular structure at a buried interface in an organic thin film system are that it is selectively sensitive to molecules at the interface and that it can be applied to a wide variety of systems. This is the motivation for applying nonlinear spectroscopy to organic thin film systems. For SFG, the selection rules are such that there is high sensitivity to interfacial molecular structure and it can be applied to any system accessible by light.

1.3 SUM FREQUENCY GENERATION SPECTROSCOPY

Linear optical spectroscopies describe light-matter interactions at electromagnetic intensities that do not alter the material optical properties. In that regime, the familiar quantity called the refractive index $n = \eta + i\kappa$ has real and imaginary parts that vary with the frequency of light but are otherwise invariant to input field light intensity, and for this reason they are known as optical constants. Linear interactions can also be described in a more fundamental way as materials that have an optical response that is linear in the applied electromagnetic field amplitude. This relation describes our most common experiences with light-matter interactions such as reflection, transmission, diffraction, absorption, and thin film optical interference.

When the intensity of light is sufficiently high – as when illuminated by an intense laser beam – the optical response of a material may become nonlinear in the incident electromagnetic field amplitude. There are many consequences of optical nonlinearities; they lead to such effects as the optical Kerr effect (self-focusing, self-phase modulation), cross phase modulation, and wave mixing. Sum frequency generation is described within the latter of these effects. The interest in nonlinear optical techniques stems from the unique interactions that give rise to distinct selection rules relative to linear techniques. For SFG, the primary selection rule concerned here is that, within the electric dipole approximation to the interaction with light, systems that possess inversion symmetry on a macroscopic scale will have a possible SFG response only at phase interfaces where inversion is necessarily broken. Details of this statement are discussed in Section 1.3.2. The combination of wave mixing and its interfacial selection rule make SFG an experimentally powerful tool to study molecules at interfaces.

In this section a historical background for interfacial SFG is recounted followed by a review of the theory of SFG from classical electrodynamics for a single interface system. The macroscopic observables are related to the microscopic polarization described by quantum mechanics. In Section 1.3.2 a discussion on the origin of the interfacial selection rule is provided that inevitably results in the structural sensitivity of SFG. Bulk contributions are considered as a reminder that most SFG data analysis involves an approximation that may not always be valid. But in the presence of resonant enhancement and polar ordering at an interface, the conclusion is that SFG is a sensitive probe to interfacial molecular structure.

1.3.1 *Historical Perspective*

1.3.1.1 The 1960's − Classical Antiquity

With the advent of the first functional optical lasers in 1960,[112,113] scientists were exposed to a new type of light source that provided coherent radiation at unprecedented high intensities. Less than a year later the first demonstration of coherent wave mixing was reported when Franken, Hill, Peters, and Weinreich reported second harmonic generation (SHG) from a quartz crystal in July of 1961.[114] In the following year there were several experimental reports of coherent three-wave mixing in various nonlinear media[114–119] including the first report of SFG.[115] Experiments inevitably led to a more formal treatment of the theory. The theoretical implications for nonlinear response from coherent radiation (versus incoherent sources) was first recognized by Armstrong, Bloembergen, Ducuing, and Pershan in early 1962 when they formed a mathematical foundation for coherent wave mixing in a dielectric.[120] They formulated a quantum mechanical microscopic description using semiclassical perturbation theory that mapped onto the classical macroscopic description of electrodynamics given by Maxwell's equations and the Lorentz force. This work is the origin of the connection between the microscopically averaged contributions to the macroscopic nonlinear polarization commonly used today.

The importance of boundary conditions between linear and nonlinear media were acknowledged in the early theoretical work[120] and details were provided by Bloembergen and Pershan in a separate report in 1962.[121] This marked the first consideration for three-wave mixing optical nonlinearities as a possible surface boundary probe. In that paper they specifically considered SHG *reflected* from an

otherwise semi-infinite nonlinear crystal (KDP). However, as KDP lacks inversion symmetry, their discussion relied on the *bulk* electric dipole contribution to the SHG response. The reflected intensity was said to have contributions from a layer thickness on the order of the wavelength of light. They also introduced the idea of a nonlinear material slab of finite thickness for transmitted SHG although they did not make the connection to a polarized sheet (limit of zero thickness), which has become an important concept in the current theory.

It was recognized early on that the leading terms in any three-wave mixing nonlinear response are due to electric dipole interactions, which are zero in materials that possess inversion symmetry.[120–123] The next highest terms are the electric quadrupole and magnetic dipole interactions which are generally bulk active, although many orders of magnitude smaller than typical allowed electric dipole type interactions. As work on centrosymmetric systems progressed in the 1960's, much of the experimental observations were thus formulated based on the idea that dominant contributions came from electric quadrupole and magnetic dipole type interactions. The first observation of SHG from a crystal with inversion symmetry came in 1962 by Terhune, Maker, and Savage.[119] The nonzero response from calcite was attributed to the higher order terms from the bulk and a third order electric dipole effect due to application of an external static electric field.

The theory was modified a few years later to include a "surface-type" electric quadrupole term, distinct from the bulk contribution, that arose due to the predicted abrupt discontinuity of the normal component of the electric field amplitude at a material boundary.[124–126] During the early years, experimental work on

centrosymmetric systems focused on SHG (as opposed to generalized SFG) observed from metals,[126–131] semiconductors,[121,130–132] dielectrics,[131] and liquids.[133] The studies were primarily purposed to test the theories in this new field with an emphasis on determining the origin of the surface contribution. A summary of the experimental and theoretical contributions from this early work was published in 1968.[134] An important idea that emerged from these first few years of coherent three-wave mixing was that the interfacial atomic layer should provide a distinct nonlinear response as compared to the bulk of the material.

The next advancement in the theory of three-wave mixing was the recognition that the surface of a material itself is somehow intrinsically different from the bulk, as opposed to a difference in the way in which applied electromagnetic fields behave differently at a boundary. That is, to this point the surface contribution was attributed to the bulk quadrupolar interaction being amplified by the large interfacial field gradient, and there had been no consideration for distinct interfacial material properties. The idea was inspired by the possibility that surface contamination affected the surface SHG process, as was originally acknowledged by Wang in 1968 with his work on water and acetone.[133] In 1969, Brown and Matsuoka systematically studied the effects of surface contamination by observing SHG intensity changes from evaporated silver films in high vacuum before and after breaking the vacuum.[135] To explain the changed SHG response, they conjectured that the atoms at the interface experience a break in the otherwise isotropic bulk symmetry and are therefore subject to a nonzero *interfacial* electric dipole type interaction. This marked the first consideration for a unique material response due to inversion symmetry breaking at the interface. The newly

defined dipole-allowed surface states were said to be highly sensitive to adsorbed species and possibly even caused by these species (although their discussion focused primarily on the latter hypothesis, the former statement is generally considered correct today). Two years later, Rudnick and Stern produced a detailed theoretical consideration for symmetry breaking at an interface and the resultant dipole-allowed surface states.[136] That work contains a comprehensive discussion on the various source terms related to three-wave mixing in metals. Surface states at a metal interface were considered in more detail by Wang, Chen, and Bower in 1973.[137]

1.3.1.2 The 1970's − The Middle Ages

Experiments in the 1970's focused primarily on metals as interest extended beyond the basic ideas of free and core electron contributions to the SHG signal into resonant enhancement by surface waves at metal interfaces that were originally predicted in 1909.[138] The first observation of resonantly enhanced SHG by surface plasmons came in 1974 by Simon, Mitchell, and Watson,[139] which was followed by a number of theoretical and experimental reports.[140–149] Experimentally, attenuated total reflection (ATR) geometry was introduced at this time as theoretical and experimental efforts showed large enhancements in wave-mixing experiments due to better coupling between propagating fields and surface waves.[136,139,150] The primary emphasis continued to be on connecting experimental observations to theoretical predictions. As it turned out, coupling of fields to surface plasmons in metals to produce SHG was inefficient and not surface selective since the evanescent wave penetrated the metal surface on the order of the wavelengths involved, usually several hundred

nanometers.[151,152] However, resonant enhancement of the wave mixing process, which was theoretically discussed earlier,[126,130] was an important experimental initiative explored during this time.

1.3.1.3 The 1980's − The Renaissance

A report in 1973 on SHG from Ge surfaces with Na controllably evaporated to sub-monolayer coverage is perhaps the first *quantitative* report of SHG as a surface probe.[153] However, the distinction between experimentally substantiating theory and actually characterizing an interface is somewhat vague, and the switch to application of SHG and SFG as a surface analytical probe is generally attributed to work that began in 1980 in Professor Yuen-Ron Shen's research group at Berkeley. Research to this end arose when they made the connection that the large surface enhancements observed in SERS[154] could apply to wave mixing experiments and that those enhancements should report on phenomena occurring only at the metal interface. In October of 1980, Chen, Castro, and Shen reported SHG enhancement of 10^4 by a roughened silver surface.[155] Several reports from that group followed demonstrating interfacial sensitivity of SHG using surface enhancement effects.[156–158] These efforts led to a re-examination of SHG and SFG, theoretically and experimentally.[159] Early estimates predicted insensitivity of three-wave mixing to surface contamination or surface orientation of cubic crystals;[131,133,134] however, aside from the scattered earlier reports on surface adsorbates,[131,135,153] important advances during the 1980's included the realization of sub-monolayer sensitivity[156–163] as well as surface rotational anisotropy of otherwise centrosymmetric crystals.[164–169] The general recognition of the importance of

measuring well-defined surfaces with superior experimental control was introduced during this time, a number of reviews from the mid 1980's summarize the topics.[170–172]

While the connection between macroscopic three-wave mixing to microscopic structure was laid out much earlier,[120] the first reports of SHG as a probe for molecular structure at an interface only began to emerge in the early 1980's. This is generally considered to be a major strength of these techniques today. In 1981, Heinz, Chen, Ricard, and Shen reported on two rhodamine dye monolayers adsorbed on a fused silica substrate in which they measured SHG enhanced by electronic resonance and were able to deduce a rough average molecular polar orientation on the surface.[160] Absolute orientation calculations for molecules adsorbed at interfaces was a major step forward for three-wave mixing techniques as numerous studies relating surface properties on atomic and molecular scales emerged including molecular adsorbates on solids,[160,173–189] adsorbates and interfaces of liquids,[190–203] and processes occurring at electrodes in electrochemical cells.[163,204–216] A number of these studies exploited the pulsed nature of the input beams to explore kinetics on many time scales.[163,167,191,192,196,197,204,209,216] A noteworthy early study of ultrafast structural dynamics came from Shank, Yen, and Hirlimann in 1983 when they observed loss of rotational anisotropy at the Si interface on a sub-picosecond timescale by optically melting the surface.[167]

Important advances in laser science allowed for expanding three-wave mixing experiments to new wavelengths and energies. In the 1980's, Q-switched lasers (and higher harmonics thereof) were the typical source of short (ns) and high intensity pulses used for SHG. These were often used to pump dye lasers to make tunable sources in the visible in order to perform electronically resonant studies and capture the dispersion in

the response. In late 1986, Zhu, Suhr, and Shen used a frequency doubled Q-switched Nd:YAG and a CO_2TEA laser (tunable mid-infrared pulsed laser source) to demonstrate the first successful *vibrationally* resonant enhancement of an SFG (VSFG) spectrum from coumarin 504 spin coated onto a fused silica substrate.[217] The extension of three-wave mixing to surface vibrational spectroscopy was then quickly demonstrated on solid-air,[217–222] liquid-air,[218,219,223] and solid-liquid interfaces.[219] Vibrational spectroscopy was long established as a powerful tool for structurally characterizing molecules, and the monolayer and surface sensitivity of VSFG was immediately recognized as a powerful new tool for determining molecular orientation, conformation, and relative order (or disorder) at interfaces.

Along with the experimental advances in the 1980's came clarification and unification of the theories used to describe those processes.[159,171,173,177,183,184,224–240] The phenomenological polarized sheet description of the nonlinear interfacial region was the primary model for interfacial wave mixing.[184,230,241] The basic problems for centrosymmetric systems were (and continue to be) describing signals generated from the bulk volume and separating interfacial contributions due to 1) abrupt field discontinuity of the normal components (interfacial quadrupole terms), 2) a second group of quadrupole terms arising from the discontinuity in the bulk susceptibility at the interface, and 3) the dipole-allowed terms due to symmetry breaking at a phase boundary.[159,229,234,236,237] Any dipole-allowed response is commonly referred to as a "local" response whereas higher order quadrupole and magnetic dipole terms are usually referred to as contributing to the "nonlocal" response.[226,234,235] Whereas the bulk (volume) terms had been previously well described,[120,122–125,127,128,130,133,134,136] it

was shown that all the local and nonlocal contributions to the surface sheet polarization $\mathbf{P}_s(\Omega)$ can be combined into a single effective surface susceptibility $\vec{\vec{\chi}}_s^{(2)}(\Omega=\omega_1+\omega_2)$ and put into a form consistent with an *apparent* local-response-only to input field amplitudes $\mathbf{E}(\omega_1)$ and $\mathbf{E}(\omega_2)$.

$$\mathbf{P}_s(\Omega)=\vec{\vec{\chi}}_s^{(2)}(\Omega=\omega_1+\omega_2):\mathbf{E}(\omega_1)\mathbf{E}(\omega_2) \tag{1.14}$$

Arrival at the form of Eq. (1.14) came about a few different ways, varying primarily with where the input fields are measured (input fields versus local fields) and how to define the relevant contributions to $\vec{\vec{\chi}}_s^{(2)}(\Omega=\omega_1+\omega_2)$.[224,225,231,237] This is the basic equation frequently used today to describe second order nonlinear response. It was noted during this time that orientational analysis is more tractable if the response is dominated by the local (dipole-allowed due to symmetry breaking) term contained in $\vec{\vec{\chi}}_s^{(2)}(\Omega=\omega_1+\omega_2)$ but verifying that this term dominates is not trivial. However, for systems that are on resonance with either one of the fundamental beams or the sum frequency it is generally thought that the resonant enhancement of the local response will be comparable to or dominate the nonlocal response.[21,234,235,238]

1.3.1.4 The 1990's

By the 1990's, SFG and SHG had been demonstrated as effective surface probes and the theoretical framework that is used today had been more or less completely worked out. A comment by Bloembergen in a 1999 invited paper gives a retrospective evolution of coherent nonlinear surface techniques and is the basis for naming subsections in this chapter.[242]

For this topic one may designate the decade of the sixties as the period of "classical antiquity", the seventies as the Middle Ages, with the Renaissance starting in 1980.

Applied studies of SFG and SHG had become extremely prevalent, of which only a small fraction are mentioned here. Among the systems studied in the 1990's, liquid interfaces became a popular subject because second order wave mixing techniques were identified as the only experiments available with the necessary surface sensitivity in the presence of the bulk. They offered the only means by which to study liquid boundaries since they do not require a high vacuum environment such as needed by particle accelerator type interfacial measurments.[243] Systems studied included neat liquids,[244–253] binary mixtures,[247,248,254–256] liquid/liquid boundaries,[246,257–260] and adsorbates and solutes at liquid interfaces.[251,260–272] A number of review articles summarize the important aspects of these studies.[22,242,243,246,258,273–276] An essential experimental demonstration that emerged was the emphasis placed on the utility of characterizing *buried* liquid interfaces with SFG and SHG.

1.3.1.5 2000 to Present

There have been many advances since the 1990's; here a few noteworthy developments for SFG and SHG in the past 10-15 years are mentioned. The polarization null angle (PNA) method applied to SFG was developed in 2003 for better molecular orientational sensitivity relative to the method of polarization intensity ratios (PIR) for *single interface* systems. The operating principle being that the input beams are set to some fixed mixed polarization and signal is measured as a function of SFG

polarization angle. Where there is a minimum in signal corresponds to the "null angle" which can be used to extract orientational information. Interference methods using a reference field overlapped with the signal field has been demonstrated for phase-sensitive[24,277,278] and sub-monolayer sensitivity.[279] SFG microscopy has been developed and improved to reveal spatially resolved structural information and orientational distributions on micron length scales[280–285] and for high throughput measurements.[286] Nonlinear optical ellipsometry has been described and demonstrated for single interface systems.[287,288] Finally, experimental techniques have been largely confined to detect in the frequency domain. In recent years the importance of time domain phenomena, which are a result of the ultra-short femtosecond pulses commonly used, have been investigated. Specifically, the effect of apodization of the vibrational free induction decay that occurs when either the visible pulse is too short or when trying to suppress nonresonant background signals by introducing a temporal delay between the visible and mid-infrared pulses.[289–291] Along those lines, the development of mid-infrared pulse shapers have led to phase control needed to extend the detection schemes into the time domain, the advantages being that only a single element detector is needed and the elimination of time domain artifacts in the detected signal.[292]

1.3.1.6 Application to Organic Thin Film Systems

Interference effects in coherent wave-mixing experiments had been considered for bulk-allowed systems as early as 1962 with the classical report of "Maker's fringes" by Maker, Terhune, Nisenoff, and Savage.[117] In that report, oscillations in intensity were the result of phase mismatch between the pump and SHG fields through the bulk

crystal. By angle tuning, they showed there is an optimal effective crystal length related to the period of oscillation in the total SHG output intensity. However, optical interference effects due to thin film systems (which lead to oscillations similar to Maker's fringes, but of a different physical origin) were not widely explored until after calculations in the 1970's suggested that conjugated organic molecules and polymers should have large nonlinear responses.[293–296] While theoretical and experimental efforts in the 1970's and 1980's on organic materials in the solid state were primarily motivated by bulk response for higher frequency conversion efficiencies,[293–300] a specific interest in describing second order *surface* nonlinearities within multilayer thin film systems began a bit later.

In 1987, Sipe formulated a theory for calculating fields generated within a multilayer system using Green's functions for generated fields and the transfer matrix to propagate them out to either side of the system.[231] The coefficients needed to transfer internally generated fields out were given in a general form but only explicitly considered for the simplest case of a system compose of a single thin film. It was noted at that time that the Green's function approach alone can, in principle, be used to calculate the far-field generated signals from multilayer structures. The technique requires setting up Maxwell's equations for a given source polarization while using boundary conditions for each interface. However, solving this set of differential equations is fairly involved and the procedure must be done independently for unique systems. Further, it does not lead to a physically familiar picture of light progressing through the stack as a series of reflections and transmissions.[231,301–309] To date, the transfer matrix approach of Sipe has had some traction with surface nonlinear optical

experimentalists; primarily applied to systems composed of a single thin film.[23,310–320] However, within the community the picture of light (both input beams and generated beams) as a geometric series of reflections and transmissions has been the prevailing epitome used to describe experimental observations, likely because it is physically intuitive and offers insight into interpreting observations. It should be noted that Sipe's transfer matrix approach incorporated into the Green's function solution to fields generated from the interfaces of a system composed of a single thin film is equivalent to accounting for infinite reflections and transmissions at the boundaries of the thin film.

An interesting study of third harmonic generation (THG, a bulk dipole-allowed third order response) by Messier and Ledoux in 1983 touched on the two-interface optical interference phenomenon viewed as a series of reflections and transmissions.[297] In that work, they deposited LB films of polydiacetlyene on each side of a quartz substrate (THG inactive) and varied the angle of the sample to observed oscillations in the THG intensity, similar to Maker's fringes.[117] They modeled their data as two interfacial sources separated by the substrate thickness where the signal detected was a truncated coherent sum of reflections and transmissions from each source. This formally bulk-allowed experiment unexpectedly marks the earliest consideration for a system with two nonlinear interfaces that interfere at the intensity level, a primary concern of this dissertation. They noted that the very simple model they used was subject to large errors in other systems if reflection and transmission at boundaries were larger.

While studies on ultrathin LB films, surfactant monolayers, or self-assembled monolayers (SAMs)[175,178,181,185,219,222,223,236,260,261,266,267,269,321,322] may be regarded as the

first experimental application of SFG and SHG to thin film systems, the context of this dissertation is thin film systems thicker than a few monolayers but thinner than the coherence length of light in SFG experiments (c.a. microns).[323] In this regime, the macroscopic local field amplitudes as well as generated fields must be corrected for thin film interference effects. Formulating this as a series of reflections and transmissions was first explicitly considered for surface-specific SHG in 1991 by Feller, Chen, and Shen in a report on liquid crystal molecules in contact with an organic thin film.[21] In that report, there was a single SFG active interface and the factors were formulated by summing infinite reflections and transmissions through the polymer thin film. For one of their geometries, they noted the necessity of describing the field generated in the transmitted direction but reflected to the detector by the underlying substrate. This turns out to be an important effect observed in the data in Chapter 2 of this dissertation.

Since the 1980's, it has become clear that SFG and SHG are widely applicable for studying atomic and molecular structure and dynamics at any interface accessible by the input and generated light waves. With the demonstrated usefulness of these surface probes at buried interfaces and an intuitive description of thin film interference, application to organic thin film systems has grown into an important topic in the literature, especially in light of the importance of interfaces in organic semiconducting thin film systems. For these systems, there are always two interfaces present and contributing to the SHG or SFG response and so a major focus has been in devising ways to separate these contributions in the presence of optical thin film interference effects.

Researchers have approached the two-interface problem a number of ways, many of which avoid this complicated issue altogether. It is common to assume, and sometimes perform peripheral checks to substantiate, that the signal is dominated by the interface of interest (usually the outermost interface) and therefore treat the data as consisting of a single interfacial contribution. The common arguments for this reasoning include assuming or calculating that the local field factors heavily favor the interface of interest,[324–333] or that the ignored interface has a fortuitously small intrinsic nonlinear response[325,326,334–336] or some combination of both. Another common approach is to simply monitor a *change* in detected signal as correlated with a change in the sample, presumably happening strictly at one interface.[25,327,332,337–344] Other methods include chemically modifying the interface of interest[345–348] or using very thick films (an argument analogous to optimizing the local field factors).[193,349–353] The popularity among researchers to experimentally optimizing for the single interface assumption in thin film systems owes to the simple benefit that results: there is an immense reduction in the complexity of data modeling and interpretation.

Of course, the reduced complexity afforded by the single interface assumption is not without a cost. First, the necessity of optimizing the sample or experiment is fairly restrictive, debasing one of the primary benefits of SFG and SHG as *in situ* surface probes. Also, because of the coherent interference of generated fields from thin film systems, even a small interfacial contribution will optically heterodyne with the larger field so that it can significantly influence the detected signal (depending on the magnitude and phase difference), possibly degrading any qualitative or quantitative analysis of the data. To this end, a substantial amount work has been reported where

two interfaces are explicitly considered in the data modeling of SFG and SHG of organic thin film systems. Perhaps the simplest approach is to circumvent modeling of the field factors, but fit observed peaks to inner and outer interfacial contributions and take a ratio of effective amplitudes to deduce structural information.[96,336,348] This was our approach for one report[96] and will form the basis for a detailed introduction to the two-interface problem in Chapter 2. However, as will be expounded in the later chapters, this leads to some ambiguities and so methods of modeling thin film interferences are preferred.

The favorable modeling method among researchers has been the most intuitive one where the beams are evoked as propagating through the system as a series of reflections and transmissions. Local fields are calculated by coherently summing contributions at each interface, and generated fields are propagated out in the same manner. The usual approach considers infinite bounces within the thin film system,[21,354–362] but there are also reports that studied this problem with truncated series.[363,364] Other modeling methods have included considering boundary conditions for a given thin film system.[365,366] In nearly every instance of reported SFG or SHG from a thin film system where interference effects were explicitly modeled as a series of reflections and transmissions, the sample consisted of a *single* thin film. To date, modeling of SFG or SHG from systems composed of more than a single thin film layer is almost nonexistent.

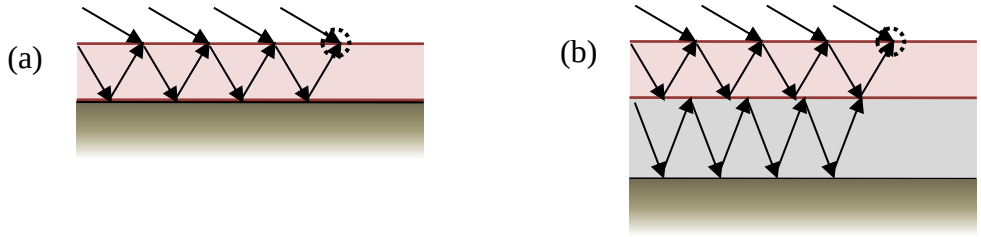

Figure 1-6. Illustration of coherently summed electric field contributions at a point for a system composed of (a) a single thin film and (b) two thin films.

Perhaps the reason more complicated structures have not typically been considered is illustrated by a simple example in Figure 1-6. The systems shown are for a single thin film (a) and two thin films (b) on an infinite substrate with a plane wave incident from the top and ray traced through each scheme. The dashed circles indicate the point at which coherent addition takes place. From this it is clear that addition of a second thin film in (b) significantly complicates the procedure as waves that transmit out of the top layer may be reflected back in by the bottom layer. Accounting for the infinite reflections and transmissions and phase shifts that may occur is cumbersome (although it has been formulated, it is known as recurrent Airy summation, which becomes significantly more complicated with each added thin film layer[367]).

A simpler technique using matrix approaches for calculating fields within a linear multilayer system has existed since 1948 when Abelés formulated the problem very elegantly in terms of boundary conditions between layers rather than Airy summation.[367–371] From that approach it is straightforward to calculate internal fields due to a wave incident from outside the system, but it was not extended to describing how *internally generated* fields propagate out of arbitrary multilayers. Describing thin film interference effects in interface-specific nonlinear optical spectroscopies from multilayer systems using the transfer matrix was reported by us[372] and is the basis for

Chapter 3 of this dissertation. The method combines the intuitive approach of multiple reflections and transmissions with the compact form of the transfer matrix for describing electromagnetic fields in multilayer systems. Our hope is that it makes modeling this complicated phenomenon more accessible to experimentalists.

1.3.1.7 Higher Order Terms in Thin Film Systems

Beyond the usual electric dipole approximation for SFG (discussed below in Section 1.3.2.5), quantifying surface quadrupole terms and bulk contributions in centrosymmetric systems continue to be issues today[373] and are a special problem for thin film systems as the spatial variation of input fields through the bulk is affected by the thin film geometry since higher order terms depend on field gradients, as will be discussed in Chapter 5. Surface quadrupole terms are very difficult to separate from dipole terms but it is usually thought that if measurements are made on resonance and there is significant polar ordering of atomic units at the interface, the dipole term should dominate.[21,171,234,235,238] While it is generally accepted that bulk contributions may be minimized in many systems by adopting experimental reflection geometry, that procedure is usually only applicable for systems composed of a single interface between otherwise bulk media where the outer medium is linear (e.g. air) and the inner medium is nonlinear.[244,351,374]

Efforts to quantify bulk and higher order interfacial response terms in thin film systems has indicated that the dipole approximation may not be suitable for some systems. For instance, in the 1990's work on fullerene (C_{60}) thin films with SHG measured in reflection as a function of thickness[311–313,354] indicated that the bulk

contribution either dominates the response[312] or is comparable to the electric dipole contribution under electronically resonant conditions.[313,354] In particular, Koopmans, Janner, Jonkman, Sawatzky, and van der Woude noted the large magnetic dipole contribution of that particular molecule due to extensive electron delocalization within the relatively large C_{60} cage.[312] Reports on SFG from a thin film of formic acid during deposition indicated the thickness dependent response of the peak amplitude for the C-H mode could be modeled by a stack of polarized sheets through the bulk of the film.[355,356] A study in 2000 of a 100-200 μm film of polyethylene on fused silica substrate with SFG measured in both reflection and transmission indicated that, while the reflected intensity could be described solely by an outer interfacial response, the transmission measurement was completely described by a bulk contribution.[351] However, they assumed a single interface due to a very thick film and did not address the two-interface possibility. A report by Hsiung and Shen in 1986 on a freely standing liquid crystal film (no substrate) was purposed to determine if the smectic phase of otherwise antiparallel 8CB molecules within a molecular layer in the bulk was subject to ferroelectric organization in the outermost film layers, that is, polar oriented parallel ordering at the interfaces due to surface energy considerations.[365] They studied thin films from two to ten molecular layers thick and measured SHG on resonance in reflection and transmission to deduce that the effective surface susceptibility was only 7% in magnitude as compared to the bulk response. They concluded that this did not provide evidence for ferroelectric ordering and that the small effective surface response may be due strictly to quadrupole coupling from the rapid variation in the fields at the

interfaces. In the absence of preferential polar orientation at the interface, the dipole term was zero.

There is also convincing evidence that the bulk and surface quadrupole terms are negligible for some systems; however, due to the complicated effects of optical interference, the evidence has been mostly gathered on single interface systems. For instance, Guyot-Sionnest and Shen reported no significant change in SHG signal under resonant conditions with p-nitrobenzoic acid adsorbed on fused silica in contact with air in comparison with the interface in contact with a silica index matched fluid. Index matching significantly reduces any field discontinuity so that the result indicated that the surface quadrupole term was negligible as compared to the dipole response.[234] When the fundamental excitation wavelength was moved off resonance, they notice an overall decline in signal and a 25% decline when in contact with the index match fluid relative to air, providing evidence that resonant enhancement is an important feature when assuming the electric dipole approximation. SFG collected in reflection and transmission applied to the alkyl region of neat solvents indicated that, for the *ssp* experiment on methanol in contact with air[244] and decane in contact with glass, the bulk contribution was negligible (although they found it was significant for *sps* and *pss* applied to decane).[374] This further highlights the importance of experimental geometry considerations.

Searching the literature for application of SFG or SHG to organic thin films where two interfaces and bulk contributions were explicitly considered emphasizes the complexity of this issue. Efforts to this end seem to be reported only when the bulk can be quantified as larger than zero, as discussed in the examples above. Otherwise

peripheral checks are made, or the electric dipole approximation is just assumed and possible bulk and higher order interfacial terms are ignored altogether when analyzing data. There appears to be a paradox: on the one hand, second order spectroscopies are promoted as extremely sensitive probes of molecular structure at interfaces, but on the other hand, bulk contributions and the problematic issues with surface quadrupolar contributions are large unknowns that seem to undermine the usefulness of these techniques. Further, *there is no systematic procedure* for measuring the individual contributions and most often the amount of experimental data is too little so that the theoretically separable contributions are underdetermined by the data. However, there are some general guidelines that indicate some *a priori* knowledge of the thin film system can assist in analyzing data.[21,171,234,235,238,374,375]

The relative strength of the terms that contribute to SFG depends on the wavelengths involved and the resonances (or lack thereof) for a given system. In order to quantify molecular structure experiments should include analysis of possible higher order terms. Nonetheless, there are some qualitative arguments that can assist with these system dependent considerations,[171,234,235,375] a very nice discussion of which was provided in 2002 by Held, Lvovsky, Wei, and Shen.[374] It has been noted that the bulk contribution from reflection measurements from single interface systems can be reduced by c.a. an order of magnitude for molecular systems that are completely isotropic. Further, oppositely oriented pairs of polar atomic groups in the bulk (e.g. molecular layers of alternating polar orientation) should yield smaller bulk contributions if the distance between atomic groups is small compared to the distance between layers. For VSFG, systems with high polar orientation of active vibrational modes at the interface,

the electric dipole term should be quite large and possibly dominate the observed signal.[238,374]

The problem of determining bulk contributions usually suffers from a lack of experimental data and a naïve sense of how microscopic molecular structure and interactions play a role in detected signal. Part of this project aims at providing extra "knobs" to experimentally tweak, so to speak, in order to better sample the intrinsic response. Also, the molecular picture is becoming clearer as computational methods have evolved over the past decade to assist in data analysis for second order wave-mixing spectroscopies, providing a microscopic picture of the origins of the macroscopic observables.[376–381]

1.3.2 *Theory*

The theory of sum frequency generation can be introduced starting with classical electrodynamics where a wave equation is formed from Maxwell's equations by considering the second order source polarization. The discussion focuses on deducing the form of that source polarization, and for the interface the phenomenological polarized sheet is introduced. The important terms are collected and can be related to microscopic structure by connecting them with quantum mechanical expectation values. To begin, some periphery details are necessary.

1.3.2.1 Definitions

All electromagnetic fields in the theory discussed here are assumed to be infinite plane waves and the primary interest is in sample interactions with the electric field of

light. Thus, this section starts with the general equation for an electric field propagating as a monochromatic plane wave.

$$\begin{aligned}\mathbf{E}(\mathbf{r},t) &= E\hat{\mathbf{e}}\exp\left[i\left(\mathbf{k}\cdot\mathbf{r}-\omega t\right)\right] \\ &= \mathbf{E}(\mathbf{r})\exp\left(-i\omega t\right)\end{aligned} \tag{1.15}$$

The vector field $\mathbf{E}$ is defined with the unit polarization vector $\hat{\mathbf{e}}$, complex amplitude E, frequency ω, and wavevector $\mathbf{k}=k\hat{\mathbf{k}}$ where $\hat{\mathbf{k}}$ is the unit wavevector and $k=2\pi n/\lambda$ is the wavenumber (in isotropic nondissipative media $\hat{\mathbf{k}}\cdot\hat{\mathbf{e}}=0$). Here, n is the complex refractive index of the medium (defined in this work as $n=\eta+i\kappa$ with η and κ real and positive so that the waves may be inhomogeneous) and λ is the vacuum wavelength. The tilde on $\mathbf{E}$ is indicates it is an oscillatory function of time and that the time dependence is separable from spatial dependence $\mathbf{r}$ as shown in the second equality of Eq. (1.15) The tilde notation is used in the same manner for other time oscillating quantities (such as $\mathbf{P}$ in Eq. (1.14)). Eq. (1.15) is provided here for reference as the details of the theory are discussed.

The unit polarization vector (the normalized Jones vector) is generally complex to allow for arbitrary elliptically polarized light. Most often this work will be concerned with linearly polarized light and in that case it is real; though, the generalized definition may be kept since it is always the case that $|\hat{\mathbf{e}}|=1$. Thus, it can be written that $\hat{\mathbf{e}}$ is a linear combination of three orthogonal unit polarization vectors of a chosen coordinate system $\hat{\mathbf{i}}$, $\hat{\mathbf{j}}$, $\hat{\mathbf{k}}$,

$$\hat{\mathbf{e}}=A\hat{\mathbf{i}}+B\hat{\mathbf{j}}+C\hat{\mathbf{k}} \tag{1.16}$$

and $|A|^2+|B|^2+|C|^2=1$.

In order to develop the SFG theory, the $\hat{\mathbf{x}}$, $\hat{\mathbf{y}}$, $\hat{\mathbf{z}}$ coordinate system of the sample must be defined and related to the experimentally convenient coordinate system of propagating laser electric fields where $\hat{\mathbf{e}}$ is decomposed into components parallel $\hat{\mathbf{p}}$ and perpendicular $\hat{\mathbf{s}}$ to the plane of incidence. The sample coordinate system forms the basis for describing the vector with components $\begin{bmatrix} E^x & E^y & E^z \end{bmatrix}$ and the propagating fields frame is a basis to describe the vector with components $\begin{bmatrix} E^p & E^s & 0 \end{bmatrix}$. Figure 1-7 illustrates the system. For the purposes of this introduction, a single interfacial boundary between semi-infinite media is presented where the upper medium is always linear (e.g. air) and the lower medium has a nonlinear response.

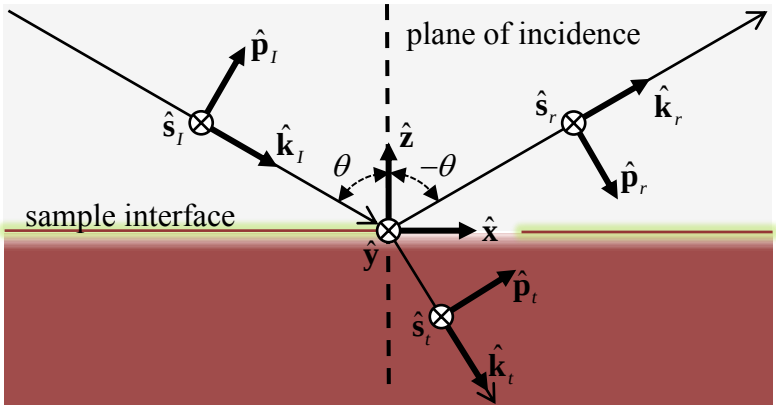

Figure 1-7. View normal to the plane of incidence of the coordinate systems used for incident, reflected, and transmitted electric field of light at a single interface system.

The origin is chosen at a point on the sample interface and is always assumed an ideal boundary, i.e. perfectly planar and no surface roughness. The figure illustrates the chosen coordinate systems for fields propagating toward the interface, present at the interface, and reflecting or transmitting through it. From this it is clear that $\hat{\mathbf{s}}\cdot\hat{\mathbf{y}}=1$ and

that $\hat{\mathbf{p}}$ contains $\hat{\mathbf{x}}$ and $\hat{\mathbf{z}}$ components, the magnitude of each depends on the angle of incidence θ.

It is important to emphasize that there are two choices when deciding how to define the direction of $\hat{\mathbf{p}}$ for incidence and reflection. Algebraically, it is sensible to define for the incident and transmitted frame so that the sign of both the normal and tangential components are preserved relative to the sample frame, i.e. $\hat{\mathbf{p}}_I \cdot \hat{\mathbf{z}} > 0$ and $\hat{\mathbf{p}}_I \cdot \hat{\mathbf{x}} > 0,$ and the same for $\hat{\mathbf{p}}_t$. For the reflected field frame, one can maintain the sign of only a single component. The choice for this work, as indicated in the figure, preserves the sign of the tangential component, i.e. $\hat{\mathbf{p}}_r \cdot \hat{\mathbf{x}} \geq 0$ but $\hat{\mathbf{p}}_r \cdot \hat{\mathbf{z}} \leq 0.$ Often, the opposite choice is made for the reflected field frame and care must be taken with this definition as it affects the description of the linear Fresnel factors. The Fresnel factors are at the core of the thin film interference model detailed in Chapter 3.

Mathematically, for linearly polarized light and the chosen propagating field frames the unit vectors are

$$\hat{\mathbf{e}}^p = \begin{bmatrix} 1 \\ 0 \\ 0 \end{bmatrix} \qquad \hat{\mathbf{e}}^s = \begin{bmatrix} 0 \\ 1 \\ 0 \end{bmatrix} \tag{1.17}$$

and the sample frame is defined with unit vectors

$$\hat{\mathbf{e}}^x = \begin{bmatrix} 1 \\ 0 \\ 0 \end{bmatrix} \qquad \hat{\mathbf{e}}^y = \begin{bmatrix} 0 \\ 1 \\ 0 \end{bmatrix} \qquad \hat{\mathbf{e}}^z = \begin{bmatrix} 0 \\ 0 \\ 1 \end{bmatrix} \tag{1.18}$$

so that

$$\begin{aligned}\mathbf{e}^{ps} &= E\hat{\mathbf{e}}^{sp} \\ &= E\left(A\hat{\mathbf{e}}^{p} + B\hat{\mathbf{e}}^{s}\right)\end{aligned} \tag{1.19}$$

$$\begin{aligned}\mathbf{e}^{xyz} &= E\hat{\mathbf{e}}^{xyz} \\ &= E\left(C\hat{\mathbf{e}}^{x} + D\hat{\mathbf{e}}^{y} + E\hat{\mathbf{e}}^{y}\right)\end{aligned} \tag{1.20}$$

where, again, the coefficients in each frame must satisfy $|A|^2 + |B|^2 = 1$ and $|C|^2 + |D|^2 + |E|^2 = 1$. The sample field frame is related to the propagating field frames by a rotation matrix about the $\hat{\mathbf{s}}$ (or $\hat{\mathbf{y}}$) axis.

$$\hat{\mathbf{e}}^{xyz} = \vec{\vec{R}}(\theta)\hat{\mathbf{e}}^{ps} \tag{1.21}$$

$$\vec{\vec{R}}(\theta) = \begin{bmatrix} \cos(\theta) & 0 & 0 \\ 0 & 1 & 0 \\ \sin(\theta) & 0 & 0 \end{bmatrix} \tag{1.22}$$

The coefficients are then related by

$$\begin{aligned} C &= A\cos(\theta) \\ D &= B \\ E &= A\sin(\theta) \end{aligned} \tag{1.23}$$

where θ is defined positive or negative as in the figure so that the proper sign is placed on *E* depending on which propagating field frame is under consideration.

The discussion in this section should include a word on tensor notation as tensors of several ranks will be encountered. The rank of a tensor indicates how many indices are required to specify a single scalar element. Scalar quantities (rank 0 tensors) are indicated by italics, vectors (rank 1 tensors, e.g. $\mathbf{E}$ with elements E_i) are bold, and tensors of rank 2 (e.g. 3×3 matrix with elements T_{ij}) and higher (T_{ijk}, T_{ijkl} etc.) are

denoted with a double sided arrow on top $\vec{\vec{T}}$. The rank of any higher order tensor will be specified or can be deduced by the ranks of the tensors it is operating on by knowing that, in this work, the operating tensor is always a rank above or below the operand (except for scalar multiplication and unless otherwise noted). So, for instance soon expressions of the form

$$\mathbf{P} = \vec{\vec{\chi}} : \mathbf{E} \otimes \mathbf{E} \tag{1.24}$$

will be encountered, which indicate that $\vec{\vec{\chi}}$ is a higher rank tensor operating on the tensor product of two vectors (results in a rank 2 tensor) to give the vector **P**. Therefore, $\vec{\vec{\chi}}$ is either a vector or a rank 3 tensor, and the double arrow specifies the latter.

The colon symbol indicates that $\vec{\vec{\chi}}^{(2)}$, being a third rank tensor (3×3×3), operates on the tensor (outer) product of the electric field, which is a second rank tensor (3×3).

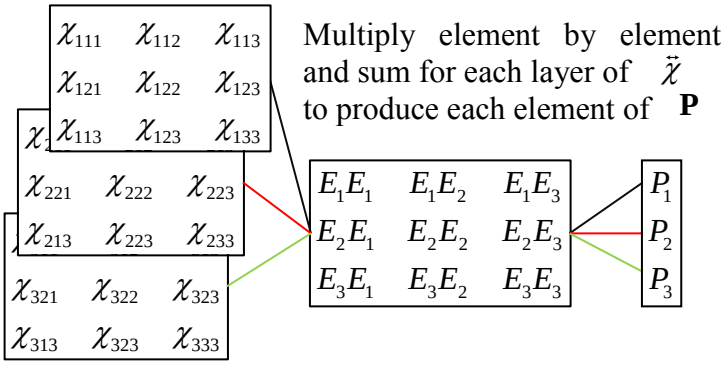

Figure 1-8. Graphical depiction of the tensor colon operation in SFG.

This operation results in a rank 1 tensor **P** (a vector) describing the second order contribution to the polarization density field. Mathematically, we multiply element by element the input fields tensor product matrix with each level (first index) of $\vec{\vec{\chi}}^{(2)}$ and sum all elements in a layer to produce an element of **P**. It can be thought of as a higher

order dot product operation. A graphical representation in Figure 1-8 is illustrative as this is an important part of understanding the notation in the theory of SFG. Another way to understand the tensor mathematics of Eq. (1.24) is by writing it in the Einstein summation convention for the i'th element of $\mathbf{P}$.

$$P_i = \chi^{(2)}_{ijk} E_j E_k \tag{1.25}$$

Here, i, j, and k are elements of the chosen coordinate axes system (e.g. 1, 2, 3 are x, y, and z, respectively) and there is an implicit sum on the right side of the equation over indices appearing twice (e.g. $P^{(2)}_x = \sum_{jk} \chi^{(2)}_{xjk} E_j E_k$). The colon operation can be generalized in an analogous way to higher order operations where a rank n tensor operates on a rank n-1 tensor to always produce a vector.

1.3.2.2 Maxwell's Wave Equation

The theory of SFG can be introduced starting with classical electrodynamics. Much of what follows is available in a number of texts on standard electromagnetic theory.[159,323,382–385] Start by writing down the general forms of Maxwell's equations when an external electromagnetic field interacts with a classical system composed of nuclei and electrons where the size is large enough so that the granularity of atomic structure is sufficiently averaged. The equations that relate the induced electric $\tilde{\mathbf{E}}(\mathbf{r},t)$ and magnetic $\tilde{\mathbf{B}}(\mathbf{r},t)$ fields of light emitted from the system due to the dynamically induced quantities can be written in Gaussian units as

$$\nabla \cdot \tilde{\mathbf{D}} = 4\pi\tilde{\rho} \tag{1.26}$$

$$\nabla \cdot \tilde{\mathbf{B}} = 0 \tag{1.27}$$

$$\nabla \times \tilde{\mathbf{E}} = -\frac{1}{c}\frac{\partial \tilde{\mathbf{B}}}{\partial t} \tag{1.28}$$

$$\nabla \times \tilde{\mathbf{H}} = \frac{1}{c}\frac{\partial \tilde{\mathbf{D}}}{\partial t} + \frac{4\pi}{c}\tilde{\mathbf{J}} \tag{1.29}$$

This is the most general form of the equations. This work will be concerned with regions that have no free charges $\tilde{\rho} = 0$ and no free currents $\tilde{\mathbf{J}} = 0.$ The constitutive equations, which relate the electric displacement $\tilde{\mathbf{D}}$ to electric and polarization density $\tilde{\mathbf{P}}$ fields and the magnetic induction $\tilde{\mathbf{H}}$ to magnetic $\tilde{\mathbf{B}}$ and magnetization $\tilde{\mathbf{M}}$ fields, are written

$$\tilde{\mathbf{D}} = \tilde{\mathbf{E}} + 4\pi\tilde{\mathbf{P}} \tag{1.30}$$

$$\tilde{\mathbf{H}} = \tilde{\mathbf{B}} \tag{1.31}$$

where it has been assumed all materials are nonmagnetic $\tilde{\mathbf{M}} = 0$ so that the magnetic induction is just the magnetic field in Eq. (1.31). By taking the curl of Eq. (1.28) and using the relation $\nabla \times \nabla \times \tilde{\mathbf{E}} = \nabla\left(\nabla \cdot \tilde{\mathbf{E}}\right) - \nabla^2\tilde{\mathbf{E}}$ while realizing the divergence of a plane wave is zero $\nabla \cdot \tilde{\mathbf{E}} = 0,$ a wave equation can be obtained.

$$\left(-\nabla^2 + \frac{1}{c^2}\frac{\partial^2}{\partial t^2}\right)\tilde{\mathbf{E}} = -\frac{4\pi}{c^2}\frac{\partial^2}{\partial t^2}\tilde{\mathbf{P}} \tag{1.32}$$

One can choose to remain in the time domain; however, for the purposes of this dissertation Eq. (1.32) can be Fourier transformed to the frequency domain.

$$\left(-\nabla^2 + \frac{\omega^2}{c^2}\right)\mathbf{E}(\omega) = -\frac{4\pi\omega^2}{c^2}\mathbf{P}(\omega) \tag{1.33}$$

Here the tilde is removed to indicate the changed space and the fields are explicitly expressed as frequency dependent.

1.3.2.3 Linear Optics

Of primary concern is the form of the polarization, which is generally not known. However, for a sufficiently weak electric field the polarization density can be expanded as a power series in $\mathbf{E}$ where it is written as a sum of a linear term plus all higher order terms grouped together into a nonlinear polarization term.

$$\begin{aligned}\mathbf{P} &= \mathbf{P}^{(1)} + \cancel{\mathbf{P}^{(2)} + \mathbf{P}^{(3)} \ldots} \\ &= \ddot{\chi}^{(1)} \cdot \mathbf{E} + \cancel{\ddot{\chi}^{(2)} : \mathbf{E} \otimes \mathbf{E} + \ddot{\chi}^{(3)} : \mathbf{E} \otimes \mathbf{E} \otimes \mathbf{E} + \ldots} \\ &= \ddot{\chi}^{(1)} \cdot \mathbf{E} + \cancel{\mathbf{P}^{NL}}\end{aligned} \tag{1.34}$$

For common light sources, the electric field amplitude is small so that all nonlinear terms may be considered zero for all practical purposes as indicated in the equation. Then the constitutive relation for the electric displacement can be rewritten in terms of the linear response.

$$\mathbf{D} = \mathbf{D}^{(1)} + \cancel{4\pi \mathbf{P}^{NL}} \tag{1.35}$$

$$\begin{aligned}\mathbf{D}^{(1)} &= \mathbf{E} + 4\pi \mathbf{P}^{(1)} \\ &= \ddot{\varepsilon}^{(1)} \cdot \mathbf{E}\end{aligned} \tag{1.36}$$

The linear dielectric tensor $\ddot{\varepsilon}^{(1)}$ is related to the linear susceptibility $\ddot{\chi}^{(1)}$ by

$$\ddot{\varepsilon}^{(1)} = 1 + 4\pi \ddot{\chi}^{(1)} \tag{1.37}$$

Then the wave equation of Eq. (1.33) can be rewritten

$$\left(-\nabla^2 + \frac{\omega^2}{c^2} \ddot{\varepsilon}^{(1)}(\omega) \right) \mathbf{E}(\mathbf{r}, \omega) = 0 \tag{1.38}$$

Generally, $\ddot{\varepsilon}^{(1)}$ is complex for dissipative media and is a second rank tensor in anisotropic materials; however, for isotropic systems it is a scalar. It is related to the (linear) refractive index by $\varepsilon^{(1)} = n^2$.

In the absence of nonlinear interactions, the wave equation admits solutions of plane waves and can be used to solve for such optical phenomena as Beer's law or the (linear) Fresnel amplitude coefficients for reflection and transmission at a boundary. One subtlety of this equation is that it exemplifies the principle of superposition for the electric field, which states that the total field at any point is just the sum of all fields at that point. To see this, consider that $\mathbf{E}(\mathbf{r},\omega)$ is a sum of Fourier components.

$$\mathbf{E}(\mathbf{r},\omega) = \sum_n \mathbf{E}_n(\mathbf{r},\omega_n) \tag{1.39}$$

Inserting Eq. (1.39) into (1.38) shows there are only solutions for each component with no possibility for coupling, that is, Eq. (1.38) is written and solved independently for each frequency component of **E**. Linear optics *does not* predict such phenomena as wave-mixing (violates the superposition principle) or intensity dependent refractive index.

1.3.2.4 Nonlinear Optics

Adding to the wave equation the nonlinear polarization terms results in a rich extension of classical optics. With $\mathbf{P}^{NL}$ included, Eq. (1.38) becomes nonzero on the right side.

$$\left(-\nabla^2 + \frac{\omega^2}{c^2}\ddot{\varepsilon}^{(1)}(\omega)\right)\mathbf{E}(\mathbf{r},\omega) = -\frac{4\pi\omega^2}{c^2}\mathbf{P}^{NL}(\mathbf{r},\omega) \tag{1.40}$$

Separating the linear from the nonlinear polarization has served to include the linear effects of dispersion and dissipation in the wave equation by including the dielectric constant in the second term on the left. Each higher order term in Eq. (1.34) is usually several orders of magnitude smaller than the last so that nonlinear effects are only important when the field amplitudes are comparable to characteristic atomic field strength and is usually practical only with short, intense laser pulses. To simplify further discussion, only second order effects will be considered (since SFG is contained in this term) so that

$$\begin{aligned} \mathbf{P}^{NL} &= \mathbf{P}^{(2)} \\ &= \vec{\vec{\chi}}^{(2)} : \mathbf{E} \otimes \mathbf{E} \end{aligned} \tag{1.41}$$

The notation here was discussed in Section 1.3.2.1. The physical interpretation is that in general, any two components of $\mathbf{E}$ may interact with the sample to produce any component of $\mathbf{P}^{(2)}$ and the interaction, or material response to the fields, is described by the second order susceptibility. It will be shown later that of the 27 possible interactions, only 4 are independent and nonzero for centrosymmetric systems.

Before continuing, it is worth mentioning a few details pertaining to Eq.(1.40), which states that the nonlinear polarization density acts as a source term for emitted radiation. Consider $\mathbf{E}(\mathbf{r},\omega)$ as a sum of just three Fourier components

$$\mathbf{E}(\mathbf{r},\omega) = \sum_{n=1}^{3} \mathbf{E}_n(\mathbf{r},\omega_n) \tag{1.42}$$

with

$$\omega_1 + \omega_2 = \omega_3 \tag{1.43}$$

and the amplitude of the third wave is small compared to the other two $|\mathbf{E}_3| \approx 0$. Assuming the solution will consist of plane waves, the time-dependent phase factor can be applied to each wave and the reality condition on E requires the fields to be expressed as summed with each respective complex conjugate (c.c.). With these modifications the sum of arbitrary components for each input field of Eq. (1.42) can be inserted into (1.41) which leads immediately to multiple second order polarization source terms (ignoring nonlinearity from $\mathbf{E}_3$).

$$\begin{aligned} P^{(2)} &= \chi^{(2)}\left[\left(E_1 e^{-i\omega_1 t} + E_2 e^{-i\omega_2 t}\right) + c.c.\right]^2 \\ &= \chi^{(2)}\left(E_1^2 e^{-i2\omega_1 t} + E_2^2 e^{-i2\omega_2 t} + c.c.\right) \quad \text{(SHG)} \\ &+2\chi^{(2)}\left(E_1 E_2 e^{-i(\omega_1+\omega_2)t} + c.c.\right) \quad \text{(SFG)} \\ &+2\chi^{(2)}\left(E_1 E_2^* e^{-i(\omega_1-\omega_2)t} + c.c.\right) \quad \text{(DFG)} \\ &+\chi^{(2)}\left(|E_1|^2 + |E_2|^2\right) \quad \text{(OR)} \end{aligned} \tag{1.44}$$

The index notation is dropped here for simplicity in order to highlight that for two intense laser input fields there are source polarizations that radiate at twice either fundamental (SHG), at the sum (SFG) and difference (DFG) of both frequencies, and a static contribution described by optical rectification (OR) when $\chi^{(2)} \neq 0$. The significance of the wave-mixing terms is clear; frequencies other than the pump fields are emitted which carry information on the sample response, whereas OR is important in such processes as terahertz light generation.[386] The radiating contributions are experimentally separable simply by tuning a spectrograph to the desired frequency.

Returning to Eq. (1.44) and considering the radiating source terms (all others beside OR) there are multiple wave-mixing processes possible. Contrasted with linear

optics, these terms obviously do not depend linearly on the total field so that the Fourier components are coupled by the second order susceptibility in the cross terms. The most correct procedure for solving for field amplitudes involves setting up the wave equation for each frequency component (thus Eq. (1.42) includes all 6 Fourier components for the input, SHG, SFG, and DFG fields and there is a wave equation for each frequency) subject to boundary conditions (e.g. all wave-mixing amplitudes start at zero at the edge of the nonlinear medium) and energy conservation. The set of differential equations are coupled so that they must be solved simultaneously; however, there are usually approximations that are applied in order to facilitate the solution.

An example of the solution to the couple wave equations is instructive. Usually the undepleted pump is a good approximation, that is, the exchange of energy from the pump fields to the higher order fields is a negligible fraction of the total pump intensities. This allows for the wave equations to be solved for each frequency mixing process separately (actually, for bulk-allowed second order effects through thick materials, phase-matching can generally only be optimized for one term at a time so that each term can be separately solved due to this effect).[323] Effects from OR are ignored and the slowly varying amplitude approximation removes the $-\nabla^2$ term from Eq. (1.40) . For SFG in the bulk of a nonlinear material slab of finite thickness L (ignoring reflection effects at the interfaces), the solution results in signal intensity at ω_3 described by

$$I_3 \propto \left(L \frac{\sin\left[\Delta kL/2\right]}{\Delta kL/2} \right)^2 \tag{1.45}$$

with

$$\Delta k = k_1 + k_2 - k_3 \tag{1.46}$$

The intensity I_3 is obtained for some finite value of L that depends on the wavevector (phase) mismatch Δk. Phase matching is almost always nonzero for real materials due to dispersion so that the detected intensity from a bulk medium is a very strong function of both Δk and the total length of the nonlinear material. This is the origin of the Maker's fringe effect mentioned at the beginning of Section 1.3.1.6. For perfect phase matching $\Delta k = 0$ (which is practically never possible) so that the phase relation between the pump fields and the SHG field is constant and I_3 scales quadratically with L. Another possibility for quadratic dependence on L is at small thicknesses, satisfying $\Delta kL \ll 1$, where Eq. (1.45) can be series expanded around $L = 0$ and truncated at the first term. However, this is in the regime of thin film thicknesses and is the basis for a common back-of-the-envelope calculation for deducing if bulk contributions are important in these systems. That is, a quadratic rise in SFG signal with thin film thickness is often dismissed as a completely bulk signal. In Chapters 4 and 5 we show that this is not an accurate indication of bulk contributions and cannot be used as such. Fully *interfacial* contributions combined with thin film interference effects often mimic this behavior.

To close this discussion it should be mentioned that the validity of expressing the polarization density as a power series in the electric field (Eq. (1.34)) relies on the assumption that the nonlinear interactions can be considered a small perturbation to the system. If the output frequencies are much less intense than the input beams (which is

always the case for systems concerned in this dissertation), this is an indication that the perturbative treatment is valid. Also, thus far the nonlinear susceptibilities have been kept in their most general form so that no approximations have been made (e.g. the electric dipole approximation has not been considered yet and magnetic interactions discussed in the next section can be absorbed by the current definition of the susceptibility). Finally, microscopic local field effects have not been included in the wave equation. For condensed phases, molecules are in close proximity so that each atomic group feels both the externally applied pump fields as well as dipole fields from surrounding molecules which contributes to the induced polarization. However, as this is just a scaling factor on the field components, its exclusion does not change the discussion here. Otherwise, using a very simple model it can be shown that microscopic field corrections result in a factor of $\left(\varepsilon^{(1)}+2\right)/3$ applied to the source polarization for each frequency involved.[323,382,387]

1.3.2.5 The Electric Dipole Approximation

In this section a brief account is given of the approximation that is employed in order to arrive at the ubiquitous selection rule of SFG as a surface sensitive probe. The full form of the nonlinear source polarization in the wave equation is rarely known so that expansions are applied. Here, all expansions are truncated at terms involving derivatives up to first order. The earlier assumption involving the neglected magnetism of the materials is eased and second order effects may now contain terms involving magnetism and magnetic interactions.

The theory of SFG that specifies interfacial sensitivity begins with considering how the form of the SFG polarization from the bulk relates to the polarization at the interface. The total second order polarization source term for $\Omega = \omega_1 + \omega_2$ can be described in the bulk by a multipole expansion.[122,171,234,388]

$$\mathbf{P}^{(2)}_{total}(\mathbf{r},\Omega) = \mathbf{P}^{(2)}(\mathbf{r},\Omega) - \nabla \cdot \ddot{Q}^{(2)}(\mathbf{r},\Omega) - \frac{ic}{2\omega}\nabla \times \mathbf{M}^{(2)}(\mathbf{r},\Omega) + \cdots \qquad (1.47)$$

Here $\mathbf{P}$, $\ddot{Q}$, and $\mathbf{M}$ denote electric dipole polarization, electric quadrupole polarization, and magnetic dipole polarization, respectively, induced by the input fields. The polarization density (dipole moment per unit volume) is formally due to a convolution of interactions. Physically, the polarization at any point $\mathbf{r}$ is due to the material response $\ddot{\chi}^{(2)}$ to the input fields in the *vicinity* of that point, which includes influences from neighboring points also interacting with the input fields.[171,384,389,390] Another important detail is that, just as the material polarization is described by a series of electric and magnetic multipoles, each pole can be written as a result of interaction with the electric and magnetic $\mathbf{B} = -\sqrt{\varepsilon^{(1)}}\nabla \times \mathbf{E}$ components of the *input fields*.[373,391] The most correct relation includes influences from "neighbors" over all space since neighbors are influenced by their neighbors and so on[171] so that the terms in $\mathbf{P}^{(2)}_{total}$ are written[234]

$$\begin{aligned}
\mathbf{P}^{(2)}(\mathbf{r},\Omega) &= \int_B \vec{\vec{\chi}}^{(2)}_{D_{EE}}(\mathbf{r},\mathbf{r}',\mathbf{r}'',\Omega=\omega_1+\omega_2):\mathbf{E}(\mathbf{r}',\omega_1)\mathbf{E}(\mathbf{r}'',\omega_2)\,d\mathbf{r}'d\mathbf{r}'' \\
&+\int_B \vec{\vec{\chi}}^{(2)}_{D_{BE}}(\mathbf{r},\mathbf{r}',\mathbf{r}'',\Omega=\omega_1+\omega_2):\left[\nabla\times\mathbf{E}(\mathbf{r}',\omega_1)\right]\mathbf{E}(\mathbf{r}'',\omega_2)\,d\mathbf{r}'d\mathbf{r}'' \\
&+\int_B \vec{\vec{\chi}}^{(2)}_{D_{EB}}(\mathbf{r},\mathbf{r}',\mathbf{r}'',\Omega=\omega_1+\omega_2):\mathbf{E}(\mathbf{r}'',\omega_1)\left[\nabla\times\mathbf{E}(\mathbf{r}',\omega_2)\right]d\mathbf{r}'d\mathbf{r}'' \qquad (1.48)\\
\vec{\vec{Q}}^{(2)}(\mathbf{r},\omega_3) &= \int_B \vec{\vec{\chi}}^{(2)}_{Q}(\mathbf{r},\mathbf{r}',\mathbf{r}'',\Omega=\omega_1+\omega_2):\mathbf{E}(\mathbf{r}',\omega_1)\mathbf{E}(\mathbf{r}'',\omega_2)\,d\mathbf{r}'d\mathbf{r}'' \\
\mathbf{M}^{(2)}(\mathbf{r},\omega_3) &= \int_B \vec{\vec{\chi}}^{(2)}_{M}(\mathbf{r},\mathbf{r}',\mathbf{r}'',\Omega=\omega_1+\omega_2):\mathbf{E}(\mathbf{r}',\omega_1)\mathbf{E}(\mathbf{r}'',\omega_2)\,d\mathbf{r}'d\mathbf{r}''
\end{aligned}$$

with the integration performed over the bulk volume. Here terms in the electric dipole polarization involving the magnetic field $\mathbf{B}=-\sqrt{\varepsilon^{(1)}}\nabla\times\mathbf{E}$ have been retained (the term involving both magnetic fields, and all magnetic field interactions in $\vec{\vec{Q}}^{(2)}$ and $\mathbf{M}^{(2)}$, are neglected).

The physical explanation for the integration limits is that, most generally, the sample response at $\mathbf{r}$ is influence by the interactions of input field 1 at all possible positions $\mathbf{r}'$ and the same for input field 2 at all positions $\mathbf{r}''$. The integration can be performed over all space but the surrounding influence to the polarization at $\mathbf{r}$ is usually fairly local. The result is that the contribution to the integrals is spatially localized by the definition of $\vec{\vec{\chi}}^{(2)}$ at that point. For molecular systems considered here (indeed in most systems studied) the susceptibilities describe interactions with molecular units and so they are expected to behave very locally. Thus, each response can be expanded into a power series of position completely localized at $\mathbf{r}$.[234]

$$\begin{aligned}
\vec{\vec{\chi}}^{(2)}_{u}(\mathbf{r},\mathbf{r}',\mathbf{r}'') &= \vec{\vec{\chi}}^{(2)}_{u0}(\mathbf{r})\delta(\mathbf{r}-\mathbf{r}')\delta(\mathbf{r}-\mathbf{r}'') \\
&+\vec{\vec{\chi}}^{(2)}_{u1}(\mathbf{r})\left[\nabla\delta(\mathbf{r}-\mathbf{r}')\right]\delta(\mathbf{r}-\mathbf{r}'') \\
&+\vec{\vec{\chi}}^{(2)}_{u2}(\mathbf{r})\delta(\mathbf{r}-\mathbf{r}')\left[\nabla\delta(\mathbf{r}-\mathbf{r}'')\right] \\
&+\ldots
\end{aligned} \qquad (1.49)$$

Here δ is the Dirac delta function. By substituting Eq. (1.49) into Eq. (1.48), each term in Eq. (1.47) satisfying $\Omega = \omega_1 + \omega_2.$ can now be expressed as[373]

$$\mathbf{P}^{(2)}_{total}(\mathbf{r},\Omega) = \left\{ \begin{array}{l} \ddot{\chi}^{(2)}_{D0_{EE}}(\mathbf{r},\Omega) : \mathbf{E}(\mathbf{r},\omega_1)\mathbf{E}(\mathbf{r},\omega_2) \\ + \ddot{\chi}^{(2)}_{D1_{EE}}(\mathbf{r},\Omega) : \left[\nabla \mathbf{E}(\mathbf{r},\omega_1)\right]\mathbf{E}(\mathbf{r},\omega_2) \\ + \ddot{\chi}^{(2)}_{D2_{EE}}(\mathbf{r},\Omega) : \mathbf{E}(\mathbf{r},\omega_1)\left[\nabla \mathbf{E}(\mathbf{r},\omega_2)\right] \\ + \ddot{\chi}^{(2)}_{D0_{BE}}(\mathbf{r},\Omega) : \left[\nabla \times \mathbf{E}(\mathbf{r},\omega_1)\right]\mathbf{E}(\mathbf{r},\omega_2) \\ + \ddot{\chi}^{(2)}_{D0_{EB}}(\mathbf{r},\Omega) : \mathbf{E}(\mathbf{r},\omega_1)\left[\nabla \times \mathbf{E}(\mathbf{r},\omega_2)\right] \end{array} \right\} \\ + \nabla \cdot \left[\ddot{\chi}^{(2)}_{Q0}(\mathbf{r},\Omega) : \mathbf{E}(\mathbf{r},\omega_1)\mathbf{E}(\mathbf{r},\omega_2) \right] \\ - \frac{ic}{2\omega} \nabla \times \left[\ddot{\chi}^{(2)}_{M0}(\mathbf{r},\Omega) : \mathbf{E}(\mathbf{r},\omega_1)\mathbf{E}(\mathbf{r},\omega_2) \right] \\ + \ldots \qquad (1.50)$$

Again, only terms up to first order derivatives have been retained. All terms belonging to the electric dipole polarization are grouped in curly brackets. In this approximation, the total polarization is due to effects localized at $\mathbf{r}$ and contains electric dipole, electric quadrupole, and magnetic dipole polarization contributions and the electric dipole polarization is a result of electric dipole- and quadrupole-, and magnetic dipole-type interactions with each input field.

The approximation introduced by Eq. (1.49) allows for categorizing the types of interactions considered. Terms involving curls are due to magnetic field interactions or the magnetization source polarization whereas terms involving gradients or divergence are due to quadrupole interactions or the electric quadrupole source polarization. The first term in Eq. (1.50) is the only source term that does not involve a differential operator. It is the electric dipole polarization resulting from electric dipole interactions with both input fields. Dipole interactions are considered far stronger than quadrupolar or magnetic terms in most nonmagnetic condensed phase systems, so that when they are

symmetry allowed, they usually dominate the total polarization density and the higher order terms are ignored. In this case, Eq. (1.47) is greatly simplified.

$$\mathbf{P}^{(2)}_{total}(\mathbf{r},\Omega) = \vec{\vec{\chi}}^{(2)}_{D0_{EE}}(\mathbf{r},\Omega=\omega_1+\omega_2):\mathbf{E}(\mathbf{r},\omega_1)\mathbf{E}(\mathbf{r},\omega_2) \tag{1.51}$$

This is the electric dipole approximation. The physical interpretation is that the polarizable volume elements are highly localized and are much smaller than the wavelengths of the input fields so that each volume element "feels" spatially constant (but time oscillating) input fields.

Using the principle of spatial invariance,[384] one could rewrite Eq. (1.48) with the $\mathbf{r}$ – dependence placed instead on the input fields. Carrying out a similar expansion analysis for the input fields, an equivalent (and possibly more familiar) way to phrase the interpretation is that the wavelengths of the input fields are large compared to the polarizable volume element. For the angstrom size of molecular functional groups as compared with input beams in the visible to infrared (hundreds to thousands of nanometers) in the bulk, this is certainly a very good approximation. The electric dipole approximation is the basis for most phenomena predicted in linear optics (e.g. absorption selection rules),[392,393] the success of which is an indication of the power of this approximation.

A final note on the electric dipole approximation should be mentioned. It has been pointed out that the multipole expansion of the polarization is generally valid in the bulk but may not be valid at an interface.[171,235] Guyot-Sionnest and Shen discussed this issue[235] and found that higher order terms would scale as $(d/\lambda)^{l+k-1}$ where d is the interface thickness, λ is the smallest wavelength, and l and k are related to higher

order derivatives in the multipole expansion ($l+k-1$ is always greater or equal to 1) as compared to the lowest order terms considered here. Thus, higher order terms that have been omitted in Eq. (1.48) are not important, which is an indication that the multipole expansion is valid for the analysis presented.

1.3.2.6 Symmetry and Selection Rules

Within the electric dipole approximation, the second order susceptibility is a third rank tensor that is subject to symmetry rules, specifically intrinsic permutation symmetry and spatial symmetry. Intrinsic permutation symmetry is a fundamental property of all nonlinear susceptibilities that results from the principles of causality and time reversal. It states that the result of exchanging the coordinate and frequency pairs of input fields leaves the susceptibilities unchanged. Practically, this means that the expressions for the polarization may be equally written with either input field first. It is through intrinsic permutation symmetry that the susceptibilities can be written in the common compact form used in this work. Spatial symmetry follows from a fundamental postulate known as Neumann's principle.[384,394] It states that for any system that exhibits spatial symmetry, any physical property must remain unchanged under all the symmetry operations of the point group.

For centrosymmetric systems (e.g. isotropic or cubic point groups) the operation of inversion results in a sign change of all axes. In keeping with Neumann's principle the susceptibility should remain unchanged so that

$$\chi_{ijk}^{(2)} = \chi_{-i-j-k}^{(2)} \tag{1.52}$$

But the inversion operation is an improper rotation defined as $-\delta_{ij}$ (the Kronecker delta) that results in a sign change for all odd-ordered tensors.

$$\begin{aligned}\chi_{ijk}^{(2)} &= -\delta(i-i)\delta(j-j)\delta(k-k)\chi_{-i-j-k}^{(2)} \\ &= -\chi_{-i-j-k}^{(2)}\end{aligned} \tag{1.53}$$

The only way to satisfy both Eqs. (1.52) and (1.53) is for $\chi_{ijk}^{(2)} = 0$. This simple argument provides the central selection rule for SFG: within the electric dipole approximation, SFG is forbidden in media that possess inversion symmetry.

The bulk of centrosymmetric materials are SFG inactive; however, at interfaces inversion symmetry is *necessarily* broken. At a planar interface between two isotropic materials there exists a C_∞ rotation along the $\hat{\mathbf{z}}$-axis. Any arbitrary rotation θ about this axis leaves the system unchanged since $\hat{\mathbf{x}} = \text{-}\hat{\mathbf{x}} = \hat{\mathbf{y}} = \text{-}\hat{\mathbf{y}}$. According to Neumann's principle, this is written

$$\chi_{ijk}^{(2)} = \chi_{i'j'k'}^{(2)} \tag{1.54}$$

The general case for rotation can be illustrated by picking a convenient angle that simplifies the derivation. For $\theta = \pi/2$ the axes transform as $x \to y$, $y \to -x$, and $z \to z$ (i.e. $x' = y$, $y' = -x$, and $z' = z$) so that

$$\chi_{ijk}^{(2)} = \text{sign}(i')\text{sign}(j')\text{sign}(k')\chi_{i'j'k'}^{(2)} \tag{1.55}$$

The sign function gives the sign of the argument and is equal to ± 1. To satisfy both Eq. (1.54) and (1.55) it must be that $i = j = k = z$ or one index is z and the other two are both x or both y and that $\chi_{zxx}^{(2)} = \chi_{zyy}^{(2)}$, $\chi_{xzx}^{(2)} = \chi_{yzy}^{(2)}$, and $\chi_{xxz}^{(2)} = \chi_{yyz}^{(2)}$. All other elements are zero.

The result is that symmetry breaking at the interface of an otherwise isotropic bulk medium leads to only 4 (out of 27 total) independent and nonvanishing elements of $\ddot{\chi}^{(2)}$. A direct consequence is that all possible contributions can be experimentally sampled with only four polarization combinations and used to deduce average molecular polar orientation at an interface (details on this follow in Section 1.3.2.8). The polarization combinations are usually labeled in order of decreasing photon energy, i.e. for vibrationally resonant SFG the order is VSFG, visible, mid-infrared. The results are summarized in Table 1-1.

Polarization Combination	**Elements of $\ddot{\chi}^{(2)}$**
pss	$\chi^{(2)}_{zyy}$
sps	$\chi^{(2)}_{yzy}$
ssp	$\chi^{(2)}_{yyz}$
ppp	$\chi^{(2)}_{xzz}$ $\chi^{(2)}_{xzx}$ $\chi^{(2)}_{xxz}$ $\chi^{(2)}_{zzz}$

Table 1-1. Summary of polarization experiments and elements sampled of the second order susceptibility. Polarization denotes electric field polarization and is in order of decreasing photon energy: SFG-input beam 1-input beam 2. For this work, input beam 1 is 800 nm and input beam 2 is in the mid-infrared.

Another consequence is that by inverting the z-axis of the system, the sign of all susceptibility elements change. This makes SFG sensitive to the polar orientation of resonances through the relative phase (0 or π) of the output field.

1.3.2.7 SFG from an Interface and Boundary Conditions

With the elements of $\ddot{\chi}^{(2)}$ at an interface determined (within the electric dipole approximation), the wave equation remains to be solved. The common approach is to consider a thin nonlinear polarized sheet sandwiched between semi-infinite (linear)

media 1 and 2 on either side. The wave equation takes the form of Eq. (1.38) on either side of the sheet (no source terms). Within the sheet, the source nonlinear polarization is assumed a 2-dimensional infinite plane wave of the form[184,224,230,236,237]

$$\mathbf{P}^{NL}(\mathbf{r},\Omega)=\mathbf{P}_s^{(2)}(\mathbf{r},\Omega)=\delta(z)\mathbf{P}_s\left[\exp(i\mathbf{p}\cdot\mathbf{r}-\Omega t)+c.c\right] \tag{1.56}$$

with wavevector $\mathbf{p}$ and the wave equation is

$$\left(-\nabla^2+\frac{\omega^2}{c^2}\vec{\vec{\varepsilon}}^{(1)}(\Omega)\right)\mathbf{E}(\mathbf{r},\Omega)=-\frac{4\pi\omega^2}{c^2}\mathbf{P}_s^{(2)}(\mathbf{r},\Omega) \tag{1.57}$$

The connection to Eq. (1.51) is

$$\begin{aligned}\mathbf{P}_s^{(2)}(\mathbf{r},\Omega)&=\mathbf{P}_{total}^{(2)}(\mathbf{r},\Omega)\\&=\vec{\vec{\chi}}_s^{(2)}(\mathbf{r},\Omega=\omega_1+\omega_2):\mathbf{E}^{local}(\mathbf{r},\omega_1)\mathbf{E}^{local}(\mathbf{r},\omega_2)\end{aligned} \tag{1.58}$$

where the subscript notation now indicates this is a surface-allowed susceptibility (i.e. $\vec{\vec{\chi}}_s^{(2)}=\vec{\vec{\chi}}_{D0_{EE}}^{(2)}$) and the superscript *local* indicates that the total input fields within the sheet are different from the incident amplitudes. The wave equation is solved subject to boundary conditions[237] and the phase-matching restriction.

$$\mathbf{k}_\Omega=\mathbf{k}_1+\mathbf{k}_2 \tag{1.59}$$

The resulting electric field propagating into medium *m* is[i]

$$\mathbf{E}_m(\mathbf{r},\Omega)=\frac{i2\pi\Omega\sec\left[\theta_m(\Omega)\right]}{c\sqrt{\varepsilon_m(\Omega)}}\vec{\vec{L}}_{mn}(\Omega)\left[\vec{\vec{\chi}}_s^{(2)}\vec{\vec{L}}_{mn}(\omega_1)\mathbf{E}(\mathbf{r},\omega_1)\vec{\vec{L}}_{mn}(\omega_2)\mathbf{E}(\mathbf{r},\omega_2)\right] \tag{1.60}$$

The subscript *m* and *n* indicate medium 1 or 2, depending on which side of the polarized sheet the field is being calculated (they do not indicate elements of the matrices).

[i] The units of the emitted electric field are actually E/m. This is a result of the infinite plane wave approximation, it is rectified when one goes to calculate irradiance (proportional to (E/m)^2) scaled by beams of finite area.

The $\ddot{\vec{L}}_{mn}$ matrices account for the fact that the total externally applied fields within the polarized sheet are not just the incident and emitted field amplitudes; rather, they must be connected by continuity conditions at an interface.

$$\mathbf{E}^{local} = \ddot{\vec{L}}_{mn}\mathbf{E} \tag{1.61}$$

The $\ddot{\vec{L}}_{mn}$ matrix takes the same form for the incident and emitted fields. For fields incident from medium 1 (or generated into medium 1), in the xyz coordinate system it is[237]

$$\ddot{\vec{L}}_{12} = \begin{pmatrix} \cos(\theta)t_{12}^{p} & 0 & 0 \\ 0 & t_{12}^{s} & 0 \\ 0 & 0 & \dfrac{n_2}{\bar{n}}\sin(\theta)t_{12}^{p} \end{pmatrix} \tag{1.62}$$

where all refractive indices and angles of incidence are specific to the field under consideration and $\bar{n}$ is the refractive index within the polarized sheet. Here, $t_{mn}^{p/s} = E_t^{p/s}/E_I^{p/s}$ are the linear Fresnel amplitude coefficients for transmission (detailed in Chapter 3). For fields incident from medium 2, one simply rewrites Eq. (1.62) with the indices switched and replace θ with $-\theta$.

Upon inspection, it is evident that the fields within the polarized sheet are related by the continuity condition on the tangential components of $\mathbf{E}$ and the normal component of $\mathbf{D}$. The continuity conditions are already satisfied in the derivation of the linear Fresnel coefficients.[382,385] To make this clearer, consider that the elements of $\ddot{\vec{L}}_{12}$ are expressed as a ratio to the incident amplitudes. They are equivalently written

$$
\begin{aligned}
L_{12}^{xx} &= \frac{E^{local,x}}{E_I^x} = \cos(\theta) t_{12}^p = \cos(\theta)\left[1 + r_{12}^p\right] \\
L_{12}^{yy} &= \frac{E^{local,y}}{E_I^y} = t_{12}^s = 1 + r_{12}^s \\
L_{12}^{zz} &= \frac{D^{local,z}}{E_I^z} = \frac{\bar{n}^2 E^{local,z}}{E_I^z} \\
&= n_1^2 \sin(\theta) t_{12}^p = n_2^2 \sin(\theta)\left[1 - r_{12}^p\right]
\end{aligned}
\tag{1.63}
$$

with $r_{12}^{p/s} = E_r^{p/s} / E_I^{p/s}$ as the linear Fresnel amplitude coefficients for reflection that will be detailed in Chapter 3. Multiplying out the ratios leads to (see Figure 1-7 for the various quantities, the minus sign on r_{12}^p in L_{12}^{zz} is a result of the coordinate frames defined there)

$$
\begin{aligned}
E^{local,x} &= \cos(\theta) E_t^p = \cos(\theta)\left[E_I^p + E_r^p\right] \\
E^{local,y} &= E_t^s = E_I^s + E_r^s \\
D^{local,z} &= \bar{n}^2 E^{local,z} \\
&= n_1^2 \sin(\theta) E_t^p = n_2^2 \sin(\theta)\left[E_I^p - E_r^p\right]
\end{aligned}
\tag{1.64}
$$

This shows that the local fields can be calculated by summing the total electric field amplitude on either side of the interface for the tangential components. For the normal component of **D**, the same can be done and is related to the normal component of **E** through a well-defined ratio of refractive indices. Thus, for thin film systems where interference effects complicate the fields adjacent to the interface, the problem is solved in a completely analogous way by using the transfer matrix to analytically calculate adjacent fields. This highlights one idea of fundamental importance to the thin film model that will be presented in Chapter 3.

The polarized sheet model is central to the multilayer thin film model developed in this work and presented in Chapter 3. However, Eq. (1.60) suggests that, whatever

form the susceptibility takes, if one can perform relative measurements on a system where the local field corrections do not change (much), amplitude ratios could be used to deduce changes in the susceptibility since the extra factors would cancel in the ratio. This is the idea presented in Chapter 2 with thermally annealed samples, along with some difficulties with that approach when considering SFG from thin film systems.

1.3.2.8 Microscopic Origin of the Macroscopic Susceptibility

In order to extract information about molecular structure, the macroscopic polarization $\mathbf{P}$ must be connected with its microscopic origin. The polarization of a material is defined as the dipole moment per unit volume so that it results from the sum of all induced molecular dipoles $\boldsymbol{\mu}_{ind}$. Within the electric dipole approximation, the incident electric fields exert a force on the electrons and nuclei (separately, within the Born-Oppenheimer approximation). The induced dipole can be expanded analogous to the polarization in Eq. (1.34).[159,323,384,395]

$$\boldsymbol{\mu}_{ind} = \ddot{\alpha}\mathbf{E} + \ddot{\beta}\mathbf{E}\mathbf{E} + \ddot{\gamma}\mathbf{E}\mathbf{E}\mathbf{E} + \ldots \tag{1.65}$$

Here $\ddot{\alpha}$ is the molecular polarizability of the material and $\ddot{\beta}$ and $\ddot{\gamma}$ are the second and third order hyperpolarizabilities. Using completely analogous arguments as in Sections 1.3.2.3 and 1.3.2.4 one can show that the process of SFG is contained in the second order term. The second order susceptibility for SFG is then an average of the second order hyperpolarizability satisfying $\Omega = \omega_1 + \omega_2$ weighted by the number density of volume elements in the sampling region N.

$$\ddot{\chi}_R^{(2)} = N\left\langle \ddot{\beta} \right\rangle \tag{1.66}$$

The discussion in this section considers molecular vibrational modes as the smallest polarizable volume element.

The microscopic quantity $\ddot{\beta}$ is usually presented in the molecular coordinate system *abc* (dummy indices $\alpha\beta\gamma$) which is generally different from the lab *xyz* frame (dummy indices *ijk*). A quantum mechanical expression that includes damping for the elements of $\ddot{\beta}$ can be derived using the density matrix and second order perturbation theory.[120,159,323,384,396] A consequence of the electric dipole approximation (Section 1.3.2.5) is that the quantum mechanical operator for the electric field perturbation is just the electric dipole operator used extensively in linear optics, obtained by expanding plane wave electric fields and truncating at the first term (the long wavelength approximation).

$$\boldsymbol{\mu} = e\mathbf{r} \tag{1.67}$$

When one of the input beams is tuned to the vicinity of a vibrational mode in the infrared the hyperpolarizability elements take the form[396]

$$\beta_{\alpha\beta\gamma} = -\frac{1}{2\hbar}\frac{M_{\alpha\beta}A_{\gamma}}{\bar{\omega} - \omega_{IR} - i\Gamma} \tag{1.68}$$

where $M_{\alpha\beta}$ is the anti-Stokes Raman tensor of the mode

$$M_{\alpha\beta} = \frac{1}{\hbar}\sum_{s\neq 1\neq 0}\left[\frac{\langle 0|\mu_{\alpha}|s\rangle\langle s|\mu_{\beta}|1\rangle}{\omega_{s0} - \Omega - i\Gamma} - \frac{\langle 0|\mu_{\beta}|s\rangle\langle s|\mu_{\alpha}|1\rangle}{\omega_{s0} + \omega_{vis} + i\Gamma}\right] \tag{1.69}$$

and A_{γ} is the IR electric dipole transition moment.

$$A_{\gamma} = \langle 1|\mu_{\gamma}|0\rangle \tag{1.70}$$

Immediately it is seen that, in order for a vibrational mode to be SFG active, it must be both IR and Raman active and that SFG is enhanced when ω_{IR} is resonant with a molecular vibration at $\bar{\omega}$. For the purposes of this dissertation, the system is assumed to consist of two real levels, the ground $|0\rangle$ and first excited state $|1\rangle$ for the vibrational mode, and a nonresonant state $|s\rangle$ (also referred to as a virtual state). Here now it is specified that $\omega_2 = \omega_{IR}$ and $\omega_1 = \omega_{vis}$ to indicate the input fields are in the visible and mid-infrared. Then, ω_{s0} corresponds to the transition frequency between the virtual level and the ground state, $\bar{\omega}$ is the peak center of the mode, and Γ is the damping constant that accounts for the homogenous vibrational linewidth and other relaxation pathways. The system is assumed to start in the ground state.

In order to arrive back at the laboratory frame, the elements of $\ddot{\chi}_R^{(2)}$ are related to the elements of $\ddot{\beta}$ through the unit vector projections.[238]

$$\chi_{R,ijk}^{(2)} = N\sum_{\alpha\beta\gamma}\left\langle\left(\hat{\mathbf{i}}\cdot\hat{\boldsymbol{\alpha}}\right)\left(\hat{\mathbf{j}}\cdot\hat{\boldsymbol{\beta}}\right)\left(\hat{\mathbf{k}}\cdot\hat{\boldsymbol{\gamma}}\right)\beta_{\alpha\beta\gamma}\right\rangle = \frac{N\left\langle\beta_{ijk}\right\rangle}{\bar{\omega}-\omega_{IR}-i\Gamma} \tag{1.71}$$

with

$$\left\langle\beta_{ijk}\right\rangle = \left\langle M_{ij}A_k\right\rangle \tag{1.72}$$

Broad and frequency independent responses are often observed in experimental data (e.g. from metals) from what is referred to as the vibrationally nonresonant response, $\ddot{\chi}_{NR}^{(2)}$. When a detectable response is not resonantly enhanced, it will typically have a much more complex microscopic description due to the likelihood of higher order quadrupole and/or magnetic dipole terms having an appreciable contribution.

Since a microscopic understanding is not necessary in many cases, these effects can be grouped into a macroscopic nonresonant susceptibility $\vec{\vec{\chi}}^{(2)}_{NR}$ that is constant but generally complex. An energy level diagram showing vibrationally resonant and nonresonant response is shown in Figure 1-9.

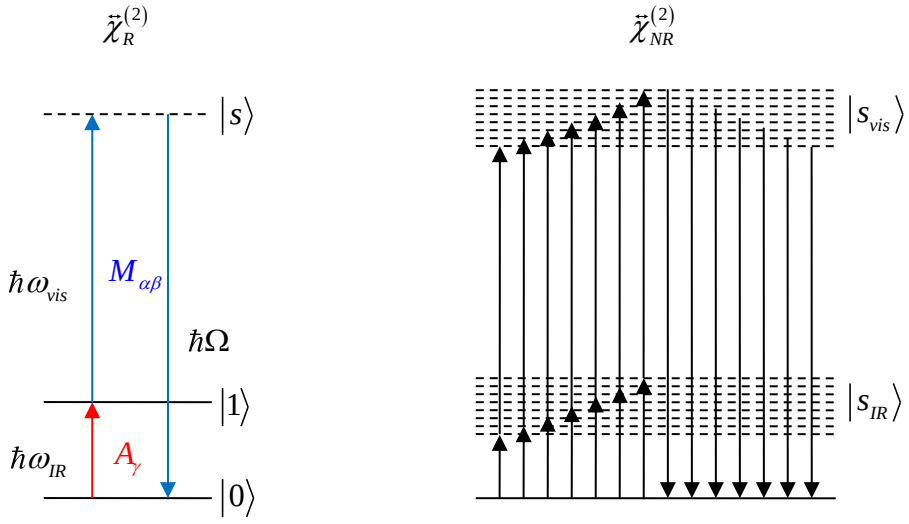

Figure 1-9. Jablonski diagrams of vibrationally resonant and nonresonant SFG showing response using a broad bandwidth mid-infrared source.

1.3.2.9 Modeling SFG Data

Modeling experimentally collected SFG spectra from a single interface is usually implemented by considering that the total signal is due to the macroscopic local field corrections and the sample response. Experiments primarily utilize linearly polarized input fields so that the polarization experiments in Table 1-1 are executed individually. For experiments that sample a single element of $\vec{\vec{\chi}}^{(2)}_{s}$ the intensity expression can be written

$$I_{sfg} \propto I_{vis} I_{IR} \left(\hat{\mathbf{e}}^{sp} \cdot \hat{\mathbf{e}}^{i}\right)\left(\hat{\mathbf{e}}^{j} \cdot \hat{\mathbf{e}}^{sp}_{vis}\right)\left(\hat{\mathbf{e}}^{k} \cdot \hat{\mathbf{e}}^{sp}_{IR}\right)\left|L^{ii}_{sfg} \chi^{(2)}_{ijk} L^{jj}_{vis} L^{kk}_{IR}\right|^2 \tag{1.73}$$

The prefactor projections account for the changed coordinate system (from the sample *xyz* frame to propagating fields *sp* frame for the generated field and opposite for input fields). The unit vectors were defined in Section 1.3.2.1. For the *ppp* experiment, the expression contains multiple contributions due to *p*-polarized input fields.

$$I^{ppp}_{sfg} \propto I_{vis} I_{IR} \sum_{i \neq y}\left(\hat{\mathbf{e}}^{sp} \cdot \hat{\mathbf{e}}^{i}\right)\left(\hat{\mathbf{e}}^{j} \cdot \hat{\mathbf{e}}^{sp}_{vis}\right)\left(\hat{\mathbf{e}}^{k} \cdot \hat{\mathbf{e}}^{sp}_{IR}\right)\left|L^{ii}_{sfg} \chi^{(2)}_{ijk} L^{jj}_{vis} L^{kk}_{IR}\right|^2 \tag{1.74}$$

The second order susceptibility is usually taken as a sum of q vibrationally resonant modes and a nonresonant response.

$$\chi^{(2)}_{ijk} = \chi^{(2)}_{NR,ijk} + \sum_{v} \chi^{(2)}_{R,v,ijk} \tag{1.75}$$

The vibrational resonances take the form of Eq.(1.71), each with a unique amplitude $A_{q,ijk} = \left\langle \beta_{q,ijk} \right\rangle$, center frequency $\bar{\omega}_q$, and damping constant Γ_q.

The complex nature of the resonant and nonresonant susceptibilities leads to phase relationships between source terms that interfere at the intensity level since

$$I \propto \left| \chi^{(2)}_{NR,ijk} + \sum_{q} \chi^{(2)}_{R,q,ijk} \right|^2 \tag{1.76}$$

A single vibrational resonance has a Lorentzian lineshape at the intensity level. In the presence of a nonresonant contribution; however, it may appear as a dip, peak, or derivative-looking lineshape, depending on the relative phase.

$$\begin{aligned} I &\propto \left| \chi^{(2)}_{NR,ijk} + \chi^{(2)}_{R,ijk} \right|^2 \\ &\propto \left| \chi^{(2)}_{NR,ijk} \right|^2 + \left| \chi^{(2)}_{R,ijk} \right|^2 + 2\left| \chi^{(2)}_{NR,ijk} \right| \left| \chi^{(2)}_{R,ijk} \right| \cos\left(\phi_{NR} - \phi_R\right) \end{aligned} \tag{1.77}$$

In spectrally congested regions with multiple SFG active modes, pulling apart the complicated interferences at the susceptibility level can be quite challenging, and often fit results are not unique. This emphasizes an additional challenge when interpreting SFG data. A review is available that has a nice discussion on the phase relationships among the susceptibility contributions.[395]

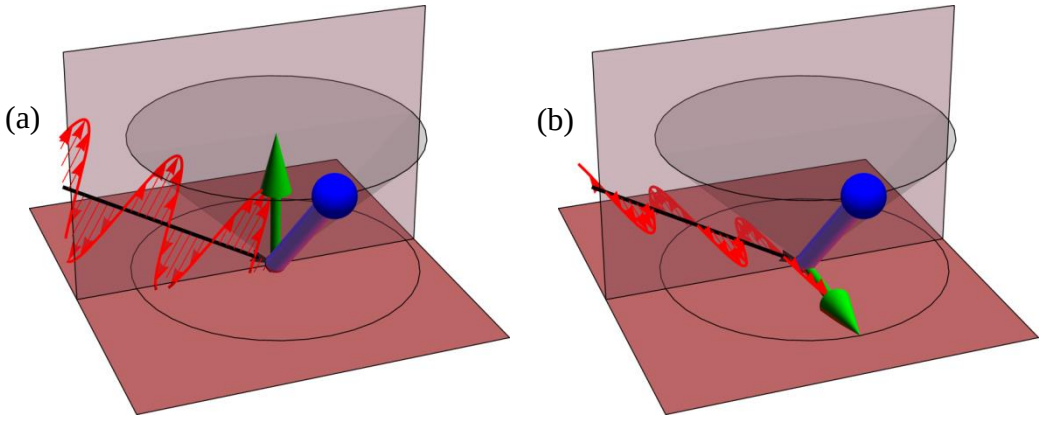

Figure 1-10. Graphics illustrating the interaction of the mid-infrared beam for (a) *p*-polarized input sampling the transition normal component and (b) *s*-polarized input sampling the in-plane transition component of a polar oriented mode that is otherwise isotropically distributed in the plane.

All nonzero hyperpolarizability elements (Eq. (1.68)) in the molecular frame can potentially contribute to every element of the macroscopic $\ddot{\chi}_R^{(2)}$ response in the laboratory frame, but with restrictions based on molecular symmetry and average polar orientation.[239,240] It is through the evaluation of the microscopic elements, either through *ab initio* methods or by direct measurement using linear absorption and Raman techniques, that molecular structure can be deduced. For instance, it is common to implement a ratio calculation from an experiment that samples the in-plane IR transition moment (e.g. *sps*) to one that samples the out-of-plane (e.g. *ssp*) transition moment. The interactions of the mode with orthogonal components of the mid-infrared are illustrated in Figure 1-10. As the molecular hyperpolarizabilities depend on the

symmetry of the mode under consideration, a unique expression will be obtained for modes of different symmetry. For example, modes with C_{3v} symmetry (e.g. the methyl group) it can be shown that the intensity ratio is related to the average cosine of the polar angle by the expression[274]

$$\frac{\langle \beta_{yyz} \rangle}{\langle \beta_{yzy} \rangle} = 1 - \frac{2r}{\left[1 - \langle \cos(\theta) \rangle^2\right](1-r)} \tag{1.78}$$

where $r = \beta_{aac}/\beta_{ccc}$. It is through these types of relations that SFG can be used to deduce molecular structure.

1.3.3 *Conclusion*

The theory of SFG from an interface within the dipole approximation depends primarily on two conditions: resonant enhancement and polar ordering at the interface. The discussion on higher order bulk-allowed terms is important to keep in mind when analyzing SFG data from molecular systems that are more than a single monolayer thick, and even in the case of a monolayer one must be sure the signal is dominated by dipole interactions and are not from quadrupole enhancement through rapid variation in the field amplitudes at the interface. These considerations are important in order to properly quantify molecular structure.

As it turns out, the mathematical treatment indicates that the dipole approximation only really comes into play when analyzing data, that is, when one tries to say something physical about the system under interrogation. As pointed out by Shen's group back in the 1980's, the bulk contributions can be put in a form that is consistent with an interfacial dipole-type interaction so that a single measurement

cannot differentiate the interaction source of SFG signal. Measurements in reflection as well as transmission can be used to determine if there is a non-negligible bulk response for single interface systems. More knobs are required for determining if the interfacial response is truly dominated by a dipole-type interaction (e.g. varying the refractive index of the outermost semi-infinite material).

The local field factors relate input beams to the fields within the polarized sheet and the nonlinear polarization to outgoing fields. Calculation of the input local fields is readily extended to arbitrary multilayers simply by calculating the total field amplitudes adjacent to an interface using the transfer matrix approach. However, it will be discussed in the following chapters that calculating optical interference effects on fields generated within an arbitrary multilayer system is not as straightforward. This is a primary contribution from this work and is accomplished in Chapter 3 by considering the single interface result (Section 1.3.2.7) in combination with reducing the multilayer thin film system to a single layer with newly defined coefficients of reflection and transmission. With these results, the electric dipole approximation can be better tested by improved sampling of SFG data from thin film systems where additional degrees of freedom may be varied. This is demonstrated experimentally in Chapter 5 with data collected from gradient thickness organic thin films.

Project Synopsis

This dissertation describes advances made in applying sum frequency generation spectroscopy (SFG, in particular *vibrational* SFG or VSFG) to multilayer thin film systems by providing an intuitive model of optical interference effects; postulating a solution to the two-interface problem of SFG applied to planar and stratified multilayer structures. The first chapter explains the need for surface sensitive techniques for *buried* interfaces in thin film systems. This is motivated by the complex nature of charge carrier phenomena that occur at buried interfaces within organic semiconductor devices, specifically in organic field-effect transistors (oFETs). Section 1.3 on the history and theory of SFG has been written from my point of view as the inaugural student of SFG in a research group that had no formal background in this technique. The goal of the introduction to SFG is to provide a compact reference for some important aspects to consider for future students of the project, but is by no means comprehensive. The introductory theory has centered on *single interface* systems. The conclusion is that within the electric dipole approximation, SFG can fill the need of a surface sensitive probe to molecular structure in organic thin film systems. The electric dipole approximation is most likely to be valid for systems that possess resonant enhancement and where there is significant polar ordering of the molecules at the interface. A discussion on SFG applied to thin film systems emphasizes that the two-interface problem and optical interference effects from *multilayer* thin film systems are issues that have been largely avoided in the literature. It is surmised that the reason

this is the case is that there has been a lack of an intuitive model to describe these effects.

In the chapters following the background information, the chronology of my considerations for the two-interface problem is laid out. The second chapter goes beyond the discussion of SFG focused on a single interface and presents the two-interface problem for SFG applied to thin film systems.[96] At this point, data from thin organic films deposited on multiple silica substrates are fit to a very simple model where VSFG vibrational mode peaks are considered to contain signals from both interfaces of the organic, and each has associated optical interference effects. The local field corrections and optical interference effects *are not calculated* but are eliminated by taking a ratio of fit results for data collected before and after thermal annealing. The model system for this dissertation is introduced in this chapter: thin films of the small molecule N,N'-dioctyl-3,4,9,10-perylenedicarboximide (PTCDI-C_8) vapor deposited on silica thin film substrates, consistent with an oFET thin film geometry. VSFG data obtained from PTCDI-C_8 deposited on multiple silica surfaces demonstrates that optical interferences influence the detected VSFG intensity, and the simple model used in the analysis leads to some ambiguities in data interpretation.

The next three chapters aim to reduce or eliminate some of the ambiguities in VSFG data analysis. In Chapter 3, a refined model is presented for interface-specific coherent nonlinear optical spectroscopies applied to ideal arbitrary multilayers that explicitly calculates optical interference effects.[372] The model is based on the transfer matrix and reduces the multilayer thin film system to a single layer with newly defined coefficients of reflection and transmission at the layer boundaries. Chapter 4 uses the

model to simulate data and present some intricacies contained in the intensity data of SFG taken from the model oFET system.[397] Chapter 5 presents experimental evidence for the model by obtaining VSFG data along the length of thickness gradients of PTCDI-C_8 deposited on silicon wafers with two different oxide thicknesses. The thickness dependence in the intensity data is reproduced well by the *interfacial* thin film model. However, I find evidence that the response is not fully consistent with the electric dipole approximation. The model is then extended to describe optical interferences from possible *bulk* sources and an analysis of the data indicates that higher order bulk *and* interfacial terms are both likely present in this system. Some considerations for imposing better constraints on experimental data and modeling are discussed. It is pointed out that, while contributions from the bulk may complicate data analysis, the interfacial contributions are significant and that the model developed in my thesis work combined with the thin film geometry provides a new and unique way to quantify contributions to the VSFG signal. Finally, Chapter 6 provides a discussion on early efforts from my graduate work including key experiments that ultimately led to my focus on the two-interface and optical interference problems associated with SFG applied to organic thin film systems.

2 Surface Chemistry and Annealing-Driven Interfacial Changes in Organic Semiconducting Thin Films on Silica Surfaces

Adapted with permission from

Daniel B. O'Brien, Timothy C. Anglin, and Aaron M. Massari. Surface Chemistry and Annealing-Driven Interfacial Changes in Organic Semiconducting Thin Films on Silica Surfaces. *Langmuir*. **2011**, 27, pp 13940-13949.

CHAPTER SUMMARY

In this chapter, interface-specific VSFG spectroscopy was used to investigate the structure of the initial monolayer of N,N'-dioctyl-3,4,9,10-perylenedicarboximide (PTCDI-C_8) thin films deposited on silica surfaces and their behavior upon thermal annealing. The major goals are to present the model system of this dissertation, introduce the effects of thin film interference on VSFG intensity data, and introduce a very simple two-interface model for VSFG applied to organic thin film systems. The data fitting routine uses the model to simultaneously fit and extract apparent amplitude contributions from the outer (exposed) and inner (buried) interfaces for the symmetric

imide carbonyl mode before and after thermal annealing. A ratio of amplitudes before and after thermal annealing is used to cancel unknown variables and deduce that the structure of the outer interface is always subject to reorganization, whereas the inner interface resists change when deposited on a well ordered trimethoxy(octadecyl)silane self-assembled monolayer. A number of important aspects emerge from this work such as the significance of optical interferences on data interpretation, the sensitivity of VSFG to substrate functionalization, and ambiguities associated with modeling two-interfaces and the associated issues with fitting data to such a model.

2.1 INTRODUCTION

Semiconducting organic thin films are held together by weak non-bonding forces that enable them to be prepared through cost-effective methods, such as solution casting and vapor deposition. Unfortunately, the same forces that make them technologically attractive also result in relatively weak electronic couplings. This leads to fundamentally different mechanisms of charge transport, with organic materials favoring thermally activated charge hopping over the more efficient band-type conduction. Within this mechanism, charge transport is impeded by energetic barriers between states as well as self-trapping due to molecular rearrangement and polaron formation.[51,66]

At first glance, the successful integration of organic materials into electronic devices relies upon their ability to conduct charge carriers (electrons and/or holes) through the bulk. Yet, in many cases, it is not the characteristics of the bulk material, but rather the *interfaces* between materials that dominate device performance.[11,398] As described in Section 1.2.2, a striking example of this behavior is found in the organic field-effect transistor (oFET). Charge conduction in these devices occurs exclusively along the buried interface of the organic thin film and a dielectric material where an applied gate bias drives the accumulation of charge carriers.[15,16,18] The conducting layer is generally considered to be on the order of a monolayer thickness for a typical organic material despite the fact that even the thinnest semiconductor films are on the order of several to tens of monolayers thick. The thin and buried nature of the active interface in oFETs makes it a difficult region to study spectroscopically due to its short optical path

length and contamination of its spectroscopic signals with those generated in the bulk (non-accumulated) of the material.[15,399]

Vibrational sum frequency generation (VSFG) spectroscopy has been demonstrated as a surface-specific nonlinear optical technique useful for elucidating structural information at interfaces. As detailed in Section 1.3.2, in the context of perturbation theory VSFG is a second order spectroscopy. Within the electric dipole approximation all even order spectroscopies have selection rules that make their observables zero anywhere there is inversion symmetry on a macroscopic scale.[395,400] Planar and stratified systems such as organic thin films are generally isotropic everywhere except at the material layer interfaces where inversion symmetry is lost. Therefore the accumulation layer in oFETs is amenable to characterization by VSFG.[236,401] VSFG makes use of two input beams with well-defined polarizations. The IR beam is tuned to the vibrational resonances of interest and the generated signals can be used to extract information about average molecular orientations and relative ordering at interfaces.[25,343]

In this work, interface-specific VSFG spectroscopy was used to investigate the structure of the initial monolayer of N,N'-dioctyl-3,4,9,10-perylenedicarboximide (PTCDI-C_8, a common n-type organic semiconductor) thin films deposited on silica surfaces and its behavior upon thermal annealing. The system was designed to give an accurate representation of the interfacial layer of PTCDI-C_8 thin films while minimizing optical phase shifts between layers inherent to thicker films. First we consider qualitative trends in the data when VSFG is performed on reflective versus transparent substrates. Additionally we consider the dependence of film morphology with subtle

differences in the SiO_2 substrate chemistry. Modeling of the VSFG data from the imide carbonyl vibrational region was used to identify changes in the ensemble molecular ordering of the interfacial phase on bare and self-assembled monolayer (SAM) functionalized SiO_2 dielectrics before and after sample annealing. Modification of SiO_2 substrates with SAMs and thermal annealing procedures have been shown to significantly impact oFET device performance and stability under ambient conditions.[65,402,403] Thus, we also compared the electrical behaviors of oFETs to the VSFG spectra from samples prepared and annealed under identical conditions to assist in interpreting the structural information from the buried interfacial signals.

2.2 PTCDI-C_8 BACKGROUND

Derivatives of perylene tetracarboxylic acid have been demonstrated for use as n-type semiconductors in oFETs because of their high electron affinities.[18,103,402,404,405] This work is focused on the derivative N,N'-dioctyl-3,4,9,10-perylenedicarboximide (PTCDI-C_8, structure shown in Figure 2-5) vapor deposited on SiO_2, a commonly used dielectric for oFETs. It has been reported that films grown by vapor deposition assemble in terraced two-dimensional polycrystalline layers. Each layer is ~2 nm tall, indicating that the molecules stand upright with a small tilt angle between the long molecular axis and the surface normal. The bulk structure is independent of the chemical nature of the substrate and consists of stacked terraces.[95] Each layer is composed of two-dimensional polycrystalline grains where the grain sizes are dependent on the substrate temperature during vapor deposition but the polycrystalline domain sizes within individual grains remains essentially constant.[406] Through the bulk

of the films, the molecules orient for lateral π-π interactions of the perylene cores within each layer and alkyl chain interactions with adjacent layers.[95,103,407]

Details on the structure of the initial layer that forms directly on the substrate are less established, yet it is this layer that dictates device performance in oFETs. In particular, reports are conflicting on whether the initial monolayer phase is different from the bulk layers. Krauss and coworkers utilized grazing incidence X-ray diffraction (GIXD) to determine that the interfacial layer thickness for a 27 nm thin film vapor deposited at 90 °C and post-annealed to 100 °C was ~0.6 nm, which suggested that the molecules were in a reclined phase relative to the bulk layers.[95] X-ray reflectivity (XRR) has shown that annealing a monolayer of PTCDI-C_8 (deposited at 130 °C) to 160 °C reduced its thickness from 2.7 to 1.2 nm, which was attributed to reorientation of an initially metastable phase.[407] In contrast, X-ray diffraction (XRD) measurements on 36 nm thin films deposited at 75 °C showed no evidence of a distinct interfacial phase when deposited on either bare or polystyrene coated SiO_2 surfaces.[18] A closely related molecule, PTCDI-C_5, deposited on bare and octadecyltrichlorosilane treated SiO_2 was studied by AFM, XRR, and XRD. The interfacial phase was observed on both substrates but disappeared at high deposition temperatures.[103] In all of the X-ray studies, the molecular orientation in the first monolayer were deduced from an indirect measurement of the thickness of the interfacial phase. This region, in which the molecules may be reclined or upright relative to the surface normal, has important implications for interpreting oFET device performance. The apparent contradictions among these and other reports regarding the initial monolayer structure can be understood from the fact that the film formation depends on both deposition

temperature and surface chemistry, and there is no consistency to these parameters amongst the investigations cited.

2.3 EXPERIMENTAL

2.3.1 *Materials*

Silicon wafers with a 300 nm polished thermal oxide (TO, University Wafer), silicon wafers with a polished native oxide side (NO, Silicon Quest International), fused quartz slides (QS, SPI Supplies), and glass slides (GS, Gold Seal Cat. No. 3010) were used as substrate materials. N,N'-dioctyl-3,4,9,10-perylenedicarboximide (PTCDI-C_8, 98%) and trimethoxy(octadecyl)silane (ODTMS, technical grade 90%) were used as received from Sigma-Aldrich. ODTMS was transferred directly into a standard anhydrous and anaerobic (dinitrogen) glovebox prior to use. Anhydrous trichloroethylene (TCE, Sigma-Aldrich) was prepared by drying over $CaCl_2$ followed by vacuum transfer into a sealed flask and was stored in the glovebox. All other solvents were reagent grade and were used as received.

2.3.2 *SFG Sample Substrate Preparation*

NO, QS, and GS substrates were cut into roughly 1×2 cm rectangular substrates and were prepared for PTCDI-C_8 vapor deposition as follows. All substrates were cleaned following a modified RCA procedure.[408,409] Substrates were initially blown free of any particles and sonicated for 10 minutes in distilled water. Standard clean 1 (SC1) consisted of a solution of distilled water, hydrogen peroxide (30% in water), and concentrated ammonium hydroxide (~5:1:1 H_2O:30% H_2O_2:NH_4OH by volume) heated

to 80 °C and poured over the substrates in preheated vials followed by removal from the hotplate for 5 minutes of sonication. The substrates were quickly removed and rinsed with distilled water followed by 10 minute sonication in distilled water. Standard clean 2 (SC2) consisted of a 10 minute sonication in concentrated HCl diluted with distilled water (~20:1 H_2O:HCl by volume) followed by a distilled water rinse and a 10 minute sonication. Substrates were capped in vials after SC2 and stored in distilled water until further use. No further preparation was used for bare substrates prior to PTCDI-C_8 deposition.

ODTMS functionalized silica substrates were prepared by a spin-casting technique that yields very smooth well-ordered SAMs.[98] In a nitrogen glove box a 3 mM solution of ODTMS in anhydrous TCE was prepared and sealed in a glass vial with a septum cap and transferred out of the glove box. RCA cleaned substrates were removed from water and quickly blown dry with house N_2. The substrates were covered with 50 μL of ODTMS solution from a syringe, allowed to sit for 10 seconds, and then spun at 3000 rpm for 2 minutes followed by transfer into a sealed container that contained a small vial of concentrated NH_4OH for 12 hours. After NH_3 vapor-curing, the substrates were sonicated in toluene for 2 hours followed by a toluene rinse and a second 2 hour sonication in fresh toluene. ODTMS substrates were capped in individual vials and stored in toluene until further use. It is worth noting that we found by replacing the spinning step with a simple method of drawing off the ODTMS solution by touching the substrate to a glass beaker gave comparable results to the spinning method, although it was a bit more difficult to control and was not used in the present study.

Just prior to PTCDI-C_8 vapor deposition, surface energies were characterized by static distilled water contact angles measured at three spots across each substrate surface utilizing a Ramé-Hart model 100-00 goniometer. Ellipsometry and AFM were performed at the University of Minnesota Characterization Facility on substrates prepared identically to those used for VSFG measurements. Spectroscopic ellipsometry (J.A. Woollam Co. VASE) was performed at three different angles of incidence (65°, 70°, and 75°) in the region of 700-1100 nm on NO substrates to determine oxide and ODTMS SAM thicknesses. The Ψ and φ data were fit for the native oxide using a known model for native oxide optical constants and a transparent Cauchy model for the ODTMS refractive index.[410] The surface roughness and topography were characterized by AFM (Agilent 5500) performed in AC mode and stabilized in the attractive regime under dry N_2 gas purge (<1% relative humidity, room temperature).

2.3.3 *Field-Effect Transistor Substrate Preparation*

Bottom contact field-effect transistors (FETs) were prepared in a Class 10 cleanroom at the University of Minnesota Nanofabrication Center as described in detail previously.[25] TO substrates were prepared as follows: The unpolished side was selectively etched and a universal gate electrode was produced by electron beam deposition of 50 nm of aluminum followed by 200 nm of gold onto the exposed silicon surface. Multiple devices were then patterned by photolithography on the polished side. The source and drain electrodes consisted of a 2 nm chromium adhesion layer with 250 nm gold contacts. Each device had three channel lengths to choose from: 15 μm, 100 μm, and 500 μm with a constant width of 3 mm. Devices were cleaned following the RCA procedure described in the last section but with some minor changes: substrates

were submerged in SP1 for just 1-2 minutes with intermittent sonication during SP1 and SP2. ODTMS treatment followed as above. Substrates were characterized by static water contact angle measurements.

2.3.4 *PTCDI-C_8 Thin Film Preparation*

Vapor deposition was performed in a homebuilt high vacuum chamber. It consisted of a substrate holder mounted with an 11" throw above a crucible furnace (RADAK I, Luxel Corp). Just prior to vapor deposition of PTCDI-C_8, substrates were removed from storage solvents and immediately blown dry with house nitrogen. All depositions were done at or below 5×10^{-6} Torr. A crucible loaded with PTCDI-C_8 was heated following a temperature profile of 5 °C/minute to a final temperature near 230 °C. The crucible soaked for 10 minutes prior to film deposition and the temperature was adjusted to yield 0.1 Å/s average deposition rate to a total thickness of 8 nm as monitored by a quartz crystal microbalance (QCM) and verified by spectroscopic ellipsometry.

Vapor deposition was done in sets for VSFG substrates. Each set consisted of one each of bare and ODTMS surface preparations for NO, QS, and GS substrates for a total of six samples per set. There were three sets. After each deposition, sample sets were removed from the instrument and placed in individual vials and capped in air. After all samples had been through VSFG data collection they were thermally annealed at 110 °C for 1 hour in an oven followed by post-annealed VSFG data collection.

For electrical characterization, eight oFET substrates were loaded into the vapor deposition chamber concurrently to give four each of bare and ODTMS surface

preparations. Devices were removed from the instrument and placed in vials capped in air prior to electrical characterization.

2.3.5 *VSFG Spectroscopy of PTCDI-C_8 Thin Films*

2.3.5.1 VSFG Spectrometer Description

The femtosecond VSFG spectrometer utilized the tunable broadband IR and narrowband visible outputs of a regeneratively amplified laser and parametric amplifier system. The system consisted of a titanium sapphire (Ti:Sapph) oscillator (Kapteyn-Murnane Laboratories) pumped by a frequency-doubled continuous wave (CW) neodymium vanadate laser (Spectra-Physics, Millennia 5W) to generate mode-locked pulses at 93 MHz and centered at 800 nm with 50 nm of bandwidth (FWHM) and 3 nJ of power per pulse.

The oscillator output was used to seed the regeneratively amplified Ti:Sapph laser (Spectra-Physics, Spitfire-Pro 40f, 1kHz) pumped by a diode-pumped Q-switched neodymium yttrium lithium fluoride (Nd:YLF) laser (Spectra-Physics, Empower 15) to produce amplified 1.7 mJ chirped pulses at 1kHz. The majority of the amplified output was compressed to produce 1.0 mJ pulses as the output from the amplifier system, while a smaller portion ($\sim$ 300 mW) was diverted for use in the generation of the narrowband visible light.

To generate the mid-IR pulses, half of the total power from the regenerative amplifier (500 mW) was used to pump an optical parametric amplifier (OPA) (Spectra-Physics, OPA- 800C). The OPA utilizes a 3mm thick β-barium borate (BBO) crystal and parametric amplification to produce angle-tuned signal and idler pulses. The signal

and idler outputs from the OPA were difference frequency mixed in an angle-tuned silver gallium sulfide crystal ($AgGaS_2$, 1.0 mm thick) to generate tunable mid-IR pulses.

The narrowband visible light source was generated by passing the remaining 300 mW chirped output from the regenerative amplifier through an angle-tuned narrow bandpass filter (Semrock Inc., 3 nm FWHM) to obtain ~25 μJ pulses centered at 800 nm. These spectrally narrowed pulses were used to seed a home-built multipass amplifier (MPA). The MPA consisted of a Ti: Sapph crystal (Altos Photonics, 6 mm diameter, 1 mm thick, 0.25% doping) pumped by a portion (~3-4 W) of the output from the Q-switched Nd:YLF laser. The crystal was antireflection coated (AR) at 527 nm on both sides and AR at 800 nm on one side with a high reflective coating at 800 nm on the other. These coatings allowed the amplifier to be pumped in transmission geometry while the seed pulses were focused on the crystal from the opposite side in reflection geometry.[411] The ~25 μJ narrowband pulses were focused onto the crystal in a reflection geometry consisting of three passes so that the total path length on a single pass with reflection was 2 mm. The MPA produced ~110 μJ pulses which were then passed through a 4-f pulse shaper for further spectral narrowing.

2.3.5.2 VSFG Sample Measurements

The visible and mid-IR pulses were focused onto the sample and the SFG output collected and recollimated with a pair of 60° off-axis parabolic mirrors. Beam characteristics at the sample were 5 ps (FWHM) pulses centered at 799 nm with 5 cm^{-1} of bandwidth (FWHM) and 4 μJ/pulse for the visible and 100 fs (FWHM) pulses

centered around 1680 cm^{-1} with 160 cm^{-1} of bandwidth (FWHM) and 2 μJ/pulse for the mid-IR. The mid-IR and visible pulses were incident at 55° and 63° respectively from the sample normal and were focused and spatially overlapped in a ~100 μm 1/e radius spot. Temporal overlap was achieved by second order cross-correlation on a ZnO thin film and set to a delay of 0 fs. The generated signal was collected in reflection geometry and was spectrally resolved using multiplex detection by focusing into a 150 mm dispersive monochromator coupled to a liquid N_2 cooled CCD detector (Princeton Instruments, Spec-10). The work presented in this chapter utilized the *ssp* polarization combination: *s*-polarized VSFG, *s*-polarized visible, and *p*-polarized mid-IR. The optical system was sealed and purged with dry air at -80 to -100 °F dew point.

For VSFG measurements, the PTCDI-C_8 thin film samples were loaded into a magnetic mount sample holder so that each substrate surface was held in the same plane, which was perpendicular to the plane of incidence. Laser spot sizes were optimized so that laser annealing was not evident. The sample was continuously moved horizontally and data were taken along a stripe ±2 mm relative to the initial laser setup. Each sample was placed in the instrument at least twice for data collection. Data collected on samples after reloading into the instrument indicated good overall reproducibility. The spectra were then averaged for each sample.

Data were collected using a custom LabVIEW program written in-house and employed a sequential background subtraction scheme with a simple algorithm for removing cosmic rays. A single frame consisted of integrating on the CCD for a given time followed by blocking of the mid-IR beam and integrating for the same time with subsequent subtraction of the two spectra after cosmic ray removal. Cosmic rays were

removed by collecting five frames and executing a discrimination procedure for each pixel in the raw and background data separately. Each pixel value was compared to the median value for that pixel in all frames. Values that were beyond four standard deviations of the median were rejected and replaced with the mean of the remaining pixel values. The five cosmic ray corrected and background subtracted spectra were then averaged and scaled to integration times which varied from 1 to 10 minutes among samples. A reference spectrum was collected for each sample spectrum using a ZnO thin film to normalize by the mid-IR power spectrum. The ZnO film was deposited on a Si wafer substrate at 230 °C by atomic layer deposition (ALD) by alternating the precursors diethylzinc and water vapor to a thickness of 75 nm. The ZnO film was prepared at the University of Minnesota NanoFabrication Center.

2.3.6 *PTCDI-C_8 oFET Electrical Characterization*

Electrical characterization was performed in a cryostat at room temperature under vacuum at or below 1×10^{-4} Torr. Transfer curves were collected in the saturation regime ($V_D = 100$ V) using two Keithley 617 electrometers. Thermal annealing at 110 °C for 1 hour followed and the samples were allowed to cool to room temperature. Then, post-annealed transfer curves were collected without removing them from vacuum. Transfer curves were obtained on each of the three channel lengths for each of four devices for both bare and ODTMS treated substrates. Saturation mobilities μ_{sat} were extracted from fits to the square root of the source-drain current $\sqrt{I_{D,sat}}$ versus gate voltage as detailed in Eq. (1.8) in Section 1.2.2.1. For these devices, the width varies but the length is a constant 3 mm. The capacitance of SiO_2 was measured in

these devices to be $C_{ox} = 1.190 \pm 0.006 \times 10^{-8}$ F cm^{-2}. The threshold voltage V_T and saturation mobilities were used as fitting parameters.

2.4 RESULTS AND DISCUSSION

2.4.1 *Substrate Characterization*

The cleaning process described above resulted in hydrophilic surfaces for all substrates (NO, QS, GS, and TO) as indicated by low water contact angles in Table 2-1. Functionalization of all four substrate types with ODTMS produced surfaces that were equally hydrophobic with water contact angles approaching 110°. Surface morphologies and roughnesses characterized by AC mode AFM indicated very smooth interfaces for bare and ODTMS functionalized surfaces with only slightly lower RMS roughnesses for the highly polished NO wafers (Table 2-1). The topographic images are shown in Figure 2-1. These consistencies across all sample types are important for the interpretation of the VSFG data below in terms of substrate surface energies with minimal effects from differences in substrate topographies. Spectroscopic ellipsometry indicated that the bare NO substrates had a 2.6 nm oxide layer, and the ODTMS SAM thicknesses were 2.2 nm, consistent with a single layer of crystalline ODTMS with the alkyl chains standing on-end.[98]

Table 2-1. Water contact angles and RMS roughnesses for bare substrates, and PTCDI-C_8 thicknesses and field-effect electron mobilities[i]

substrate	bare substrate properties		PTCDI-C_8 thickness (nm)[ii]	unannealed mobility $\times 10^2$ (cm^2/Vs)	improvement factor upon annealing
	ϕ_{H2O} (degrees)	RMS (nm)[iii]			
NO	3.7 ± 1.3	0.18 ± 0.02	8.0 ± 0.3		
QS	4.2 ± 0.8	0.42 ± 0.08			
GS	3.1 ± 0.8	0.53 ± 0.12			
TO	2.5 ± 0.3			3.7 ± 1.3	2.1 ± 0.3
NO-ODTMS	107.4 ± 0.8	0.28 ± 0.12	8.3 ± 0.7		
QS-ODTMS	104.9 ± 0.6	0.57 ± 0.13			
GS-ODTMS	109.2 ± 0.5	0.77 ± 0.44			
TO-ODTMS	104.3 ± 1.7			1.1 ± 0.3	2.1 ± 0.2

[i] Error values represent the standard error of the mean.
[ii] Measured on NO samples only, but all PTCDI-C_8 samples were deposited at the same time.
[iii] RMS roughness values calculated over the entire 2 x 2 μm images for the bare substrates.

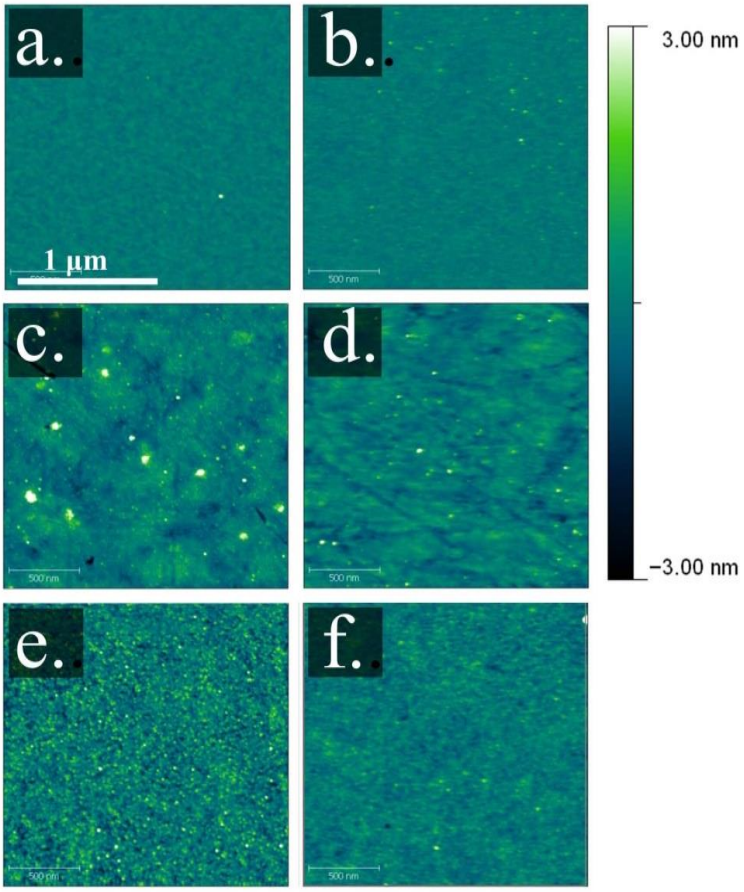

Figure 2-1. AFM topographic images of bare and ODTMS functionalized substrates. Substrates shown: a) NO, b) NO-ODTMS, c) QS, d) QS-ODTMS, e) GS, and f) GS-ODTMS.

VSFG data were collected from the ODTMS SAMs prior to PTCDI-C_8 deposition using the *ssp* beam polarization combination in the alkyl vibrational region. The results from all three substrates are shown in Figure 2-2.

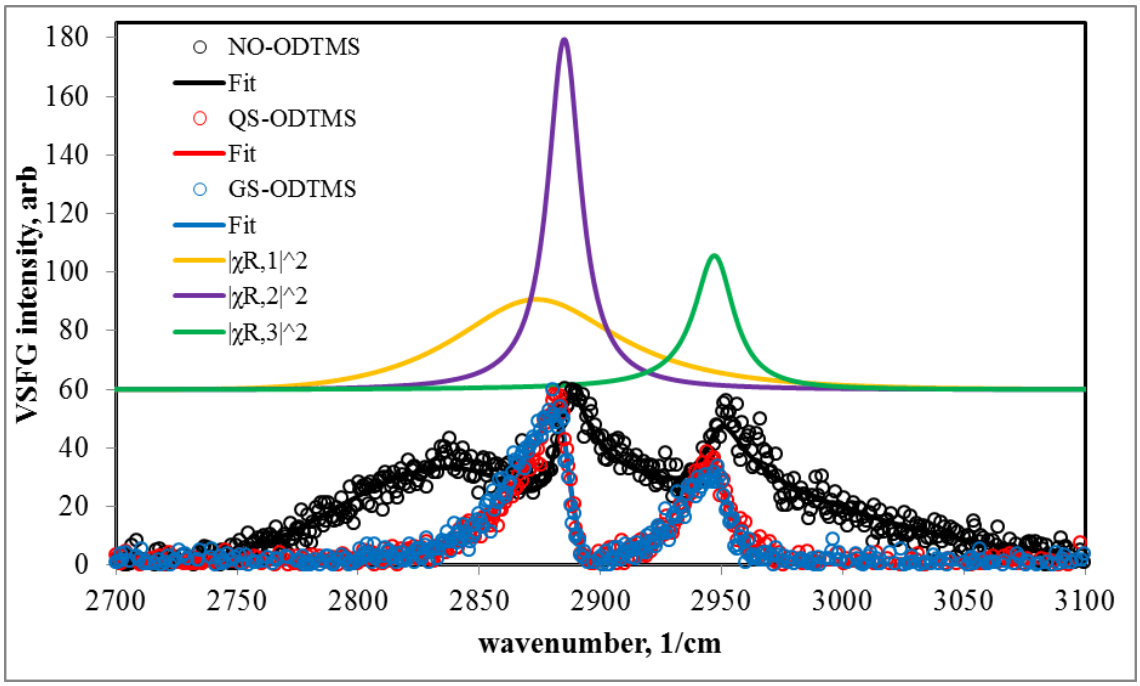

Figure 2-2. VSFG spectra in the CH stretching region for ODTMS SAMs on the three substrates studied in this work. Data are shown as markers, and the fits (using Eqs. (2.1) - (2.4) for a single interface system) are overlaid in solid lines. Offset (by 60) are the three resonances that were extracted from the fits.

All three datasets were fit with the same resonant parameters and the nonresonant amplitude was allowed to vary between the samples to accommodate the larger NR background on the NO substrates. A unique transfer coefficient was assigned to NO-ODTMS (will be discussed Section 2.4.4) due to differences in the local field factors for a reflective relative to transparent substrate. The presence of strong CH_3 vibrations on all substrates (symmetric stretch and Fermi resonance at 2880 and 2940 cm^{-1}, respectively) indicates well-ordered monolayers. Also, the fact that all three spectra are fit by the same resonant parameters indicates that the only difference between the samples is the presence of a non-resonant background from the underlying silicon wafer that interferes with the resonant lineshapes.[412]

On the basis of these measurements on all substrates, we conclude that the NO, QS, and GS samples did not have significantly different surface roughnesses, and the ODTMS functionalized samples differed only in their surface energies from the bare SiO_2 substrates.

2.4.2 *PTCDI-C_8 Thin Film Characterization*

Spectroscopic ellipsometry was performed on PTCDI-C_8 thin films deposited on NO and revealed that the organic thin film thicknesses were approximately 8 nm (Table 2-1). Figure 2-3 shows representative AFM images for PTCDI-C_8 grown on bare and ODTMS functionalized NO, QS, and GS substrates. The films on NO and QS substrates for both bare and ODTMS preparations exhibit similar surface morphologies (Figure 2-3a-d). Discrete ~2 nm steps are clearly evident in the pixel density plots adjacent to each frame. The topography is consistent with the reported growth method of vapor deposited PTCDI-C_8 on SiO_2 and ODTMS SAM surfaces in which 2D polycrystalline terraces proceed in a Stranski-Krastanov fashion (layer-by-island growth) with molecules oriented with the long axis of the perylene core standing up with a small tilt relative to the substrate normal.[95]

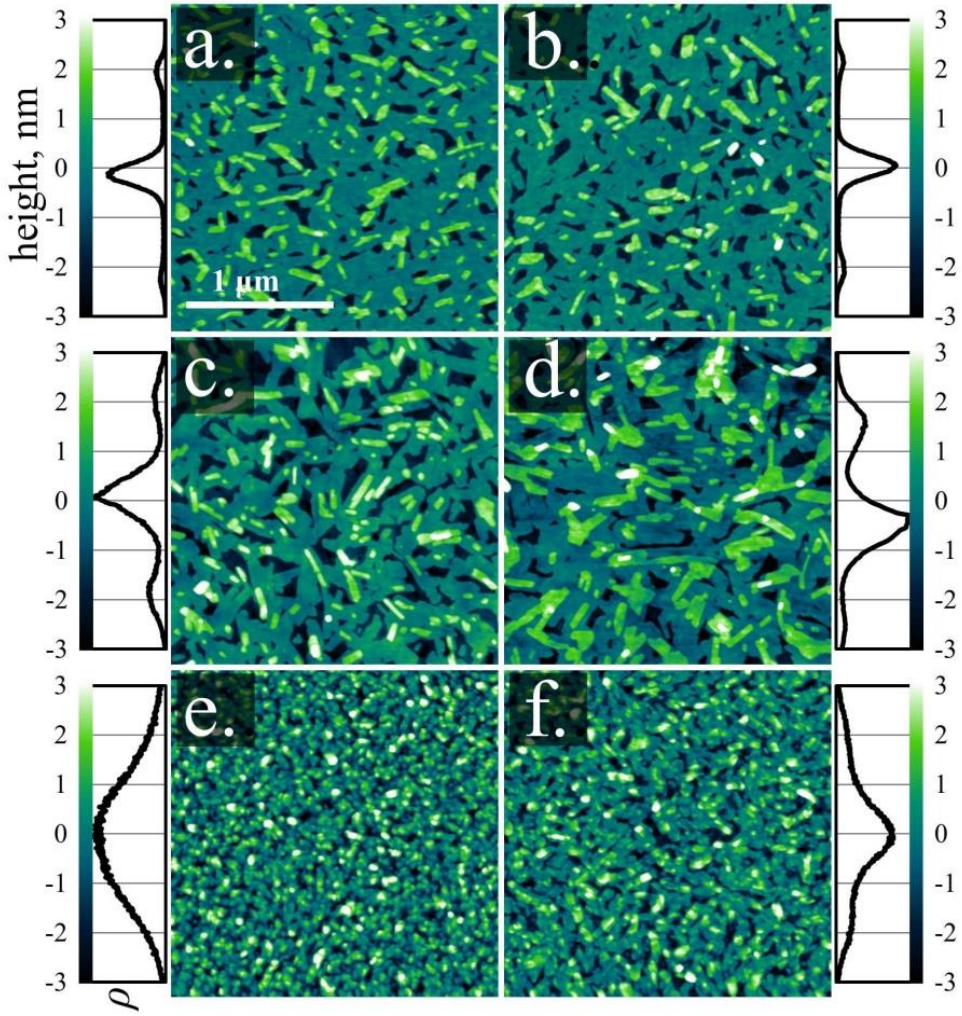

Figure 2-3. AFM topographic images of pre-annealed PTCDI-C_8 vapor deposited onto a) bare NO, b) NO-ODTMS, c) QS, d) QS-ODTMS, e) GS, f) GS-ODTMS. Pixel density plots are included adjacent to each image.

Comparison of Figure 2-3a-d to Figure 2-3e and f reveals that the GS substrates produce more fractured films, which is also apparent in the larger inhomogeneity in the pixel density plots. We have found that the morphologies of PTCDI-C_8 films on GS are consistently different from those on QS and NO surfaces. Island growth is partially apparent for GS-ODTMS but is absent for bare GS. Although it is beyond the scope of the current study, these topographical changes suggest a different growth mechanism of PTCDI-C_8 on GS surfaces. Because the surface roughnesses are identical, we

tentatively attribute the differences in film morphologies to a chemical difference. GS is a soda lime glass that is only ~70-75% SiO_2 by mass, while the remaining components include Na_2O, CaO, MgO and other trace compounds. By coating the GS surface with ODTMS, the stepwise growth is somewhat recovered (more apparent in the pixel density plot in Figure 2-3f), but the impact of the GS surface chemistry is not completely nullified by the overlaid SAM. These chemical differences are subtle at the silica and SAM level based on the fact that the water contact angles cannot differentiate the surface energies, AFM cannot discern differences in surface roughnesses, and the VSFG spectra of the CH vibrational region report identically packed monolayers. However, seemingly minor differences in surface chemistry can be amplified when they perturb the kinetics of the earliest nucleating molecules during thin film formation. These data highlight the well-known fact that the kinetics and thermodynamics of film growth from vapor deposited PTCDI-C_8 are exquisitely sensitive to substrate preparation, and the observation is significant since GS substrates are often used as surrogates for silica wafers.

Upon thermally annealing the same six samples at 110 °C for 1 hour, AFM images were collected and are shown in Figure 2-4. The behaviors of the film topographies upon annealing are again similar between the NO and QS substrates (Figure 2-4a-d) with no obvious differences in the images or pixel density plots on bare versus ODTMS functionalized surfaces. Compared to the pre-annealed NO and QS samples in Figure 2-3a-d, there is a clear coalescence of grains upon annealing that forms larger islands and more complete terraced layers. The pixel density plots show layer heights that are ~2 nm tall as were observed before annealing and similar height

distributions. There are small differences between the NO and QS pixel height distributions, but we attribute these to difficulties encountered in stabilizing the tip-sample interactions on QS (and GS) substrates due to electrostatic effects. Figure 2-4e and f demonstrate that PTCDI-C_8 on the GS substrate also undergoes an increase in grain size through the annealing procedure, but the final topographies of films on these substrates continue to be more fractured than the NO and QS surfaces.

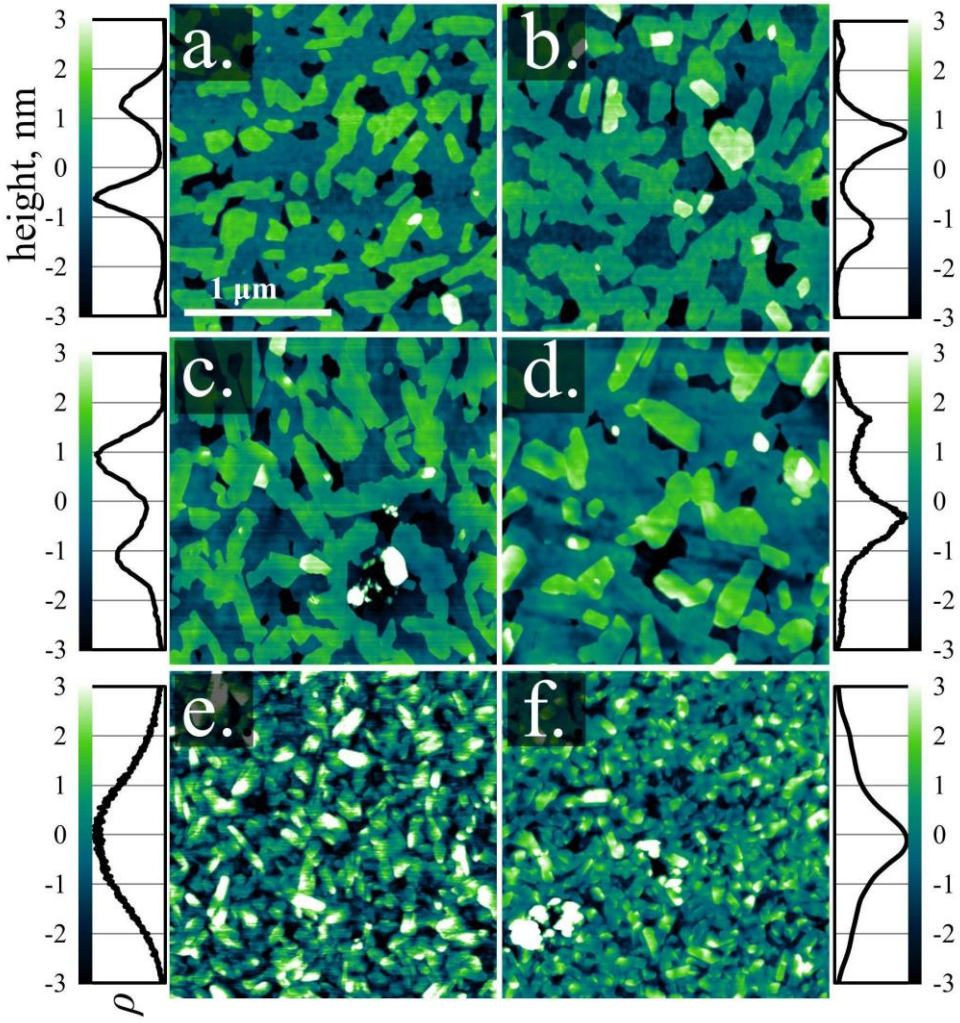

Figure 2-4. AFM topographic images of post-annealed PTCDI-C_8 vapor deposited onto (a) bare NO, (b) NO-ODTMS, (c) QS, (d) QS-ODTMS, (e) GS, (f) GS-ODTMS. Pixel density plots are included adjacent to each image.

2.4.3 *PTCDI-C_8 Vibrational Spectroscopy*

Figure 2-5 shows the FTIR absorption spectrum for a 30 nm thin film of PTCDI-C_8 deposited on a CaF_2 window with graphical representations of the molecule and the modes in the inset. Absorption peaks at 1655 cm^{-1} and 1697 cm^{-1} have been previously assigned to the imide carbonyl asymmetric (ν_{asym}) and symmetric (ν_{sym}) stretching vibrations. [413] The Raman activities of these modes are notoriously weak but have been measured through surface-enhanced Raman and are consistent with the assignments above.[414] The linear vibrational spectrum reports the mean frequencies and distributions of frequencies for these vibrational degrees of freedom for the entire film thickness with the majority of the signal resulting from absorption in the bulk rather than at the material interfaces. Nonetheless, this provides a starting point for assigning the vibrational resonances to specific nuclear motions.

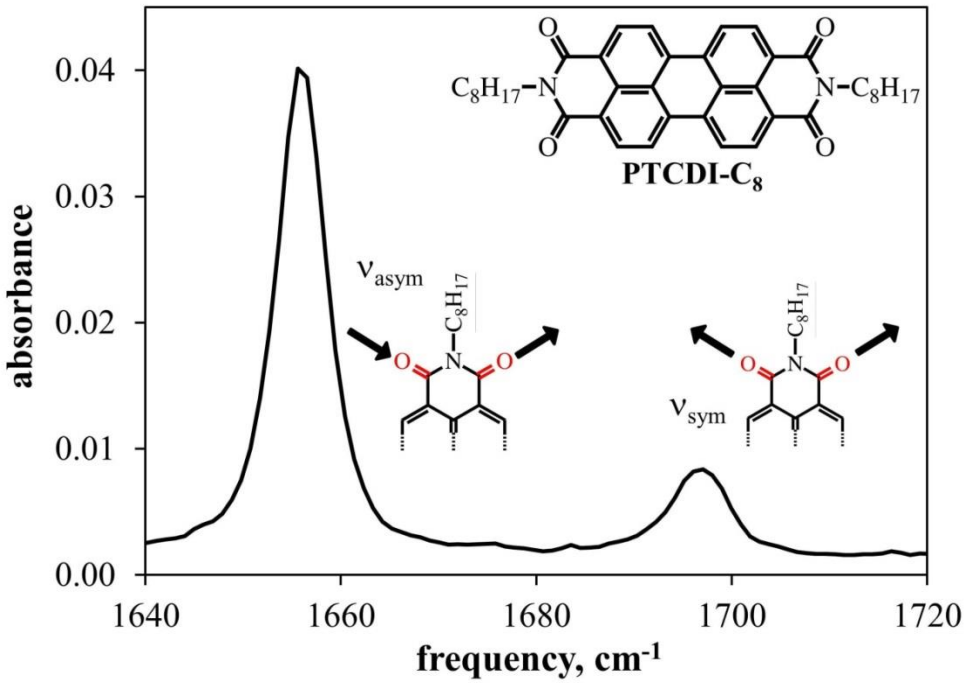

Figure 2-5. FTIR spectrum of the carbonyl vibrational region for a thin film of PTCDI-C_8 on CaF_2. Inset are structural diagrams showing the nuclear motions for ν_{asym} and ν_{sym}.

2.4.4 *Two-Interface Model for Fitting VSFG Spectra*

VSFG spectroscopy was used to determine the vibrational spectra of the interfacial species, with the goal of monitoring structural changes at the PTCDI-C_8–substrate interface where charge conduction occurs in oFETs. The VSFG electric field generated at a given interface can be written as a sum of vibrationally resonant and nonresonant contributions.[21,359,415]

$$\chi^{(2)} = \chi^{(2)}_{NR} + \sum_q \chi^{(2)}_{R,q} \tag{2.1}$$

$$E^{VSFG}_{v,0} = T_v \chi^{(2)}_v E^{vis}_0 E^{IR}_0 \tag{2.2}$$

Here T_v is the total transfer product for interface v, which relates the input fields E^{vis}_0 and E^{IR}_0 to the output field $E^{VSFG}_{v,0}$, and accounts for thin film interference effects and local field corrections at material junctions. $\chi^{(2)}_{R,q}$ is the second order susceptibility for the q'th vibrational resonance at the interface and $\chi^{(2)}_{NR}$ describes all other vibrationally non-resonant contributions to the material response.

For an organic thin film, the same modes appear at both interfaces but generally are not in identical chemical environments. Equation 2.3 is the general quantum mechanical result for a homogeneously broadened vibrational mode outlined in Section 1.3.2.8:

$$\chi^{(2)}_R = \frac{A}{\bar{\omega} - \omega_{IR} - i\Gamma} \tag{2.3}$$

Here $\bar{\omega}$ is the central frequency, Γ is the linewidth, and A is the amplitude of a given vibrational mode. In VSFG spectroscopy A is proportional to the product of the IR transition dipole moment and Raman molecular polarizability and can be used to deduce

average molecular orientation as described in Section 1.3.2.8.[396,416,417] As in linear spectroscopy, the $\bar{\omega}$ and Γ parameters report on the chemical environments surrounding the vibrational modes at a given interface. Each resonance is associated with a particular vibrational mode q at a particular interface v. In stratified systems, where multiple parallel interfaces contribute signal, the total VSFG intensity detected includes the output fields from all interfaces. In this work, there is one organic thin film with two interfaces.

$$I_0 \propto \left| \sum_{v=1}^{2} E_{v,0}^{VSFG} \right|^2 \tag{2.4}$$

This is the concise mathematical description of the two-interface problem in VSFG applied to organic thin films.

2.4.5 *Overview of the Two-Interface System*

In this chapter, the resonant VSFG data from PTCDI-C_8 thin films are interpreted as arising from the outer (air–PTCDI-C_8) and inner (PTCDI-C_8–substrate) interfaces. Figure 2-6 shows an illustration of the system model and an exemplary VSFG spectrum (data markers) with overlaid fit calculated from Eqs. (2.1) - (2.4) (black line) and the individual interfacial vibrational mode contributions that produced the fit (red and blue lines). Each interface contributes distinct ν_{asym} and ν_{sym} resonances that are unique in their parameters in Eq. (2.3). The PTCDI-C_8 vibrational modes between these boundaries are in a centrosymmetric environment leaving them VSFG silent. The outer interfacial spectrum has opposite polar orientation and is assigned a π phase shift relative to the inner interface.

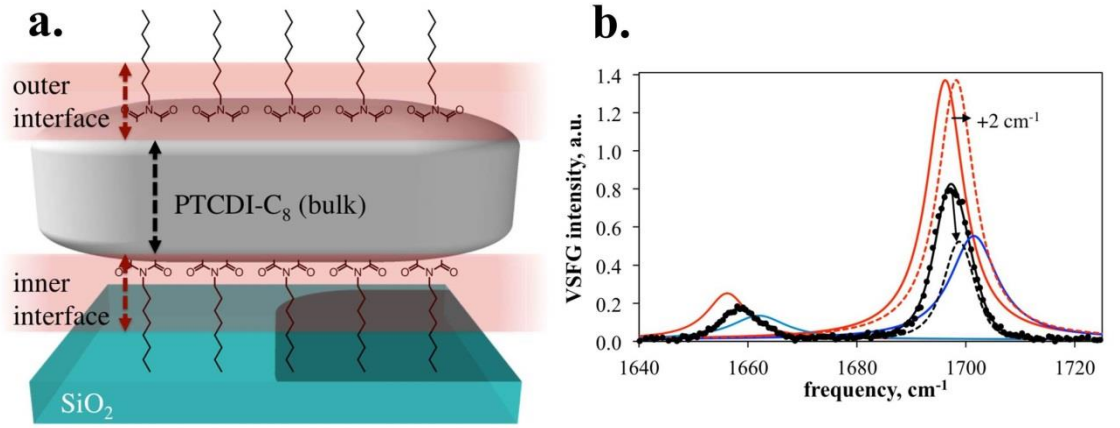

Figure 2-6. (a) Conceptual model used to fit and interpret the VSFG data showing the inner and outer interfacial imiide functional groups. (b) Calculated VSFG data (black solid line) and the component Lorentzian peaks from each interface (solid red and blue lines). The fit spectrum is overlaid on actual QS-ODTMS data (black markers). Also shown with dotted lines of the same colors is the resultant VSFG spectrum when the lower frequency (buried interfacial) mode experiences a 2 cm^{-1} shift.

The inner and outer interfaces (Figure 2-6a) have their own unique T_v values (Eq. (2.2)) that depend on the optical properties of the entire system. T_v is wavelength dependent and complex valued $(T_v = |T_v| \exp(i\phi T_v)$ with $\phi T_v = \arg(T_v))$, and it imparts a system dependent scaling factor and phase shift on one interface relative to the other.[367] In this work, the wavelength window for an entire vibrational spectrum (after upconversion) is quite narrow (~150 cm^{-1} is detected over ~5 nm); hence we treat T_v as being constant across the spectrum from a given interface. Reflections at media interfaces with primarily real refractive indices can introduce a zero or π phase shift depending on the wave polarization, angle of incidence, and refractive indices. Arbitrary phase shifts can be introduced by the spatial geometry of a layered system or from the transfer coefficients at interfaces of materials with refractive indices that include appreciable imaginary components.[367] In the current system, the refractive indices of all system materials for all wavelengths are primarily real and all layers are

negligibly thick compared to the experimental wavelengths so that the phase shift introduced by T_v is approximated to be zero. In this scheme $T_v = |T_v|$ simply acts as a scaling factor on the VSFG spectral contribution from a given interface.

In Figure 2-6b the four vibrational modes (ν_{asym} and ν_{sym} from an inner and outer interface) generate second order fields that are combined to produce the net detected VSFG signal intensity. The spectral contributions from the two interfaces are scaled by different $|T_v|$ but the product $|T_v| A_{v,q}$ has not been separated. The vibrational modes on opposite interfaces are assumed π out of phase and have center frequencies that differ by 5 cm^{-1}. The small frequency shift is important since identical modes with a π phase difference and similar $|T_v| A_{v,q}$ values would perfectly cancel leading to no detectable VSFG signal. The frequency dependence of the phase of the vibrational resonances renders the interference between π phase shifted modes such that there is constructive interference between them and destructive interference outside of them. The amount of constructive interference (and thus the intensity of the signal detected) is extremely sensitive to changes in the frequency difference when it is small (within only a few wavenumbers).[359] The dotted line in Figure 2-6b shows how the model predicts the signal intensity would change when the red-side symmetric mode center frequency is blue-shifted by only 2 cm^{-1} with no changes in resonant signal amplitudes, widths, or T_v. Interference at the susceptibility level dramatically changes the amount of signal that is observed experimentally.

The intensity level resonant VSFG spectrum has peak heights and lineshapes that depend on the transfer coefficients and susceptibilities at each interface (Eq. (2.2))

as well as how they mix at the electric field level (Eq. (2.4)). When complex interferences such as these are considered, interpreting seemingly simple VSFG spectra quickly becomes challenging. An increase in measured peak intensities could be the result of an increase in VSFG activity (higher amount of order, changed average polar orientation, etc.) at one or both interfaces, or could be due to a change in the vibrational frequencies, lineshapes, or transfer coefficients at either interface leading to less destructive interference. The results are not always intuitive, especially when several vibrational resonances overlap as is the case for a two-interface system. In the following sections, the VSFG data will be first presented and discussed qualitatively in the context of Eqs. (2.1) - (2.4). Details of the fitting routine will follow and results from nonlinear fits to the data will be presented to reveal the underlying resonant changes upon annealing.

2.4.6 *Qualitative Aspects of Interference in VSFG Data*

Representative VSFG spectra of PTCDI-C_8 thin films from NO, QS, and GS bare (solid lines) and ODTMS functionalized (dashed lines) substrates are presented in Figure 2-7. On all surfaces, the ν_{sym} intensity at ~1700 cm^{-1} in the VSFG spectra is noticeably stronger than the asymmetric mode. Using the *ssp* VSFG polarization combination, the *p*-polarized IR beam primarily measures the component of the VSFG transition moments that are orthogonal to the surface (see Figure 1-10(a) in Section 1.3.2.9). Consistent with the notion that PTCDI-C_8 molecules orient vertically on the substrates, this aligns the imide symmetric stretch vibrational dipole moment with the IR driving field, whereas the asymmetric vibration is orthogonal. However, the orientation cannot be quantitatively defined by this measurement alone since the

intrinsic VSFG activities of these resonances are not known nor are the extents to which the vibrational modes are depolarized or interfering from opposite interfaces.

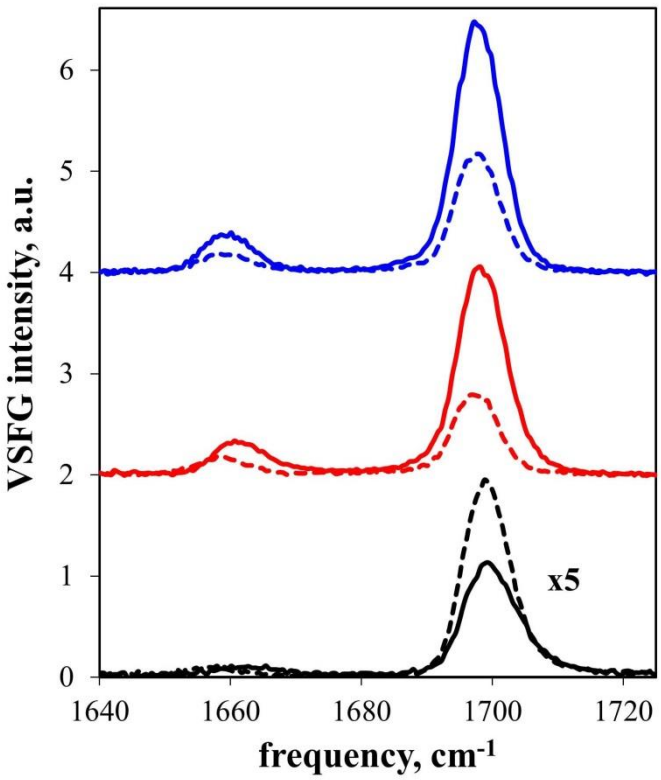

Figure 2-7. Pre-annealed VSFG spectra collected on bare (solid lines) and ODTMS functionalized (dashed lines) versions of the NO (black), QS (red), and GS (blue) substrates. Spectra from each substrate type are offset by two units and the NO spectra were multiplied by five for clarity.

A comparison of the data in Figure 2-7 shows that the spectra generated from NO substrates (black lines) are about a factor of 5-10 weaker than those from QS and GS surfaces. A modulation of the full spectrum could be the result of an increase in disorder at the interfaces that are sampled by VSFG. However, based on the nearly identical bare surface characterization shown in Section 2.4.1, this cannot be the explanation for such a dramatic difference. We attribute this effect to $|T_v|$ which can be separated into the individual transfer coefficients for each field involved $|T_v| = |t_v^{VSFG} t_v^{vis} t_v^{IR}|$. The reflectivity of the underlying silicon substrate in the visible to

near-IR changes the local field of the visible beam at both interfaces by reflecting out most of the portion that is otherwise lost through the back of QS and GS substrates. Upon reflection the field undergoes a π phase shift and destructively interferes with the incident field making t_v^{vis} smaller at both interfaces. At the same time, the VSFG signal is emitted in the reflected and transmitted directions from both interfaces and a similar argument can be made for collecting the transmitted portion upon reflection from the silicon substrate, effecting t_v^{VSFG} in the same way. In short, the NO system has smaller transfer coefficients (Eq. (2.2)) due to the reflectivity of the substrate in the visible to near-IR range leading to lower signal intensities.

A comparison of the VSFG spectra for PTCDI-C_8 on bare (solid lines) versus ODTMS functionalized (dashed lines) surfaces reveals another interesting trend. The signal strength from the NO-ODTMS substrate data is about twice that of bare NO while it is roughly a half to a quarter of the intensity for QS-ODTMS and GS-ODTMS compared to their bare substrates. It is striking that modifying the dielectric surface with an organosilane monolayer can cause the VSFG signals from NO wafers to increase while the transparent silica substrates decrease. Based on the nearly indistinguishable nature of the bare and ODTMS substrates shown in Table 2-1 and the corresponding AFM images in Figure 2-1, the PTCDI-C_8 buried monolayer should not be significantly different on NO-ODTMS relative to QS-ODTMS. The AFM topographies and pixel density plots in Figure 2-3 indicate the outer interfaces are similar as well. Therefore we hypothesize that the difference is likely a result of two phenomena: a relative difference in transfer coefficients of the two interfaces on reflective versus transparent substrates as well as chemically different environments

experienced by the first monolayer on bare versus ODTMS treated substrates. However, a detailed investigation of these phenomena is beyond the scope of the current study and is not necessary for the conclusions drawn here.

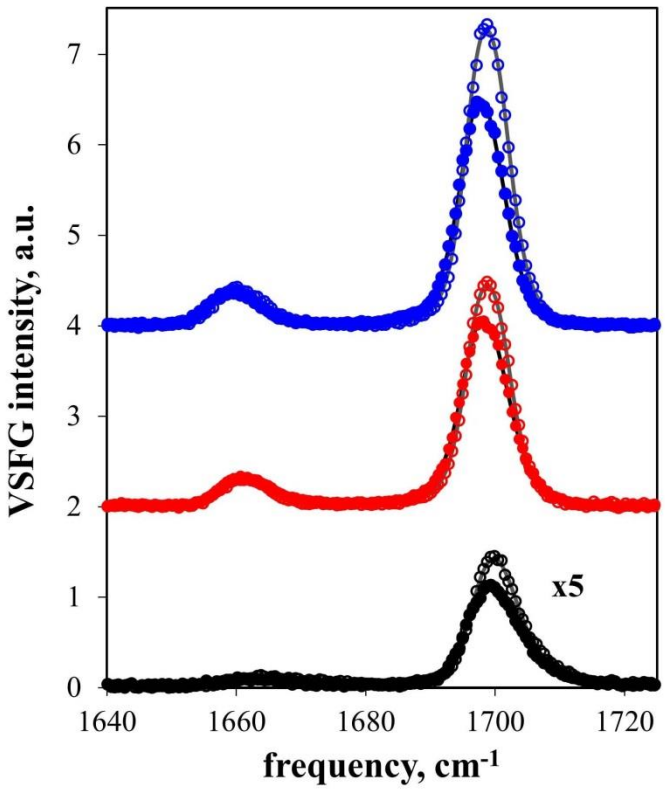

Figure 2-8. VSFG spectra collected from pre-annealed (open markers) and post-annealed (filled markers) PTCDI-C_8 films on NO (black), QS (red), and GS (blue) substrates. Spectra from different surface types are offset by two units and NO spectra are multiplied by five for clarity.

Upon annealing the PTCDI-C_8 films on bare and ODTMS functionalized substrates, the VSFG spectra from all six sample types reported similar changes. Figure 2-8 and Figure 2-9 show the pre- and post-annealed spectra for each surface preparation. The apparent blue-shift upon annealing for all substrates and surface preps is tentatively attributed to a larger reorganization and ordering at one interface relative to the other. It is clear from the post-annealed AFM images in Figure 2-4 that the

molecules on the outer interface undergo a substantial reorganization leading to increased grain sizes and a filling-in of the observable incomplete layers.

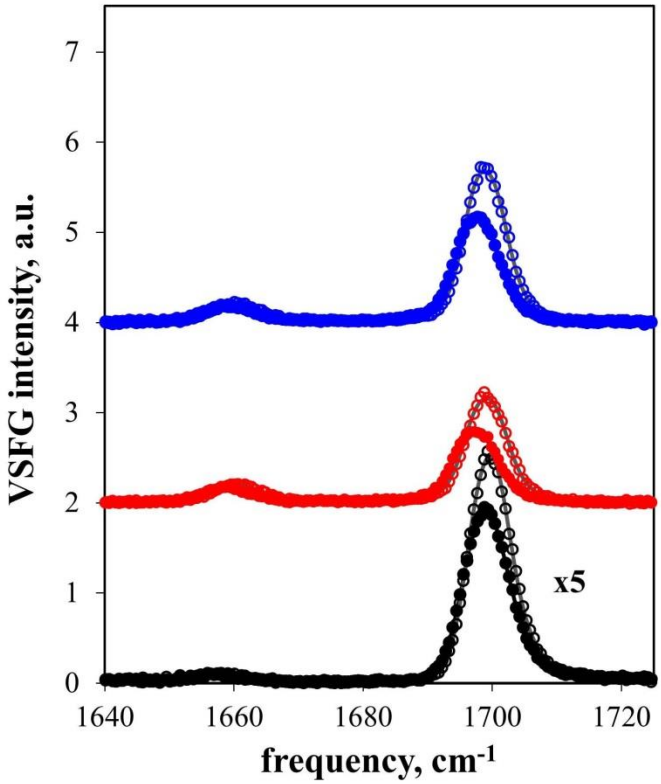

Figure 2-9. VSFG spectra collected from pre-annealed (open markers) and post-annealed (filled markers) PTCDI-C8 films on NO-ODTMS (black), QS-ODTMS (red), and GS-ODTMS (blue) substrates. Spectra from different surface types are offset by two units and NO spectra are multiplied by five for clarity.

2.4.7 *VSFG Data Fitting*

2.4.7.1 Fit Details: Amplitude Ratios

In order to quantify the relative amount of reorganization upon annealing from each interface the data were fit using Eqs. (2.1) - (2.4) as follows. With three sets of samples, six samples per set (NO, QS, GS, NO-ODTMS, QS-ODTMS, and GS-ODTMS), and VSFG data collected before and after thermal annealing there were 36 total spectra to fit. When the samples are considered individually the resulting fit

parameters are highly correlated. In order to minimize these ambiguities a global fitting scheme was employed. Data were fit 12 spectra at a time (each sample set pre- and post-annealed) using the nonlinear fitting algorithm available in Mathematica 8.0. All resonant center frequencies were shared across all data sets but allowed to float (i.e. $\bar{\omega}_{air,sym}$ was the same in all 12 spectra for a given sample set). Each resonance had its own width and amplitude that were independent of the other resonances. The substrate interfaces were assigned a unique $\phi T_{substrate}$ for each substrate and surface prep but the pre- and post-annealed data sets shared this parameter. The parameters for the vibrational resonances were assigned starting values and allowed to minimize with $\phi T_{substrate}$'s all set to zero. The final optimization floated all parameters including all $\phi T_{substrate}$'s, which ended up still close to zero and had a very small effect on the resultant parameters. The product of $|T_v| A_{v,q}$ is not separable in this scheme so that the fitting parameter $\tilde{A}_{v,q} = |T_v| A_{v,q}$ was defined (Equations 1 and 2). All values were then reported as a ratio of $\tilde{A}_{v,q}/\Gamma_{v,q}$ post-annealed to pre-annealed where $\tilde{A}_{v,q}/\Gamma_{v,q}$ is the metric for the total contribution from a given resonance.[347,395,418,419] Here $|T_v|$ is assumed approximately constant upon annealing and therefore cancels in the ratios. $\tilde{A}_{v,q}$ is assumed real and set positive so that relative polar orientation was assigned by changing the sign on $\chi^{(2)}_{R,v,q}$. The data were fit best by assigning opposite signs to the resonances from a given interface $(\chi^{(2)}_{R,air,sym} - \chi^{(2)}_{R,air,asym})$ and assigning the spectrum from the substrate interface to be opposite to that of the air interface

$(-\chi^{(2)}_{R,substrate,sym} + \chi^{(2)}_{R,substrate,asym})$. The substrate interfacial modes were assigned a bathochromic shift based on a simple solvation argument.[420–422] We rationalize that the outer interface should be more similar to the gas phase vibrational frequencies, which would be blue-shifted in the absence of solvation. A small vibrationally nonresonant contribution was observed in all NO and NO-ODTMS substrate data. A constant modulus and phase for $\chi^{(2)}_{NR,substrate}$ was used in the fitting, which was shared across NO and NO-ODTMS pre- and post-annealed data sets.

2.4.7.2 Fit Results

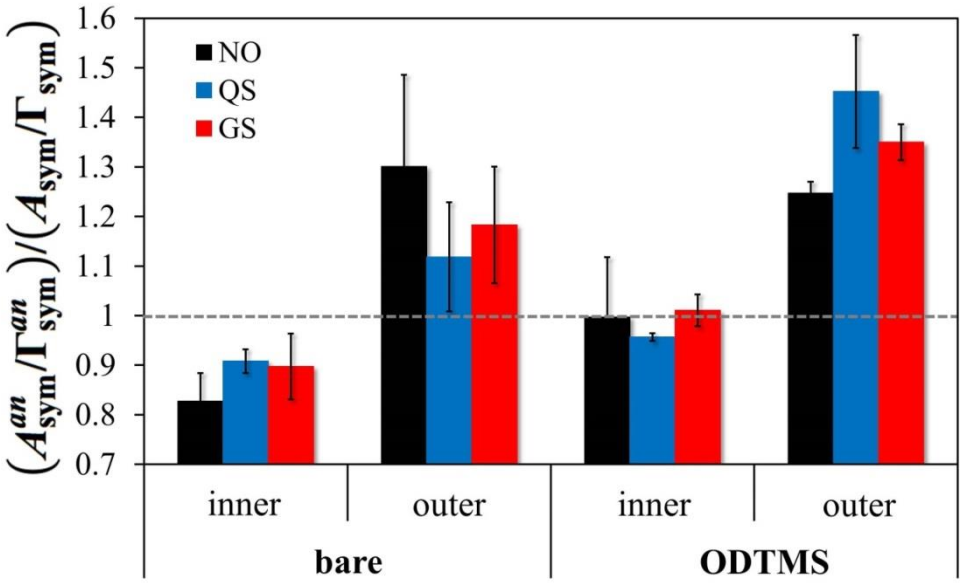

Figure 2-10. Final fit parameters for C=O ν_{sym} PTCDI-C_8 films on NO (black), QS (blue), and GS (red) substrates on bare and ODTMS functionalized surfaces. Shown are the $\left(A^{an}_{sym}/\Gamma^{an}_{sym}\right)/\left(A_{sym}/\Gamma_{sym}\right)$ ratios to demonstrate the increase or decrease of a contribution from the inner (substrate) or outer (air) interface, where unity (gray dashed line) implies no change. Error bars reflect the standard error from the average of three sample sets.

The fitted VSFG spectra are overlaid onto the data in Figure 2-8 and Figure 2-9 as solid black (pre-annealed) and gray (post-annealed) lines, demonstrating that the agreement with the spectral data is excellent. In the following discussion we focus

attention on ν_{sym} due to the fact that ν_{asym} is generally low amplitude in the VSFG spectra. The results from fitting for the ν_{sym} mode are presented in Figure 2-10 and the full table of resultant fitting parameters is shown in Table 2-2. For VSFG with the *ssp* polarization combination, a decrease in resonant contribution upon annealing is interpreted as primarily the result of a decrease in the ensemble average z-projection of the transition dipole moment (relative to the substrate normal) for that mode. For the ν_{sym} mode, this translates to an increase in the average tilt along the long axis of the perylene core. The molecules become more reclined. The apparent blue-shift in the VSFG spectra upon annealing can be explained by a disproportionate change in the total contribution from the two interfaces upon annealing. Figure 2-10 shows that on bare substrates the buried interfacial (lower frequency) contribution tends to decrease while the outer (higher frequency) contribution increases for all substrates. For ODTMS substrates the buried total contribution remains approximately unchanged while the outer contribution increases. The large relative change at the outer interface for both surface preps is consistent with the topographic changes observed in the AFM images (Figure 2-3 versus Figure 2-4). These molecules have more freedom to restructure compared to the buried interface. The reorientation that occurs eliminates smaller islands which suggests the molecules join larger grains with less tilt along the long axis.[95] The results for the buried interfaces are consistent with reports that the interfacial phase on bare SiO_2 is subject to reorientation upon thermal annealing. The decrease in the VSFG contribution suggests that the molecules reorient in favor of a reclined phase as was observed previously.[95,103,407] The essentially unchanged buried

modes on the ODTMS substrates are evidence for thermodynamic stability of the initial PTCDI-C_8 layer.

Table 2-2. Full VSFG fitting routine parameter results.

		Bare			ODTMS		
		Set 1	Set 2	Set 3	Set 1	Set 2	Set 3
Common	$\omega_{air,sym}$	1701.45	1701.4	1700.93	Shared Values		
	$\omega_{substrate,sym}$	1696.21	1696.16	1695.74			
	$\omega_{air,asym}$	1661.98	1660.32	1661.34			
	$\omega_{substrate,asym}$	1656.18	1656.98	1655.75			
	$\left\|\chi^{(2)}_{NR,NO}\right\|$	0.06284	0.06238	0.05249			
	$\phi\chi^{(2)}_{NR,NO}$	1.07462	1.27013	1.4134			
Inner	ϕT_{NO}	0.16506	-0.0844	0.02184	0.1571	0.03053	0.0723
	ϕT_{QS}	0.16895	0.16414	0.10098	-0.0142	0.00826	0.04813
	ϕT_{GS}	-0.0647	-0.0326	0.1222	-0.0422	-0.1608	-0.0766
Inner Resonances	$\tilde{A}_{NO,sym}$	2.759	2.93944	2.75735	2.91575	3.0332	2.65858
	$\Gamma_{NO,sym}$	5.56374	5.20714	5.61068	4.41631	4.73099	4.47729
	$\tilde{A}_{NO,asym}$	0.687	1.21669	0.43181	0.73395	1.14201	0.53885
	$\Gamma_{NO,asym}$	5.50177	5.43459	4.97397	6.3719	5.38141	5.79521
	$\tilde{A}_{annealNO,sym}$	2.16802	3.13533	1.93385	2.48501	3.09756	2.18814
	$\Gamma_{annealNO,sym}$	4.83023	6.44961	5.48795	4.04435	3.92283	4.43751
	$\tilde{A}_{annealNO,asym}$	0.41575	1.26208	0.09348	0.39204	0.78402	1.2646
	$\Gamma_{annealNO,asym}$	5.03987	4.70231	2.2693	3.27494	4.62109	6.33136
	$\tilde{A}_{QS,sym}$	7.38743	7.70496	7.52223	4.82356	4.47708	3.51342
	$\Gamma_{QS,sym}$	4.68612	4.54189	4.90728	4.13523	4.11969	4.12019
	$\tilde{A}_{QS,asym}$	1.30572	4.08395	1.69417	2.25299	3.98359	2.24455
	$\Gamma_{QS,asym}$	3.83188	5.27158	4.28266	4.57899	5.8331	5.12497
	$\tilde{A}_{annealQS,sym}$	5.70626	6.60507	5.18649	4.26558	4.10748	3.05849
	$\Gamma_{annealQS,sym}$	3.88619	4.17276	3.93299	3.85562	3.88898	3.77447
	$\tilde{A}_{annealQS,asym}$	1.06291	2.98702	1.26155	1.82594	3.66854	1.38072
	$\Gamma_{annealQS,asym}$	3.66143	4.35269	3.5156	4.69088	4.88975	4.10816
	$\tilde{A}_{GS,sym}$	9.41807	11.1526	8.67221	5.87374	6.57083	5.18804
	$\Gamma_{GS,sym}$	4.46516	4.56582	4.50677	4.14135	4.22844	3.9523

$\tilde{A}_{GS,asym}$	3.57782	8.83272	2.21873	2.74165	4.48826	2.30902
$\Gamma_{GS,asym}$	4.86794	6.08572	4.83507	4.96478	4.89047	4.88758
$\tilde{A}_{annealGS,sym}$	7.88013	9.92935	5.53751	5.01709	6.2561	4.68413
$\Gamma_{annealGS,sym}$	3.84387	4.25236	3.75994	3.61779	3.74587	3.64297
$\tilde{A}_{annealGS,asym}$	2.62299	5.28579	1.57968	2.0016	6.2163	1.59885
$\Gamma_{annealGS,asym}$	4.30162	5.64377	4.3044	4.35952	5.22396	3.84951

Outer Resonances

$\tilde{A}_{NO,sym}$	2.9698	2.29263	3.19017	2.75849	2.72688	2.65917
$\Gamma_{NO,sym}$	6.59578	6.31823	5.82495	5.0599	5.44341	5.00878
$\tilde{A}_{NO,asym}$	1.60757	2.05677	1.859	0.74017	1.68789	0.60922
$\Gamma_{NO,asym}$	7.50237	6.482	8.80699	4.10178	6.73352	3.8093
$\tilde{A}_{annealNO,sym}$	2.95852	3.551	2.77031	2.93402	2.95782	2.80017
$\Gamma_{annealNO,sym}$	5.69791	5.86516	4.67426	4.35129	4.57381	4.34404
$\tilde{A}_{annealNO,asym}$	1.37244	2.58087	0.75047	0.55372	1.16707	2.41672
$\Gamma_{annealNO,asym}$	6.44548	8.55286	3.68137	3.3075	4.84974	12.9937
$\tilde{A}_{QS,sym}$	7.06503	7.50674	7.9352	3.91473	3.63127	3.15511
$\Gamma_{QS,sym}$	5.44504	6.25598	5.3246	5.31272	4.9882	4.30496
$\tilde{A}_{QS,asym}$	3.22745	7.18683	3.59187	2.20603	3.74825	2.33197
$\Gamma_{QS,asym}$	5.83609	7.98342	5.63801	6.24084	7.79263	6.62176
$\tilde{A}_{annealQS,sym}$	6.0693	8.36184	5.46225	4.64289	4.50211	3.41245
$\Gamma_{annealQS,sym}$	4.10848	5.36515	3.99021	3.952	4.02592	3.79555
$\tilde{A}_{annealQS,asym}$	2.49514	7.09156	2.26981	2.52361	4.63877	1.89919
$\Gamma_{annealQS,asym}$	4.51238	8.16165	4.24395	4.75264	7.26718	5.13834
$\tilde{A}_{GS,sym}$	8.34439	10.3346	7.74609	5.05048	5.83015	4.72172
$\Gamma_{GS,sym}$	5.20587	5.60308	4.81377	5.14122	5.0847	4.77417
$\tilde{A}_{GS,asym}$	4.42836	10.7229	3.23486	3.08482	5.7803	2.57529
$\Gamma_{GS,asym}$	6.38371	7.99918	5.13732	7.18066	9.26888	5.3453
$\tilde{A}_{annealGS,sym}$	8.08111	11.1467	6.13326	5.39805	6.06406	5.14124
$\Gamma_{annealGS,sym}$	4.10579	4.44094	3.96722	3.90338	4.12147	3.82374
$\tilde{A}_{annealGS,asym}$	4.0697	8.04414	2.89046	2.923	7.66797	2.35411
$\Gamma_{annealGS,asym}$	5.35555	6.3639	4.7043	5.435	6.94356	4.80973

2.4.7.3 Ambiguities in the Fitting Routine

The limitations of the fitting routine should be discussed. We found that the VSFG spectra presented here could not be fit using a single interface model. However,

there were two problems encountered when applying the multiple interface model to VSFG data. The main difficulty is the high correlation between parameters so that it was necessary to constrain the system by making informed choices on how to share parameters between data sets. The other problem stems from the fact that VSFG is extremely sensitive to molecular ordering so that when contributions to the observed spectra were somewhat varied between samples it had a large effect on the detected spectra making the choice of shared parameters across samples problematic. Our approach here is to depict how the total contributions from the buried and outer interfaces change upon annealing under the assumption that the center frequencies do not change appreciably. Other fitting schemes involving multiple interfaces were tested and generally showed the same trends as presented above. A major focus of this dissertation is contributing a mathematical description of T_v so that it can be modeled, reducing some of the ambiguities encountered in this chapter. This is the focus of the next three chapters.

2.4.8 *PTCDI-C_8 Field-Effect Transistor Electrical Characterization*

In an effort to connect the structural changes that were extracted from fits to the VSFG data with device performances, electron mobilities were measured on PTCDI-C_8 oFETs at room temperature under vacuum at or below 1×10^{-4} Torr in the saturation regime (μ_{sat}) before and after thermal annealing at 110 °C. The mobilities were averaged from all channels and all devices for bare and ODTMS surface preps and are included in Table 2-1. Mobilities from the bare substrate devices were on average more than a factor of three higher than those of ODTMS devices. It has been shown that

depositions of PTCDI-C_8 at relatively low substrate temperatures (such as the 30 °C used in this study) result in finer grain structure and that oFET device performances are significantly degraded by grain boundaries.[17,51,66,403,423] Although we did not discern topographical differences at the outer interface among these films by AFM, the higher mobilities on bare substrates is likely due to the formation of more grain boundaries at the buried interface on ODTMS substrates. The initial stage growth of a closely related molecule deposited on bare SiO_2 and alkyl-SAM treated SiO_2 showed a tendency to nucleate into finer grains in the initial perylene monolayer on the SAM.[103]

Interestingly, the mobilities doubled upon annealing for both bare and ODTMS devices. Field-effect conduction occurs only at the buried (inner) interface, thus we would expect that both substrate types experienced a structural change during annealing that resulted in increased carrier mobilities. The fits to the VSFG spectra shown above reported that there was a notable change in structure for the bare substrates and no change on ODTMS. These results seem contradictory, though they are consistent with previous reports of device improvement with annealing and preferential structural rearrangement on bare silica. The observations can be rationalized by first recognizing that annealing helps to better coalesce grains, including those at the substrate interface. Coalescence leads to better lateral π-π orbital overlap of the PTCDI-C_8 molecules at grain boundaries, which leads to improved mobilities on both substrates. This grain boundary improvement may have no direct connection to the VSFG data, but the formation of the reclined phase upon annealing that was recovered from the fits to these data was expected to have some impact on the carrier mobility.

One perspective on these observations is that the devices on ODTMS, which had improved carrier mobilities but no structural change reported by VSFG, achieved their improvements primarily through grain boundary coalescence. The oFETs on bare silica had fewer grains to begin with, and, assuming only coalescence, should not have improved by as much as the ODTMS devices (a factor of two). It is conceivable that the bare substrate samples were improved by grain boundary coalescence as well as molecular rearrangement within the grains, thereby enabling them to have the same improvement factor as the ODTMS surfaces. In other words, on ODTMS devices, where there are more grains but the film is thermodynamically stable, the improvement factor is mostly due to coalescence; whereas on bare devices, with fewer grains but thermodynamic instability, the improvement factor is due to improved π-π overlap between grains as well as within the grains. It is not yet clear how the reclined phase in the bare substrates might lead to more favorable conduction, but the structure-function relationships for monolayers of PTCDI-C_8 would be an excellent future study.

2.5 CONCLUSION

In this work thin films of an n-type organic semiconductor, PTCDI-C_8, were vapor deposited at low temperatures on bare and ODTMS functionalized silica substrates. After analyzing the film properties with AFM and steady state spectroscopy we utilized VSFG spectroscopy to extract the vibrational spectra from the film interfaces. It was necessary to treat these data as arising from two interfaces in order to properly fit the spectral lineshapes. The results show that the manner in which the interfacial signals change with surface chemistry and annealing procedures can be

extracted by making some assumptions about the optical constants of the materials and by using signal ratios to cancel unknown variables. Within the model presented and for our experimental parameters, we were able to demonstrate that the initial PTCDI-C_8 monolayer phase that forms on bare silica is subject to reorientation upon thermal annealing, whereas on ODTMS functionalized surfaces it is more stable and resistant to restructuring. Interpreting the electrical characteristics of oFETs with the same conduction channel preparations was not straightforward and highlights the fact that there is a complex interplay between the molecular structures at this interface and their impact on device performance. The results show that VSFG approaches can be useful to test hypotheses about the molecular arrangements at buried interfaces in electronic devices.

Efforts beyond the simple model used here are presented in the next chapters of this dissertation. Specifically, modeling of T_v is presented in the next chapter and is an important step towards a better physical understanding of optical interferences effects present in VSFG data that will be discussed in Chapter 4. In Chapter 5 the model is applied to experimental data where it is shown that it provides a good description of the data. With improved constraints for fitting routines some of the ambiguities are reduced and this leads to increased sensitivity to other effects present in the data.[i]

[i] This work was supported by the National Science Foundation under Award Number DMR-1006386, and partially supported by a Seed Grant from the MRSEC Program of the National Science Foundation under Award Number DMR-0212302 and DMR-0819885. TCA was supported by an American Competitiveness in Chemistry Fellowship (ACC-F) from the National Science Foundation under Award Number CHE-1041955. Part of this work was carried out in the Institute of Technology Nanofabrication Center, University of Minnesota, which receives partial support from the NSF through the NNIN program. Parts of this work were also carried out in the Characterization Facility, University of Minnesota, which receives partial support from NSF through the MRSEC program.

3 Modeling Multilayer Thin Film Interference Effects in Interface-Specific Coherent Nonlinear Optical Spectroscopies

Adapted with permission from

Daniel B. O'Brien and Aaron M. Massari. Modeling multilayer thin film interference effects in interface-specific coherent nonlinear optical spectroscopies. *Journal of the Optical Society of America B.* **2013**, 30 (6), pp 1503-1512.

CHAPTER SUMMARY

This chapter presents the optical interference model developed in my graduate work for describing effects from thin film geometries on nonlinear spectroscopic signals. Development of the model was inspired by the two-interface problem for VSFG applied to oFETs, inherently multilayer systems. However, it is derived here in a completely generalized way to describe optical interferences effects on nonlinear signals generated from any interface within a system composed of an arbitrary number of thin film layers. It is based on the transfer matrix formalism for thin film optics.

3.1 INTRODUCTION

When the interaction of the electric field of light with matter is framed in the context of perturbation theory (expanding the electric field to higher order terms), a set of coherent nonlinear optical spectroscopies are described that access new information on the static and dynamic states of physical systems.[159] The symmetry of a system under interrogation then provides selection rules for simplifying the model used to describe those interactions. The present scope is contingent upon one such selection rule that applies to all even-ordered spectroscopies. Within the electric dipole approximation, systems that possess inversion symmetry on a macroscopic scale are inactive to even ordered interactions. While the bulk of most materials possess this symmetry, inversion is necessarily broken at interfaces. It is for this reason that techniques such as second harmonic generation (SHG) and sum frequency generation (SFG) have been widely demonstrated as probes of molecular structure and dynamics at interfaces.[25,217,400,424,425]

When such coherent techniques are applied to planar and stratified thin film systems, data interpretation is complicated by interference effects. The local fields present at the active interfaces depend on the geometry of the entire system as do the fields emitted from those interfaces. Approaches taken in the literature to account for these effects were detailed in Section 1.3.1.6. They include techniques that eliminate thin film system dependence such as a method of amplitude ratios used in the last chapter[96] or experimental separation of contributing signals.[324,328,353] Direct modeling schemes include approximation by simple reflections,[363] modified Airy summation for infinite reflections.[21,356,359,361,362] direct solutions using boundary conditions for a given

sample geometry,[366] and transfer matrix methods with Green's function solutions for generated fields.[23,231,371,426]

For a more general approach it is desirable to have a model that is readily applicable to any arbitrary thin film system and does not involve numerically solving differential equations. The available models typically include simplifying assumptions, are applicable to a system composed of only a single thin film, or require extensive calculations and are not readily extended to an arbitrary layered system in a clear and concise way. In this sense, a fully transfer matrix approach is most appealing. It is well known that the transfer matrix provides a direct analytical solution to the fields present within an ideal arbitrary layered thin film system.[367,382]

The objective in this chapter is to provide a general multilayer model for describing thin film interference effects present in interface-specific coherent spectroscopies using the transfer matrix approach. We ignore bulk nonlinear source terms and focus specifically on the layer interfaces, treating them as source polarized sheets in the usual way.[236] We do not take into account transverse input beam variation, i.e. we consider systems where the total thickness of the thin film stack is much smaller than the spot sizes of the input beams (the infinite plane wave approximation). The systems are modeled as isotropic and all fields maintain coherence.

3.2 MODEL OVERVIEW

All fields in the thin film model are assumed to be plane waves as outlined in Section 1.3.2.1. Figure 3-1 shows the schematic of an arbitrary multilayer system and contains the definitions of variables used in the model as well as the coordinate frames.

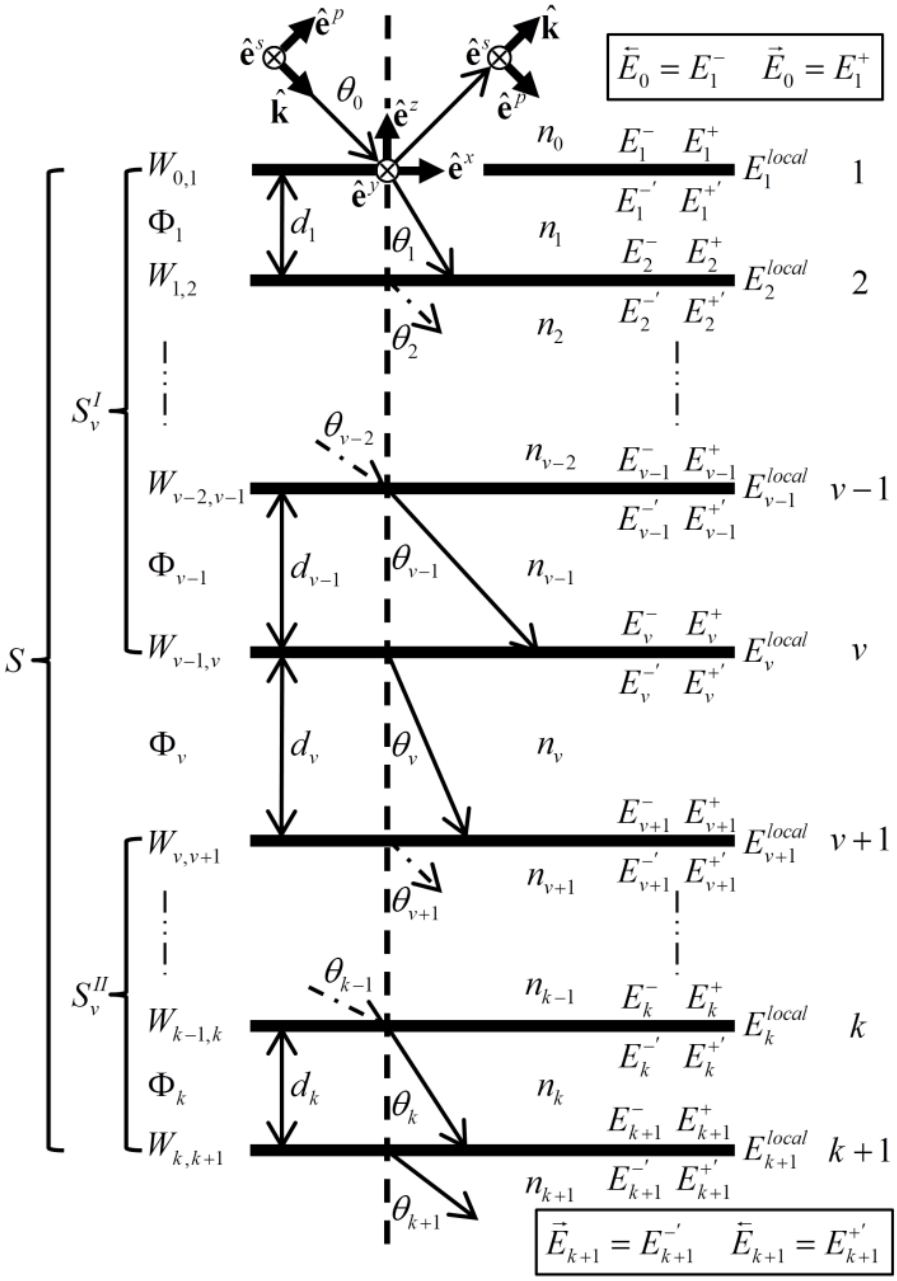

Figure 3-1. Schematic of model and definitions of variables for an arbitrary layered thin film system.

3.2.1 *General Description of Interface-Specific Spectroscopy*

The definitions for an arbitrary layered thin film system are shown in Figure 3-1. The system consists of k thin film layers bounded by semi-infinite media 0 and $k+1$. Most of the details of Figure 3-1 will be discussed in the coming sections but we start

by considering that the individual layer interfaces numbered on the right from 1 to $k+1$ are all potential sources in interface-specific nonlinear spectroscopy. In what follows, the subscript $0/k+1$ indicates fields can be incident from and generated into either side of the system (read "0 or $k+1$"). The total intensity of the detected signal $I_{0/k+1}$ is proportional to the squared modulus of the sum of all nonlinear sources $\vec{\mathbf{E}}^{NL}_{v,0/k+1}$ that make it out of the system in the phase matched direction.

$$I_{0/k+1} \propto \left| \sum_{v=1}^{k+1} \vec{\mathbf{E}}^{NL}_{v,0/k+1} \right|^2 \tag{3.1}$$

Here subscript $v,0/k+1$ indicates that the field generated at interface v is transferred to medium $0/k+1$. The generated fields depend on the interfacial nonlinear polarizations $\mathbf{P}^{NL}_v$ induced by the local amplitudes of all input fields (indexed by m over all n input fields, $\mathbf{E}^{m,local}_v$) and an output transfer coefficient matrix $\vec{T}_{v,0/k+1}$

$$\vec{\mathbf{E}}^{NL}_{v,0/k+1} = \vec{T}_{v,0/k+1} \mathbf{P}^{NL}_v \tag{3.2}$$

Where

$$\mathbf{P}^{NL}_v = \vec{\vec{\chi}}^{NL}_v : \prod_{m=1}^{n} \mathbf{E}^{m,local}_v \tag{3.3}$$

with the $\prod$ symbol indicating the outer products and

$$\mathbf{E}^{m,local}_v = \vec{\vec{T}}^{m}_{0/k+1,v} \vec{\mathbf{E}}^{m}_{0/k+1} \tag{3.4}$$

The local fields are related to the input fields $\vec{\mathbf{E}}^{m}_{0/k+1}$ through the input transfer coefficient matrices $\vec{\vec{T}}^{m}_{0/k+1,v}$.

The interfacial susceptibility tensor $\vec{\vec{\chi}}_v^{NL}$ of Eq. (3.3) contains all of the molecular information on the interfaces of the system under study. We seek to separate this quantity from thin film interference effects. So it is clear that the objective is to compute the transfer coefficient matrices for the input and output fields from each interface within an arbitrary layered system. We proceed by detailing the transfer matrix formalism in Section 3.3 followed by Section 3.4 where we describe how these results are applied to arrive at the transfer coefficient matrices of interest.

3.2.2 *Notation Comments*

We will introduce various transfer coefficients which are always defined as the ratio of one field at one position in the system to another field at another position. To start we define two general types of fields that will be encountered: those that are in the semi-infinite media 0 and $k+1$ (*external* fields) and those within the thin film layers (*internal* fields). We make a distinction between internal and external fields by placing an arrow on top of the external fields. A left facing arrow indicates an incident field propagating towards the thin film system (left arrow implying "before encountering the thin film system.") For example, $\vec{E}_0^m$ is the amplitude of external input field m incident onto the system in medium 0 at interface 1. A right facing arrow indicates a field propagating away from the system (right arrow implying "after encountering the system"). There are three types of outgoing external fields. They can be due to an incident field either reflecting at or transmitting through the system or they can be due to an internally generated nonlinear field transferred out of the system. For instance, $\vec{E}_{k+1}$ is the amplitude of an outgoing external field in medium $k+1$ that could be due to

reflection of $\overleftarrow{E}_{k+1}$ or transmission of $\overleftarrow{E}_0$ (Section 3.3.1), whereas $\vec{E}_{v,0}^{NL}$ is the amplitude of a nonlinear field generated at interface v that is transferred to medium 0 and is outgoing (Sections 3.3.3 and 3.4.2). Matrices involving transfer into and out of the system follow the same convention. Thus, the input transfer coefficient matrix $\overleftarrow{T}_{0/k+1,v}^{m}$ of Eq. (3.4) transfers input field m from medium 0 or $k+1$ to the local field at interface v and so has a left arrow. The output transfer coefficient matrix $\vec{T}_{v,0/k+1}$ of Eq. (3.2) transforms the nonlinear polarization at interface v into internally generated fields and transfers them out of the system and so has a right arrow.

There are three types of internal fields encountered: those adjacent to the interfaces due to external input fields (Section 3.3.2), the local fields at the interfaces due to external input fields (Section 3.4.1), and generated fields immediately adjacent to the generating interfaces (Sections 3.3.3 and 3.4.2). The internal fields adjacent to the interfaces are shown in Figure 3-1. They have associated with them a superscript which denotes the direction of travel and position ($+/-$ indicates the sign of k^z and a prime indicates the -*z* side of the interface) and a subscript, which specifies the interface to which the field is adjacent (i.e. $E_v^-, E_v^+, E_v^{-'}$, and $E_v^{+'}$ account for all fields adjacent to interface v in media $v-1$ and v). In Figure 3-1 we have also shown how the external field notation relates to the internal field notation on the outer sides of interfaces 1 and $k+1$ ($E_1^- = \overleftarrow{E}_0$, $E_1^+ = \vec{E}_0$, $E_{k+1}^{-'} = \vec{E}_{k+1}$, and $E_{k+1}^{+'} = \overleftarrow{E}_{k+1}$). The local field is the total field at interface v and is related to the adjacent fields as will be described in Section 3.4.1 (e.g. $E_v^{m,local}$ is the local field amplitude at interface v due to input field *m*). The

generated fields have the same subscript notation as the local fields but the superscript indicates in which direction (and therefore into which layer) the field is generated. For instance, $\varepsilon_v^{NL,+}$ indicates the amplitude of the nonlinear field generated in the positive *z* direction and immediately adjacent to interface *v* (therefore generated into medium $v-1$). We use ε to describe the field amplitude because it is the field radiated from the induced polarization at a specific point at the interface but it is *not* in general the total of that field at that point. This detail will be elucidated in Sections 3.3.3 and 3.4.2.

A generalized transfer coefficient τ describes the ratio of the field at one position and directionality to another in the system where the specified positions are always immediately adjacent to either side of an interface. It requires two subscripts that denote the starting and ending interfaces and two superscripts that denote directionality $(+/-)$ and position (prime or no prime) in "from,to" notation. For instance, the generalized transfer coefficient for describing an incident field in medium 0 transmitting through the entire system and outgoing in medium $k+1$ would be $\tau_{1,k+1}^{-,-'} = \vec{E}_{k+1} / \overleftarrow{E}_0 = E_{k+1}^{-'} / E_1^-$ where the transfer coefficient adopts the more general internal field notation. The generalized form is helpful for understanding the basic idea behind the transfer matrix approach. However, it is redundant for our purposes and so we use abbreviated forms that will be described as they are encountered in the coming sections.

3.3 TRANSFER MATRIX FORMALISM

The transfer matrix formalism follows from e.g. Knittl Chapter 2 and is summarized here for completeness (our axes are rotated so that the *x*- and *z*-axes are

opposite from Knittl).[367] The formalism uses boundary conditions to construct matrices that relate fields on either side of an interface. We consider plane wave fields linearly polarized *s* or *p* (unit polarization vectors $\hat{\mathbf{e}}^s$ and $\hat{\mathbf{e}}^p$ that form an orthogonal basis with the unit wavevector $\hat{\mathbf{k}}$) so that we may work with the complex amplitudes $E^{s/p}$ of the vector fields $\mathbf{E}^{s/p}$. The transfer matrix operates on the basis of waves polarized either *s* or *p* moving with positive and negative k^z. Note the choice of axis orientation in Figure 3-1 preserves the signs of the tangential field components ($\hat{\mathbf{e}}^x$ and $\hat{\mathbf{e}}^y$) for waves moving in either direction. This is important for the definition of the linear Fresnel coefficients and the derivation of the local fields.

3.3.1 *The Total System Transfer Coefficients*

It can be shown that the matrix of refraction $W_{v-1,v}$ that relates the fields traveling in the $+z$ and $-z$ directions adjacent to either side of interface *v* is[367]

$$W_{v-1,v} = \frac{1}{t_{v-1,v}} \begin{bmatrix} 1 & r_{v-1,v} \\ r_{v-1,v} & 1 \end{bmatrix} \tag{3.5}$$

so that

$$\begin{bmatrix} E_v^- \\ E_v^+ \end{bmatrix} = W_{v-1,v} \begin{bmatrix} E_v^{-\prime} \\ E_v^{+\prime} \end{bmatrix} \tag{3.6}$$

The field notation follows that of the internal fields discussed in Section 3.2.2. Note that *W*, *t*, *r*, and *E* are all associated with either *s* or *p* polarization (excluded from the superscript for simplicity). Here $t_{v\text{-}1,v}$ and $r_{v\text{-}1,v}$ are the linear Fresnel factors for transmission and reflection at interface *v* and traveling from medium v-1 to medium *v*

$$r_{v-1,v}^{p} = \frac{n_{v-1}\cos(\theta_v) - n_v\cos(\theta_{v-1})}{n_{v-1}\cos(\theta_v) + n_v\cos(\theta_{v-1})} \tag{3.7}$$

$$r_{v-1,v}^{s} = \frac{n_{v-1}\cos(\theta_{v-1}) - n_v\cos(\theta_v)}{n_{v-1}\cos(\theta_{v-1}) + n_v\cos(\theta_v)} \tag{3.8}$$

$$t_{v-1,v}^{p} = \frac{2n_{v-1}\cos(\theta_{v-1})}{n_{v-1}\cos(\theta_v) + n_v\cos(\theta_{v-1})} \tag{3.9}$$

$$t_{v-1,v}^{s} = \frac{2n_{v-1}\cos(\theta_{v-1})}{n_{v-1}\cos(\theta_{v-1}) + n_v\cos(\theta_v)} \tag{3.10}$$

where n_v and θ_v are the complex refractive index and angle of refraction relative to normal in medium *v*.

A phase matrix accounts for the spatial phase offset due to traversing layer *v* (the layer phase)

$$\Phi_v = \begin{bmatrix} \exp(-i\phi_v) & 0 \\ 0 & \exp(i\phi_v) \end{bmatrix} \tag{3.11}$$

so that

$$\begin{bmatrix} E_v^{-'} \\ E_v^{+'} \end{bmatrix} = \Phi_v \begin{bmatrix} E_{v+1}^{-} \\ E_{v+1}^{+} \end{bmatrix} \tag{3.12}$$

and

$$\phi_v = \left|\mathbf{k}_v \cdot \Delta\mathbf{r}_v\right| \equiv \left|k_v^z d_v\right| = \frac{2\pi n_v}{\lambda} d_v \cos(\theta_v) \tag{3.13}$$

as defined in Figure 3-2. Here λ is the vacuum wavelength of the incident beam and d_v is the thickness of layer *v*. Note that with this definition of the layer phase all computations for the fields within the thin film system involve perpendicular momentum transfer (perpendicular to a reference point on interface 1 or $k+1$) shown

by the vertical dashed line in Figure 3-1. This greatly simplifies calculations in the thin film model when more than one beam is considered since the calculation considers a path independent of dispersion. The layer phase is calculated from a phase difference at points on each interface corresponding to the ends of the red arrow in Figure 3-2.

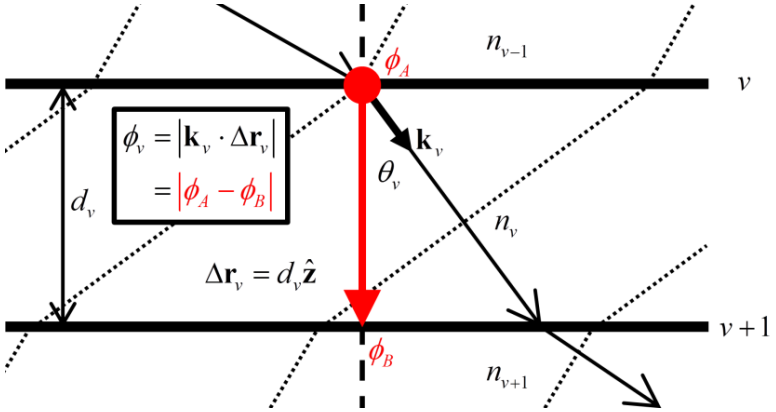

Figure 3-2. Definition of the layer phase calculation showing planes of constant phase.

From these definitions the total system transfer matrix (S) can be built

$$S = \left(\prod_{v=0}^{k-1} W_{v,v+1} \Phi_{v+1} \right) W_{k,k+1} \tag{3.14}$$

so that

$$\begin{bmatrix} E_1^- \\ E_1^+ \end{bmatrix} = S \begin{bmatrix} E_{k+1}^{-'} \\ E_{k+1}^{+'} \end{bmatrix} \tag{3.15}$$

A graphical look at Eq. (3.14) is shown on the left side in Figure 3-1. It is clear now for a beam incident from medium 0 that $E_{k+1}^{+'} = 0$. In our external field notation we take $E_1^- = \vec{E}_0$, $E_1^+ = \vec{E}_0$, and $E_{k+1}^{-'} = \vec{E}_{k+1}$. The total *system* transfer coefficient into the incident medium $(r_{0,sys})$ and medium $k+1$ $(t_{k+1,sys})$ are then[367]

$$r_{0,sys} = \frac{\vec{E}_0}{\vec{E}_0} = \frac{s_{(21)}}{s_{(11)}} \tag{3.16}$$

$$t_{0,sys} = \frac{\vec{E}_{k+1}}{\vec{E}_0} = \frac{1}{s_{(11)}} \tag{3.17}$$

where $s_{(ij)}$ are the elements of *S*. For a beam incident from medium $k+1$ we have

$$r_{k+1,sys} = \frac{\vec{E}_{k+1}}{\vec{E}_{k+1}} = -\frac{s_{(12)}}{s_{(11)}} \tag{3.18}$$

$$t_{k+1,sys} = \frac{\vec{E}_0}{\vec{E}_{k+1}} = \frac{|S|}{s_{(11)}} \tag{3.19}$$

Here *r* and *t* are defined similarly to Eqs. (3.7) - (3.10) with *sys* indicating the entire system as the effective second medium (e.g. $t_{k+1,sys}$ may be read "transmit through the thin film system to medium 0 from medium $k+1$", $r_{0,sys}$ is read "incidence from medium 0 reflect from the thin film system into medium 0"). We have dropped the general transfer coefficient form discussed at the end of Section 3.2.2 in favor of this simpler form for the total system coefficients in order to keep them distinct (e.g. the generalized forms of $r_{0,sys}$ and $t_{k+1,sys}$ are $\tau_{1,1}^{-,+}$ and $\tau_{k+1,1}^{+',+}$, respectively).

3.3.2 *Internal Transfer Coefficients*

In this section we highlight two procedures for accessing the fields adjacent to any arbitrary interface within the system due to beams incident from medium 0 ($\vec{E}_0$) or $k+1$ ($\vec{E}_{k+1}$). The internal transfer coefficients are defined as the ratio of an internal field to an incident field. We start by dividing the system up at medium *v* into subsystems *I* and *II*

$$S_v^I = \left(\prod_{i=0}^{v-2} W_{i,i+1} \Phi_{i+1} \right) W_{v-1,v} \tag{3.20}$$

$$S_v^{II} = \left(\prod_{i=v}^{k-1} W_{i,i+1} \Phi_{i+1} \right) W_{k,k+1} \tag{3.21}$$

so that $S = S_v^I \Phi_v S_v^{II}$ (refer to left side of Figure 3-1). By examining this form and considering the total system transfer coefficients it is straightforward to calculate the internal transfer coefficients from subsystem I or II. For instance, using subsystem II we have

$$\begin{bmatrix} \tau_{0,v}^{-'} \\ \tau_{0,v}^{+'} \end{bmatrix} = \Phi_v S_v^{II} \begin{bmatrix} t_{0,sys} \\ 0 \end{bmatrix} \tag{3.22}$$

$$\begin{bmatrix} \tau_{0,v}^{-} \\ \tau_{0,v}^{+} \end{bmatrix} = S_{v-1}^{II} \begin{bmatrix} t_{0,sys} \\ 0 \end{bmatrix} \tag{3.23}$$

$$\begin{bmatrix} \tau_{k+1,v}^{-'} \\ \tau_{k+1,v}^{+'} \end{bmatrix} = \Phi_v S_v^{II} \begin{bmatrix} r_{k+1,sys} \\ 1 \end{bmatrix} \tag{3.24}$$

$$\begin{bmatrix} \tau_{k+1,v}^{-} \\ \tau_{k+1,v}^{+} \end{bmatrix} = S_{v-1}^{II} \begin{bmatrix} r_{k+1,sys} \\ 1 \end{bmatrix} \tag{3.25}$$

Here the notation for the transfer coefficients is an abbreviation of the generalized form stated at the end of Section 3.2.2. For example, $\tau_{k+1,v}^{-'} = E_v^{-'} / \overleftarrow{E}_{k+1}$ indicates transfer of an input beam from medium $k+1$ ($+'$ directionality and position is implied) to the $-'$ directionality and position of interface v. Notice these equations rely on the total system transfer coefficients so that the internal fields depend on the *entire* system.

A useful alternate approach to the internal transfer coefficients involves viewing the two subsystems as individual total systems separated by medium v. The derivation involves properties of the partial and total system transfer matrices. The result shows the system can be thought of as the single layer v bounded by interfaces with media 0

and $k+1$.[367] We define partial system transfer coefficients analogous to Eqs. (3.16) - (3.19) treating the subsystems as being isolated. The notation on the subscripts now uses I or II to specify the effective second medium is a subsystem. The necessary quantities are

$$t_{0,I} = \frac{\varepsilon_v^{-'}}{\overleftarrow{E}_0} = \frac{1}{s^I_{v,(11)}} \tag{3.26}$$

$$r_{v,I} = \frac{\varepsilon_v^{-'}}{\varepsilon_v^{+'}} = -\frac{s^I_{v,(12)}}{s^I_{v,(11)}} \tag{3.27}$$

$$t_{k+1,II} = \frac{\varepsilon^+_{v+1}}{\overleftarrow{E}_{k+1}} = \frac{\left|S^{II}_v\right|}{s^{II}_{v,(11)}} \tag{3.28}$$

$$r_{v,II} = \frac{\varepsilon^+_{v+1}}{\varepsilon^-_{v+1}} = \frac{s^{II}_{v,(21)}}{s^{II}_{v,(11)}} \tag{3.29}$$

so that, for example, $t_{0,I}$ is read "transmit from medium 0 to medium v through subsystem I" and $r_{v,II}$ is read "reflect from medium v off subsystem II back into medium v". We have used ε to show that the fields described here are not the internal fields of the total system. Rather, they lead to terms which must be summed over infinite reflections to obtain the system internal fields. Thus, the problem of the internal fields is reduced to a single layer system with the pseudo-boundaries of subsystems I and II. Here simple reflection and transmission are described by the partial system transfer coefficients. An illustration of this view of the system along with the partial system transfer coefficients is presented in Figure 3-3.

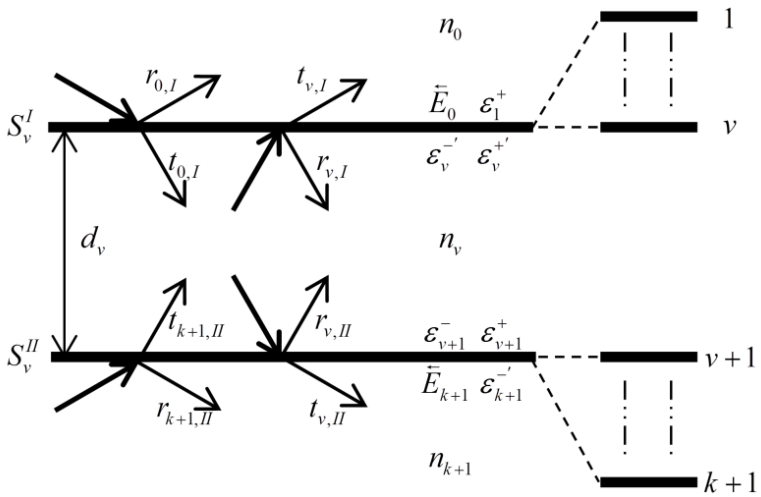

Figure 3-3. Graphical depiction of the effective boundaries of subsystems *I* and *II* for layer *v* showing partial system transfer coefficients as the newly defined transmission and reflection coefficients at the boundaries.

The internal transfer coefficients are then geometric series in the partial system transfer coefficients and the layer phase. For a beam incident from medium 0 we have (with geometric series shown only for $\tau_{0,v}^{-'}$ and $\tau_{k+1,v}^{+'}$)

$$\begin{aligned}\tau_{0,v}^{-'} &= \frac{E_v^{-'}}{\vec{E}_0} = t_{0,I}\sum_{j=0}^{\infty}\left[r_{v,I}r_{v,II}\exp\left(2i\phi_v\right)\right]^j \\ &= \frac{t_{0,I}}{1-r_{v,I}r_{v,II}\exp\left(2i\phi_v\right)}\end{aligned} \tag{3.30}$$

$$\tau_{0,v}^{+'} = \frac{E_v^{+'}}{\vec{E}_0} = \tau_{0,v}^{-'}r_{v,II}\exp\left(2i\phi_v\right) \tag{3.31}$$

$$\tau_{0,v}^{-} = \frac{E_v^{-}}{\vec{E}_0} = \tau_{0,v-1}^{-'}\exp\left(i\phi_{v-1}\right) \tag{3.32}$$

$$\tau_{0,v}^{+} = \frac{E_v^{+}}{\vec{E}_0} = \tau_{0,v-1}^{+'}\exp\left(-i\phi_{v-1}\right) \tag{3.33}$$

and for a beam incident from medium $k+1$

$$\tau_{k+1,v}^{-'} = \frac{E_v^{-'}}{\vec{E}_{k+1}} = \tau_{k+1,v}^{+'}r_{v,I} \tag{3.34}$$

$$\tau_{k+1,v}^{+'} = \frac{E_v^{+'}}{\tilde{E}_{k+1}} = t_{k+1,II}\exp\left(i\phi_v\right)\sum_{j=0}^{\infty}\left[r_{v,I}r_{v,II}\exp\left(2i\phi_v\right)\right]^j = \frac{t_{k+1,II}\exp\left(i\phi_v\right)}{1-r_{v,I}r_{v,II}\exp\left(2i\phi_v\right)} \tag{3.35}$$

$$\tau_{k+1,v}^{-} = \frac{E_v^{-}}{\tilde{E}_{k+1}} = \tau_{k+1,v-1}^{-'}\exp\left(i\phi_{v-1}\right) \tag{3.36}$$

$$\tau_{k+1,v}^{+} = \frac{E_v^{+}}{\tilde{E}_{k+1}} = \tau_{k+1,v-1}^{+'}\exp\left(-i\phi_{v-1}\right) \tag{3.37}$$

This discussion on deriving the coefficients from the partial system transfer coefficients is important for the next section on the external transfer coefficients whereas calculating them directly from the subsystems is included because it is more concise. The results are identical.

We make a final note in this section about the outermost boundary interfaces. When applying the model it is helpful to realize how the internal transfer coefficients relate to the total system transfer coefficients at these boundaries, for instance, $\tau_{0,k+1}^{-'} = t_{0,sys}$, $\tau_{0,k+1}^{+'} = 0$, and $\tau_{0,1}^{+} = r_{0,sys}$.

3.3.3 *External Transfer Coefficients*

The external transfer coefficients relate internally generated fields to fields external and outgoing from the thin film system. The internally generated fields are treated as incident fields that originate from within the system. The distinction is made clear by referring to the generated fields as ε_v. They can be thought of in the same way as described in the last section but without initial transfer into the system from 0 or $k+1$. When considering generated fields it makes sense only to discuss the fields

generated and outgoing from interface v, $\varepsilon_v^{-'}$ and ε_v^{+}. Once again we split the system up at medium v or $v-1$ (depending on the side of the interface with which we are concerned, see Figure 3-1) and reduce the problem to a single layer system. We then propagate the field through the thin film system allowing for infinite reflections and transmissions at the boundaries of subsystems I and II. The additional partial system transfer coefficients needed are

$$t_{v,I} = \frac{\varepsilon_1^{+}}{\varepsilon_v^{+'}} = \frac{\left|S_v^I\right|}{s_{v,(11)}^I} \tag{3.38}$$

$$t_{v,II} = \frac{\varepsilon_{k+1}^{-'}}{\varepsilon_{v+1}^{-}} = \frac{1}{s_{v,(11)}^I} \tag{3.39}$$

For transfer to medium 0 we have

$$\begin{aligned} \tau_{v,0}^{-'} = \frac{\vec{E}_0}{\varepsilon_v^{-'}} &= t_{v,I} r_{v,II} \exp\left(2i\phi_v\right) \sum_{j=0}^{\infty} \left[r_{v,I} r_{v,II} \exp\left(2i\phi_v\right) \right]^j \\ &= \frac{t_{v,I} r_{v,II} \exp\left(2i\phi_v\right)}{1 - r_{v,I} r_{v,II} \exp\left(2i\phi_v\right)} \end{aligned} \tag{3.40}$$

$$\begin{aligned} \tau_{v,0}^{+} = \frac{\vec{E}_0}{\varepsilon_v^{+}} &= t_{v-1,I} \exp\left(i\phi_{v-1}\right) \sum_{j=0}^{\infty} \left[r_{v-1,I} r_{v-1,II} \exp\left(2i\phi_{v-1}\right) \right]^j \\ &= \frac{t_{v-1,I} \exp\left(i\phi_{v-1}\right)}{1 - r_{v-1,I} r_{v-1,II} \exp\left(2i\phi_{v-1}\right)} \end{aligned} \tag{3.41}$$

and to medium $k+1$

$$\begin{aligned} \tau_{v,k+1}^{+} = \frac{\vec{E}_{k+1}}{\varepsilon_v^{+}} &= t_{v-1,II} r_{v-1,I} \exp\left(2i\phi_{v-1}\right) \sum_{j=0}^{\infty} \left[r_{v-1,I} r_{v-1,II} \exp\left(2i\phi_{v-1}\right) \right]^j \\ &= \frac{t_{v-1,II} r_{v-1,I} \exp\left(2i\phi_{v-1}\right)}{1 - r_{v-1,I} r_{v-1,II} \exp\left(2i\phi_{v-1}\right)} \end{aligned} \tag{3.42}$$

$$\tau_{v,k+1}^{-'} = \frac{\vec{E}_{k+1}}{\varepsilon_v^{-'}} = t_{v,II}\exp\left(i\phi_v\right)\sum_{j=0}^{\infty}\left[r_{v,I}r_{v,II}\exp\left(2i\phi_v\right)\right]^j = \frac{t_{v,II}\exp\left(i\phi_v\right)}{1-r_{v,I}r_{v,II}\exp\left(2i\phi_v\right)} \tag{3.43}$$

Here the abbreviated form of the generalized transfer coefficient (Section 3.2.2) omits the implied position and directionality of the outgoing field. For instance, $\tau_{v,k+1}^{+} = \vec{E}_{k+1}/\varepsilon_v^{+}$ is read "transfer the field generated at the $+$ position and directionality of interface v to medium $k+1$ ($-'$ position and directionality implied).

3.4 THIN FILM INTERFERENCE MODEL

Returning to the objective, we want to compute the transfer coefficient matrices of the system. We will consider spatially propagating waves in the $\left[E^p \quad E^s \quad 0\right]$ basis (a rotating frame) whereas the local and induced fields are in the sample $\left[E^x \quad E^y \quad E^z\right]$ fixed reference frame of Figure 3-1. The sample frame is chosen so that the generated signal is in the *xz*-plane and traveling with positive k^x. So the $\overleftarrow{T}^m_{0/k+1,v}$ matrices of Eq. (3.4) serve to transfer all *n* input beams to interface *v* in the propagating fields frame and project them onto the local fields in the sample frame. The $\vec{T}_{v,0/k+1}$ matrices of Eq. (3.2) then relate the nonlinear polarization to generated fields followed by transfer out of the thin film system. With the internal transfer coefficients in hand we start with the computation of the input field coefficients.

3.4.1 *The Input Field Transfer Coefficient Matrices*

We seek to build the matrix $\overleftarrow{T}^m_{0/k+1,v}$ so

$$\begin{bmatrix} E_v^{m,local,x} \\ E_v^{m,local,y} \\ E_v^{m,local,z} \end{bmatrix} = \overleftarrow{T}_{0/k+1,v}^{m} \begin{bmatrix} \overleftarrow{E}_{0/k+1}^{m,p} \\ \overleftarrow{E}_{0/k+1}^{m,s} \\ 0 \end{bmatrix} \tag{3.44}$$

for beams incident from either medium 0 or $k+1$ in the sample *xz*-plane. We omit superscript m in what follows for clarity but recognize all quantities are for a given input field.

First we note that the matrix for projecting the $\begin{bmatrix} E^p & E^s & 0 \end{bmatrix}$ basis onto the sample $\begin{bmatrix} E^x & E^y & E^z \end{bmatrix}$ basis in medium v is given as

$$\Pr(\theta_v) = \begin{bmatrix} \cos(\theta_v) & 0 & 0 \\ 0 & 1 & 0 \\ \sin(\theta_v) & 0 & 0 \end{bmatrix} \tag{3.45}$$

so that

$$\begin{bmatrix} E^x \\ E^y \\ E^z \end{bmatrix} = \Pr(\theta_v) \begin{bmatrix} E^p \\ E^s \\ 0 \end{bmatrix} \tag{3.46}$$

where $-\pi/2 \le \theta_v \le \pi/2$ relative to the surface normal. Care must be taken with the sign of θ_v so that it is defined as positive or negative when the *z*-component of *p*-polarized light projects on the positive or negative sample *z*-axis (as discussed in Section 1.3.2.1). In Figure 3-1 (and Figure 1-7) we have defined the axes so that $\text{sign}(\theta_v) = -\text{sign}(k^z)\text{sign}(k^x)$.

The local fields are solved by considering the boundary conditions within the polarized sheet as discussed in Section 1.3.2.7. It is required that E^x, E^y, and $D^z = n^2 \epsilon_o E^z$ (the displacement vector amplitude for nonmagnetic materials and no

surface charge) are continuous across the interface[121,236]. These requirements are already met using the transfer matrix approach. Thus, the local fields are related to the total fields adjacent to the interface by summing in the projected basis.

$$E_v^{local,x} = \cos\left(\theta_{v-1}\right)\left(E_v^{-,p} + E_v^{+,p}\right) \tag{3.47}$$

$$E_v^{local,y} = E_v^{-,s} + E_v^{+,s} \tag{3.48}$$

$$\bar{n}_v{}^2 E_v^{local,z} = n_{v-1}{}^2 \sin\left(\theta_{v-1}\right)\left(E_v^{-,p} - E_v^{+,p}\right) \tag{3.49}$$

Here $\bar{n}_v$ is the refractive index of the interfacial polarized sheet[236,237,427]. Normalizing by an input wave from medium 0 or $k+1$ we use the internal transfer coefficients from Eqs. (3.30) - (3.37) and define

$$\overleftarrow{f}_{0/k+1,v}^{+/-} = \begin{bmatrix} \tau_{0/k+1,v}^{+/-,p} & 0 & 0 \\ 0 & \tau_{0/k+1,v}^{+/-,s} & 0 \\ 0 & 0 & 0 \end{bmatrix} \tag{3.50}$$

$$J_v = \begin{bmatrix} 1 & 0 & 0 \\ 0 & 1 & 0 \\ 0 & 0 & \left(n_{v-1} \middle/ \bar{n}_v\right)^2 \end{bmatrix} \tag{3.51}$$

where J_v accounts for the continuity of D^z so that

$$\overleftarrow{T}_{0/k+1,v} = J_v\left(\Pr\left(-\theta_{v-1}\right)\overleftarrow{f}_{0/k+1,v}^{+} + \Pr\left(\theta_{v-1}\right)\overleftarrow{f}_{0/k+1,v}^{-}\right) \tag{3.52}$$

We have chosen the positive *z* side of the interface in Eqs. (3.47) - (3.49) but the fields on the opposite side yield the same result if we define

$$\overleftarrow{f}_{0/k+1,v}^{+'/-'} = \begin{bmatrix} \tau_{0/k+1,v}^{+'/-',p} & 0 & 0 \\ 0 & \tau_{0/k+1,v}^{+'/-',s} & 0 \\ 0 & 0 & 0 \end{bmatrix} \tag{3.53}$$

$$J'_{\nu} = \begin{bmatrix} 1 & 0 & 0 \\ 0 & 1 & 0 \\ 0 & 0 & \left(n_{\nu} \middle/ \overline{n}_{\nu} \right)^2 \end{bmatrix} \tag{3.54}$$

then

$$\overleftarrow{T}_{0/k+1,\nu} = J'_{\nu} \left[\Pr\left(-\theta_{\nu}\right) \overleftarrow{f}^{+'}_{0/k+1,\nu} + \Pr\left(\theta_{\nu}\right) \overleftarrow{f}^{-'}_{0/k+1,\nu} \right] \tag{3.55}$$

An equivalent approach is to include the interfacial sheet as a layer in the system and simply sum the internal fields while taking the limit of zero thickness. With this method one needs only to consider E^z (rather than D^z) for the normal component because boundary conditions are not used. It is important to note that all three procedures just described give identical results for the local fields (numerically verified on the example system presented in the next chapter)[397] and they converge to the same result reported in the literature for the local fields in a single interface system.[236,237]

For a beam incident from a plane rotated from the sample *xz*-plane we can follow as above and compute the local fields in a rotated sample frame (clockwise rotation about the *z*-axis by an angle φ when looking from above the system and $-\pi < \varphi \leq \pi$). If we call this matrix $\overleftarrow{T}^{rot}_{0/k+1,\nu}$ we can project the tangential components on the sample fixed frame by a rotation matrix $R^z\left(\varphi\right)$

$$R^z\left(\varphi\right) = \begin{bmatrix} \cos\left(\varphi\right) & -\sin\left(\varphi\right) & 0 \\ \sin\left(\varphi\right) & \cos\left(\varphi\right) & 0 \\ 0 & 0 & 1 \end{bmatrix} \tag{3.56}$$

so that

$$\overleftarrow{T}_{0/k+1,\nu} = R^{z}\left(\varphi\right)\overleftarrow{T}^{rot}_{0/k+1,\nu} \tag{3.57}$$

Together with our range specification of θ_ν this covers the entire half-spaces above and below an interface.

3.4.2 *The Output Field Transfer Coefficient Matrices*

Returning to Eq. (3.2) we have

$$\begin{bmatrix} \vec{E}^{NL,p}_{\nu} \\ \vec{E}^{NL,s}_{\nu} \\ 0 \end{bmatrix} = \vec{T}_{\nu,0/k+1} \begin{bmatrix} P^{NL,x}_{\nu} \\ P^{NL,y}_{\nu} \\ P^{NL,z}_{\nu} \end{bmatrix} \tag{3.58}$$

Considering these bases we can write

$$\vec{\mathbf{E}}^{NL}_{\nu,0/k+1} = \left(p^{+}_{\nu}\vec{T}^{+}_{\nu,0/k+1} + p^{-'}_{\nu}\vec{T}^{-'}_{\nu,0/k+1} \right)\mathbf{P}^{NL}_{\nu} \tag{3.59}$$

to show that in general each polarized sheet can potentially contribute fields initially generated in the positive and negative z -directions into the layers on either side of the interface followed by transfer to medium $0/k+1$. Here

$$p^{+}_{\nu} = \frac{i2\pi\sec\left(\theta_{\nu-1}\right)}{c\lambda n_{\nu-1}} \tag{3.60}$$

$$p^{-'}_{\nu} = \frac{i2\pi\sec\left(\theta_{\nu}\right)}{c\lambda n_{\nu}} \tag{3.61}$$

are factors resulting from the solution to a field radiating from a polarized sheet where c is the speed of light and λ is the vacuum wavelength of emitted light, as outlined in Section 1.3.2.7.[237]

We consider $\vec{T}^{+/-'}_{\nu,0/k+1}$ as consisting of two transformations.

$$\vec{T}^{+/-'}_{\nu,0/k+1} = \vec{f}^{+/-'}_{\nu,0/k+1} L^{+/-'}_{\nu} \tag{3.62}$$

Together with the $p_v^{+/-'}$ factors, the $L_v^{+/-'}$ matrices transform the polarized sheet into fields emitted immediately adjacent to the interface. With the projected basis we have

$$\begin{bmatrix} \varepsilon_v^{NL,+/-',p} \\ \varepsilon_v^{NL,+/-',s} \\ 0 \end{bmatrix} = p_v^{+/-'} L_v^{+/-'} \begin{bmatrix} P_v^{NL,x} \\ P_v^{NL,y} \\ P_v^{NL,z} \end{bmatrix} \tag{3.63}$$

where now all angles, refractive indices, and wavelengths refer to the generated signal. The angle is dictated by the phase-matching condition for all *n* input fields in medium *v*.

$$\mathbf{k}_v^{NL} = \pm\mathbf{k}_v^1 \pm \mathbf{k}_v^2 \cdots \pm \mathbf{k}_v^n \tag{3.64}$$

It is of interest to note that once the angle is calculated in one material it is related to all other materials simply through Snell's Law. The fields emitted immediately adjacent to the interface are not in general the total fields at that point and so we have used ε to represent the amplitude as described in Sections 3.3.2 and 3.3.3.

With the local input fields already determined, our approach will be to consider each interface in isolation, treating the materials on either side as semi-infinite. In this case the $L_v^{+/-'}$ matrices have already been solved as presented in Section 1.3.2.7.[236] The elements are found by the solution to Maxwell's wave equation in the presence and absence of the sheet boundaries subject to the phase-matching restriction and the same boundary conditions as the input fields. The results can be written

$$L_v^{+} = \left[\Pr\left(\theta_{v-1}\right)^T + f_{v-1,v} \Pr\left(-\theta_{v-1}\right)^T \right] J_v' \tag{3.65}$$

$$L_v^{-'} = \left[\Pr\left(-\theta_v\right)^T + f_{v,v-1} \Pr\left(\theta_v\right)^T \right] J_v \tag{3.66}$$

with

$$f_{i,j} = \begin{bmatrix} r_{i,j}^{p} & 0 & 0 \\ 0 & r_{i,j}^{s} & 0 \\ 0 & 0 & 0 \end{bmatrix} \tag{3.67}$$

where the elements are the linear Fresnel factors for reflection from Eqs (3.7) and (3.8). This is equivalent to the result reported in the literature for the commonly used L_{ii} Fresnel factors when care is taken with the definition of all field frames.[236,428]

The final transformation comes from transfer of the internally generated fields out of the thin film system to medium $0/k+1$. If we consider $\varepsilon_{\nu}^{NL,+} = \varepsilon_{\nu}^{+}$ and $\varepsilon_{\nu}^{NL,-'} = \varepsilon_{\nu}^{-'}$ (for either *s* or *p* fields) we can use the external transfer coefficients of Eqs. (3.40) - (3.43).

$$\begin{aligned} \vec{E}_{\nu,0/k+1}^{NL} &= \vec{E}_{\nu,0/k+1}^{NL,+} + \vec{E}_{\nu,0/k+1}^{NL,-'} \\ &= \varepsilon_{\nu}^{NL,+}\tau_{\nu,0/k+1}^{+} + \varepsilon_{\nu}^{NL,-'}\tau_{\nu,0/k+1}^{-'} \end{aligned} \tag{3.68}$$

which gives

$$\vec{f}_{\nu,0/k+1}^{+/-'} = \begin{bmatrix} \tau_{\nu,0/k+1}^{+/-',p} & 0 & 0 \\ 0 & \tau_{\nu,0/k+1}^{+/-',s} & 0 \\ 0 & 0 & 0 \end{bmatrix} \tag{3.69}$$

so that $\vec{T}_{\nu,0/k+1}$ may be constructed by Eqs. (3.59) - (3.69). In this way the outgoing electric field generated by a nonlinear polarized sheet driven by multiple input fields is propagated out of an arbitrary layered thin film system.

3.5 CONCLUSION

This chapter has provided a generalized model to describe thin film interference effects in surface-selective nonlinear spectroscopies on multilayer systems. The model

is based on reducing the multilayer problem to a single layer with newly defined coefficients of reflection and transmission at the effective boundaries. Summation over infinite reflections within the layer is then analytical for the total fields of the ideal system. With this view we add to the literature external transfer coefficients which serve to transfer internally generated fields out of the system without needing to resort to truncated summations or Green's function approaches. Input local fields are determined from the internal transfer coefficients and the usual boundary conditions. We envision this model will have implications in a wide range of problems from those as straightforward as rational experimental design to some of the more vexing challenges in surface-specific spectroscopy such as quantification of bulk contributions or microscopic local field corrections (i.e. local dipole effects).[227,351,429] Further, we see this as a step forward for such techniques as nonlinear ellipsometry[287,288] on thin film systems. The equations presented allow for a multitude of experimental geometries. Any input beam may be incident from either side of the system and from any plane of incidence and the generated signals are described on both sides of the system as well, providing experimental flexibility and control. Application of the model provides the ability to separate optical interference effects from the true sample response contained in the intensity data from potentially complex layered systems. Modeling these effects should impart confidence in data interpretation from such systems and open up the possibility for many new and interesting studies on interfacial structure and dynamics. Finally, the matrix notation presented here should lend itself to extending the model to optically anisotropic systems.

In the next chapter the model is specified for VSFG and used to simulate optical interference effects in VSFG signals generated from the model PTCDI-C_8 oFET system. Then, in Chapter 5 VSFG data collected from wedged samples is used to validate that this approach provides a good description of optical interference effects from multilayer thin film systems with two active interfaces. The interference model is extended in that chapter to include sources terms that originate from the bulk of the thin film layers.[i]

[i] This work was supported by the National Science Foundation under Award Number DMR-1006386, and partially supported by a Seed Grant from the MRSEC Program of the National Science Foundation under Award Number DMR-0212302 and DMR-0819885.

4 Simulated Vibrational Sum Frequency Generation from a Multilayer Thin Film System with Two Active Interfaces

Reprinted with permission from

Daniel B. O'Brien and Aaron M. Massari. Simulated vibrational sum frequency generation from a multilayer thin film system with two active interfaces. *Journal of Chemical Physics*. **2013**, 138 (15), 154708.

CHAPTER SUMMARY

In the field of surface-specific vibrational sum frequency generation spectroscopy (VSFG) on organic thin films, optical interferences combined with the two-interface problem presents a challenge in terms of qualitative assessment of the data and quantitative modeling. The difficulty is amplified when considering systems comprised of more than a single material thin film layer. In Chapter 3, a generalized model was developed that describes thin film interference in interface-specific nonlinear optical spectroscopies from arbitrary multilayer systems. In this chapter the model is used to simulate VSFG spectra from the model system of primary concern in this

dissertation. The oFET geometry is the simplest multilayer: a system of two thin films, one of which is an organic small molecule and the other is a dielectric layer on a semiconductor substrate system. For the purposes of these simulations, the organic interfaces are idealized as being equally VSFG active (i.e. $\vec{\vec{\chi}}_1^{(2)} = \vec{\vec{\chi}}_2^{(2)}$ in the notation of the previous chapter). Of specific concern is the model system of this dissertation: the small molecule N,N'-dioctyl-3,4,9,10-perylenedicarboximide (PTCDI-C_8) deposited on a silicon wafer with a thermally grown oxide dielectric. Results are presented for the four polarization experiments that sample the nonzero nonlinear susceptibility elements of macroscopically centrosymmetric materials (*ssp*, *sps*, *pss*, and *ppp*) and in two mIR frequency windows (the imide carbonyl stretches around 1680 cm^{-1} and the alkyl stretches around 2900 cm^{-1}) as a function of both thin film thicknesses with fixed input beam angles. Frequency dependent refractive indices are used for all materials. The goal is to illustrate some of the intricacies contained in the intensity data of such systems. Of particular interest is the effect of the relative polar orientation of modes at the interfaces and the possibility of designing a system where the collected signal is exclusively attributable to a single interface. The calculations indicate that in order to unambiguously identify the relative polar orientation one must experimentally vary an additional system parameter such as thin film thickness or input beam angle and for quantitative modeling one cannot ignore either interfacial contribution. The results show that proper modeling of thin film interference effects is essential for accurate data analysis and should include the frequency dependent refractive indices, especially for modes with larger mIR absorption cross sections, even when absorptive losses are small.

4.1 INTRODUCTION

The interfaces of organic thin films play important roles in materials research, often dictating the performance of the material function of interest. This is apparent in studies on adsorption and adhesion[2,324,330,430,431] but also extends to charge transport in organic semiconducting devices such as organic field-effect transistors (oFETs) where conduction occurs in the first monolayers of a bulk film.[17,25,343] Characterizing the molecules at the interface of interest is confounded by the presence of bulk material or is difficult because the active interface is buried. Second order nonlinear spectroscopies of macroscopically centrosymmetric systems possess the surface-specificity necessary to characterize the structure and dynamics of molecules at interfaces.[159,236,237] However, when interface-specific nonlinear optical spectroscopies are applied to layered thin film systems, the detected signal is subject to optical interference effects. The amplitudes of the input fields at the active interfaces depend on the geometry of the entire system as do the generated fields that propagate out to the detector. In the case of vibrational sum frequency generation (VSFG) spectroscopy of an organic thin film in a multilayer system the challenge is to accurately separate the contributions to the detected signal from two very similar interfaces.[96]

When a single thin film layer is present between two semi-infinite media, the problem of modeling these effects is tractable by considering the Fresnel formula for reflection and transmission at boundaries. The usual procedure is to sum the input field contributions at each active interface, accounting for infinite reflections and transmissions at the boundaries as well as phase changes due to propagating through the thin film. Then, generated fields are propagated out of the system in a similar manner,

summing the contributions on the side of the system at which the signal is collected.[21,359,361–363,432] However, as soon as subsequent layers are added, the expressions for describing infinite reflections and transmissions become cumbersome because the contributions that transmit out of one layer may subsequently be reflected back in from the other layers. Accounting for the infinite reflections and transmissions quickly becomes unwieldy and so the usual solution is to avoid directly modeling thin film interference effects by experimentally optimizing the system for a single interface[324,328,353] or to monitor a change in the signal that is presumably due to only a single interface.[25,344] The disadvantage is that, in general, it is better to have a model that describes thin film interference effects in order to impart confidence in data interpretation. One approach is to use the transfer matrix to describe the input fields and a Greens function solution to the internally generated fields, the drawback being the necessity of solving a differential equation by approximation for each system.[23,231] Another option might be to truncate the infinite reflections and transmissions at some finite sum, however, these results are not analytical and the choice of where to truncate so as not to introduce excessive error is system dependent.[363]

The fields within ideal multilayer thin film systems have long been well described by the transfer matrix.[367–370] This method differs from above in that it builds matrices that describe the internal fields based on boundary conditions at the individual layer interfaces. One aspect of this approach is that it allows for the simplification of an arbitrary layered system to a *single* layer with newly defined coefficients of reflection and transmission at the two pseudo-boundaries. The model developed in Chapter 3 is based on this idea. Within the plane wave approximation, the model analytically

describes interference effects in interface-specific nonlinear spectroscopies from ideal multilayer thin film systems for the input fields as well as the generated fields.[372] This allows for the separation of the individual layer interfacial responses from optical thin film interference effects.

The goal of this chapter is to utilize the model developed in Chapter 3 to demonstrate some of the intricacies contained in the VSFG intensity data collected from a multilayer system that has two similarly VSFG active interfaces. Calculated results are present for the organic/dielectric/semiconductor model system of this dissertation, which is representative of other organic electronic assemblies that we and others have studied by VSFG.[23,25,96,343,433] The analysis is restricted to the common experimental geometry of coplanar input beams with VSFG collected in reflection. The specific system is the organic molecule N,N'-dioctyl-3,4,9,10-perylenedicarboximide (PTCDI-C_8) deposited on a silicon wafer substrate with a thermally grown silicon dioxide dielectric (Figure 4-1).[96]

4.2 MODEL OVERVIEW

The model equations are generalized for any interface-specific coherent optical spectroscopy from any arbitrary layered thin film system. In Section 4.2.1 those equations are specified for VSFG of a two layer system where only the interfaces of the organic layer contribute to the VSFG response of the system detected in reflection geometry (Figure 4-1). Presented in Section 4.2.2 are simplified equations for the four typical VSFG polarization experiments. The notation developed in Chapter 3 is used throughout this work.[372]

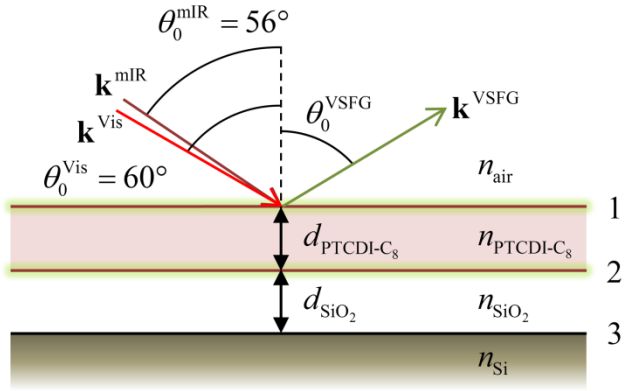

Figure 4-1. Illustration of the system under consideration showing the interfaces numbered on the right.

4.2.1 *General Description of VSFG*

VSFG is a 3-wave mixing process in which a visible pulse is spatially and temporally overlapped at the sample with a mIR pulse tuned to a vibrational mode of interest. The detected signal is then collected at the sum of the two frequencies. The signal collected from our system (I_0) will contain sum frequency electric field contributions ($\vec{\mathbf{E}}_{v,0}^{\mathrm{VSFG}}$) from interfaces 1 and 2 of the organic film.

$$I_0 \propto \left| \sum_{v=1}^{2} \vec{\mathbf{E}}_{v,0}^{\mathrm{VSFG}} \right|^2 \tag{4.1}$$

Each external field contribution is the result of internally generated fields radiating in the phase matched directions from the second order sum frequency source polarized sheet induced at interface v ($\mathbf{P}_v^{(2)}$ as discussed in Section 1.3.2.7)[236,237] followed by transfer through the thin film system into the bounding air medium.

$$\vec{\mathbf{E}}_{v,0}^{\mathrm{VSFG}} = \vec{T}_{v,0}^{\mathrm{VSFG}} \mathbf{P}_v^{(2)} \tag{4.2}$$

Here $\vec{T}_{v,0}^{\mathrm{VSFG}}$ is the external transfer coefficient matrix. It describes how the nonlinear polarization in the sample frame $\begin{bmatrix} P_v^{(2),x} & P_v^{(2),y} & P_v^{(2),z} \end{bmatrix}$ is transformed into internally generated fields and propagated out of the system in the propagating fields frame $\begin{bmatrix} \vec{E}_{v,0}^{\mathrm{VSFG},p} & \vec{E}_{v,0}^{\mathrm{VSFG},s} & 0 \end{bmatrix}$.[372] The nonlinear polarization depends on the sample response and the local field amplitudes of the visible ($\mathbf{E}_v^{\mathrm{vis},local}$) and mIR ($\mathbf{E}_v^{\mathrm{mIR},local}$) input beams at interface *v*.

$$\mathbf{P}_v^{(2)} = \vec{\vec{\chi}}_v^{(2)} : \mathbf{E}_v^{\mathrm{vis},local} \otimes \mathbf{E}_v^{\mathrm{mIR},local} \tag{4.3}$$

The second order susceptibility ($\vec{\vec{\chi}}_v^{(2)}$) is a third rank tensor that describes the sample sum frequency response to the input fields at the interface. It provides molecular information from the layer interfaces and we seek to separate its contribution to the detected signal from thin film interference effects. The input beam local field *m* (visible or mIR) is related to the external input field ($\vec{\mathbf{E}}_0^m$) through the input field transfer coefficient matrix ($\vec{T}_{0,v}^m$).

$$\mathbf{E}_v^{m,local} = \vec{T}_{0,v}^m \vec{\mathbf{E}}_0^m \tag{4.4}$$

The $\vec{T}_{0,v}^m$ matrices (defined uniquely for each of the mIR and visible input beams) account for thin film interference effects as well as the basis change from the propagating fields frame $\begin{bmatrix} \vec{E}_0^{m,p} & \vec{E}_0^{m,s} & 0 \end{bmatrix}$ to the sample frame $\begin{bmatrix} E_v^{m,local,x} & E_v^{m,local,y} & E_v^{m,local,z} \end{bmatrix}$ at the interface.

The $\vec{T}_{v,0}^{\mathrm{VSFG}}$ and $\vec{T}_{0,v}^m$ matrices describe all optical thin film interference effects and local field factors at the interfaces. They depend on the angles of incidence of the

input beams, the refractive indices of all materials, and the thicknesses of all thin films in the system. They provide for the separation of the sample $\chi_v^{(2)}$ response from thin film interference effects and the construction of each is detailed in Chapter 3.[372]

4.2.2 *Simulated VSFG Experiments*

The selection rules for VSFG on a macroscopically centrosymmetric system state that of the 27 elements of $\chi_v^{(2)}$ there are only four nonzero and independent contributions: $\chi_v^{(2),xxz} = \chi_v^{(2),yyz}$, $\chi_v^{(2),xzx} = \chi_v^{(2),yzy}$, $\chi_v^{(2),zxx} = \chi_v^{(2),zyy}$, and $\chi_v^{(2),zzz}$.[22,236] These can be probed with four beam polarization combinations experimentally: *ssp*, *sps*, *pss*, and *ppp* where the polarization is in the order VSFG-visible-mIR. We will discuss the model results pertaining to all four polarization combinations while making no assertion on the functional form of $\chi_v^{(2)}$ until the last section.

In these experiments the input beams are linearly polarized either *s* or *p* and the selection rules dictate the polarization of the output VSFG fields. We define the transfer product at interface v ($T_v^{\alpha i,j\beta,k\gamma}$) as the product of transfer coefficient matrix elements for the given element of $\chi_v^{(2),ijk}$ with i, j, and $k = x$, y, or z and α, β, and $\gamma = s$ or p. The superscript on T_v indicates the basis change for each beam grouped in order: VSFG,visible,mIR. We will use an abbreviated form of the superscript that indicates only the sample basis T_v^{ijk}. The model allows us to write very succinct descriptions of the signal intensity for three of the four polarization combinations that sample individual $\chi_v^{(2)}$ elements.

$$I_0^{ssp} \propto \left| \left(\sum_{v=1}^{2} T_v^{yyz} \chi_v^{(2),yyz} \right) \overleftarrow{E}_0^{\mathrm{vis},s} \overleftarrow{E}_0^{\mathrm{mIR},p} \right|^2 \tag{4.5}$$

$$I_0^{sps} \propto \left| \left(\sum_{v=1}^{2} T_v^{yzy} \chi_v^{(2),yzy} \right) \overleftarrow{E}_0^{\mathrm{vis},p} \overleftarrow{E}_0^{\mathrm{mIR},s} \right|^2 \tag{4.6}$$

$$I_0^{pss} \propto \left| \left(\sum_{v=1}^{2} T_v^{zyy} \chi_v^{(2),zyy} \right) \overleftarrow{E}_0^{\mathrm{vis},s} \overleftarrow{E}_0^{\mathrm{mIR},s} \right|^2 \tag{4.7}$$

The sums run over the two interfaces of the organic thin film and the transfer products are defined as

$$T_v^{yyz} \equiv \vec{t}_{v,0,(22)}^{\mathrm{VSFG}} \overleftarrow{t}_{0,v,(22)}^{\mathrm{vis}} \overleftarrow{t}_{0,v,(31)}^{\mathrm{mIR}} \tag{4.8}$$

$$T_v^{yzy} \equiv \vec{t}_{v,0,(22)}^{\mathrm{VSFG}} \overleftarrow{t}_{0,v,(31)}^{\mathrm{vis}} \overleftarrow{t}_{0,v,(22)}^{\mathrm{mIR}} \tag{4.9}$$

$$T_v^{zyy} \equiv \vec{t}_{v,0,(13)}^{\mathrm{VSFG}} \overleftarrow{t}_{0,v,(22)}^{\mathrm{vis}} \overleftarrow{t}_{0,v,(22)}^{\mathrm{mIR}} \tag{4.10}$$

where t with subscripts in parentheses indicate elements of the transfer matrices of Eq. (4.4) for the input fields and Eq. (4.2) for the generated field.[372] The expression for the ppp combination is somewhat more complex because the experiment samples all four independent elements of the interfacial susceptibility.

$$I_0^{ppp} \propto \left| \left(\sum_{v=1}^{2} T_v^{xxz} \chi_v^{(2),xxz} + T_v^{xzx} \chi_v^{(2),xzx} + T_v^{zxx} \chi_v^{(2),zxx} + T_v^{zzz} \chi_v^{(2),zzz} \right) \overleftarrow{E}_0^{\mathrm{vis},p} \overleftarrow{E}_0^{\mathrm{mIR},p} \right|^2 \tag{4.11}$$

$$T_v^{xxz} \equiv \vec{t}_{v,0,(11)}^{\mathrm{VSFG}} \overleftarrow{t}_{0,v,(11)}^{\mathrm{vis}} \overleftarrow{t}_{0,v,(31)}^{\mathrm{mIR}} \tag{4.12}$$

$$T_v^{xzx} \equiv \vec{t}_{v,0,(11)}^{\mathrm{VSFG}} \overleftarrow{t}_{0,v,(31)}^{\mathrm{vis}} \overleftarrow{t}_{0,v,(11)}^{\mathrm{mIR}} \tag{4.13}$$

$$T_v^{zxx} \equiv \vec{t}_{v,0,(13)}^{\mathrm{VSFG}} \overleftarrow{t}_{0,v,(11)}^{\mathrm{vis}} \overleftarrow{t}_{0,v,(11)}^{\mathrm{mIR}} \tag{4.14}$$

$$T_v^{zzz} \equiv \vec{t}_{v,0,(13)}^{\mathrm{VSFG}} \overleftarrow{t}_{0,v,(31)}^{\mathrm{vis}} \overleftarrow{t}_{0,v,(31)}^{\mathrm{mIR}} \tag{4.15}$$

We take the visible pulse as an 800 nm monochromatic wave and focus on two regions of mIR activity in PTCDI-C_8: the imide carbonyl stretches centered in the region around 1680 cm^{-1} and the alkyl C-H stretches around 2900 cm^{-1}. The bulk refractive indices for all materials in the mIR and VSFG frequency regions are shown in Figure 4-2(a) and (b), respectively. The black traces comprise the real parts (η) and are scaled on the left, and the red traces are the imaginary parts (κ) scaled on the right with the definition of the complex refractive index $n = \eta + i\kappa$. The refractive indices at 800 nm are shown in Table I. We take $n_{air} = 1$ for all wavelengths and use the frequency dependent refractive indices for all the other materials. PTCDI-C_8 refractive indices (Figure 4-2 solid lines) were obtained through analysis of spectroscopic ellipsometry data at all wavelengths of interest from thin films vapor deposited on a silicon wafer with polished native oxide (sample preparation available,[96] ellipsometry data unpublished). Thermal oxide optical constants (Figure 4-2 dashed lines) are from a three term Sellmeier equation for all wavelengths.[434–436] Silicon indices (Figure 4-2 dot-dashed lines) in the mIR are also from a three term Sellmeier equation.[437] Tabular data for silicon at the visible and VSFG wavelengths are available[438] and were used to construct a third-order interpolating function for use in the thin film model. All optical constants were obtained from models that are Kramers-Kronig consistent.

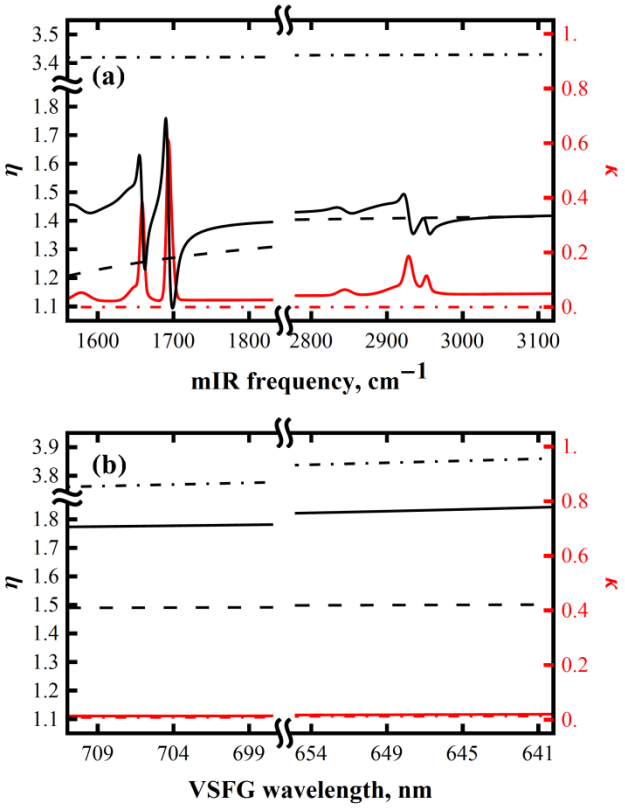

Figure 4-2. Complex refractive indices of PTCDI-C_8 (solid), SiO_2 (dashed), and Si (dot-dashed) at (a) mIR frequencies and (b) VSFG wavelengths. The black traces are the real parts and are scaled on the left, the red traces are the imaginary parts and are scaled on the right.

Table 4-1. Refractive Indices at 800 nm

$n_{\text{PTCDI-C}_8}$	n_{SiO_2}	n_{Si}
1.741 + 0.012i	1.480	3.679 + 0.004i

The out-of-plane component of the local fields ($E_v^{m,local,z}$) and the generated fields depend on the refractive index of the source polarized sheet $\bar{n}_v$.[372] There has been considerable discussion on the difficulty in quantifying the interfacial sheet refractive index.[427,428,439] In the simulations that follow we consider only the organic layer as contributing to the VSFG signal. Thus the source polarized sheets are the inner and outer interfaces of PTCDI-C_8. We idealize that the refractive indices of these sheets do not differ significantly from the bulk values and take $\bar{n}_1 = \bar{n}_2 = n_{\text{PTCDI-C}_8}$ where

$n_{\text{PTCDI-C}_8}$ is the bulk value. For the SiO_2-Si interface we use $\bar{n}_3 = n_{Si}$ for comparison of the total transfer product at that interface (although we consider the second order susceptibility equal to zero at this interface).

4.3 RESULTS AND DISCUSSION

Within this framework we have several degrees of freedom with which to explore the model. They include the input beam angles and the thicknesses of the organic and dielectric thin films. In these simulations we have sampled a very small portion of this space with an effort towards a logical progression through some of the more prominent model predictions. We will confine ourselves to fixed input beam angles ($\theta_0^{\text{vis}} = 60°$ and $\theta_0^{\text{mIR}} = 56°$) so that in total we have three coordinates in parameter space (the two thin film thicknesses and frequency space, see Figure 4-1). In what follows, all transfer products have been scaled by the same factor so that the relative scales are meaningful. We are interested in exploring the role of T_v^{ijk} on the detected VSFG signal and so we set the input field amplitudes equal to unity. We consider all complex quantities in polar form so that complex A has a magnitude and phase ($A = |A| Exp[i\phi A]$).

4.3.1 *Transfer Product Magnitudes*

We begin by considering how the magnitude of T_v^{ijk} affects the $T_v^{ijk}\chi_v^{(2),ijk} = \left|T_v^{ijk}\right|\left|\chi_v^{(2),ijk}\right| \exp\left[i\left(\phi T_v^{ijk} + \phi\chi_v^{(2),ijk}\right)\right]$ terms of Eqs. (4.5) - (4.7) and (4.11) as a function of frequency. If we choose a dielectric thickness of 300 nm, Figure 4-3 shows

$\left|T_v^{ijk}\right|$ in the imide carbonyl and alkyl C-H stretching regions at all three interfaces for the *ssp*, *sps*, and *pss* experiments as a function of frequency and PTCDI-C_8 thickness. Figure 4-4 shows the results for the component transfer products of the *ppp* experiment. The magnitude change when going from contour line to contour line represents a 5% change in the total scale in these plots.

There are several items worth noting from the results in Figure 4-3 and Figure 4-4. The first is that for strong mIR absorbers such as the imide carbonyl modes (see Figure 4-2(a)), there is a frequency dependence of $\left|T_v^{ijk}\right|$ through the vicinity of the modes. This is important because it will add frequency dependent modulations to the $T_v^{ijk}\chi_v^{(2),ijk}$ terms that are independent of $\chi_v^{(2),ijk}$ (the true interfacial response). This effect may skew data interpretation in two ways. If all modes in the mIR refractive index data are VSFG active, the detected nonlinear response will contain this frequency modulation. If there are multiple modes in proximity and not all modes are VSFG active, the transfer product will affect the response in the shoulders of the active modes so that there may appear more VSFG modes than are truly present. This effect is especially evident in the results that sample the z component of the mIR (Figure 4-3(a) and (b), and Figure 4-4(a), (b), (j), and (k)) where the magnitude modulation can span over 50% of the total scale across the frequency window for certain values of the PTCDI-C_8 thickness. The effect is relaxed (but present) for the weaker absorbing alkyl C-H modes. There are primarily three influences contributing to this phenomenon. The first is due to absorption of mIR by the organic layer which obviously becomes larger with film thickness but is nonetheless a small effect in this space. The second

contribution is a consequence of the *dispersive* part of the mIR refractive index within the polarized sheets and is primarily responsible for the large modulations on the z component of the mIR at any thickness. When going from air into the organic, the mIR beam refracts so its wavevector is closer to normal. The projection of the *p*-polarized field onto the *z* axis within the polarized sheet is small and so is very sensitive to the angle of refraction which is a function of frequency (due mainly to the real part of the mIR refractive index in Figure 4-2(a) although dispersion is a consequence of both the real and imaginary components). The third effect is neither new nor specific to our model (it appears even in the limit of a system with a single interface). It is well known that reflections and transmissions at the boundaries of media with appreciable and rapidly varying absorption will lead to rapidly varying Fresnel coefficients due to the Kramers-Kronig relation between the real and imaginary parts of the refractive index.[410,440] However, often this effect is overlooked or dismissed and we take this opportunity to draw attention to the importance of the frequency dependent mIR refractive index, especially for modes with large mIR absorption cross sections, even in systems where the layer thicknesses are much smaller than the mIR wavelength and absorptive losses are negligible. The last comment we make pertains to the residual effect of the PTCDI-C_8 layer on the frequency dependent transfer product at the Si-SiO_2 interface (Figs. 3(c), 3(f), 3(i), 4(c), 4(f), 4(i), and 4(l)). If this interface contains a vibrationally nonresonant contribution ($T_3^{ijk}\chi_{3,\mathrm{NR}}^{(2),ijk}$), this term will also contain a frequency modulation due to T_3^{ijk}. This effect will show up in the cross terms with the VSFG active interfaces at the signal intensity level which could be large if the

nonresonant susceptibility is large, or if the vibrational modes are VSFG inactive there may appear to be “resonances” in the nonresonant signal.

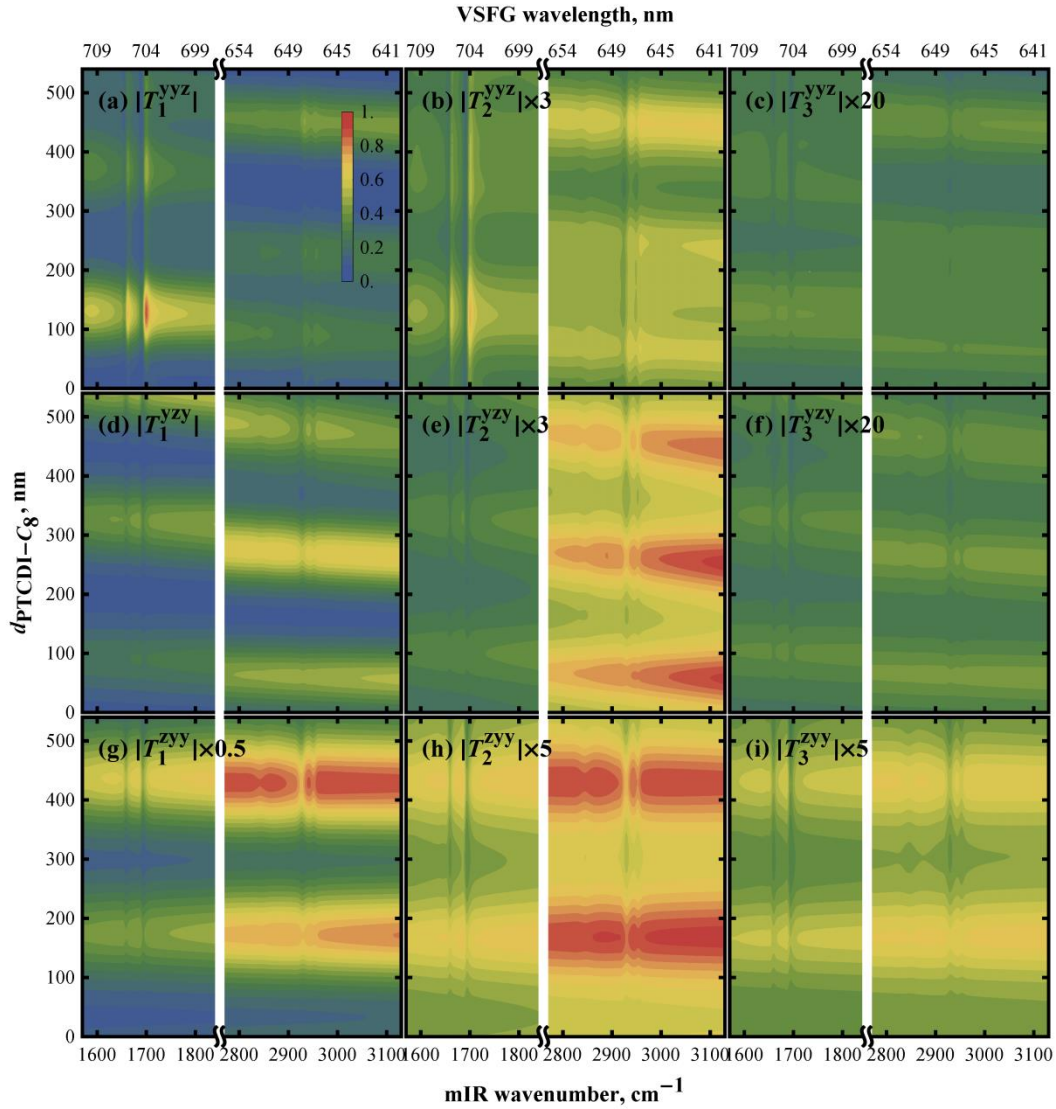

Figure 4-3. Transfer product magnitudes $\chi_v^{(2)}$ for *ssp*, *sps*, and *pss* (rows) at the three interfaces of the system (columns) for $\phi\chi_{1-2}^{(2),ijk} = \pi$ nm, where interface 1 = air/PTCDI-C_8, interface 2 = PTCDI-C_8/SiO_2, and interface 3 = SiO_2/Si.

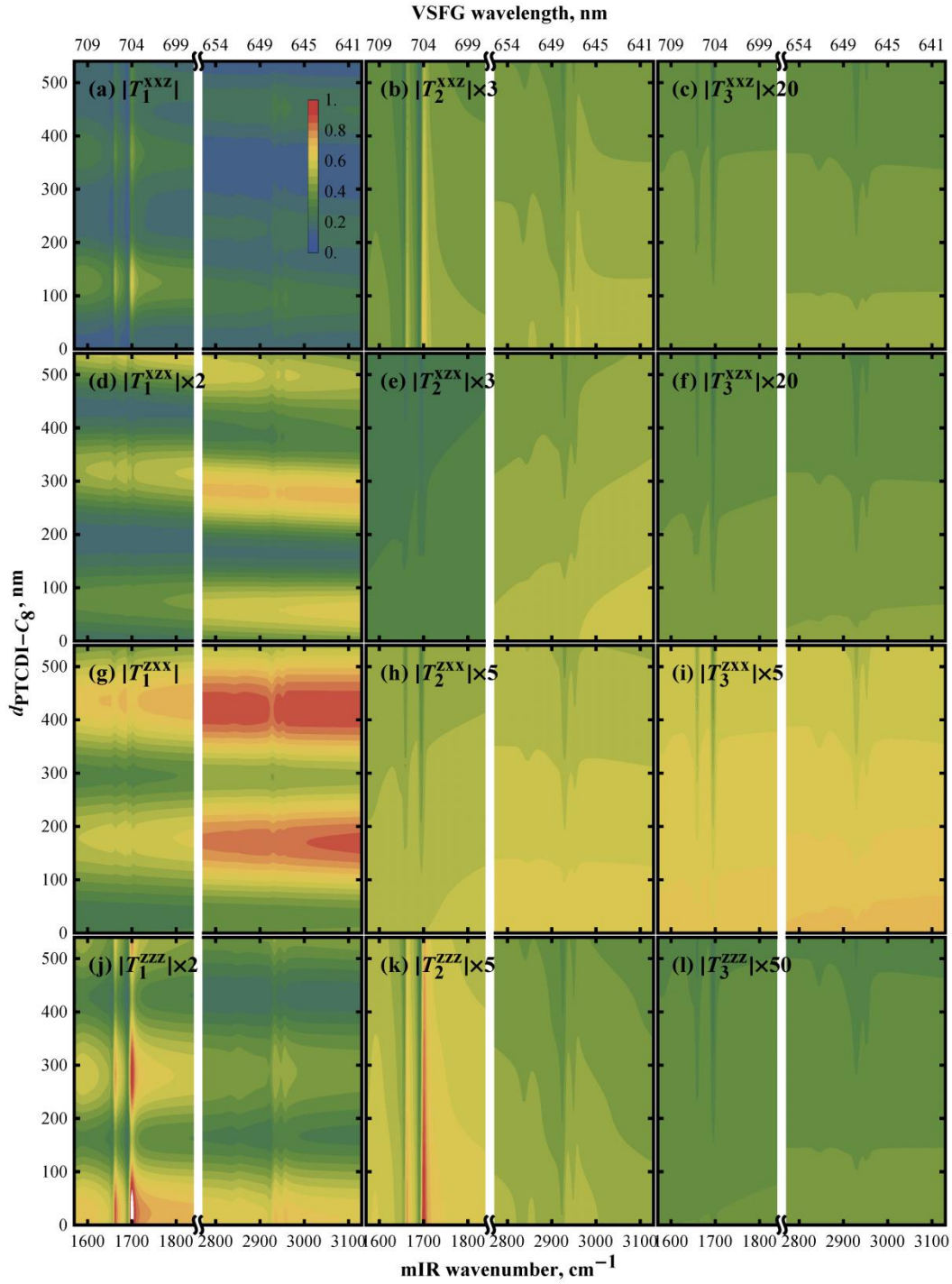

Figure 4-4. Magnitudes for the component transfer products $\left|T_v^{ijk}\right|$ of the *ppp* experiment (rows) at the three interfaces of the system (columns) for $d_{SiO_2} = 300$ nm.

The transfer product analogs in Figures 4–3 and 4–4 (e.g. Figure 4-3(a), $\left|T_1^{yyz}\right|$ and Figure 4-4(a), $\left|T_1^{xxz}\right|$) show different thickness dependences due to the way the component *s* or *p* fields propagate differently through the system. It is notably different at the buried interfaces (columns 2 and 3 in Figure 4-3 versus Figure 4-4). We point out that one cannot generally express the *ppp* signal intensity simply as a sum of individual *ssp*, *sps*, and *pss* contributions plus a *zzz* contribution because while the susceptibilities are related ($\chi_v^{(2),xxz} = \chi_v^{(2),yyz}$, $\chi_v^{(2),xzx} = \chi_v^{(2),yzy}$, and $\chi_v^{(2),zxx} = \chi_v^{(2),zyy}$) the transfer products are not ($T_v^{xxz} \neq T_v^{yyz}$, $T_v^{xzx} \neq T_v^{yzy}$, and $T_v^{zxx} \neq T_v^{zyy}$).

With the change in optical interference due to PTCDI-C_8 thickness relaxed at the buried interfaces of Figure 4-4 ($\partial\left|T_v^{ijk}\right| / \partial d_{\text{PTCDI-C}_8}$ is small and approximately constant) it is easy to point out some of the effects mentioned above. First, the dispersive effect is constant across the entire range of thicknesses in Figure 4-4(b) and (k). Also, the growth of weak vibrational features with organic film thickness shows how the absorptive effect is manifest (Figure 4-4(e) and (h)) and that it is the primary contributor to the apparent "resonances" on the third interface (Figure 4-4(c), (f), (i), and (l)).

Our observations from Figures 4–3 and 4–4 are consequences of the fixed choices we made for parameter space, of which we have sampled a very small subset. These results highlight the importance of properly accounting for thin film interference effects for accurate analysis of VSFG experimental data. Yet it is clear that the changes in the transfer product magnitudes associated with PTCDI-C_8 thickness are only weakly correlated with frequency within either frequency region. The same is true of the transfer product phase plots (not shown). This observation is important for the next

sections. Finally, upon close inspection of Figures 4–3 and 4–4 it is apparent that $\left|T_v^{ijk}\right|$ can be tuned to enhance the contribution from either interface of the organic by changing the thickness and that this relationship is generally different in either frequency window for a given thickness. We investigate this feature in more detail next.

4.3.2 *Transfer Product Magnitude Ratios*

When designing VSFG experiments on thin films it is most often the case that only one of the two interfaces is of principal interest and so considerable effort is made to isolate or make separable one from the other (indeed, this is the primary emphasis of this dissertation). One way this is done is by attempting to make one of the two terms in the sums of Eqs. (4.5) - (4.7) and (4.11) dominate. In the $T_v^{ijk}\chi_v^{(2),ijk}$ product we focus on tuning the factor T_v^{ijk}. For the *ppp* experiment this is complicated by the fact that one needs to simultaneously minimize (or maximize) four separate contributions to a single interface.

With the weak correlation between thickness and frequency noted in the last section we can choose a single mIR frequency in each spectral region, observe the log ratio $(\log_{10}\left|T_2^{ijk}/T_1^{ijk}\right|)$, and consider the results for each respective spectral window. Figure 4-5 shows plots of the log ratio as a function of SiO_2 and PTCDI-C_8 thicknesses at 1720 cm^{-1} and 2900 cm^{-1}. Columns 1 and 3 show the ratios for the individual component experiments (*ssp*, *sps*, and *pss* corresponding to T^{yyz}, T^{yzy}, and T^{zyy}) at the two frequencies, respectively, while columns 2 and 4 show the *ppp* components with

analogs placed adjacent to one another. The contours at $\log_{10}\left|T_2^{ijk}/T_1^{ijk}\right|=0$ are drawn dot-dashed. Thus, redder colors indicate contrast favoring interface 2 whereas bluer colors favor interface 1.

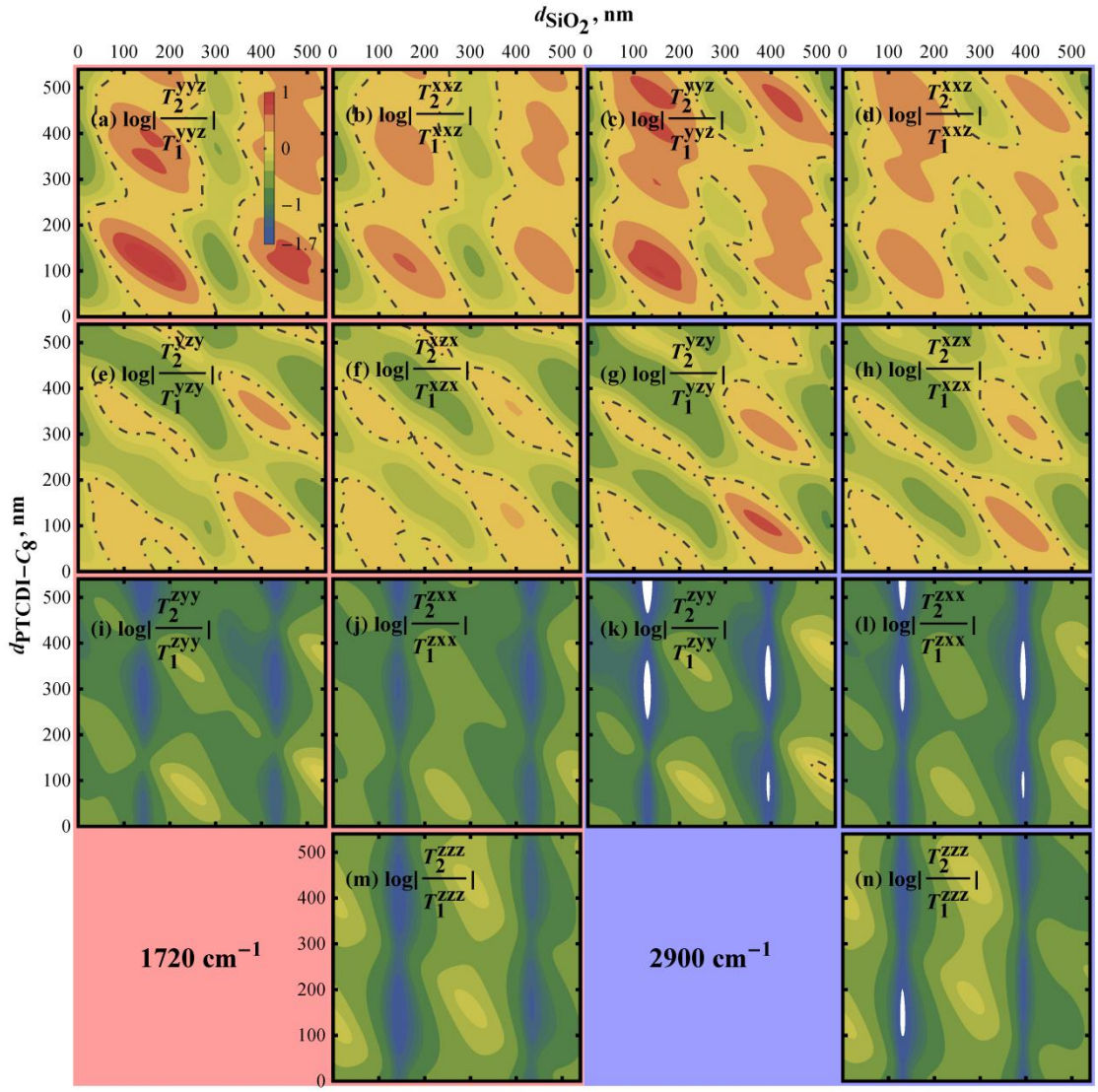

Figure 4-5. Log_{10} ratio of transfer product magnitudes at interface 2 to interface 1 showing how contrast is tunable as a function of thin film thicknesses. Columns 1 and 3 show results for *ssp*, *sps*, and *pss* at each mIR frequency. Columns 2 and 4 show results for the components of the *ppp* experiment with analogs placed adjacent so that the out-of-plane index is on the mIR in (a) – (d), the visible in (e) – (f), the VSFG in (i) – (l), and on all three fields in (m) and (n). The contours at $\log\left(T_2^{ijk}/T_1^{ijk}\right)=0$ are drawn dot-dashed.

We first observe that there is an irregular periodicity in the ratio for all cases. This is expected since we are sampling layer thicknesses comparable to the VSFG and

visible wavelengths. We find that for these thickness ranges the model predicts contrast as high as an order of magnitude in favor of interface 2 (PTCDI-C_8/SiO_2) in the case of $\log_{10}\left|T_2^{iiz}/T_1^{iiz}\right|$ (e.g. Figure 4-5(a)) and more than an order of magnitude in favor of interface 1 (air/PTCDI-C_8) for $\log_{10}\left|T_2^{zii}/T_1^{zii}\right|$ and $\log_{10}\left|T_2^{zzz}/T_1^{zzz}\right|$ (e.g. Figure 4-5(k)). Contrast can be achieved at specific thin film thickness combinations for the buried interface only for the *ssp* and *sps* experiments (with the exception of a very small area in Figure 4-5(k)). For the *ppp* experiment it is clear that one can never tune all components in favor of the buried interface due to Figure 4-5(j), (l), (m), and (n) never crossing the contour at 0, and to tune for the outer interface is never optimal for all components.

The log ratio analogs behave very similarly at either mIR frequency (e.g. Figure 4-5(a) – (d)) but quite dissimilarly when considering signal generated with the VSFG polarization component in the sample plane (Figure 4-5(a) – (h)) versus out-of-plane (Figure 4-5(i) – (n)). For the in-plane components we see periodicity that alternates contrast at each interface, whereas the out-of-plane components almost always favor interface 1 (again, the exception being a small area in Figure 4-5(k)). This contrast can be explained similarly to the strong frequency dependence observed in Figure 4-3 and Figure 4-4 due to the *z*-component of the input mIR field. The projection of the VSFG field on the *z*-axis of the *p*-polarized signal generated in the phase matched direction is small in the layers that have a small phase matching angle. Thus, the outer interface will always have a larger projection due to the phase matching angle always being

largest on the outer side of that interface since the input fields refract closer to normal within the thin film layers.

The log ratios show that one can achieve magnitude contrast as high as ~10:1 in favor of interface 2 and ~70:1 in favor of interface 1. For quantitative modeling, these relative magnitudes may not be large enough to nullify either interfacial contribution to the total signal on their own. Interference between the outer and inner contributions may produce a significant cross term at the signal intensity level, thus, we explore the relative phase of the interfacial contributions in the next section.

4.3.3 *Transfer Product Phase Differences*

The transfer products are complex quantities and so their phases will affect how the contributions from each interface interfere to produce the detected signal. In this section we will consider only those polarization combinations that sample individual $\chi_v^{(2)}$ components (*ssp*, *sps*, and *pss*) since these have only one interference term (in the *ppp* experiment there are six). It is easily seen if we expand Eqs. (4.5) - (4.7) in polar form, remembering that we have set the input field amplitudes to unity.

$$\begin{aligned} I_0^{\alpha\beta\gamma} \propto & \left|\chi_1^{(2),ijk} T_1^{ijk}\right|^2 + \left|\chi_2^{(2),ijk} T_2^{ijk}\right|^2 \\ & +2\left|\chi_1^{(2),ijk} T_1^{ijk}\, \chi_2^{(2),ijk} T_2^{ijk}\right| \cos\left(\phi T_{1-2}^{ijk} + \phi\chi_{1-2}^{(2),ijk}\right) \end{aligned} \tag{4.16}$$

Here $\phi A_{1-2} = \phi A_1 - \phi A_2$ ($A = T^{ijk}$ or $\chi^{(2),ijk}$) is the phase difference between the outer and inner interfaces of the complex transfer products and nonlinear susceptibilities.

For the moment we take $\phi\chi_{1-2}^{(2),ijk} = 0$ and present results for $\cos\left(\phi T_{1-2}^{ijk}\right)$ since it is this factor that contains the phase-dependent effect in the interference term of Eq.(4.16).

Figure 4-6 shows the results for the three experiments of interest at 1720 cm^{-1} and 2900 cm^{-1} as a function of thin film thicknesses. We have drawn the contours at 0 dot-dashed to highlight the vicinity where the interference term is nullified. Each contour color represents a 5% change in the total scale.

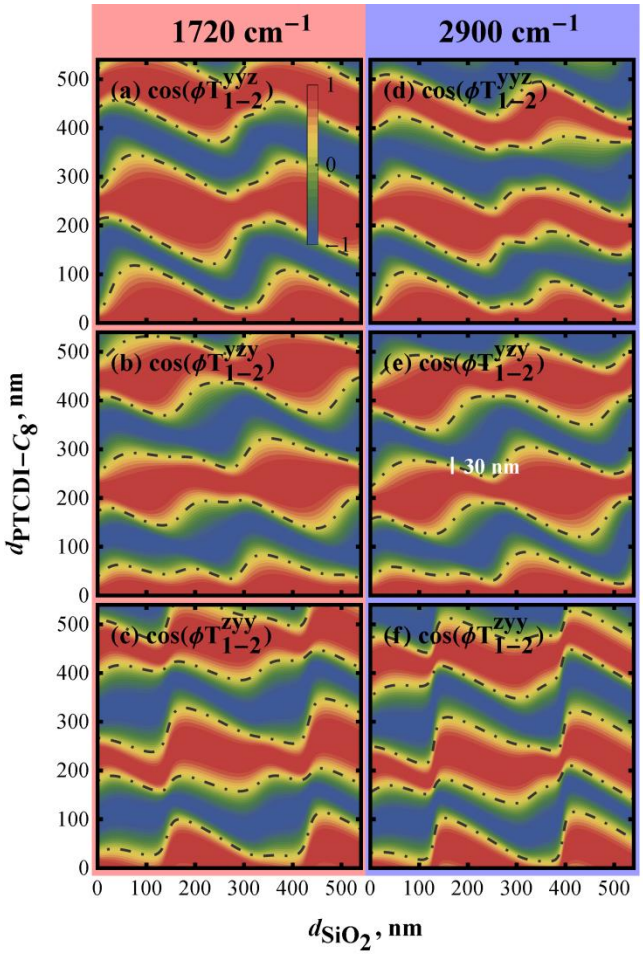

Figure 4-6. The phase dependent factor $\cos\left(\phi T_{1-2}^{ijk}\right)$ in the interference term for *ssp*, *sps*, and *pss* (rows) at each mIR frequency (columns). The white line in (e) provides a scale bar of 30 nm to demonstrate how quickly the interference terms can change sign as a function of PTCDI-C_8 thickness.

These results show irregular periodicity in this space. Consider that ϕT_{1-2}^{ijk} is a difference of sums of the phases of the component transfer coefficient matrix elements from Eqs.(4.8) - (4.10).

$$\phi T_{1-2}^{ijk} = \phi \vec{t}_{1,(mn)}^{\,\mathrm{VSFG}} + \phi \vec{t}_{1,(op)}^{\,\mathrm{vis}} + \phi \vec{t}_{1,(qr)}^{\,\mathrm{mIR}} - \left(\phi \vec{t}_{2,(mn)}^{\,\mathrm{VSFG}} + \phi \vec{t}_{2,(op)}^{\,\mathrm{vis}} + \phi \vec{t}_{2,(qr)}^{\,\mathrm{mIR}} \right) \tag{4.17}$$

The visible and VSFG terms in Eq. (4.17) are all expected to be similar at small thicknesses (because they are similar wavelengths with similar refractive indices) but will vary differently with thin film thicknesses so that *differences* in the quantities from the inner and outer interfaces change in a complex way to produce the plots in Figure 4-6. In all experiments and for both mIR wavelengths there are bands that represent 90% constructive (red) or destructive (blue) interference that span these plots which are a strong function of both thicknesses.

There are areas in these plots showing that $\left| \partial \cos\left(\phi T_{1-2}^{ijk} \right) / \partial d_{\mathrm{PTCDI\text{-}C_8/SiO_2}} \right|$ may be large or small. We generalize that in areas of large interference (red and blue bands) the change in interference is relatively insensitive to either thickness. Conversely, in areas around the contour at $\cos\left(\phi T_{1-2}^{ijk} \right) = 0$ the phase difference can be particularly sensitive to thicknesses and a shift of only a few nanometers can cause the interference to change quite rapidly. For example, Figure 4-6(e) shows a white line representing a 30 nm change in the organic thickness results in a shift from 90% constructive to 90% destructive interference. These observations are due to the contour at 0 existing at the inflection point of the cosine function ($\left| \partial \cos(\phi) / \partial \phi \right|$ is maximal) whereas areas close to ±1 are at the maximum and minimum ($\left| \partial \cos(\phi) / \partial \phi \right|$ is minimal).

The phase results presented here show only a portion of how thin film interference contributes at the signal intensity level. In order to get a full sense of how experimental data will behave as a function of thin film thicknesses, both the phases and

magnitudes (the full amplitudes) of all fields must be considered along with the sample response. We will explore signal intensity as a function of thin film thicknesses in Section 4.3.5 but first we discuss the possibility of designing experiments that sample only a single interface.

4.3.4 *Single Interface Assumption*

In order to design an experiment that conceivably samples only a single interface of our system we will want to minimize the cross term in Eq. (4.16) while optimizing $\left|T_2^{ijk}/T_1^{ijk}\right|^2$ for the interface of interest. When analyzing data in Figure 4-6 the contours at $\cos\left(\phi T_{1-2}^{ijk}\right)=0$ necessarily eliminate the cross term. Thus, when searching thickness space we will want to find an area in the vicinity of these contours that is also in a region of favorable contrast (Figure 4-5) so that ideally the error introduced by the single interface assumption is zero $(I_{\text{error}}=\left(\left|\chi_v^{(2),ijk}T_v^{ijk}\right|^2-I_0^{\alpha\beta\gamma}\right)\Big/I_0^{\alpha\beta\gamma}=0)$. We will focus strictly on finding the best scenario for each interface. In the case of interface 1, we can see maximal contrast is attainable in the alkyl region of the *pss* experiment (Figure 4-5(k) and Figure 4-6(f)). For interface 2 we choose the *ssp* experiment in the imide region (Figure 4-5(a) and Figure 4-6(a)). We set $\chi_v^{(2),ijk}$ equal to 1 at both interfaces.

Table 4-2. Errors due to the single interface assumption. Boldfaced values indicate changed variables and their resulting errors.

Interface of Interest, v	Experiment	mIR (cm^{-1})	$d_{\text{PTCDI-C}_8}$ (nm)	d_{SiO_2} (nm)	$\left\|T_1^{ijk}\right\|^2$	$\left\|T_2^{ijk}\right\|^2$	$\left\|T_2^{ijk}/T_1^{ijk}\right\|^2$	cross term	I_{error}
1	*pss*	2900	299.0	136.6	2.33	0.000830	2810^{-1}	-0.0011	0.00
			299.0	**130.6**	2.35	0.000456	5150^{-1}	-0.0381	**0.02**
2	*ssp*	1720	111.3	126.5	0.0070	0.217	27.2	-0.0081	0.00
			117.3	126.5	0.0051	0.203	39.9	-0.0265	**0.12**

Table II shows the results of our analysis as well as the effect of some deviations we will discuss. For both interfaces we see it is possible to achieve $I_{\text{error}} = 0.00$ at specific points in parameter space (top rows for each experiment in the table). However, the underlying cause is different in each case. Whereas interface 1 achieves very favorable contrast (2810^{-1}) and a very small cross term so that the $\left|\chi_1^{(2),ijk} T_1^{ijk}\right|^2$ term truly dominates the signal intensity, interface 2 has modest contrast (27.2) but the cross term is nearly matched and opposite from the outer interfacial contribution, canceling it. Now, if we change the SiO_2 thickness by 6 nm, we can see that in the case of interface 1 the cross term begins to get larger which introduces a small error ($I_{\text{error}} = 0.02$) even as the contrast has increased in favor of interface 1 to 5150^{-1}. Examination of Figure 4-6(f) reveals that at these thicknesses there is a rapid change in interference along the d_{SiO_2} coordinate so that the error ratio will be most sensitive to this parameter. Again, the contours at $\cos\left(\phi T_{1-2}^{ijk}\right) = 0$ tend to be in regions of rapid phase change so that this will almost always be an issue when designing experiments that favor one interface. For interface 2 we change the PTCDI-C_8 thickness by 6 nm and find that the cross term and contribution from interface 1 rapidly become unmatched, which introduces error

very quickly ($I_{error} = 0.12$). As a result, the single interface assumption error is quite sensitive to both thicknesses for interface 2.

For quantitative modeling it is probably best not to strive to design a system that totally favors one interface for this system. First, it is clear that even in the best-case scenario for interface 1 that the error can fairly quickly appear when the thickness of SiO_2 is not controlled very carefully. A 2% error may not seem critical, but if we include other nonidealities, such as surface roughness, possible errors in refractive indices or input beam angles, as well as differences in the nonlinear response at each interface (which will affect the plots in Figure 4-6 by making $\phi\chi_{1-2}^{(2),ijk}$ nonzero), the error from the single interface assumption may become appreciable. Another drawback of designing experiments that attempt to sample a single interface is that it limits the measurements to very specific points in parameter space. Sample to sample differences for the various experiments requiring an assortment of thickness combinations may cause the interfaces to be structurally different (especially the outer interfaces), complicating fitting procedures (this will be discussed in some detail in Chapter 5).

4.3.5 *Spectral Window Signal Intensities*

In Section 4.3.4 we determined that one cannot generally ignore interference between the outer and inner interfaces of the PTCDI-C_8 thin film for this system. If one cannot disregard either term in the sums of Eqs. (4.5) - (4.7) and (4.11), then perhaps we can pick a thickness combination that makes the experiment easier. If we consider that the frequency dependence of $\phi\chi_{v}^{(2),ijk}$ is nearly the same at both PTCDI-C_8 interfaces (and therefore the phase difference $\phi\chi_{1-2}^{(2),ijk}$ is zero), then the interference

between the outer and inner terms is controlled by ϕT_{1-2}^{ijk} as illustrated in Section 4.3.3. Now, if we estimate that $\left|\chi_2^{(2),ijk}\right|$ is not drastically different from $\left|\chi_1^{(2),ijk}\right|$ we can set them equal and examine Eqs. (4.5) - (4.7) and (4.11) to get a sense of the detected signal intensity as a function of thin film thicknesses due to thin film interference effects. We set $\chi_1^{(2),iiz}=\chi_2^{(2),iiz}=\chi_1^{(2),zzz}=\chi_2^{(2),zzz}=1$ and $\chi_1^{(2),izi}=\chi_2^{(2),izi}=\chi_1^{(2),zii}=\chi_2^{(2),zii}=\sqrt{0.1}$ since the signal intensities from individual components that sample the in-plane mIR transition dipoles are usually considered to be roughly an order of magnitude lower than the out-of-plane magnitudes[427,441] (although the true in-plane to out-of-plane ratio will depend on the molecular structure).

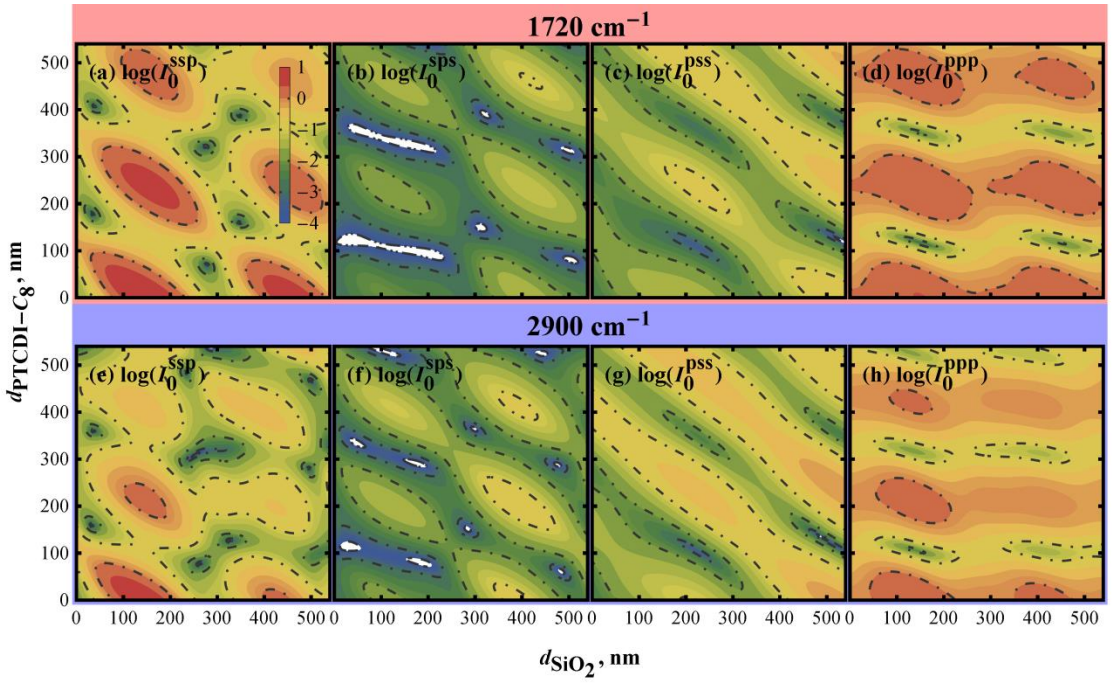

Figure 4-7. $\mathrm{Log_{10}}$ of the VSFG signal intensity in the case of $\phi\chi_{1-2}^{(2),ijk}=0$ for all four polarization experiments (columns) at each mIR frequency (rows) showing the orders of magnitude (contours drawn dot-dashed) spanned in the space of thin film thicknesses.

Figure 4-7 shows the results for $\log_{10}\left(I_0^{\alpha\beta\gamma}\right)$ at 1720 cm^{-1} (top row) and 2900 cm^{-1} (bottom row) with contours at each order of magnitude drawn dot-dashed.

These plots are a consequence of the absolute (Figure 4-3 and Figure 4-4) and relative (Figure 4-5) transfer products at the interfaces of interest and the interferences between them (Figure 4-6). First, we note that the patterns are similar but not the same in both frequency windows as should be expected. This is due mainly to the effect that the mIR frequency has on the VSFG wavelengths, shifting to shorter wavelengths in the alkyl region relative to the imide region (Figure 4-2). Different VSFG wavelengths have unique transfer matrix elements that beat differently with the visible field transfer matrix elements in Eqs. (4.8) - (4.10) and (4.12) - (4.15), as discussed in Section 4.3.3. Second, we can see the detected signal in this picture can be very low when in regions of non-optimal thickness combinations, or very high in regions of optimal thicknesses, and that the signal intensity of a given experiment can span several orders of magnitude in this space. We have previously reported dramatic differences in VSFG signals for identical thicknesses of PTCDI-C_8 but varied SiO_2 thicknesses (Chapter 2).[96]

For electronically nonresonant VSFG, the amplitude of a given mode is real and the sign of its contribution to $\chi_v^{(2)}$ can be either positive or negative. By inverting the sample axes the amplitude of the mode will change sign due to the tensor properties of $\chi^{(2)}$ as mentioned in Section 1.3.2.6. In a typical VSFG experiment and when the electric dipole approximation is valid (discussed throughout Section 1.3), the signs among modes can be used to quickly deduce the relative polar orientations of those molecular moieties (on average functional groups point "up" or "down").[5,22,26,395,442] If we consider the same mode at both interfaces (which is always true for an organic thin film that is thicker than a single monolayer) the sample axes for that mode may or may not be inverted. Setting both contributions to the same sign (as in Figure 4-7) is

equivalent to interpreting the relative polar orientation as the same at both interfaces (e.g. on average the outer dipole transition points into the air, the inner transition points into the organic film). But if we now consider the modes have opposite polar orientation (i.e. the inner dipole transition now points toward the SiO_2) then $\chi_2^{(2),iiz} = \chi_2^{(2),zzz} = -1$ and $\chi_2^{(2),izi} = \chi_2^{(2),zii} = -\sqrt{0.1}$ so that $\phi\chi_{1-2}^{(2),ijk} = \pi$ (this result reverses the scale of Figure 4-6).

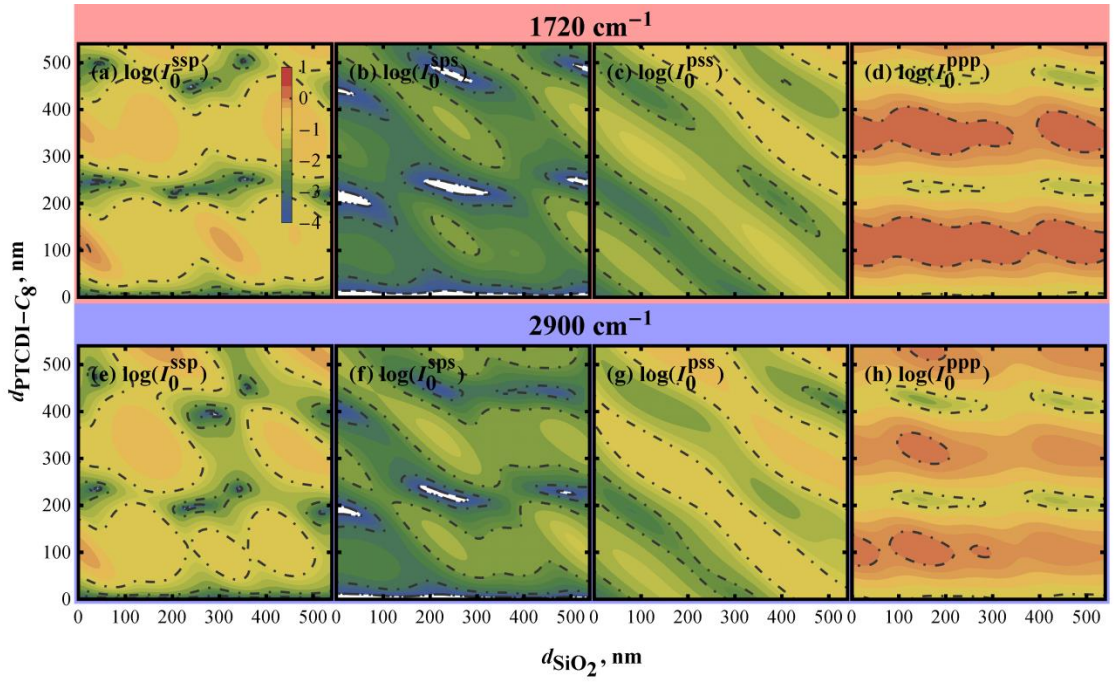

Figure 4-8. Log_{10} of the VSFG signal intensity in the case of $\phi\chi_{1-2}^{(2),ijk} = \pi$ for all four polarization experiments (columns) at each mIR frequency (rows) showing the orders of magnitude (contours drawn dot-dashed) spanned in the space of thin film thicknesses.

The intensity plots in this case are shown in Figure 4-8. We observe that there is less overall signal compared to Figure 4-7 but again the intensity can drop many orders of magnitude for non-optimal thickness combinations. But perhaps more importantly there is a clear difference in signal as a function of thin film thickness between Figure 4-7 and Figure 4-8 for all experiments in both frequency windows. Barring any large deviations from our assumptions on the nonlinear responses of the two interfaces, a

careful VSFG thickness study of a given organic thin film should unambiguously differentiate the relative polar orientation of all vibrational modes at the interfaces.

4.3.6 *Simulated VSFG Spectra*

The primary goal in VSFG is to discern interfacial molecular structure from experimental data. Going beyond the qualitative discussion on the amplitude sign in the last section, the usual analysis involves calculating the average polar tilt angles for multiple modes and relating these results to pre-knowledge of the structure of the bulk molecule to deduce the molecular orientation at the interface using either the bond additivity model,[239,240,427,443] local mode approximation,[261,427] or more recently a whole-molecule approach.[444] The calculation can be done using the ratio of VSFG data that sample the $\chi^{(2),ijk}$ components with in-plane mIR (*sps* or *pss*) to out-of plane mIR (*ssp* or *ppp*).[240,261,274,335,428,444,445] Additional information can be obtained by considering the relative amplitude ratio of two different modes within a given polarization combination.[284,446,447] In this section we investigate the effects of thin film interference on these experiments at the signal intensity level in VSFG spectra in order to illustrate the meaning of the *apparent* amplitudes in experimental data. It is important to note that the discussion on the interfacial susceptibility that follows is highly idealized in order to more easily separate susceptibility effects from transfer product effects on spectral data.

We consider the nonlinear susceptibilities at the inner and outer interfaces of the organic film as a sum of five Lorentzian oscillators, as discussed in Section 1.3.2.8 and 1.3.2.9.

$$\chi_1^{(2),ijk} = C^k \sum_{q=1}^{5} \chi_{1,q}^{(2)} \tag{4.18}$$

$$\chi_{1,q}^{(2)} = \frac{A_{1,q}}{\omega_{1,q} - \omega_{mIR} - i\Gamma_{1,q}} \tag{4.19}$$

The collection of oscillators are assumed identical or opposite in sign at the two interfaces

$$\chi_2^{(2),ijk} = \pm \chi_1^{(2),ijk} \tag{4.20}$$

depending on which relative polar orientation we are discussing. Here ω_{mIR} is the mIR input field frequency, $A_{1,q}$ is the amplitude of the q^{th} mode at interface 1, $\omega_{1,q}$ is its center frequency, and $\Gamma_{1,q}$ is the damping constant. All of the orientational information is contained in $A_{1,q}$. The prefactor C^k is equal to 1 for $k = z$ ($\chi_1^{(2),iiz}$ and $\chi_1^{(2),zzz}$) or $\sqrt{0.1}$ for $k = x$ or y ($\chi_1^{(2),zii}$ and $\chi_1^{(2),izi}$), as discussed in the previous section.

Table 4-3. Resonant VSFG Parameters

$\omega_{1,q}$ $\left(\text{cm}^{-1}\right)$	$A_{1,q}/\Gamma_{1,q}$	$\Gamma_{1,q}$ $\left(\text{cm}^{-1}\right)$
1657.7	$-\sqrt{0.5}$	5
1693.5	1	5
2844.3	$\sqrt{0.7}$	5
2928.0	$-\sqrt{0.7}$	5
2952.0	$\sqrt{0.7}$	5

We have chosen for our simulation to use the modes present in the mIR refractive index data of Figure 4-2. We set the center frequencies to be the same as five primary peaks found in the imaginary part of the mIR refractive index. The parameters for all VSFG active modes are shown in Table 4-3.

With the interfacial nonlinear susceptibilities assumed equal we can factor out the pure susceptibility spectrum from Eqs. (4.5) - (4.7).

$$I_0^{\alpha\beta\gamma} \propto \left|\chi_1^{(2),ijk}\right|^2 \left[\left|T_1^{ijk}\right|^2 + \left|T_2^{ijk}\right|^2 + 2\left|T_1^{ijk}\right|\left|T_2^{ijk}\right|\cos\left(\phi T_{1-2}^{ijk} + \phi\chi_{1-2}^{(2),ijk}\right)\right] \qquad (4.21)$$

Here ϕT_{1-2}^{ijk} is frequency dependent and $\phi\chi_{1-2}^{(2),ijk} = 0$ or π depending on the relative polar orientation of the modes at interface 2 (the sign in Eq. (4.20)) so that changing the polar orientation of molecules at interface 2 simply changes the sign of the interference term in Eq. (4.21). We will analyze how the inner, outer, and interference terms in Eq. (4.21) contribute to the total signal. For the *ppp* experiment of Eq. (4.11) the number of terms involved is ten and so we simplify the analysis by absorbing the prefactor value in Eq. (4.18) into the transfer products. We define an effective *ppp* transfer product

$$T_v^{ppp} \equiv T_v^{xxz} + \sqrt{0.1}T_v^{xzx} + \sqrt{0.1}T_v^{zxx} + T_v^{zzz} \qquad (4.22)$$

so that we can replace T_v^{ijk} with T_v^{ppp} in Eq. (4.21) and perform a similar analysis for the *ppp* experiment, separating the total inner and outer interfacial contributions along with their interference term.

With this set of assumptions, for all modes the true in-plane to out-of-plane ratio of individual tensor elements at the intensity level is 0.1. Of course, this is artificial but makes it easier to analyze thin film interference effects on the apparent ratios of the individual modes. Also note that in general each mode may have either polar orientation, here we have chosen to examine the two extremes where all modes have either the same or opposite relative polar orientation at each interface. If a mix is considered, the analysis is more complex.

If we choose an experimental geometry that maximizes contrast in favor of interface 2 we can see from Figure 4-5 that for this system there is no optimum choice of thin film thicknesses that satisfies this requirement for all four experiments and both

possible relative polar orientations of modes. Focusing on optimizing only for one in-plane and one out-of-plane experiment we can see in Figure 4-7 and Figure 4-8 that the in-plane experiment should be *sps* (since *pss* almost never provides contrast in favor of interface 2). For the out-of-plane experiment we select *ssp* since the thin film model analysis is more straightforward than for *ppp*. Examining Figure 4-5 - Figure 4-8 we select the vicinity of $d_{SiO_2} = 100$ nm and $d_{PTCDI\text{-}C_8} = 120$ or 150 nm. We have chosen to present results for the case of two PTCDI-C_8 thicknesses in order to further illustrate the sensitivity of the collected signal to similar thin film thicknesses.

Figure 4-9 shows simulated VSFG spectra for all four experiments at both organic thicknesses. The simulated intensity spectra ($I_0^{\alpha\beta\gamma}$) are shown as solid dark gray and black for the case of $\chi_2^{(2),ijk} = \chi_1^{(2),ijk}$ and $\chi_2^{(2),ijk} = -\chi_1^{(2),ijk}$, respectively. The $\left|\chi_1^{ijk}\right|^2$ spectrum is drawn dashed green and is full scale in all plots. The first two terms in Eq. (4.21) ($\left|T_1^{ijk}\right|^2$ and $\left|T_2^{ijk}\right|^2$) are shown dashed gray and black, respectively. These all share a common scale on the left. The interference term is solid lighter red for $\chi_2^{(2),ijk} = \chi_1^{(2),ijk}$ and dark red in the case of $\chi_2^{(2),ijk} = -\chi_1^{(2),ijk}$. The corresponding scale is on the right for these terms.

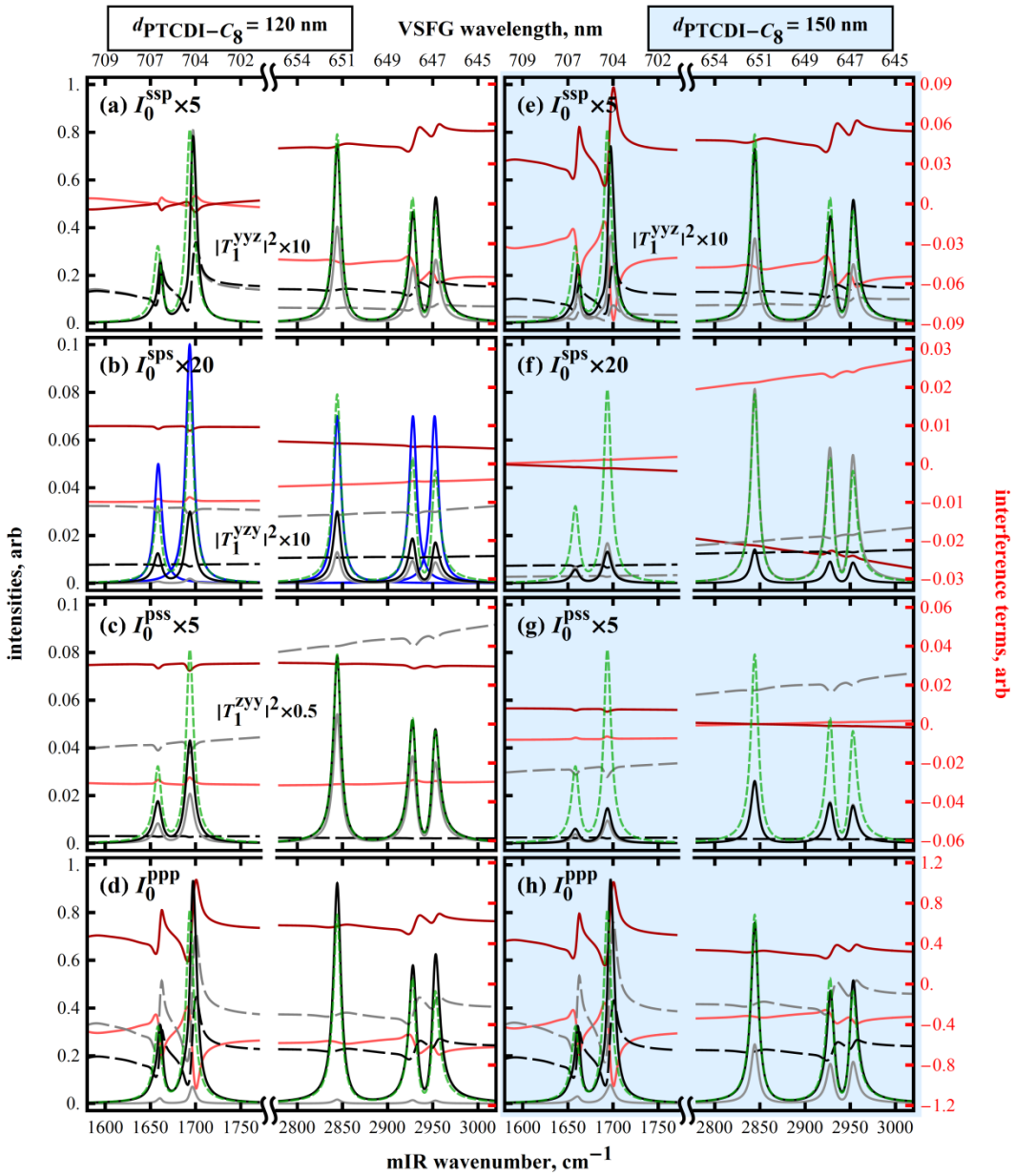

Figure 4-9. Simulated VSFG spectra and component transfer product terms in Eq. (4.21) with $d_{SiO_2} = 100$ nm for all four polarization experiments (rows) shown at two PTCDI-C$_8$ thicknesses (columns). Each plot contains traces of $\left|\chi_1^{ijk}\right|^2$ (dashed green), $\left|T_1^{ijk}\right|^2$ (dashed gray), and $\left|T_2^{ijk}\right|^2$ (dashed black). The transfer terms for the *ppp* experiment are defined in Eq. (4.22). For the cases of $\phi\chi_{1-2}^{(2),ijk} = 0$ and π the signal intensity $(I_0^{\alpha\beta\gamma})$ is drawn solid gray and black, respectively, and the interference terms are drawn solid light and dark red, respectively. The component $\left|\chi_1^{ijk}\right|^2$ resonances are shown in (b) (solid blue). The interference terms are scaled on the right and all others are scaled on the left.

Examining the $\left|\chi_1^{ijk}\right|^2$ spectrum (dashed green) relative to the individual Lorentzian oscillators (blue) in Figure 4-9(b) we can see that the total interfacial spectrum has different maximum amplitudes relative to the component resonances due to interferences among the components as is well described elsewhere.[395] This effect is not related to thin film interference. We provide the $\left|\chi_1^{ijk}\right|^2$ spectrum as a reference in all plots of Figure 4-9 because the thin film interference model affects this spectrum, not the individual Lorentzian contributions. Thus, in Figure 4-9 the detected signal is composed of each of the dashed traces ($\left|T_v^{ijk}\right|^2$) plus its corresponding interference term (red trace) times the $\left|\chi_1^{ijk}\right|^2$ spectrum. Which of the signal traces is detected ($I_0^{\alpha\beta\gamma}$, solid black or solid gray) depends on the relative polar orientation of the molecules at the two interfaces. The polar orientation relation for a given mode is maintained in all plots (since inversion of the axes changes the sign of the entire $\chi^{(2)}$ tensor, all elements). Thus, in the plots of Figure 4-9 if one performs measurements for all polarization experiments the collected intensity data will correspond to either all the black traces or all the gray traces. This provides a useful constraint when analyzing data.

The sign of the interference term will determine for which polar orientation the detected signal intensity is higher. In this space we find that in all cases the interference term is negative for the same polar orientation except the imide region of Figure 4-9(a), both regions in Figure 4-9(f) and the alkyl region in Figure 4-9(g). In general this relation will depend on the experiment geometry (film thicknesses, angles of incidence, etc.) which dictates the value of ϕT_{1-2}^{ijk}. It should be noted that if we design an

experiment where the interference term is nearly zero, we clearly lose sensitivity to the relative orientation of modes at the interfaces (e.g. imide region of Figure 4-9(a) and Figure 4-9(f) and alkyl region of Figure 4-9(g)) since this sensitivity is contained in $\phi\chi_{1-2}^{(2),ijk}$ within the interference term.

Our thickness choices were based on attempting to maximize contrast in favor of interface 2 for the *ssp* and *sps* experiments. In Figure 4-9(a), (b), (e), and (f) we can see that by first considering the results of Figure 4-5 – Figure 4-8 we can design the experiment to meet these needs. The $\left|T_2^{ijk}\right|^2$ trace is larger than $\left|T_1^{ijk}\right|^2$ in all cases except the alkyl region for the *sps* experiment with $d_{\text{PTCDI-C}_8} = 150$ nm. However, we have chosen thickness combinations that are not optimal for *sps* signal intensity (see Figure 4-7 and Figure 4-8). Also, in attempting to satisfy the contrast condition for both experiments and at both mIR frequencies, we did not obtain a single spectral region in which the contrast was maximally an order of magnitude in favor of interface 2 as we noted could be the case in Section 4.3.2. The highest ratio we observe is for the *ssp* experiment in the imide region with $d_{PTDCI-C_8} = 150$ nm (Figure 4-9(e) where $\left|T_2^{yyz}/T_1^{yyz}\right| \approx 6$). If we had chosen a thickness combination that resulted in higher contrast for the *ssp* experiment, it would have been at the expense of the desired contrast for the *sps* experiment (see Figure 4-5). This is in fact the case for the alkyl region in the *sps* experiment of Figure 4-9(f).

Of course, both interfaces contribute to all the signal intensities of Figure 4-9, thus, the apparent amplitudes at the intensity level are complicated by the fact that every observable resonance is composed of contributions from both interfaces. The amplitude

ratio orientational analysis mentioned at the beginning of this section is therefore dubious based on the apparent amplitudes, and the full thin film interference model is essential to separate the interfacial contributions and discern *quantitative* molecular structure. Even if one could attribute the full response to a single interface, there is still the issue of the relative field strengths at the interface, analogous to the L_{ii} factor corrections commonly reported for single interface systems and discussed in Section 1.3.2.7.[236,428] Thus, Figure 4-9 is meant to illustrate the wide variety of apparent responses due to thin film interference together with the possibility of two polar orientations. For these similar PTCDI-C_8 film thicknesses the experimental response can be very similar (e.g. the *ppp* response for same polar orientation, Figure 4-9(d) and (h)) or drastically different (e.g. the *sps* response for opposite orientation, Figure 4-9(b) and (f)). The experimentally observed relative peak intensities may follow the same relative true $\left|\chi_1^{(2),ijk}\right|^2$ peak heights when the individual terms of Eq. (4.21) are spectrally flat (e.g. imide region of the *sps* experiment of Figure 4-9(b)). However, the relative peak heights are generally modulated by either a gradual change in the transfer product terms across the spectral window (almost all cases for the in-plane experiments, *sps* and *pss*) or are modulated by very distinct frequency variations as in the case of the out-of-plane *ssp* and *ppp* experiments as discussed in Section 4.3.1. Frequency modulations in the imide region for the out-of-plane experiments even cause a discernible apparent frequency shift in the intensity plots of Figure 4-9(a), (d), (e), and (h). Finally, we point out that the frequency windows we have shown are sufficiently far apart that in many cases the magnitude of the signal amplitude relative to the true $\left|\chi_1^{(2),ijk}\right|^2$ response may be

quite different in the imide region versus the alkyl region (e.g. Figure 4-9(b), (c), and (f) for same orientation show the apparent imide response is *smaller* than the alkyl response) but is not necessarily dissimilar (e.g. Figure 4-9(e)). The results from Figure 4-9 emphasize the importance of accurate modeling of interference effects in nonlinear surface-specific spectroscopy in order to arrive at the true sample response.

4.3.7 *Additional Comments*

We end our discussion with a few comments. Obviously, the assumption that the inner and outer interfaces of the organic film have the same VSFG response implies that all modes are identically ordered and are in the same chemical environment at either interface. This is clearly not the case in general (indeed, discerning molecular structure and structural differences *is* the goal in most VSFG experiments). Thus, $A_{v,q}$, $\Gamma_{v,q}$, and $\omega_{v,q}$ may vary for all modes at either interface. The result is that in general one cannot factor out $\left|\chi_v^{(2),ijk}\right|^2$ in Eq. (4.21) and $\phi\chi_{1-2}^{ijk}$ is frequency dependent. We simply state that our suppositions are a reasonable starting ground for evaluating VSFG data taken from thin film systems with two similarly VSFG active interfaces and that complete data analysis must factor in deviations from this ideality. In fact, by using our model these results may be used to test these assumptions.

Experimentally there is rarely prior knowledge of the true interfacial responses and so we want to point out a problem of correlation between the magnitudes of the contributions from the inner and outer interfaces. Consider the simplest case in which I_0^{ssp} and I_0^{sps} data are measured on the ideal system outlined above for $d_{\text{PTCDI-C}_8} = 120$ nm. Here, the interfacial response is identical on the inner and outer interfaces for each

experiment and therefore *ssp* and *sps* experimental data match either the black or gray traces in Figure 4-9(a) and (b). While the transfer products at the two interfaces generally have different absolute magnitudes, it is apparent from Figure 4-9 that they are nearly proportional ($\left|T_2^{ijk}\right| \approx C\left|T_1^{ijk}\right|$ where C is the proportionality constant that depends on the experiment, thin film thicknesses, and input beam angles). Now, if we consider the possibility for scaling the interfacial nonlinear responses (i.e. $a\left|\chi_1^{(2),ijk}\right|$ and $b\left|\chi_2^{(2),ijk}\right|$ where $\left|\chi_2^{(2),ijk}\right| = \pm\left|\chi_1^{(2),ijk}\right|$ as outlined in the last section) while maintaining the *same* detected signal intensity we can rewrite Eq. (4.21) with scaling factors a and b on the appropriate terms.

$$I_0^{\alpha\beta\gamma} \propto \left|\chi_1^{(2),ijk}\right|^2 \left[\left|aT_1^{ijk}\right|^2 + \left|bCT_1^{ijk}\right|^2 + 2abC\left|T_1^{ijk}\right|^2 \cos\left(\phi T_{1-2}^{ijk} + \phi\chi_{1-2}^{(2),ijk}\right)\right] \qquad (4.23)$$

From our example we know that the true response is described by $a = b = 1$ but a second possibility for describing the detected signal is for $a = C$ and $b = 1/C$. So that when fitting the data, even with the constraints of the thin film model, extracted parameters from a single point in parameter space may not be unique and identifying which is the correct physical picture may be ambiguous. Before we address this further we consider an additional issue.

We want to highlight the importance of discerning the relative polar orientation for all modes of interest.[448] Deviations from our assumptions in $\chi_v^{(2),ijk}$ will cause the differences that are obvious in the spectra of Figure 4-9 to become less clear in experimental data (this is indeed the case for data presented in the next chapter). Discerning the black lines from the gray lines for any individual thickness combination

with no reference may be ambiguous and modeling for one case when the true case is opposite will lead to large errors in fit parameters as they are adjusted to make up for an erroneous model. For instance, if we were to experimentally measure I_0^{ssp} and I_0^{sps} in the alkyl region of Figure 4-9(e) and (f) and, using the thin film model, extracted resonant parameters by assuming one polar orientation when the actual case was the opposite, there would be a very large disparity in the extracted mode amplitude ratios relative to the true ratios.

In order to resolve the problems associated with correlations between interfacial responses and nonidealities within those responses, more information is required. For instance, if Kleinman symmetry can be invoked then $\left|\chi_1^{zyz}\right|^2 = \left|\chi_1^{zyy}\right|^2$ [22] and ideally one need only to do the additional *pss* measurement in order to constrain the model. However, it is more likely that the analysis will need to include more complicated effects. For instance, the refractive index of PTCDI-C_8 has a small imaginary component in the visible (Table 4-1) and VSFG wavelengths (Figure 4-2(b)). This may mean that this particular molecule contains a small doubly or triply resonant VSFG contribution which makes the amplitudes of the modes ($A_{v,q}$'s) complex.[396,449] Additional degrees of freedom need to be sampled in order to sort these issues out. Thus, any interface-specific coherent spectroscopy of thin film systems with two similarly active interfaces may realistically require multiple thicknesses to be prepared or beam angles to be varied in order to extract unambiguous resonant parameters.

We have taken a preliminary look into the effect on intensity level ratios with an amplitude *change* at one or the other interface. The result suggests that, for the

thicknesses sampled in Figure 4-9, the apparent ratio can reproduce qualitative trends (i.e. actual in-plane to out-of-plane ratio goes down at the buried interface, intensity level ratio goes down). However, we stress that this may not be true for all experimental geometries and that the problem of reliably changing only one interface experimentally without changing the other complicates this analysis. Consider the terms in Eq. (4.16). If $\left|\chi_1^{(2),ijk}T_1^{ijk}\right|^2 > \left|\chi_2^{(2),ijk}T_2^{ijk}\right|^2$ and $\left|2\left|\chi_1^{(2),ijk}T_1^{ijk}\chi_2^{(2),ijk}T_2^{ijk}\right|\cos\left(\phi T_{1-2}^{ijk}+\phi\chi_{1-2}^{(2),ijk}\right)\right| > \left|\chi_2^{(2),ijk}T_2^{ijk}\right|^2$ with $\cos\left(\phi T_{1-2}^{ijk}+\phi\chi_{1-2}^{(2),ijk}\right)<0$, then as $\left|\chi_2^{(2),ijk}\right|$ becomes larger, $I_0^{\alpha\beta\gamma}$ goes *down*, affecting the apparent amplitude ratio opposite to the way that is expected.

The input angle space that we chose not to explore here certainly adds additional degrees of freedom to the model.[362,450,451] Allowing for different input angles for the different polarization experiments will allow for better optimization of desired properties (e.g. contrast in favor of the buried interface, higher signal intensities). However, in actual experiments there will be the issue of the relative spatial overlap of the input beams that will need to be addressed if data are to be compared with varied input beam angles. We propose that a more elegant mathematical exploration of the multidimensional parameter space will lead to better optimization of experiments and additional effects not observed here. Indeed, the model has revealed many interesting details on this system here in which we have sampled a small subset of parameter space.

4.4 CONCLUSION

The application of the thin film model to VSFG of stratified systems has important implications for the field. For certain, the results of these calculations show that inclusion of the frequency dependent transfer products is necessary for quantitative assessment of interfacial structure. In a broader sense, the qualitative metrics of orientation and order by VSFG may still be accurate, but only in cases in which the thin film thicknesses and experimental geometries are carefully chosen. With frequency dependent refractive indices and film thicknesses in hand, the multilayer thin film interference model can be used to impose additional constraints on fitting procedures, adding certainty to the conclusions from these measurements. We propose that carefully executed thickness dependent VSFG studies combined with the model presented above may be a solution to the two-interface dilemma facing many in this field. Experimental work corroborating these results is presented in the next chapter. A collection of Mathematica notebooks that were used to generate the model figures in this chapter, which can be used to investigate other multilayer thin film systems, is included in the supplementary materials.[i]

[i] D.O. wishes to thank T. Tiwald for assistance with PTCDI-C_8 ellipsometry data. This work was supported by the National Science Foundation under Award Number DMR-1006386, and partially supported by a Seed Grant from the MRSEC Program of the National Science Foundation under Award Number DMR-0212302 and DMR-0819885.

5 Experimental Evidence for an Optical Interference Model for Vibrational Sum Frequency Generation Spectroscopy on Multilayer Organic Thin Film Systems with Consideration for Higher Order Terms

"No amount of experimentation can ever prove me right; a single experiment can prove me wrong."

-Albert Einstein

CHAPTER SUMMARY

This chapter presents experimental evidence that the interfacial thin film model developed in Chapter 3 provides an accurate description of optical interference effects contained in VSFG obtained from multilayer thin film systems. The samples are PTCDI-C_8 vapor deposited as thickness gradients on silicon wafer substrates, one with a very thin 2 nm native oxide and another with a 300 nm thermally grown oxide thin film layer. Two surface substrate surface preparations were used: bare SiO_2 and silica functionalized with trimethoxy(octadecyl)silane (ODTMS) in a self-assembled monolayer (SAM). VSFG data were collected in both the *ssp* and *sps* polarization combinations from rasters along each thickness gradient to produce 2D datasets that are

a function of organic thickness and mIR frequency in the region of the imide carbonyl stretches. Treatment of the data within the electric dipole approximation indicates that the interfacial thin film model provides a good description of optical interference effects in the VSFG data and that interfacial terms are significant. However, discrepancies between the physical interpretation of the fit results and what would be expected for response within the electric dipole approximation provokes consideration for higher order interactions. The thin film model is expanded to include a description of fields generated from the bulk of the organic film and is applied to the data analysis. The conclusion is that bulk and higher order interfacial terms are present for this system. Even with this complication, an analysis is provided based on the signs of the fit results that allows for the deduction of the relative magnitudes of the interfacial electric dipole response at the buried interface between bare and ODTMS substrates. Those results indicate that the initial monolayer of PTCDI-C_8 on bare SiO_2 assembles in a more reclined phase and molecules on ODTMS are standing up but with more tilt across the short axis of the perylene core. The significance of this chapter is the demonstration that the multilayer interference model provides an accurate description of VSFG from thin film systems and that this provides a unique way to separate contributions to the VSFG intensity data.

5.1 INTRODUCTION

The molecular structure at organic interfaces can dictate the function of a material.[101,452,453] Characterizing the microscopic structure of exposed interfaces can be challenging, but interrogating the molecules that reside at internal interfaces is particularly problematic. While exposed interfaces have historically been important for fields such as adhesion,[1,2] adsorption, [3–5] or reactivity,[6,7] characterizing the molecules at buried interfaces has become an especially important challenge as the field of organic semiconducting devices has become pervasive in recent years[454] as detailed in Sections 1.1 and 1.2. Of particular concern in this dissertation is the active interface in organic field-effect transistors (oFETs) where device behavior is almost exclusively controlled by molecular structure at the buried interface. For oFETs, although the charge transfer mechanisms that occur within the active region are complex, it is effectively only the first molecular monolayer or two at the buried interface of the organic thin film and the dielectric material that participate in overall device performance.[15–20]

Various techniques for characterizing buried organic thin film interfaces were detailed in Section 1.2.3 where it was noted that none of the standard experiments possess the preferred conditions for characterizing buried interfaces. The two basic requirements of an ideal experiment for studying interfacial molecular structure are that the measurement is highly sensitive to interfacial molecules and has the ability to make measurements on a wide variety of systems. In the field of nonlinear optical spectroscopy, and within the electric dipole approximation detailed in Section 1.3.2.5, the signals generated by techniques described by even-ordered interactions are zero where there is inversion symmetry. For thin film systems, the bulk of most materials

are subject to this selection rule and it is only at the interfaces of the thin films where inversion is broken and there is a possible non-zero material response.[323] Vibrational sum frequency generation spectroscopy (VSFG) is a second-order spectroscopy that has been demonstrated as a sensitive probe to molecular structure at interfaces.[261,335,428,444] In addition to interfacial sensitivity, it also meets the second requirement of the ideal experiment with its ability to make nondestructive measurements with few limits on the types of systems that can be probed. In principle, it can be used to study any interface accessible by light. Perhaps of greatest value is its ability to study the structure of molecules at buried organic interfaces.[23,96,324,328,344,455]

Yet, despite decades of valuable contributions to the understanding of interfacial phenomena, VSFG remains somewhat exotic and specialized, and has not been adopted into the list of standard characterization techniques for organic thin films. This is in part because the technique is not without its limitations, particularly in the complexity of data interpretation. To those outside the nonlinear optics community, it is not always clear how thick of an interfacial region is probed by VSFG, and whether the bulk really has no contribution to the signals. Within the community, there is evidence showing that the interface is largely only the first layer of the functional group under interrogation and that the bulk response is negligible.[351] But arguably, these are questions that must be addressed on a system-by-system basis, as discussed in Section 1.3.1.7, and they are not easily answered. A lack of generality in data interpretation is particularly hindering for VSFG applied to thin film systems composed of arbitrary numbers of layers where there exist optical interference effects for all electromagnetic fields involved. In the case of oFETs, which are almost always multilayered, these

questions are prominent issues that we have focused on addressing with a generalized multilayer interference model.[372,397]

For any interface-specific nonlinear optical spectroscopy, the detected signal will depend on the local electric field amplitudes at each active interface as well as on the emitted waves, all of which are subject to thin film optical interference effects. For a system comprised of only a single thin film, the description of optical interference in VSFG data is tractable by considering the Fresnel formulas for reflection and transmission at interfaces. The problem is solved by considering infinite reflections and transmissions at the boundaries while accounting for phase offsets due to traversing the thin film layer.[21,359,361,362,432] However, for systems composed of more than a single thin film layer the expressions that describe optical interference very quickly become unwieldy as waves that transmit out of one layer may subsequently be reflected back in by other layers. For VSFG applied to an organic thin film within a multilayer system, the problem is further confounded by the presence of two very similar interfaces contributing to the same VSFG spectrum. Thus, every mode that appears in VSFG data from an organic thin film is potentially a result of at least two sources – the two interfaces of the organic – which must be separated.

Chapter 3 addressed modeling multilayer interference for interface-specific nonlinear optical spectroscopies by considering the transfer matrix formalism for thin film systems composed of arbitrary layers.[372] With this approach, the system is split at any layer into subsystems I and II and use partial system transfer coefficients to define reflection and transmission through each subsystem.[367] The model effectively reduces the multilayer problem to a single thin film (any layer in the system) with newly defined

coefficients of reflection and transmission at the pseudo-boundaries of subsystems I and II. The local and emitted fields are then calculated in a completely analogous way to the single thin film system described above.

Chapter 4 provided further efforts at tackling the two-interface and multilayer interference problem by detailing an extensive VSFG simulation analysis for the model system of this dissertation that is representative of a common oFET device geometry.[397] That chapter discussed the feasibility of quantifying molecular structure at the buried interface of an organic thin film by specifically considering the two-interface problem applied to the simplest multilayer, a system comprised of two thin films in which an organic layer is vapor deposited onto a thermally grown oxide dielectric on a silicon wafer substrate. By using the thin film interference model it was shown that the thicknesses of the thin films can have a profound effect on the detected signal intensity.[372,397] There was also a discussion on some of the possible issues that could be important when attempting to use the thin film model to separate the interfacial contributions in VSFG data. One uncertainty that remains is whether the detected signals are described within the electric dipole approximation. There are two complications that arise if higher order terms are appreciable. First, one must describe thin film interference effects contained in any possible bulk contributions, and second, we must separate the dipole terms from any higher order terms within the interfacial response.

The goal of this chapter is to present experimental evidence that the multilayer thin film model provides a good description of optical interference effects in VSFG spectra from thin film systems. The focus continues on the model system: the organic

semiconductor N,N′-dioctyl-3,4,9,10-perylenedicarboximide (PTCDI-C_8) vapor deposited as a thickness gradient on silicon wafer substrates (Figure 5-1). We focus on the imide symmetric (ν_s, ~1700 cm^{-1}) and asymmetric stretches (ν_{as}, ~1660 cm^{-1}). We present evidence that major features in the intensity data are predicted by interfacial response described by the multilayer model, indicating that the detected signal has significant interfacial contributions. Analysis of those results indicates some inconsistencies with what would be expected for response from this system within the electric dipole approximation. The multilayer model is then expanded to include terms that describe optical interference effects in possible bulk contributions and we present an analysis on the data based on inclusion of bulk and interfacial terms. From those results we reexamine the interfacial contributions. In particular, we consider effects from large interfacial field gradients and possible interfacial quadrupolar coupling terms and show that these higher order terms behave like dipole terms in the thin film system. Finally, we discuss some of the difficulties that must still be overcome and ways to improve upon this work in order to more quantitatively solve the two-interface problem of VSFG applied to organic thin film multilayer systems. The major contribution from this chapter is the experimental evidence that indicates the multilayer model provides a complete description of optical interference effects from interfacial as well as bulk terms, and that the thin film geometry offers a unique method to deduce relative contributions from the various VSFG source terms. We consider this a step towards interface-specific nonlinear spectroscopy becoming a viable and robust tool for studying interfaces in thin film systems.

5.2 EXPERIMENTAL

5.2.1 *Sample Preparation*

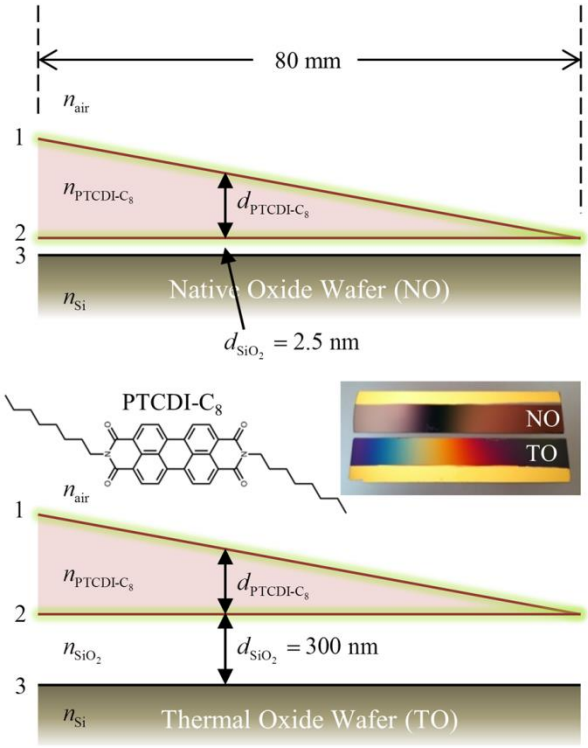

Figure 5-1. Schematic view of gradient samples on silicon wafers with two oxide thicknesses. Also shown is a the structure of PTCDI-C_8 and a photo of two bare SiO_2 samples used in this work illustrating different optical interferences present.

Sample preparation followed from Section 2.3 with some modification.[96] Substrates consisted of ~25 × 100 mm^2 silicon wafers cleaved from the center of 100 mm diameter, 0.5 mm thick, <100> wafers. Silicon wafers had either a polished native oxide (NO, Silicon Quest International) or polished 300 nm thermally grown oxide dielectric layer (TO, University Wafer). Briefly, all substrates were cleaned following the RCA cleaning procedure.[408,409] Standard clean 1 (SC1) consisted of a ~5:1:1 solution of distilled water/30%H_2O_2 in water/NH_4OH initially heated to 80 °C. Substrates were sonicated in SC1 for 5 minutes followed by distilled water rinse and

sonication. Standard clean 2 (SC2) consisted of ~50:1 solution of distilled water/concentrated HCl. Substrates were sonicated in SC2 for 5 minutes followed by distilled water rinse and sonication and were stored in distilled water until use. A ~5 mm strip of aluminum or gold was masked onto the long edge of each substrate by electron-beam vapor deposition. This provided reflectivity needed for the sample position monitoring system described below. For substrates that were modified with an trimethoxy(octadecyl)silane (ODTMS) self-assembled monolayer (SAM), we followed a spin-casting and vapor annealing procedure that gives a very smooth and well-ordered SAM[98] followed by masking on the metal strip. Finally, with the metal strips masked off, using a home built vapor deposition chamber[96] PTCDI-C_8 was deposited as a linear gradient using a programmable shutter that continuously moved back and forth over 80 mm of the length of the substrates during deposition. Substrates temperatures were held at 105 °C during deposition. Gradients were deposited pairwise for NO and TO substrates for bare and then ODTMS functionalized surface preparations. This resulted in wedged thickness gradients of PTCDI-C_8 that went from 0 to ~200 nm in the case of the bare substrates and 0 to ~400 nm in the case of the ODTMS functionalized substrates (Figure 5-1).

5.2.2 *VSFG Experiments*

The VSFG spectrometer was described in Section 2.3.5.1.[25] Briefly, the regeneratively amplified system (regen) outputs 40 fs (FWHM) pulses centered around 800 nm with 30 nm of bandwidth at 1 kHz for 1.7 W of power before compression. About 300 mW of this is spectrally filtered to 3 nm of bandwidth and used to seed a home built multipass amplifier followed by further spectral narrowing in a 4f pulse

shaper for use as the visible pulse in the VSFG experiment. Half of the 1.0 W compressed regen output is used to pump an optical parametric amplifier followed by difference frequency mixing of the signal and idler beams to give the mIR pulses used in the experiment. Typical visible beam characteristics are 6 ps (FWHM) pulses with 4 μJ/pulse centered around 798 nm with 7 cm^{-1} (FWHM) bandwidth. The mIR pulses were tuned to the imide carbonyl stretching region of PTCDI-C_8 and were typically 100 fs (FWHM) with 2 μJ/pulse centered at 1680 cm^{-1} and 150 cm^{-1} (FWHM) bandwidth. The mIR angle of incidence from normal was 56° and the visible was 65°. The optical system is enclosed in a sealed box and continuously purged with dry air (-100 °F dew point).

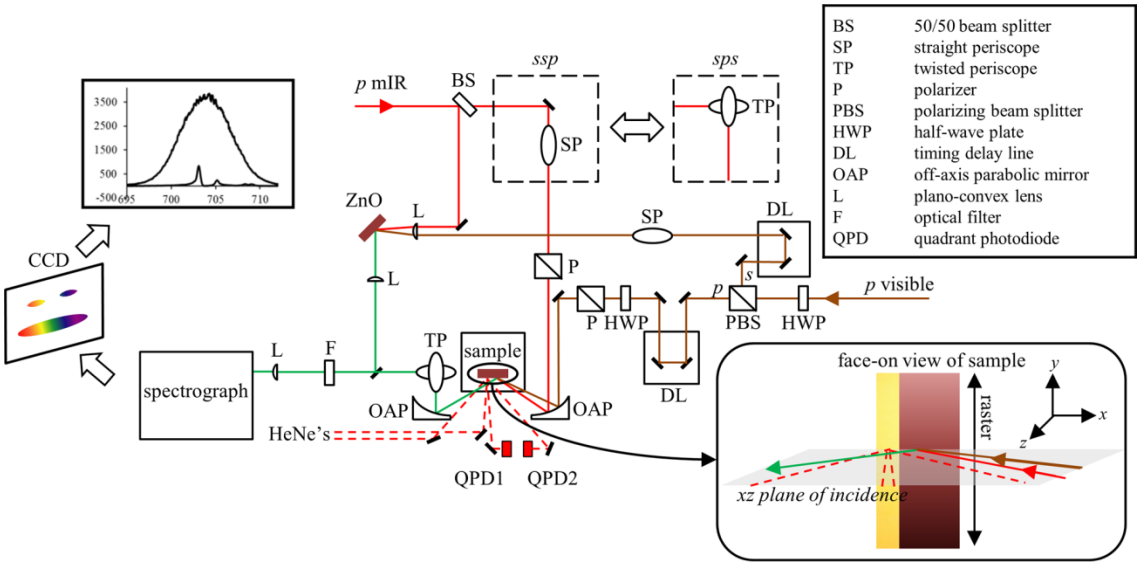

Figure 5-2. Schematic of VSFG experiment and data collection showing the sample leg and reference leg. Also shown is a face-on view of the gradient sample indicating beam placement and raster direction.

Both *ssp* and *sps* polarization experiments were performed (polarization in order of VSFG-visible-mIR). Rotating the mIR from *p*- to *s*-polarization was accomplished by replacing a turning mirror and straight periscope with a twisted periscope (Figure 5-2). The *ssp* data were collected for both bare SiO_2 samples followed by rotating the

polarization of the input beams to *sps*. The ODTMS surface functionalized samples were prepared later but adhered to the same VSFG data collection sequence. Each individual spectrum was obtained as an average of 5 data frames and 5 background frames with the mIR beam blocked. For *ssp* the CCD integration time on an individual frame was 6 minutes, for *sps* it was 10 minutes.

The VSFG experiments consisted of collecting spectra from a 1-dimensional raster along the length of each thickness gradient with step sizes of 1 or 2 mm (Figure 5-2). Thus, for a given gradient sample the total time for collecting the *ssp* data set was maximally 80 – 90 hrs, and for *sps* that time increased to 130 – 150 hrs. There were two main technical challenges involved in these experiments. The first was accounting for instability in the laser system over the many weeks and months of data collection. The second was accounting for pointing in the detection system as we translated 80-90 mm along the gradient.

In order to account for instability in the laser system, data collection consisted of a sample leg and reference leg simultaneously collected as vertically separated spectrally dispersed stripes on the CCD array (Figure 5-2). The input beams were split for use in each leg with the mIR split 50/50 and the visible split 20/80 with more power going to the gradient sample. The reference sample consisted of a 75 nm ZnO film deposited by atomic layer deposition onto a NO wafer. The reference VSFG spectrum was consistently *ssp* for both the *ssp* and *sps* sample experiments.[96] The beams were focused in each leg to around 100 μm 1/e radius spot size on the short axis of the projected spot ellipse. Temporal overlap was achieved by second order cross correlation of the input beams on a ZnO thin film in both legs with timing delays set to

0. Each data stripe was independently calibrated for wavelength. Sample spectra were then normalized by dividing by third order interpolation of the reference spectra.

To minimize walk-off in our detection system as we translated along each gradient we employed a sample positioning scheme that used two quadrant-photodiodes (QPDs) paired with two HeNe beams that reflected off the metal strip on each sample (Figure 5-2). One QPD monitored the beam at near-normal incidence and was used to correct twist and tilt of the sample plane. The other QPD monitored the beam at oblique incidence (~45° from normal) and was used to correct depth and assist with monitoring tilt. With motorized actuators on the xyz and twist/tilt degrees of freedom of the sample stage we were able to automate data collection and sample positioning along 50 mm of travel at a time using a custom LabVIEW interface. Automation consisted of an algorithm that used feedback from the QPDs to make sample plane corrections after automatically moving to a preprogrammed raster spot followed by shuttering off the QPD HeNe's for VSFG data collection. To sample the entire 80 mm gradient we used a manual linear stage and micrometer stack to translate to the unsampled region and continue data collection. The efficacy of the QPD positioning system was tested by monitoring the SFG spectrum of a ZnO reference sample and it was found to correct pointing to well within the tolerances of the detection system.

With a rasterized step size of 1 or 2 mm we can calculate the PTCDI-C_8 thickness step size. For bare substrates (~200 nm wedge over 80 mm) this results in thickness steps of about 2.5 or 5.0 nm, respectively. For ODTMS substrates (~400 nm wedge over 80 mm) the thickness steps were then doubled. Based on the spot sizes of the input beams we calculate the thickness differential to be no more than 1.0 nm (for

ODTMS gradients) within the area being sample for a given raster point along the gradient. Thus, we ignore the variation in thickness within a given measurement. This gave us excellent thickness resolution for our VSFG experiments.

The steps we took to account for the technical challenges associated with these experiments led to very reliable sample positioning and mostly reliable data normalization. We found that in particular, careful attention to maintaining the cleanliness of the reflective metal strip was important for the accuracy of the QPD positioning system, which was otherwise extremely robust. Normalizing by the reference spectra was in most cases reproducible when data were retaken after any adjustments and re-optimizations of the laser system. However, in some cases repeated datasets, which otherwise had the same spectral features, were sometimes not on the same absolute scale after reference normalization, differing by as much as a factor of 2 or more. Nonetheless, for a given gradient sample set, any fluctuations in the laser system were generally well accounted for by this scheme so that we are confident that each individual gradient dataset is at least largely self-consistent and the absolute scales among all sample datasets are nearly correct.

5.2.3 *Spectroscopic Ellipsometry*

Spectroscopic ellipsometry (SE) was performed on the thickest ends of the wedges in order to corroborate our QCM measurements. Data were collected in the spectral range of 700 to 1100 nm at 45°, 60°, and 75° angle of incidence. TO and NO data were simultaneously fit using known optical constants for air, SiO_2, and Si. We set the oxide thicknesses at constant values determined by several SE measurements on unique samples, with the ODTMS SAM adsorbed into the NO layer. The refractive

index of PTCDI-C_8 was modeled as isotropic and was tied to both TO and NO data. The resulting optical constants agreed with previous results for this material in this spectral range.[397] The thin film thicknesses are shown in Table 5-1. These were used in the multilayer VSFG model.

Table 5-1. Thin film thickness results from SE used in the VSFG multilayer model. Quantities in italics were fixed in the SE data fits.

	Bare		ODTMS	
	Oxide	PTDCI-C_8	Oxide + SAM	PTDCI-C_8
NO	*2.0*	202.7	*4.0*	406.3
TO	*295.0*	190.8	*295.0*	421.3

It should be noted that the quality of the fits to the SE data were reasonable for the 200 nm wedge (16.4 mean-squared error, MSE) and a bit lower for the 400 nm wedge (42.1 MSE). Efforts to improve the SE data fitting indicated that a graded index model and, to a lesser extent, optical anisotropy may be important; however, we found that the thickness results were consistent even when more complicated effects were introduced. There was high correlation between the resultant PTCDI-C_8 thickness and chosen oxide thickness so that it was necessary to constrain the oxide at estimated thicknesses based on previous measurements. The TO manufacturer stated that the thermal oxide was nominally 300 nm with up to 5% error. The value used is consistent with measurements on bare substrates and is well within the manufacturers stated error. Reporting these results is reasonable for the work considered here because the thickness results were only slightly different for more complicated models. Anisotropic effects may be important for future studies; however, the VSFG multilayer interference model assumes isotropic media. Extending the model to anisotropic systems is a future goal.

5.3 QUALITATIVE OBSERVATIONS

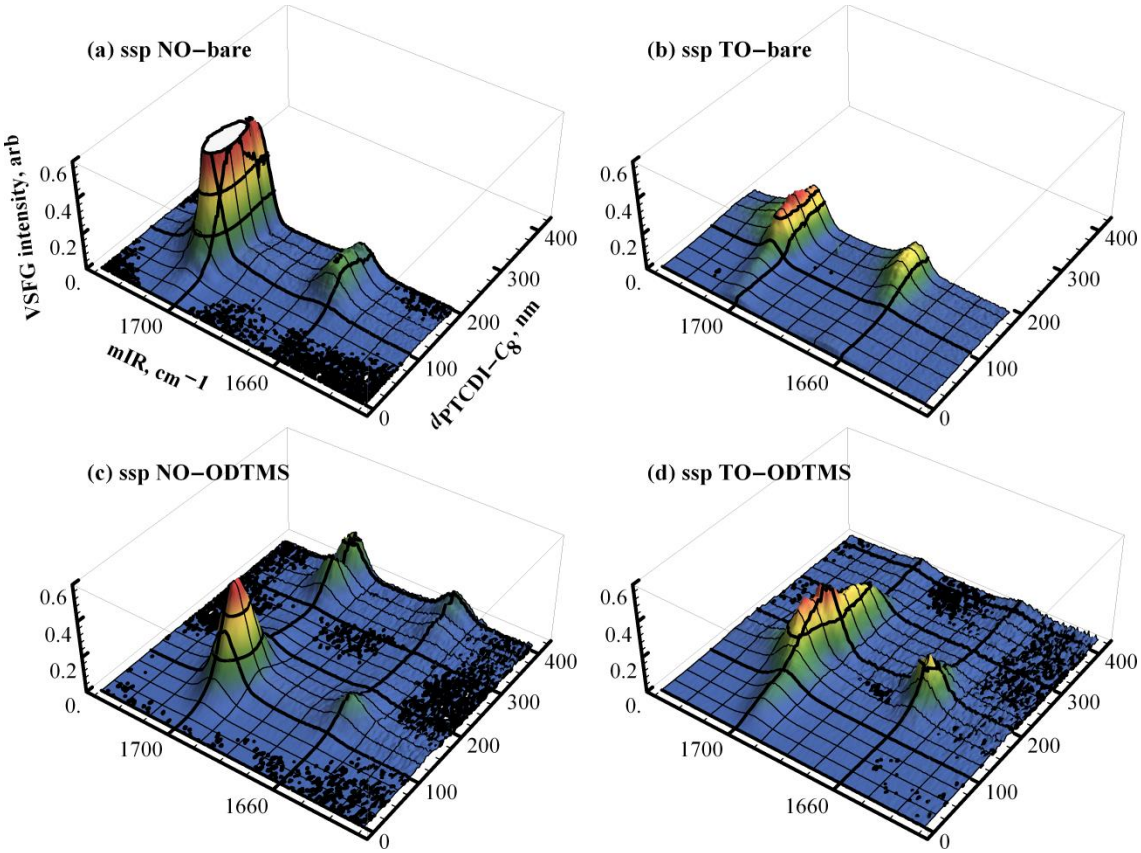

Figure 5-3. VSFG gradient experiment *ssp* results for bare substrates (first row) and ODTMS functionalized substrates (second row).

We begin by presenting the reference normalized *ssp* data for both surface preparations and oxide thicknesses in Figure 5-3. The data are all shown on the same scale with thicker gridlines for the major frame ticks drawn as well as thinner gridlines for the minor ticks from the dependent variables. The plot coloring is scaled to each individual dataset in order to bring out contrast within each plot. In all four cases, starting at 0 nm we see there is a dramatic increase in signal intensity with organic thickness for both imide modes and that the intensity peaks in the region of 120 – 200 nm PTCDI-C_8 for all datasets. The symmetric mode around 1700 cm^{-1} reaches a maximum that is larger than that of the asymmetric mode around 1660 cm^{-1} and the

symmetric mode maximum is significantly larger for NO substrates (Figures 5-3(a) and 5-3 (c)). The absolute scale for these datasets indicate that ν_s reaches a maximum peak at more than twice the intensity for NO substrate vs. TO for both surface preparations and that the maximum for ν_{as} is roughly the same in all cases. It is striking that in the data from ODTMS functionalized substrates (Figures 5-3(c) and 5-3(d)), where the gradient went to ~400 nm, we observe a second rise in the signal at the thickest end of the gradient (most apparent in Figure 5-3(c)).

There are clear differences in the response for both surface preparations indicate that functionalization of the substrate surface does have an effect on the thickness dependent VSFG response at thicknesses below 200 nm. For instance, ν_s reaches a larger maximum for NO-bare (Figure 5-3(a)) relative to ODTMS Figure 5-3(c)). A recheck of data from the bare substrates from Figure 5-3(a) (bare SiO_2 samples placed back in the laser system and the intense region measured for a second time) indicated that the relative signal intensities are real in this case and that ODTMS has lower overall signal as compared to bare native oxide. We have previously noted differences in overall signal intensities for these two surface preparations.[96] This is an early indication of the exquisite interfacial sensitivity of VSFG. A somewhat more subtle effect present in the data is an apparent frequency shift in the vibrational modes, both as a function of organic thickness (e.g. follow the gridline at 1700 cm^{-1} in Figure 5-3(d)) as well as in the frequency scales for bare relative to ODTMS substrates. That is, it appears that the mode maxima are blue-shifted in Figures 5–3(a) and 5–3(b) relative to Figures 5–3(c) and 5–3(d). Finally, we note that there is a perceptible vibrationally

nonresonant response that is most obvious in data from TO substrates (Figures 5–3(b) and 5–3(d) where the noise in the baseline below 200 nm generally does not cross zero).

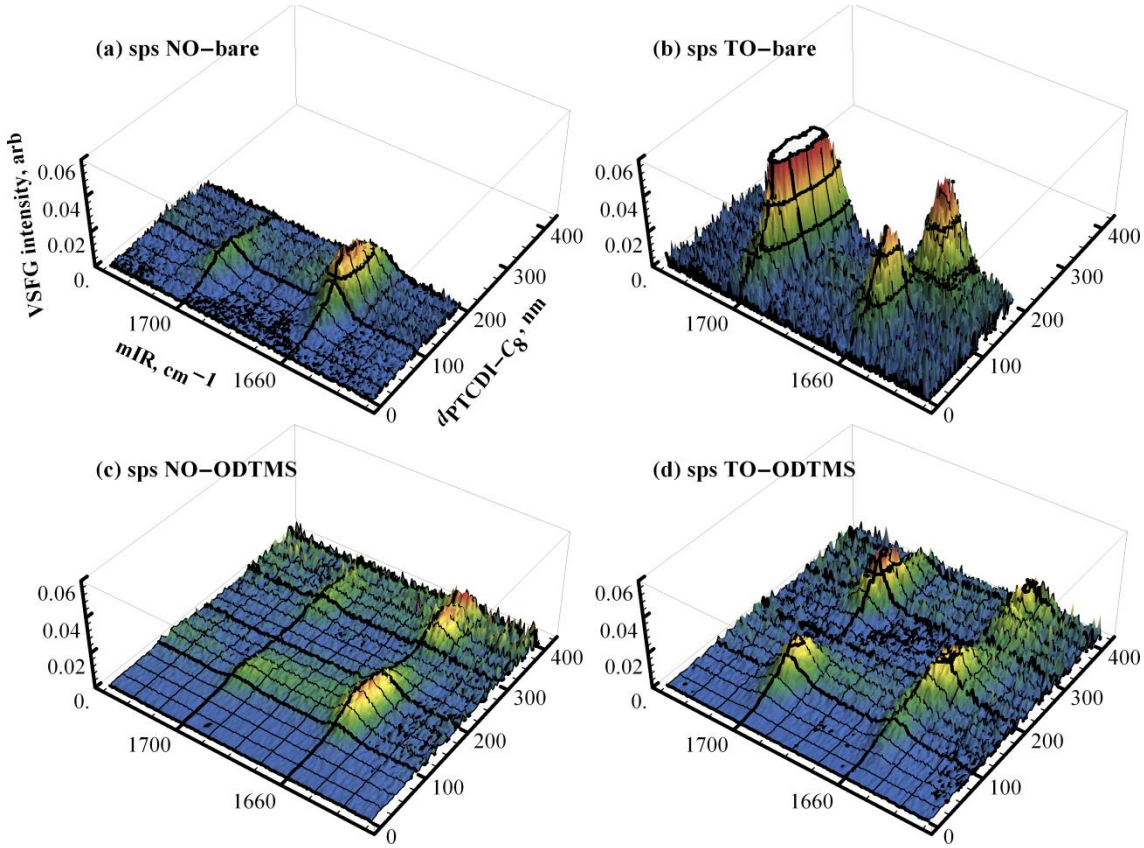

Figure 5-4. VSFG gradient experiment *sps* results for bare substrates (first row) and ODTMS functionalized substrates (second row).

The *sps* data are shown in Figure 5-4 where again, all data are on the same absolute scale but the plot coloring is scaled to each individual dataset in order to bring out contrast. Immediately we see the data are on a scale that is roughly an order of magnitude less intense than *ssp*. Again, each mode experiences a dramatic increase in signal from 0 nm but now the relative magnitudes between the symmetric and asymmetric modes are different. For instance, the maximum for ν_{as} is now larger for both surface preparations on NO (Figures 5–4(a) and 5–4(c)). Also, we see that ν_{as} shows two maxima in the 0 – 200 nm thickness range on TO-ODTMS (Figure 5-4(b)),

one around 70 nm and another around 170 nm, and actually dipping in the region that all other modes reach their maxima. This double peak is also apparent in the same thickness region of the data from TO-ODTMS in Figure 5-4(d), albeit to a lesser extent. There is also an apparent frequency shift with organic thickness for both modes, but is particularly evident for ν_{as}.

There were some common observations from the data in Figures 5–3 and 5–4. In most cases, the first peak maximum from ν_{as} occurs at slightly larger PTCDI-C_8 thicknesses relative ν_s. Noise in the data at the thickest ends of the wedges is due to difficulties with correcting for large fluorescence backgrounds. The signal intensities are generally lower for the ODTMS surface preparation relative to bare silica surfaces, which were obtained months prior. As noted in Section 5.2.2, there were some issues with maintaining consistent reference normalization over the many weeks of data collection so that the absolute scales in Figures 5–3 and 5–4 are only nearly correct. For instance, we have evidence from a rescan of a section of the data in Figure 5-4(b) that the maximum in ν_s should be nearer to the maximum for the same mode observed in Figure 5-4(b). In fact, the S/N in Figure 5-4(b) is comparable with all other datasets in the figure so that there was likely an issue with the reference spectra collected for this dataset. That is, the normalization procedure outlined in Section 5.2.2 resulted in dividing by reference spectra that were artificially smaller than the other gradient datasets. The *sps* data from TO-ODTMS contained the largest observed discrepancy in the absolute scale for all collected data. However, we will mitigate these technical difficulties in the following sections by introducing a scaling factor on the model for

each dataset that leads to very reasonable results. Finally, the oscillations in detected signal for both *ssp* and *sps* data are certainly reminiscent of thin film interference effects. Data obtained from the ODTMS substrates, where the wedge was ~400 nm at the thickest end, indicate more than a single oscillation in the response and provides some of the more compelling evidence of the necessity for an optical interference model for accurate interpretation.

5.4 DIPOLE APPROXIMATION

From our qualitative observations there is a clear dependence of VSFG signal intensities on organic film thickness as well as oxide thickness so that thin film interferences are playing a dramatic role in the observed signal intensity. From our calculations in Chapter 4[397] using the thin film interference model of Chapter 3[372] we predicted that optical interferences complicate data interpretation and that the thin film thicknesses could change signal intensity by several orders of magnitude, independent of any changes in the intrinsic VSFG response of the samples. The thin film interference model was derived under the auspices of the dipole approximation. In our simulations, we also discussed possible complicating factors that arise when using the thin film model to interpret experimental data. However, in this section we interpret the data assuming the ubiquitous selection rule for VSFG is valid and that the data are described predominately by the interfacial electric dipole response. We find evidence that, while interfacial terms are likely contributing significantly to the VSFG response, there are some discrepancies between the expected interfacial behavior and actual fit

results so that the dipole approximation may not provide a complete description of our data. We begin with a brief overview of the model.[372,397]

5.4.1 *Interfacial Thin Film Model Overview*

VSFG probes the sample susceptibility at interface *v* ($\vec{\vec{\chi}}_v^{(2)}$) and employs the vector nature of the interactions in order to deduce molecular orientation. The selection rules for VSFG on a macroscopically centrosymmetric system state that of the 27 elements of the third rank tensor $\vec{\vec{\chi}}_v^{(2)}$ there are only four nonzero and independent contributions: $\chi_v^{(2),xxz} = \chi_v^{(2),yyz}$, $\chi_v^{(2),xzx} = \chi_v^{(2),yzy}$, $\chi_v^{(2),zxx} = \chi_v^{(2),zyy}$, and $\chi_v^{(2),zzz}$.[22,236,237] These can be probed with four beam polarization combinations experimentally: *ssp*, *sps*, *pss*, and *ppp*. The work here utilizes the *ssp* and *sps* polarization experiments which sample the individual components $\chi_v^{(2),yyz}$ and $\chi_v^{(2),yzy}$, respectively. Within the dipole approximation, we can write the signal intensity ($I_0^{\alpha\beta\gamma}$) is then the modulus squared sum of VSFG contributions from each interface of the system.

$$I_0^{ssp} \propto \left| \left(\sum_{v=1}^{3} T_v^{yyz} \chi_v^{(2),yyz} \right) \vec{\bar{E}}_0^{\mathrm{vis},s} \vec{\bar{E}}_0^{\mathrm{mIR},p} \right|^2 \propto \left| \left(\sum_{v=1}^{3} T_v^{yyz} \chi_v^{(2),yyz} \right) \right|^2 I_0^{\mathrm{vis}} I_0^{\mathrm{mIR}} \tag{5.1}$$

$$I_0^{sps} \propto \left| \left(\sum_{v=1}^{3} T_v^{yzy} \chi_v^{(2),yzy} \right) \vec{\bar{E}}_0^{\mathrm{vis},p} \vec{\bar{E}}_0^{\mathrm{mIR},s} \right|^2 \propto \left| \left(\sum_{v=1}^{3} T_v^{yzy} \chi_v^{(2),yzy} \right) \right|^2 I_0^{\mathrm{vis}} I_0^{\mathrm{mIR}} \tag{5.2}$$

Each VSFG contribution depends on the interfacial second order susceptibility $\chi_v^{(2),ijk}$, an interfacial transfer product factor T_v^{ijk}, and the input field intensities $I_0^{\text{vis}} I_0^{\text{mIR}}$. Here, *i*, *j*, and *k* represent *x*, *y*, or *z*, and *α*, *β*, and *γ* represent *s* or *p* so that the transfer products account for the basis change from the propagating field *s* and *p* frame to the sample *x*, *y*, and *z* fixed reference frame in Figure 5-2. The product of T_v^{ijk} and $\chi_v^{(2),ijk}$ gives the electric field of light generated by a nonlinear polarization at interface *v* and propagated out of the thin film system and to the detector, i.e. $E_v^{ijk} = T_v^{ijk} \chi_v^{(2),ijk}$. Eqs. (5.1) and (5.2) coherently sum these contributions.

The transfer products describe all thin film optical interference effects. The details on their construction are provided in Chapters 3 and 4.[372,397] They are completely determined with knowledge of the input beam angles, thicknesses of all thin films, and optical constants for all materials. Oxide thicknesses were determined by SE and PTCDI-C_8 was assumed a linear gradient where we measured the thickest end by QCM during deposition and verified with SE. We use the frequency dependent refractive indices for all materials reported in Section 4.2.2 (see Figure 4-2).[397,434–438]

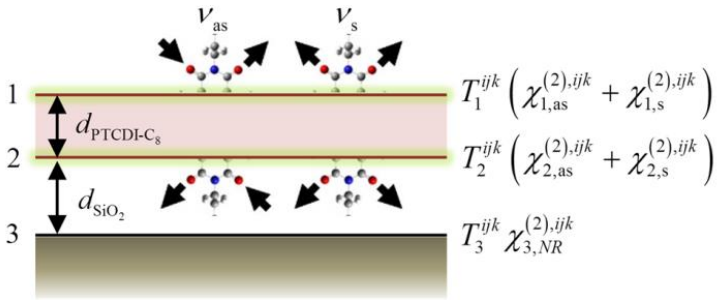

Figure 5-5. Graphical representation of the interfacial contributions to the VSFG intensity data.

Of the three interfaces of our system, we consider only vibrationally resonant responses from interfaces 1 and 2. We have not observed nonresonant response from

PTCDI-C_8 thin films themselves, therefore we attribute any possible vibrationally nonresonant contribution to interface 3 (SiO_2/Si). More will be said about the nonresonant susceptibility in Section 5.7.2. We have tuned to the imide symmetric and asymmetric stretching region of PTCDI-C_8. A graphical look at each possible contribution to the VSFG signal is shown in Figure 5-5. With our reference spectra normalization procedure detailed in Section 5.2.2, we effectively divide out the input field intensities so that we present intensity corrected data, $\hat{I}_0^{\alpha\beta\gamma} = I_0^{\alpha\beta\gamma} \Big/ \left(I_0^{vis} I_0^{mIR} \right)$. The intensity equations can then be written

$$\hat{I}_0^{\alpha\beta\gamma} = M \left| T_1^{ijk} \left(\chi_{1,\mathrm{as}}^{(2),ijk} + \chi_{1,\mathrm{s}}^{(2),ijk} \right) + T_2^{ijk} \left(\chi_{2,\mathrm{as}}^{(2),ijk} + \chi_{2,\mathrm{s}}^{(2),ijk} \right) + T_3^{ijk} \chi_{3,NR}^{(2),ijk} \right|^2 \tag{5.3}$$

where we consider the vibrational resonances as Lorentzian oscillators in the usual way.

$$\chi_{v,q}^{(2),ijk} = \frac{A_{v,q}^{ijk}}{-\left(\omega_{mIR} - \omega_{v,q} \right) - i\Gamma_{v,q}} \tag{5.4}$$

Here, $A_{v,q}^{ijk}$ is the amplitude of the q^{th} mode at interface v, $\omega_{v,q}$ is its center frequency, $\Gamma_{v,q}$ is its linewidth, and ω_{mIR} is the mIR input field frequency. The scaling factor M is discussed in what follows.

5.4.2 *PTCDI-C_8 Electric Dipole Response*

PTCDI-C_8 is a centrosymmetric molecule (see inset of Figure 5-1); therefore, in order for there to be a dipole-allowed response, the symmetry of the molecule must be somehow broken by the presence of the boundary. Interpreting the data within the electric dipole approximation requires consideration for response of the imide functional group separately at each end of the interfacial molecules. In the simplest

approximation, we may attribute any interfacial response to the imide functional group on the end of the molecules that point away from the bulk of the organic film at each of the air and SiO_2 boundaries. This is consistent with the known growth mechanism of PTCDI-C_8 on silica surfaces.[95,103] These are the truly interfacial modes and are depicted graphically in Figure 5-5. In this approximation, the two modes with which we are concerned serve as reporters of average molecular orientation. The imide symmetric and asymmetric stretches have orthogonal IR transitions that can be probed by *ssp* and *sps*, the relative response can be used to report on average tilt and twist of the perylene core of the interfacial molecules. This is shown graphically in Figure 5-6.

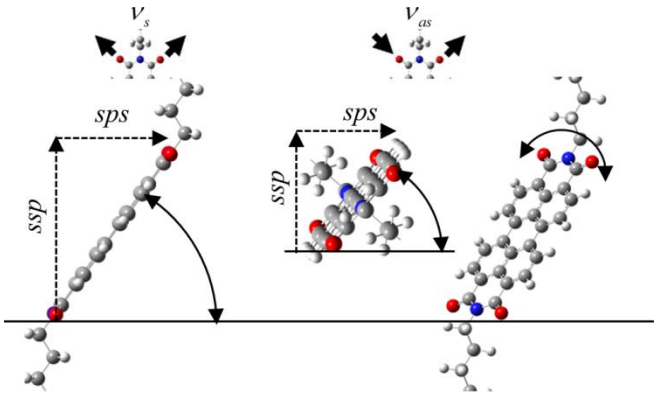

Figure 5-6. Graphical representation of the symmetric and asymmetric imide stretching modes as reporters for molecular orientation using the *ssp* and *sps* VSFG polarization combinations.

5.4.3 *Fit Details*

The system was designed to provide several ways to constrain the fitting routine in order to separate interfacial contributions and reveal differences at the buried interface for two substrate surface preparations, bare silica and ODTMS SAM. The foundation of the fitting routine is based on prior knowledge that the initial layer of vapor deposited PTCDI-C_8 may be different for different substrate surface preparations but every subsequent layer forms identically for bare and ODTMS substrates.[95] Thus, an overview of the routine is simple: for a given polarization experiment, every sample

should have the same response at the outer interface, and response at the buried interface should depend only on the surface preparation and not on the oxide thickness. Any nonresonant response will depend on the substrate (NO or TO), since these were purchased from separate vendors, but not on surface preparation. All other differences among datasets should be attributable to thin film interference effects and captured by the transfer products in Eq. (5.3).

For the measurements made here we note that, whereas the buried interfacial response should ideally not change, the outer contribution will vary with thickness. The growth mechanism of vapor deposited PTCDI-C_8 thin films proceeds in a Stranski-Krastanov fashion (layer-by-island growth) in which 2D polycrystalline terraces form and the outermost layers are incomplete islands with lateral dimension on the order of hundreds of nanometers to microns. Islanding at the outer interface results in an increased number of partial layers formed for thicker films.[95] The mesoscopic structural dependence on film thickness will certainly translate to increased surface roughness that will have an effect on the VSFG response. Thus, the outer interfacial VSFG contribution should be a function of organic thickness.

With the model presented in Section 5.4.1 and the discussion above, we present finer details of the fitting routine here. We simultaneously fit all four datasets for a given polarization combination (*ssp* and *sps*) to the model given in Eq. (5.3)and depicted graphically in Figure 5-5. Since we expect the outer response to vary with organic thickness but we have no *a priori* knowledge of how it should vary, we used a sequence of points along the $d_{\text{PTCID-C}_8}$ coordinate as fitting parameters connected by linear interpolation to describe the outer interfacial Lorentzian amplitudes ($A_{1,q}^{ijk}$ Eq.

(5.4)) for each mode. The parameters for the outer interfacial Lorentzians ($A_{1,q}^{ijk}$, $\Gamma_{1,q}$, and $\omega_{1,q}$ for ν_s and ν_{as}) were shared by all four datasets. The buried interfacial vibrational parameters were unique for both substrate preparations but shared between the two oxide thicknesses (e.g. bare NO and TO were locked to have identical response at the buried interface).

Since the absolute scales for all gradient datasets were determined to be only nearly correct (see Sections 5.2.2 and 5.3), a scaling factor (*M*) was included on the model (Eq. (5.3)) that was a unique fit parameter for each gradient dataset. Also, the data points were weighted during the fitting procedure so that residuals above 200 nm (where only ODTMS substrates contain data) had 0.5 relative weights in the nonlinear fitting algorithm. This was meant to reduce effects in the fit parameters due to fewer constraints and nonidealities in the film at the thickest ends of the 400 nm wedges.

A nonresonant contribution at the SiO_2/Si interface ($\chi_{3,NR}^{(2),ijk}$) was included only for the *ssp* experiment where there was an appreciable response present in the region of no organic film and that persisted at mIR frequencies outside of the vicinity of the vibrational modes along the wedge, especially for TO substrates (see e.g. Figure 5-3 where the noise in the baseline generally does not cross zero). The vibrationally nonresonant response was assumed far from any electronic resonances and was therefore a real number. We assigned values to the nonresonant susceptibilities for each substrate by fitting a region around 1740 cm^{-1} assuming the total SFG response is due to a nonresonant contribution at the Si–SiO_2 interface (only the last term in Eq. (5.3)). These were then held constant and included in the fit routine. We needed to account for

the scaling factors by dividing the static nonresonant factors by $\sqrt{M}$ while fitting for resonant parameters. More will be said about the nonresonant response in Section 5.7.2.

The interfacial modes are expected to be in the vicinity of the bulk modes; therefore we constrained the center frequencies during the fit routine based on the bulk properties. The FTIR centers have been assigned to 1696.5 cm^{-1} and 1655.6 cm^{-1} for the symmetric and asymmetric modes, respectively, based on reports in the literature and our own observations.[96,413] In the fitting routine, we then set restrictions on the interfacial contributions. The outer interfacial contributions were started equal to the FTIR centers but allowed to float in only the blue-shifted direction and restricted to be shifted by less than 10 cm^{-1}, consistent with a possibly less solvated environment (more gas-like phase) as would be expected for molecules in contact with air. The restriction for the buried interfacial modes is less clear since these are in contact with either SiO_2 or ODTMS. The consequences of differing surface preparations can manifest as differences in interfacial intermolecular interactions (different molecular packing) as well as different interactions with the substrate surface. Therefore, at the buried interface we limited the center frequencies to float only as large as 10 cm^{-1} in magnitude but in either the blue or red direction and independently for each surface preparation (but still identically for the same surface preparation on different oxide film thicknesses). The limited magnitude of each interfacial shift was necessary to keep the routine from sampling unphysical shifts while converging. The resulting shifts were never found to be settled at a limiting value.

Due to compounding errors from calibration at the VSFG and visible wavelengths, we estimate the error in the frequency axis to be ±4 cm^{-1}. The fitting routine is highly sensitive to errors in the wavelength axis and so we included a zero-order calibration correction in the form of frequency offset parameter (ω_{cal}) applied to the frequency axis of all resonant parameters. Since each substrate type (TO and NO) was run through data collection consecutively for each polarization experiment, we applied ω_{cal} pairwise to each substrate set but independently for each substrate preparation and polarization experiment (e.g. *ssp* from NO-ODTMS and TO-ODTMS shared this parameter).

The transfer products in Eq. (5.3) were completely determined knowing thin film thicknesses, input beam angles, and optical constants for all materials at all wavelengths of interest. We used the same refractive indices reported previously.[397] Thus, the VSFG intensities for each dataset in Figures 5–3 and 5–4 were fit with a fairly restrictive parameter set involving only the molecular responses (susceptibilities) and calibration corrections. It is important to emphasize that optical interference effects were calculated (not subject to any fit parameters) and that the amplitudes for the outer interfacial modes were all that were parameterized to vary with thickness.

5.4.4 *Fit Results and Discussion*

Contour plots for the data (top row) and fit results (bottom row) are shown in Figure 5-3 and Figure 5-4 for *ssp* and *sps*, respectively. The data and fits have been corrected by their respective fit result for M , and the wavelength axes have been adjusted relative to Figs. 3 and 4 based on the results for ω_{cal}. Figs. 9(a) and 9(b)

present a graphical look at the resulting imaginary parts of each Lorentzian used in the routine for each experiment and Figs. 9(c) and 9(d) show the fit amplitudes as a function of wedge thickness for the outer interfacial modes. The full sets of fitted parameters are presented in Table 5-2 for *ssp* and in Table 5-3 for *sps*. The tables give a clear indication of how parameters were constrained during the routine.

It is striking that the constrained model captures the major features in the experimental data. For the 200 nm wedges on bare SiO_2 in the first two columns of Figures 5–7 and 5–8 the model captures the single oscillation in intensity for ν_s around 1700 cm^{-1} and even captures the second oscillation found in the ~400 nm wedges on ODTMS surface preparations in the last two columns of the figures. Agreement between model and data for the peak intensity of ν_{as} around 1660 cm^{-1} is very good in the *ssp* experiment of Figure 5-7 and for TO substrates in the *sps* experiments of Figures 5–8(b) and 5–8(d), but is somewhat less well-behaved for NO substrates (Figures 5–8(a) and 5–8(c)). It is notable that the two peaks observed in the first 200 nm of *sps* data from TO for ν_{as} are described quite well by the fit result. The model even captures the behavior of the tails for both peaks in the outer regions of the modes. That is, it does a good job of describing the blue side of ν_s peak and the red side of the ν_{as} peak for both polarization experiments, even simultaneously satisfying the tail of ν_s for NO substrates where it extinguishes very quickly as well as on TO substrates where the tail remains quite large beyond the frequency window in the region of 100 – 200 nm. The behavior of the tails in the frequency space between the modes is captured

well for the *sps* experiment in Figure 5-8 but is less well-behaved in this region for the *ssp* experiment of Figure 5-7.

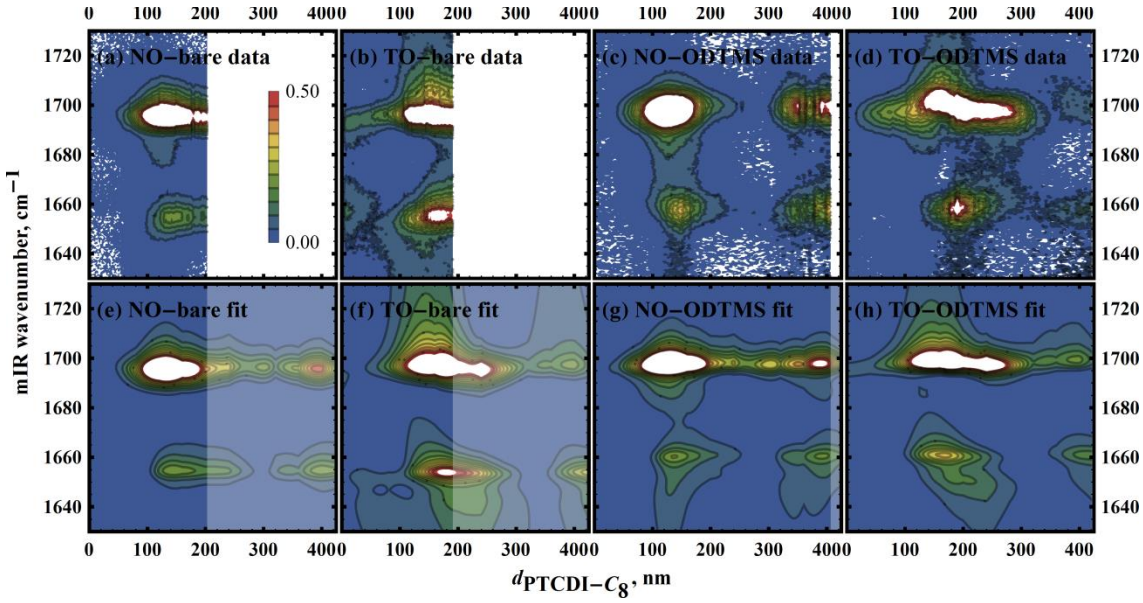

Figure 5-7. *ssp* data (a) – (d) and fit result (e) – (i) plots from modeling with interfacial contributions. Data and model plots have been scaled by the resulting *M*-factors from the routine.

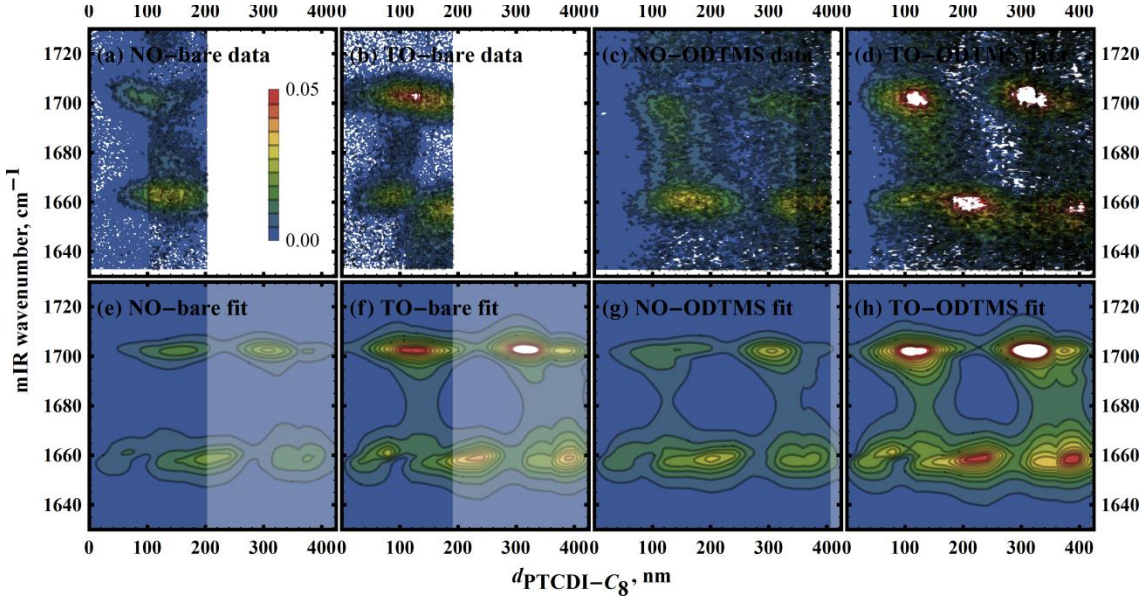

Figure 5-8. *sps* data (a) – (d) and fit result (e) – (i) plots from modeling with interfacial contributions. Data and model plots have been scaled by the resulting *M*-factors from the routine.

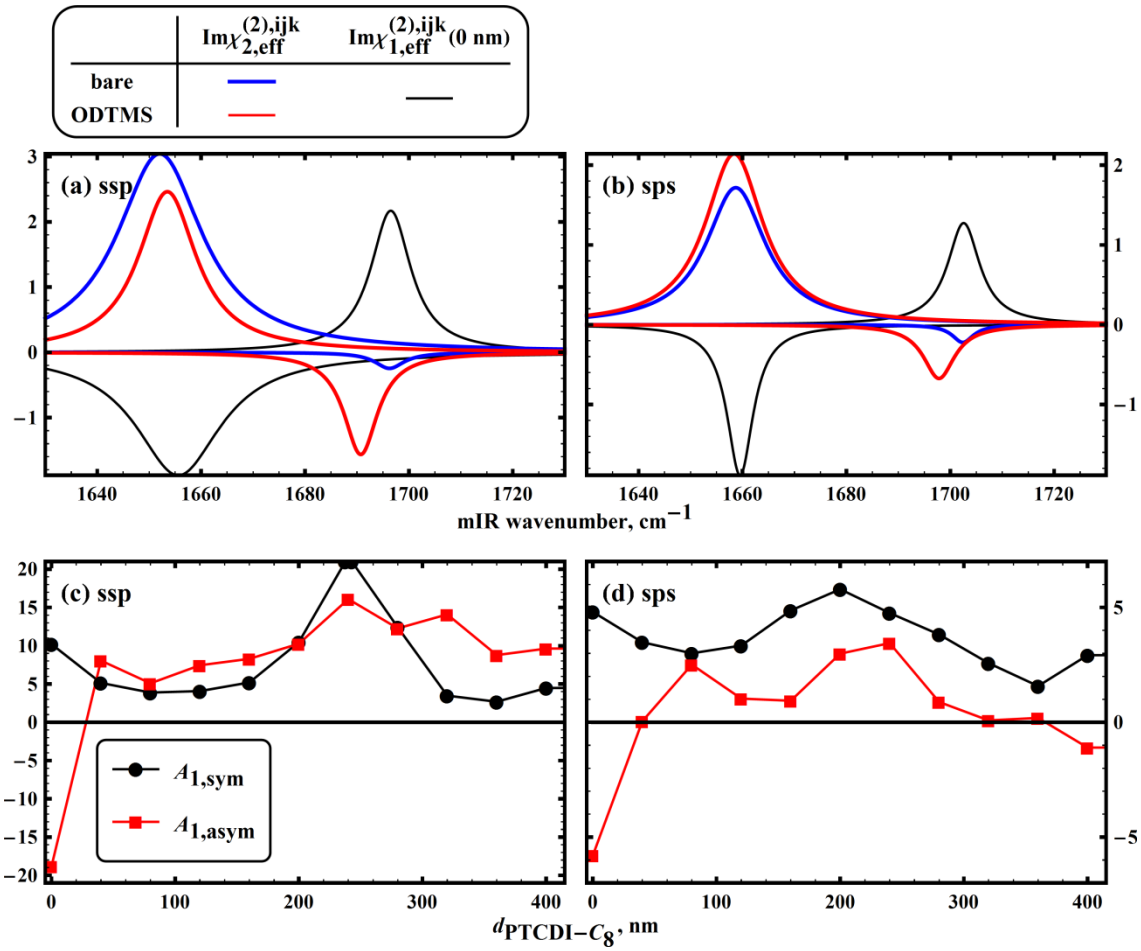

Figure 5-9. Graphical view of parameter fit results. (a) and (b) show the imaginary components for each Lorentzian used in the routine and (c) and (d) present the resulting amplitude dependence on organic thickness for the outer interfacial modes.

Table 5-2. Full parameter fit results for the *ssp* experiment. Quantities in italics indicate static parameters (not floated).

			NO	TO	NO-ODTMS	TO-ODTMS
		ω_{cal}	-8.1		-1.0	
		$\chi^{(2),yyz}_{3,NR}$	*-1.3*	*8.1*	*-2.3*	*5.0*
		M	*1*	0.30	0.40	0.40
ν_s	$\chi^{(2),yyz}_1$	ω	*1696.5* + 0.0			
		Γ	4.7			
	$\chi^{(2),yyz}_2$	ω	*1696.5* – 0.2			
		Γ	3.4		4.0	
		A	-0.8		-6.2	
ν_{as}	$\chi^{(2),yyz}_1$	ω	*1655.6* + 0.0			
		Γ	10.0			
	$\chi^{(2),yyz}_2$	ω	*1655.6* – 3.6			
		Γ	10.0		6.8	
		A	30.4		16.8	

Table 5-3. Full parameter fit results for the *sps* experiment. Quantities in italics indicate static parameters (not floated).

			NO	TO	NO-ODTMS	TO-ODTMS
		ω_{cal}	2.9		2.5	
		M	*1*	1.9	0.43	0.36
ν_s	$\chi^{(2),yzy}_1$	ω	*1696.5* + 6.1			
		Γ	3.8			
	$\chi^{(2),yzy}_2$	ω	*1696.5* + 5.9		*1696.5* + 1.3	
		Γ	2.5		3.6	
		A	-0.55		-2.5	
ν_{as}	$\chi^{(2),yzy}_1$	ω	*1655.6* + 3.9			
		Γ	3.1			
	$\chi^{(2),yzy}_2$	ω	*1655.6* + 3.1		*1655.6* + 2.8	
		Γ	7.0		6.8	
		A	11.9		14.5	

While the *differences* between ν_s and ν_{as} dependence on the $d_{\text{PTCDI-C}_8}$ coordinate are due partially to the frequency dependent transfer products T_v^{ijk} within each $T_v^{ijk}\chi_{v,q}^{(2),ijk}$ term in Eq. (5.3) (due to slightly different optical constants and wavelengths) the major contribution is the unique response $\chi_{v,q}^{(2),ijk}$ for each mode. The periodicities are in some cases very similar, as in Figure 5-7(a) – (c) and Figure 5-8(a) and (c) or may be very

different as in the remaining data plots. It is important to point out that each polarization experiment fit was constrained by shared parameters so that all cases, whether the periodicities were similar or different between modes, were simultaneously satisfied by common outer interfacial contributions for every wedge sample and common inner contributions for each surface preparation.

Differences in the periodicities for each mode within a given dataset are expected since each mode should have unique contributions to the source terms from the two interfaces of the organic film; however, the apparent frequency shifts present in the plots are less intuitive. For example, there is an apparent red shift for both modes in Figure 5-8(b). At first glance these may be interpreted as a shift in an oscillator's intrinsic center frequency or perhaps a change in line width, presumably at the outer interface, accompanied by thickness dependent interferences. But recall that all resonant responses $\chi_{v,q}^{(2),ijk}$ were modeled as having constant $\omega_{v,q}$ and $\Gamma_{v,q}$ so that our results indicate that these observations are due to interferences between two interfacial contributions that have different (but constant) center frequencies and line widths. Again, cases in which there were large apparent frequency shifts were simultaneously satisfied with cases where the shifts were smaller even with the constraints imposed by shared parameters in the fitting routine. The conclusion is that although there may be some amount of change in center frequencies or line widths at the outer interface that is not quantified here, the majority of the observable differences in response from the two modes on each substrate can be attributed to the interferences that occur between the

interfacial $T_v^{ijk}\chi_{v,q}^{(2),ijk}$ terms. Although they are complicated and not always intuitive, these effects are captured by the multilayer interference model.

The fit parameter results are shown graphically in Figure 5-9 and presented in Table 5-2 and Table 5-3 for *ssp* and *sps*, respectively. From the plots of $\mathrm{Im}\left(\chi_{v,q}^{(2),ijk}\right)$ in Figure 5-9(a) and (b) it is interesting that these results indicate the order of magnitude difference in maximum signal intensity from the *ssp* vs. *sps* measurements is *not* primarily due to the intrinsic sample response (the elements of the susceptibility tensor $\vec{\vec{\chi}}^{(2)}$) since the imaginary components are all of similar magnitudes for both polarization experiments in Figure 5-9(a) and (b). Instead, it is the transfer products that result in the lower signal for *sps* measurements. We showed in Chapter 4 that optical interference effects have very different behaviors for different polarization experiments.[397] Also, results for the *M*-factors in both tables are reasonable and consistent with what we expected the intensity scale corrections should be based on our experiences during data collection. For instance, in both tables the results for bare substrates differ by a factor of 2 – 3 whereas *M*-factors for ODTMS substrates are very similar. This is consistent with the higher number of technical difficulties we experienced in our first occurrence of data collection that was on the bare substrates in contrast with the experiment applied to the ODTMS wedges after the technical details had been refined.

The physical interpretation of the interfacial contributions from the fit results presents some important consequences. From the discussion in Section 5.4.2, for *ssp* we interpreted a larger relative response from ν_s as corresponding to molecules with the

long axis of the perylene core standing more upright on average, and for ν_{as} we interpret larger contributions corresponding to more tilt along the short axis. It is the opposite for the *sps* results. Thus, a qualitative analysis of the buried interfacial results in Figure 5-9(a) and (b) indicate that the first monolayer of PTCDI-C_8 on bare SiO_2 lies flatter along the long axis of the perylene core but is standing more upright along the short axis (i.e. there is more twist of the perylene core) relative to ODTMS functionalized substrates. That is, the magnitude of the *ssp* contribution from the symmetric mode is much larger for the ODTMS substrates and the magnitude of the asymmetric mode is largest for the bare SiO_2 substrates and vice-versa for the *sps* results (with one exception, the *sps* result for ν_s). This is consistent with previous reports that the interfacial organic thin film phase is different and more reclined on SiO_2 relative to ODTMS treated substrates.[95,103] The result that the ν_s contribution is lower at the buried interface for both polarization experiments is an indication of more disorder for PTCDI-C_8 in contact with the higher energy surface. It is noteworthy that a recent study from our group came to the same conclusion for polythiophene ring ordering at high and low surface energy silica dielectrics.[456] This same analysis for the outer interfacial modes is a bit more complicated due to the thickness dependent mode amplitudes.

The fit results for the outer modes indicate a complicated dependence on the organic thickness and so we split the analysis into regions. At the thinnest end of the wedges from 0 to ~120 nm, the outer amplitude fit results for the symmetric mode in Figure 5-9(c) and (d) (black) exhibit an asymptotic change, where $\left|A_{1,q}^{ijk}\right|$ starts largest

and decreases rapidly to a constant or very slowly changing value that is consistent for both the *ssp* and *sps* results. This result can be rationalized by considering how the orientational distribution of molecules may change with increased organic thickness. There are numerous studies of PTCDI-C_8 and its derivatives that indicate the mesoscopic morphology at the outer interface varies significantly and becomes more rough from the initial monolayer up to thicknesses of 100 nm or more[95,103,457] and our own observations from AFM in Chapter 2 are consistent with those reports.[96] Thus, for the symmetric mode the fit results are consistent with broadening of the polar orientational distribution, resulting in less VSFG signal for both polarization experiments. However, we cannot separate broadening effects from changes in the average orientation. The asymmetric mode results indicate a similar phenomenon, and while the fit results in Figure 5-9(c) and (d) (red) show asymptotic behavior in the first 100 nm as well; there is also a *sign change* within the first 20 – 40 nm of the wedge for both *ssp* and *sps*. More will be said about relative signs after we discuss results for the thicker end of the wedges.

Beyond 120 nm the outer mode amplitudes tend to increase to a peak at around 200 – 300 nm followed by a decrease back down to a continuation of the trends observed in the first 100 nm. This result is especially pronounced for the *ssp* results in Figure 5-9(c) but is also discernable for the *sps* result in Figure 5-9(d). There are many possible effects contributing to this result, some of which will be discussed in Section 5.7, however we interpret this as our first indication that the *interfacial* model used in this section may not provide a complete description of our data.

The relative sign of $\mathrm{Im}\left(\chi_{v,q}^{(2),ijk}\right)$ at each interface can be used to deduce relative polar orientation, i.e. on average functional groups point either "up" or "down".[22,397] From the discussion in 5.4.2 we determined that the electric dipole response of PTCDI-C_8 should result in opposite signs for each mode at each interface since we take for the interfacial modes the imide carbonyl groups on the end of the interfacial molecule pointing away from the organic film (see Figure 5-5). This is indeed the result in all cases for both modes at the thinnest end of the wedge as is clearly evident in Figure 5-9(a) and (b). However, the sign change on the outer interfacial amplitude for ν_{as} in Figure 5-9(c) and (d) suggests that somehow the outer asymmetric mode changes its relative polar orientation at the outer interface. In our analysis of the possible electric dipole response of PTCDI-C_8, this is clearly impossible since it is a centrosymmetric molecule. That is, from our discussion Section 5.4.2, even if the mode that is active and in contact with air at the thinnest end of the wedge becomes completely flat at some thickness and then rotates toward the bulk organic film, the imide functional group on the other end of the molecule should become the "new" interfacial mode, retaining the same relative polar orientation (the sign should not change). The result that ν_{as} changes sign with organic thickness is the second piece of evidence we have that suggests the electric dipole approximation may not be appropriate for this system.

A significant effort was put forth to produce a fit result that was physically more reasonable and that produced quality fits. This included efforts to rectify the evidence against the electric dipole approximation by tying parameters together in various ways or providing several different sets of starting parameters. However, we found that even

with constraints imposed by shared parameters, there were still some problems with parameter correlations so that an absolute minimum in the fit residuals could not be found. For instance, we could start the amplitude signs for each mode (outer and inner for both symmetric and asymmetric) in various ways and the fitting routine would not minimize to a unique position in parameter space. In particular, the signs of the oscillator amplitudes combined with the sign chosen to start each nonresonant contribution would generally result in marginally different parameter results. We could gain model agreement in some areas of the data plots while losing it in other areas. Also, it was necessary to constrain the mode widths to a physically reasonable range of 2.5 – 10 cm^{-1}. In Tables 5–2 and 5–3, we see that almost all modes floated to a value within this range, with the exception of $\Gamma_{1,as}$ and $\Gamma_{2,as}$ (width of ν_{as} at each interface) in the *ssp* result, which floated to the maximum of that range, and $\Gamma_{2,s}$ (width of ν_{s} at the buried interface), which floated to the minimum. The mode widths should likely be within the specified range and the current result is related to problems with accounting for a vibrationally nonresonant contribution, which was especially prevalent in the *ssp* data. We discuss the issue of the nonresonant response in detail in 0. Even with these difficulties, it is important to stress that other approaches always resulted in fit qualities as good as or worse than presented here and that the two major results – that there is a sign change in the asymmetric mode outer amplitude and that the outer amplitudes have maxima in the vicinity of 200 – 300 nm – were typical in most of our results.

Specific efforts to improve the fit routine for the outer interfacial amplitudes included attempting to better constrain the thickness dependent responses by parameterizing them with physically reasonable functions (e.g. exponential, root).

However, when the outer interface mode amplitudes were constrained to behave asymptotically across all thicknesses, agreement between model and data was significantly diminished. We present the response as a series of points connected by linear interpolation because it provided the most reliable and consistent results and provides some evidence that the interfacial model may not be a complete description of our system.

The scope of this section has been to provide experimental evidence that the interfacial thin film model provides a good description of optical interferences in VSFG data from multilayer thin film systems and that optical interference effects described by our interfacial model play a substantial role in the detected VSFG signal intensity, implying that interfacial contributions are significant. This is certainly indicated for thicknesses lower than 200 nm. From this we have some evidence that, while interfacial terms are likely playing a substantial role in the VSFG response, there are some results that are potentially inconsistent with the electric dipole approximation. While there are many possible other effects present in the data that we have not considered at this point (some of which will be discussed in Section 5.7), and parameter correlations certainly complicated the fit routine, the next logical step to improve the model is to go beyond the electric dipole approximation and consider higher order terms. The next highest terms are described by fourth rank tensors, which lead to the possibility for vibrationally resonant contributions from the bulk of the organic film.

5.5 BULK CONTRIBUTIONS

The description of VSFG within the electric dipole approximation is an idealization that has prompted considerable deliberation.[171,234,373,391] Separating the intrinsic interfacial (electric dipole allowed) response from possible higher order contributions, both interfacial as well as bulk terms, is a topic that impedes VSFG data interpretation and is a large barrier for nonlinear surface techniques to becoming truly standard surface analytical tools. The optical interference model was derived assuming the electric dipole allowed response, inclusion of higher order interfacial as well as bulk terms have not been considered at this point. In this section we introduce a framework for analyzing bulk terms by extending the thin film model and then apply it to our data analysis.

While the electric dipole approximation analysis of the data certainly indicates the presence of large interfacial contributions, the discrepancies in the fit result with the data signify an incomplete model for the observed signals. The difference may be due to several causes, but in particular the natural next step is to consider higher order terms, which invariably leads to the possibility of VSFG signal terms generated in the bulk of the organic film. Phase matching for wave-mixing through bulk-allowed materials is known to undergo phase modulations that cause the detected signal intensity to oscillate with thickness.[117] However, these oscillations occur when the thicknesses are much larger than the wavelengths involved, which is not the case for our thin film system. Further, the well-known oscillations in signal intensity for wave-mixing through the bulk (i.e. Maker's fringes discussed in Section 1.3.2.4) are due to phase mismatch – a fundamentally different phenomenon than thin film optical

interference effects. Therefore, a new approach to describing bulk contributions that includes effects from the thin film geometry is necessary.

The lowest order bulk-allowed sum frequency terms are described by electric quadrupole and magnetic dipole coupling of the input fields to the nonlinear source electric dipole polarization as well as coupling of the quadrupolar and magnetic dipolar nonlinear polarization to emitted fields (see Section 1.3.2.5 for a more complete account of higher order terms).[235] We ignore magnetic interactions and begin by considering only electric quadrupole interactions with the input fields. Later, we will consider coupling to the electric quadrupolar polarization. In this case, we add to Eq. (5.3) a bulk generated electric field term.

$$E_{bulk}^{(2),\alpha} = \int_{d_{PTCDI-C_8}} \left[T_{Q_{vis}}^{ijlm}(z)\,\chi_{Q_{vis}}^{(2),ijlm} + T_{Q_{mIR}}^{ijlm}(z)\,\chi_{Q_{mIR}}^{(2),ijlm} \right] dz \tag{5.5}$$

Eq. (5.5) is integrated over the organic thickness and the two integrands correspond to quadrupolar coupling with each of the visible and mIR input beams. Interactions of this sort are described by fourth rank susceptibilities and transfer products. Quadrupolar coupling with an input beam corresponds to interaction with the spatial variation (gradient) of that field. Thus, the fourth rank transfer products are defined similarly to those of Eqs. (5.1) and (5.2) with the spatial derivative taken on the appropriate transfer coefficient.

$$T_{Q_{vis}}^{ijkm} = \vec{t}_{z,0,(i,\alpha)}^{VSFG} \left[\frac{\partial \overleftarrow{t}_{0,z(\beta,j)}^{vis}}{\partial m} \right] \overleftarrow{t}_{0,z(\gamma,k)}^{mIR} \tag{5.6}$$

$$T_{Q_{mIR}}^{ijkm} = \vec{t}_{z,0,(i,\alpha)}^{VSFG} \overleftarrow{t}_{0,z(\gamma,k)}^{vis} \left[\frac{\partial \overleftarrow{t}_{0,z(\beta,j)}^{mIR}}{\partial m} \right] \tag{5.7}$$

The transfer coefficients are defined as the ratio of the field amplitude at one position in the thin film system to the amplitude at another position. In particular, for the input field transfer coefficients, they are defined as

$$\overleftarrow{t}_{0,z(\gamma,k)}^{vis/mIR} = \frac{E_z^{vis/mIR,k}}{\overleftarrow{E}_0^{vis/mIR,\gamma}} \tag{5.8}$$

where the notation in the ratio indicates the total field amplitude *k*-component (*k* is *x*, *y*, or *z*) at position *z* within the thin film system ($E_z^{vis/mIR,k}$) scaled by the γ-polarized (γ is *s* or *p*) input field as it encounters the system ($\overleftarrow{E}_0^{vis/mIR,\gamma}$). The transfer coefficients describe all thin film interference effects for each field in the VSFG experiment at position *z* within the organic film and account for the basis change from propagating fields (*s*- and *p*-polarization) to the sample *xyz* frame (this is denoted by dummy indices within parenthesis in the subscripts). They are built from the thin film model (Chapter 3) and discussed in the VSFG simulation work (Chapter 4).[372,397] Of primary importance here is that they may be computed and therefore the derivatives may also be computed. From a technical standpoint, they are calculated using the thin film model by splitting the organic layer into two thin films at position *z* and considering a three-layer system (PTCDI-C_8 – PTCDI-C_8 – SiO_2) where we compute the transfer coefficients at the organic-organic boundary in a completely analogous way to how they are computed for the material interfaces. The expression for the total transfer product can be integrated in Eq. (5.5) over all possible *z*-positions through the PTCDI-C_8 layer thickness to arrive at the total bulk contribution that makes it out of the system in the direction of the detector. In practice, we numerically evaluated the integral for all thickness ranges in 1 nm steps and across all relevant frequencies in 2 cm^{-1} steps. These

tables were used to construct third order interpolation functions for the real and imaginary parts of each quadrupolar transfer product, which evaluate much faster than the numerical integrations. Before we analyze the form of the total bulk transfer product, we will discuss the possible nonzero components and distinctive features of the individual input beam quadrupolar transfer coefficients.

5.5.1 *Input Field Quadrupole Coupling Transfer Coefficients*

Using symmetry arguments for isotropic media, it can be shown that of the 81 elements of the quadrupolar susceptibilities only three are independent and nonzero[374] and that the *ssp* and *sps* polarization combinations each sample only one of those, $\chi_Q^{(2),yyzz}$ and $\chi_Q^{(2),yzyz}$, respectively. The result is that quadrupolar coupling with each input field is possible only with spatial field variation in the *z* direction. Field derivatives with respect to the sample normal, however, are complicated by the thin film geometry.

In nondissipative and semi-infinite media, the input field amplitude has a spatially varying phase and a constant magnitude (or exponentially decreasing in absorbing media) and can be expressed as $E(z)=|E|\exp(ik_z z)$ to within a constant phase factor (dissipation can be included by allowing the wavevector component $k_z = 2\pi n\cos(\theta)/\lambda$ to be complex). However, the presence of the thin film system leads to field magnitudes that vary within each layer and the variation depends on the total system geometry (again to within a constant phase factor).

$$E(z)=|E(z)|\exp(ik_z z) \tag{5.9}$$

The result of differentiation is then

$$\frac{\partial E(z)}{\partial z} = \left[ik_z \left| E(z) \right| + \frac{\partial \left| E(z) \right|}{\partial z} \right] \exp(ik_z z) \tag{5.10}$$

For signal from single interface systems (e.g. systems where VSFG is measured from the interface of an otherwise bulk medium such as an organic solvent) the possible bulk contribution considers only the first term in brackets in Eq. (5.10) since the field magnitude is constant ($\partial_z \left| E(z) \right| = 0$) within any semi-infinite nonlinear medium.[351,374] To highlight this important distinction between single interface systems and multilayer thin film systems we can plot both $\left| E(z) \right|$ and $\partial_z \left| E(z) \right|$ through the thin film stack for both input beams. We will present our results in terms of the dimensionless input field transfer coefficients (Eq. (5.8)).

Figure 5-10 shows results for the input fields in the *ssp* experiment. The input field spatial profiles through the thin film system are plotted for the *y*-component of the visible (from the *s*-polarized input field, black traces) and the *z*-component of the mIR (from the *p*-polarized input field, red traces) for both NO substrate (Figure 5-10(a) – (d), $d_{SiO_2} = 2$ nm) and TO substrate (Figure 5-10(e) – (h), $d_{SiO_2} = 300$ nm) and several organic thicknesses ($d_{PTCDI\text{-}C_8} = \{50, 100, 200, 400\}$ nm). The plots show $\left| \tilde{t}_{0,z} \right|$ (solid lines), $\partial_z \left| \tilde{t}_{0,z} \right|$ (dashed lines), and the magnitude of the ratio of each term contributing to quadrupolar coupling in Eq. (5.10) $\left| \partial_z \left| \tilde{t}_{0,z} \right| \Big/ \left(ik_z \left| \tilde{t}_{0,z} \right| \right) \right|$ (dotted lines). The calculations were performed using the experimental details presented in Section 5.2.2 with the visible wavelength taken at 798 nm and the mIR frequency at 1680 cm^{-1}.

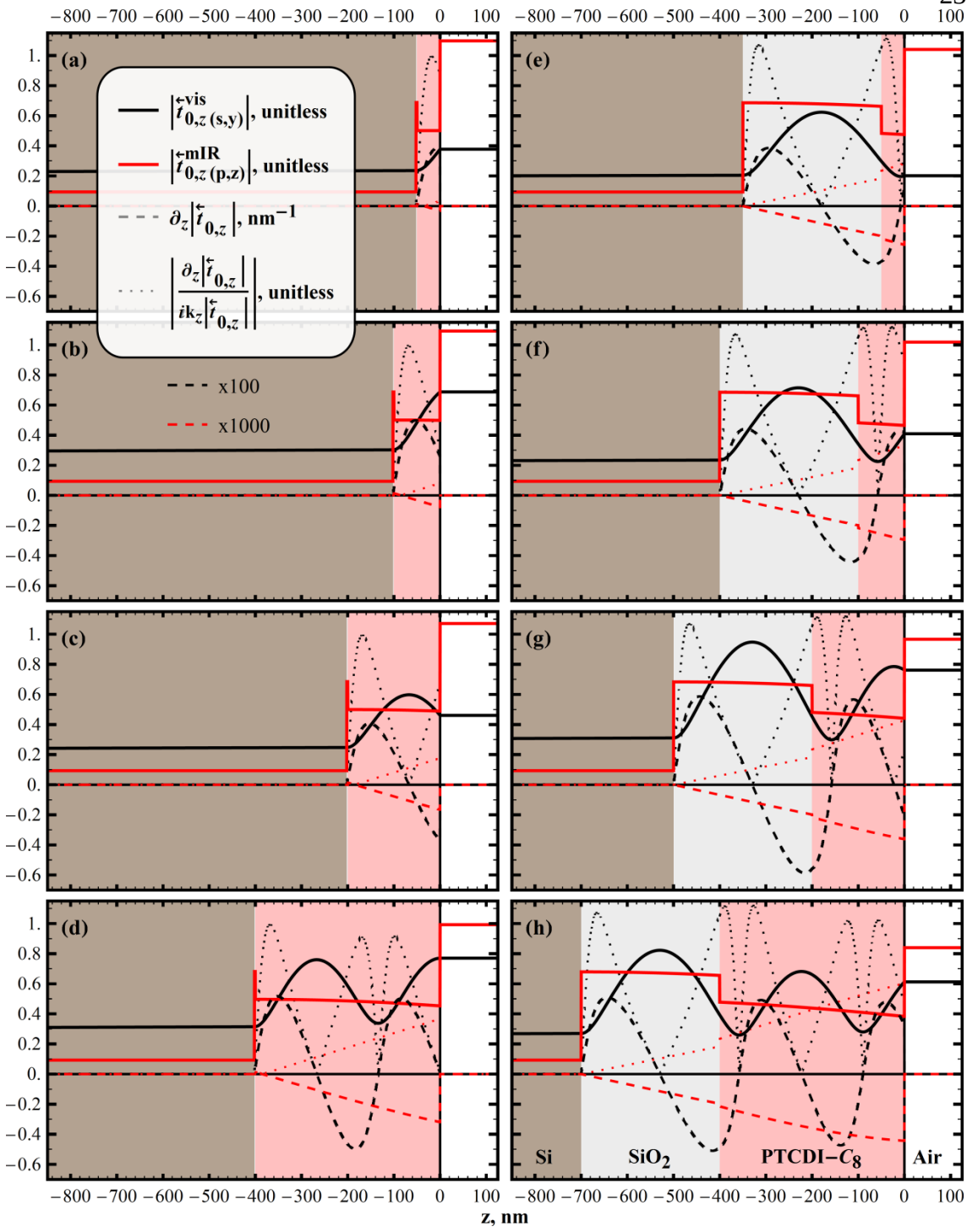

Figure 5-10. Plots showing various transfer coefficient terms through the thin film system for NO substrates (first column) and TO substrates (second column) with various PTCDI-C_8 thicknesses (50, 100, 200, and 400 nm, rows). The *s*-polarized visible beam (black) and *p*-polarized mIR beam (red) are plotted for $\left|\tilde{t}_{0,z}\right|$ (solid), $\partial_z\left|\tilde{t}_{0,z}\right|$ (dashed), and $\left|\partial_z\left|\tilde{t}_{0,z}\right|/\left(ik_z\left|\tilde{t}_{0,z}\right|\right)\right|$ (dotted).

There are several details to discuss from Figure 5-10. We first point out that the field magnitude derivatives are indeed zero ($\partial_z \left|\overleftarrow{t}_{0,z}\right| = 0$) outside of the thin film layers within the semi-infinite silicon substrate and in air as is the usual case for single interface systems. We also see that the field magnitude is continuous across all interfaces for the visible beam ($\left|\overleftarrow{t}^{vis}_{0,z,(s,y)}\right|$), but that the mIR ($\left|\overleftarrow{t}^{mIR}_{0,z,(p,z)}\right|$) experiences very abrupt changes in magnitude at each interface. It is well known that the normal field component varies rapidly at interfaces and that it is discontinuous in models that consider abrupt changes in refractive index.[234,373] Field discontinuity is the source of a possible additional effect present in the data that will be discussed in Section 5.6.

The field magnitudes vary through the film stack and their profile in each layer depends on the geometry of the entire system. For example, the magnitude of the visible within the 400 nm PTCDI-C_8 layer has a different profile for NO substrate (Figure 5-10(d)) than for the TO substrate (Figure 5-10(h)). The magnitudes for the (shorter wavelength) visible beam experience oscillations within these thickness ranges whereas the mIR has a vacuum wavelength that is comparably longer (5.95 μm) than this length scale so that there are only gradual changes within the layers. The result is that $\partial_z \left|\overleftarrow{t}_{0,z}\right|$ is variable but generally much larger for the visible beam (black dashed traces have been multiplied by 100) relative to the mIR (red dashed traces have been scaled by 1000). However, we can better quantify the importance of the $\partial_z \left|\overleftarrow{t}_{0,z}\right|$ term for quadrupole coupling by considering the ratio of that term to the single interface term $ik_z \left|\overleftarrow{t}_{0,z}\right|$ from Eq. (5.10). We have plotted the magnitude of that ratio

$\left(\left|\partial_z \left|\tilde{t}_{0,z}\right|\right/\left(ik_z \left|\tilde{t}_{0,z}\right|\right)\right|\right)$ as dotted lines in order to get a sense of their relative importance. From those traces, it is clear that the ratio varies but that the term resulting from the thin film geometry $(\partial_z \left|\tilde{t}_{0,z}\right|)$ is generally of comparable magnitude to the standard quadrupole term $\left(ik_z \left|\tilde{t}_{0,z}\right|\right)$ in the PTCDI-C_8 layer for all thin film systems shown and for both input beams. For the visible, the total contribution from the thin film term will depend on the total area under the $\vec{t}^{VSFG}_{z,0,(y,s)}\left(\partial_z \left|\tilde{t}^{vis}_{0,z(s,y)}\right|\right)\tilde{t}^{mIR}_{0,z(p,z)}$ term in the quadrupolar transfer product so that for some system geometries this may be minimized by having equal area above and below the $z=0$ axis but will lead to oscillations in the total quadrupolar contribution as the total area changes sign with thin film thicknesses. For the mIR beam, quadrupolar coupling is enhanced in thicker films so that not only does the additional material contribute more but the area under the $\partial_z \left|\tilde{t}_{0,z}\right|$ term also becomes larger so that the $\vec{t}^{VSFG}_{z,0,(y,s)}\tilde{t}^{vis}_{0,z(s,y)}\left(\partial_z \left|\tilde{t}^{mIR}_{0,z(p,z)}\right|\right)$ term in the quadrupolar transfer product may also oscillate but with larger amplitude. From the relative scaling on $\partial_z \left|\tilde{t}_{0,z}\right|$ we can also conclude that the quadrupolar transfer coefficient portions of the quadrupolar transfer products in Eq. (5.5) are about an order of magnitude lower for the mIR relative to the visible (although the overall transfer product magnitudes will be discussed in the next section).

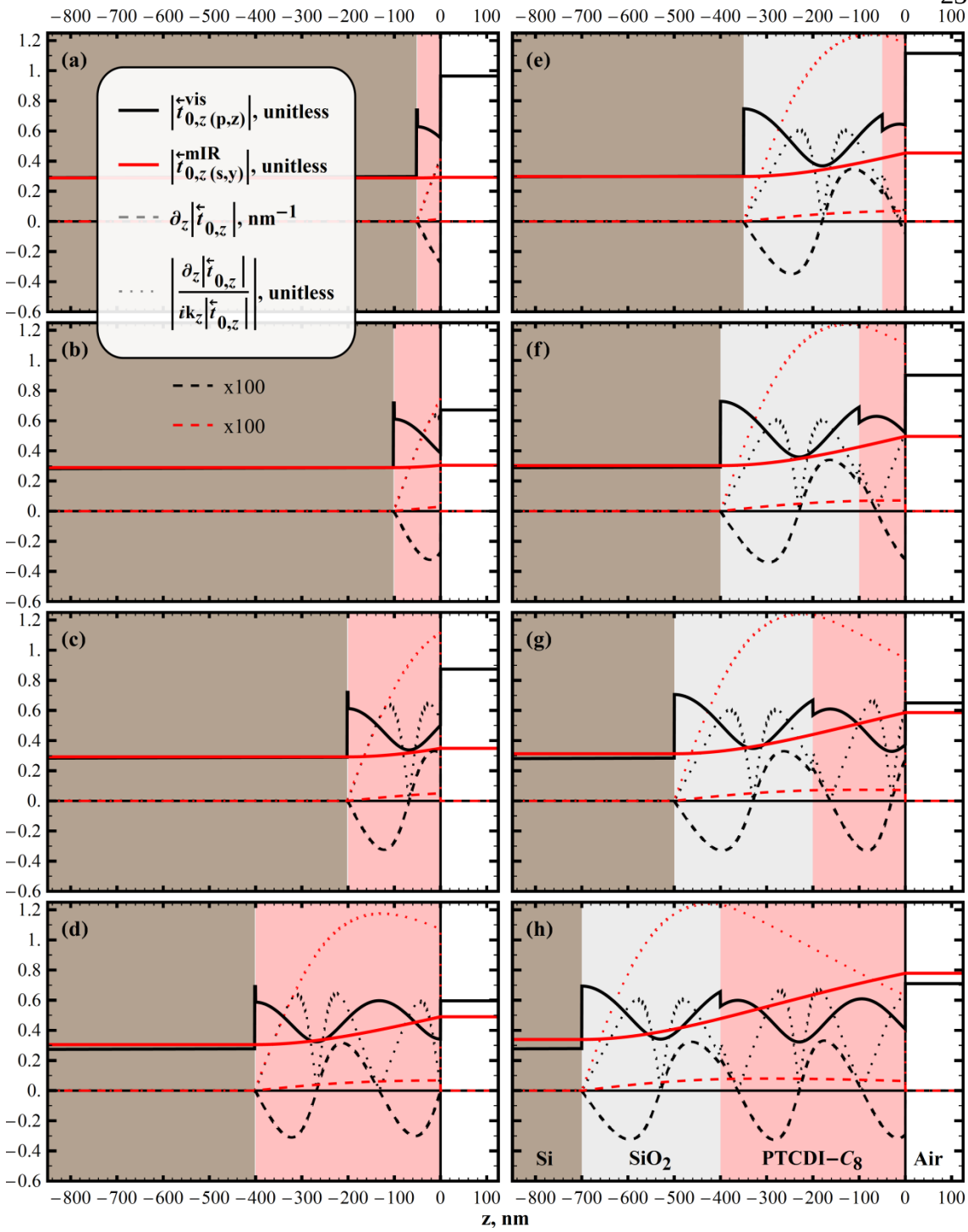

Figure 5-11. Plots showing various transfer coefficient terms through the thin film system for NO substrates (first column) and TO substrates (second column) with various PTCDI-C_8 thicknesses (50, 100, 200, and 400 nm, rows). The *z*-component of the *p*-polarized visible beam (black) and *y*-component of the *s*-polarized mIR beam (red) are plotted for $\left|\tilde{t}_{0,z}\right|$ (solid), $\partial_z\left|\tilde{t}_{0,z}\right|$ (dashed), and $\left|\partial_z\left|\tilde{t}_{0,z}\right|/\left(ik_z\left|\tilde{t}_{0,z}\right|\right)\right|$ (dotted).

We present the analogous *sps* plots in Figure 5-11. Here the *y*-component of the *s*-polarized mIR field is continuous across all interfaces and the *z*-component of the *p*-polarized visible is discontinuous. Again, there are periodic variations in the magnitude of the visible not present in the much longer wavelength mIR. The mIR derivative (red dashed) is on a scale that is an order of magnitude higher (multiplied here by only 100) than for the *ssp* experiment in Figure 5-10 which leads to the term ratio $\left|\partial_z \left|\tilde{t}_{0,z}\right| \Big/ \left(ik_z \left|\tilde{t}_{0,z}\right|\right)\right|$ (red dotted) being higher in all plots, indicating the $\partial_z \left|\tilde{t}_{0,z}\right|$ term for the mIR is more important in this experiment. At the same time, the gradient term ratios are variable for the visible (black dotted) but are generally lower in the *sps* experiment of Figure 5-11 relative to those in Figure 5-10. Nonetheless, the $\partial_z \left|\tilde{t}_{0,z}\right|$ terms for both input beams are also important for the *sps* experiment.

The result from these calculations is that thin film geometries introduce distinct effects on bulk quadrupolar coupling terms relative to the same considerations for bulk terms commonly encountered in the literature for single interface systems.[235,351,373–375,381] In order to properly model bulk contributions due to quadrupolar coupling to the input fields from within thin film systems one must include effects from the spatial variation of the fields within the thin film system.

5.5.2 *Bulk Quadrupole Coupling Transfer Products*

The discussion on how the thin film system geometry affects electric quadrupolar coupling with the input fields and the distinction from single interface systems is important to keep in mind as we move to discussing how the overall quadrupolar coupling transfer products behave. Our initial analysis of possible bulk

contributions in the data will start by considering some intensity-level contributions at a single wavelength as compared with a slice through the data plots of Figures 5-3 and 5-4 in the regions of highest intensity of the symmetric stretch around 1700 cm^{-1}. The primary goal here is to illustrate how the quadrupole bulk transfer products compare to interfacial transfer product terms considered thus far and to present some qualitative evidence from the data that higher order bulk contributions are likely present.

Figure 5-12(a) and 5-12(d) show the *ssp* data from NO and TO substrates, respectively, (averaged from a window from 1685 – 1710 cm^{-1}) and some possible intensity-level contributions to the detected signals (scaled as indicated in the legend). We present the individual interfacial transfer products $\left|T_v^{yyz}\right|^2$ (gray and red for $v=1$ and $v=2,$ respectively) as well as the sum (blue) and difference (black) of the two that represent the two possible relative polar orientations (relative sign of the interfacial susceptibilities) of modes at the interface as discussed previously.[397] These four traces are meant to present snapshots of the otherwise continuous possible relative response from each interface in the intensity expression $\left|\chi_1^{(2),ijk}T_1^{ijk}+\chi_2^{(2),ijk}T_2^{ijk}\right|^2$. All interfacial transfer products are solid lines and the bulk transfer products are dashed red for quadrupole coupling to the mIR and dashed black for coupling to the visible. The unscaled transfer product terms are also shown on a log scale in Figure 5-12(b) and 5-12(e). The phase traces relative to the outer interfacial transfer product phase (ϕT_1^{yyz}, the ϕ sign indicates the argument (phase) of the complex quantity), are presented in Figure 5-12(c) and 5-12(f). All transfer products were calculated at 1700 cm^{-1}. We

have put all data slices in Figure 5-12(a) – (d) on the same scale by normalizing by the most intense

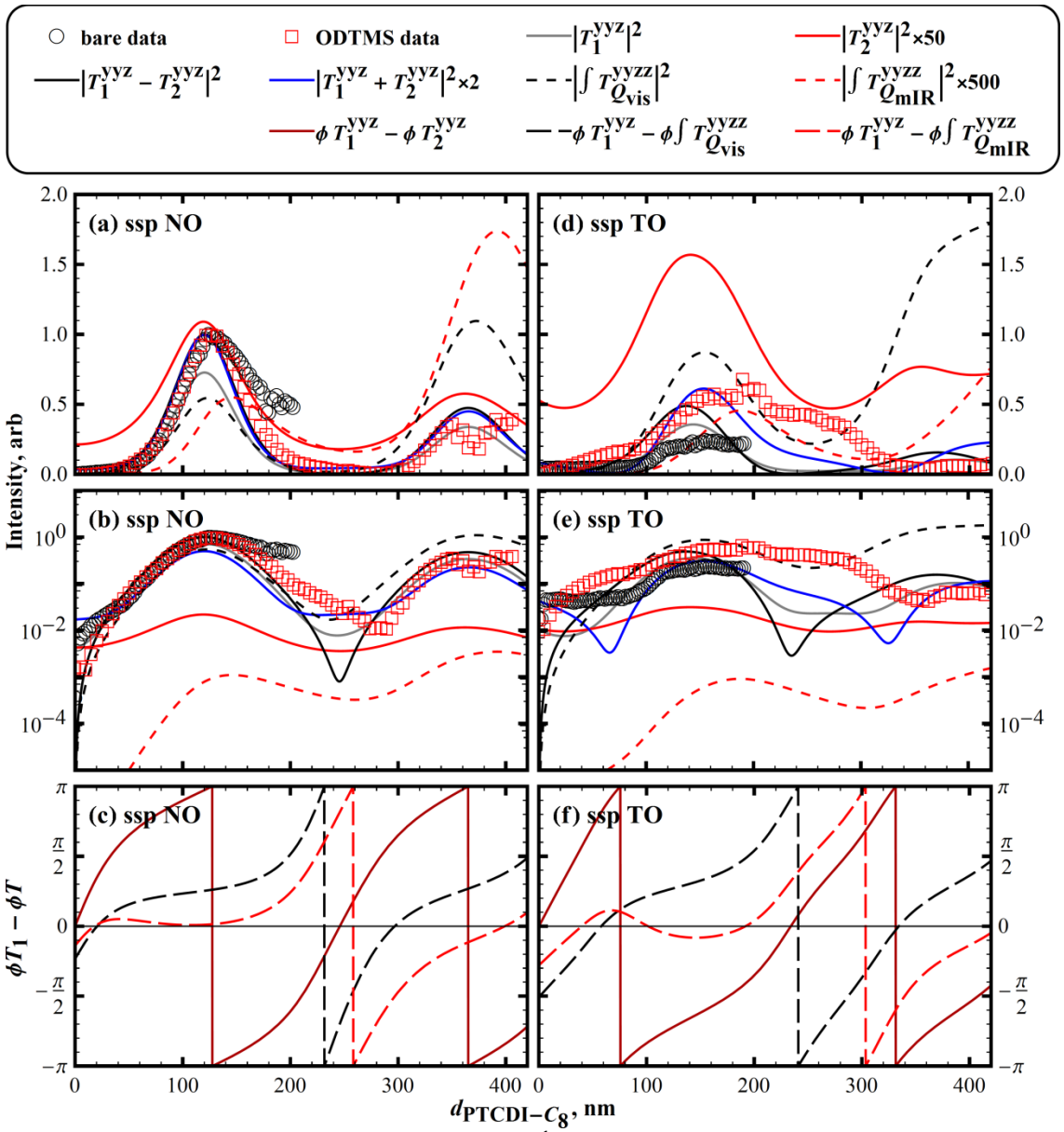

Figure 5-12. VSFG spectral slice around 1700 cm^{-1} showing averaged *ssp* intensity data (from 1685 – 1710 cm^{-1}) as a function of PTCDI-C$_8$ thickness from NO and TO substrates. The first row plots show normalized data from both surface preparations (bare black circles, ODTMS red squares) as well as multiple intensity-level terms that may contribute to the overall observed response, scaled as indicated in the legend. The second row shows the same terms (unscaled) on a log$_{10}$ scale. The transfer product phase traces in the last row show the phase relationships relative to the outer interfacial transfer product phase.

point in the peak around $d_{\text{PTCDI-C}_8} = 120$ - 140 nm for the NO substrates in Figure 5-12(a) (bare and ODTMS preparations normalized to their respective maximum on NO for both NO and TO). Similarly, all model transfer product contributions plotted have been normalized by the maximum in $\left|T_1^{yyz} - T_2^{yyz}\right|^2$ around the same point in the PTCDI-C_8 thickness. We specify that the quadrupolar transfer products in the figure have been integrated over the organic thickness (Eq. (5.5)) by placing an integral sign adjacent to each term. For example, $\left|\int T_{Q_{mIR}}^{yyzz}\right|^2$ indicates the total field intensity at the detector (assuming $\chi_{Q_{mIR}}^{(2),yyzz}$ is constant through the film) due to quadrupolar coupling of the mIR through the bulk of the organic film. Thus, the plots indicate the modeled intensity for each transfer product contribution assuming all susceptibilities are equal to unity. This is our starting point for the analysis of possible bulk contributions to our data.

From the plots in Figure 5-12 we can make some statements about contributions to the overall observed signal intensity. First, the intensity level transfer products in Figure 5-12(a) (Figure 5-12(b)) and Figure 5-12(d) (Figure 5-12(e)) exhibit very strong dependence on the thicknesses of both thin films in the system. The quadrupolar transfer product for the mIR is notably lower than all other possible contributions whereas the visible quadrupolar transfer products are of comparable magnitude to the interfacial transfer products and both bulk transfer products rapidly decrease near 0 nm PTCDI-C_8. The phase relations in Figure 5-12(c) and Figure 5-12(f) are complicated. We note that, whereas the phase difference between the two interfaces of the organic (solid dark red) goes to zero at vanishingly thin PTCDI-C_8 thicknesses as is expected,

the bulk transfer product phases are offset from zero. This is due to the phase relation introduced by the gradient operation in Eqs. (5.6) and (5.7). The transfer coefficient derivatives result in two terms contributing to the transfer product, as discussed in the last section and shown in Eq. (5.10). Of those two terms, the $\partial\left|E\left(z\right)\right|$ term contains no additional phase offset but the $ik_z\left|E\left(z\right)\right|$ term has magnitude and a phase of $\pi/2$ when $k_z = 2\pi n\cos\left(\theta\right)/\lambda$ is real. However, as PTCDI-C_8 is absorbing, especially at the mIR wavelengths, k_z is complex with an argument (phase) that depends on the complex refractive index and angle of refraction. Also contributing to the phase offset at very thin thicknesses is the fact that $\partial\left|E\left(z\right)\right|$ becomes very small relative to $\left|E\left(z\right)\right|$ for both wavelengths (e.g. see top row plots in Figure 5-10 and Figure 5-11). Thus, when the $\partial\left|E\left(z\right)\right|$ and $ik_z\left|E\left(z\right)\right|$ terms of the bulk transfer products are added in the complex plane, the resulting bulk transfer products have a non-zero phase relation relative to the outer interfacial transfer product that depends on the quadrupolar coupling field wavelength, the optical constant of PTCDI-C_8, as well as the geometry of the entire system. Note that the phase relation at 0 nm is not the same for TO and NO in Figure 5-12(c) and 5-12(f)).

If we begin by considering that the sample susceptibilities have no dependence on organic film thickness, the data on NO substrate in Figure 5-12(a) may be described fairly well by either a fully outer interfacial contribution (gray) or by either of the two choices for relative polar orientation when considering equal interfacial contributions (same $\left|T_1^{yyz}+T_2^{yyz}\right|^2$ solid blue, or opposite orientation $\left|T_1^{yyz}-T_2^{yyz}\right|^2$ solid black) since all

three lineshapes are very closely related by a scaling factor. These are in particularly good agreement with NO-ODTMS data over the full 400 nm wedge. On the other hand, none of the intensity level contributions shown in Figure 5-12(d) describe the VSFG data taken from the wedges on TO substrates nearly as well as the same lineshapes generated for the NO system. In no case does a fully buried interfacial response describe the data. In Figure 5-12(a), the $d_{\text{PTCDI-C}_8}$ axis appears to be off by about 10 nm relative to the model lineshapes that appear to describe that data best. Part of the procedure for calibrating that axis involved finding the zero point of the organic wedge by taking VSFG data at raster points before the emergence of vibrationally resonant peaks. We assigned the first spectrum with any hint of vibrational response as 0 nm. Thus, we are confident to within ±1 mm in the raster of that point which corresponds to ±3 nm in the case of bare substrates and ±5 in the case of the thicker ODTMS wedges. These are very near the apparent error in that axis, but deficiencies in the model description of the TO data indicate that none of the idealized model lineshapes are sufficient to consistently describe the wedges on both substrates and both surface preparations so that other effects may be responsible for the apparent error in the axis. Our fit results from Section 5.4.4 indicate that, even with inclusion of variation in the outer interfacial contribution with wedge thickness, the interfacial model does not result in a physically reasonable description of the intensity data from NO-ODTMS and TO-ODTMS (red squares) in the region from 200 – 300 nm. In Figure 5-12(d) and 5-12(e) it is apparent that the TO-ODTMS data are primarily responsible for the large bump in the mode amplitude of Figure 5-12(c) due to the large response at 200 – 300 nm that is not consistent with any of the interface-only transfer products in that region. It is

apparent from the transfer product plots that inclusion of bulk terms is likely to improve the physical description of the system. That is, the bulk transfer products vary with $d_{\text{PTCDI-C}_8}$ in such a way that they may add to the intensity in the region that is otherwise not well described by interface-only terms. This is true for the region of 200 – 300 nm, but may also provide a better physical description for the difference in response for bare vs. ODTMS NO substrates. For instance, in Figure 5-12(a) and Figure 5-12(d) inclusion of significant quadrupolar coupling to the mIR may improve the description of the data at thicknesses above ~150 nm and have little impact on the thinnest end of the PTCDI-C_8 wedge. Of course, the phase relations between terms are also important and these complicate this qualitative discussion. It will always be the case that the phase dependence on organic thickness in Figure 5-12(c) and Figure 5-12(f) will vary as shown in the plots, but the full $T\chi$ terms may offset these traces when including the frequency dependent (but constant with organic thickness) phase difference between interfacial responses. In other words, the phase plots retain their shapes but take on a frequency dependent offset depending on the phase relation between $\chi_Q^{(2),ijkm}$ and the interfacial responses. Nevertheless, the simplified analysis of a single spectral slice through the data informs on many important features present in the full 2D data plots.

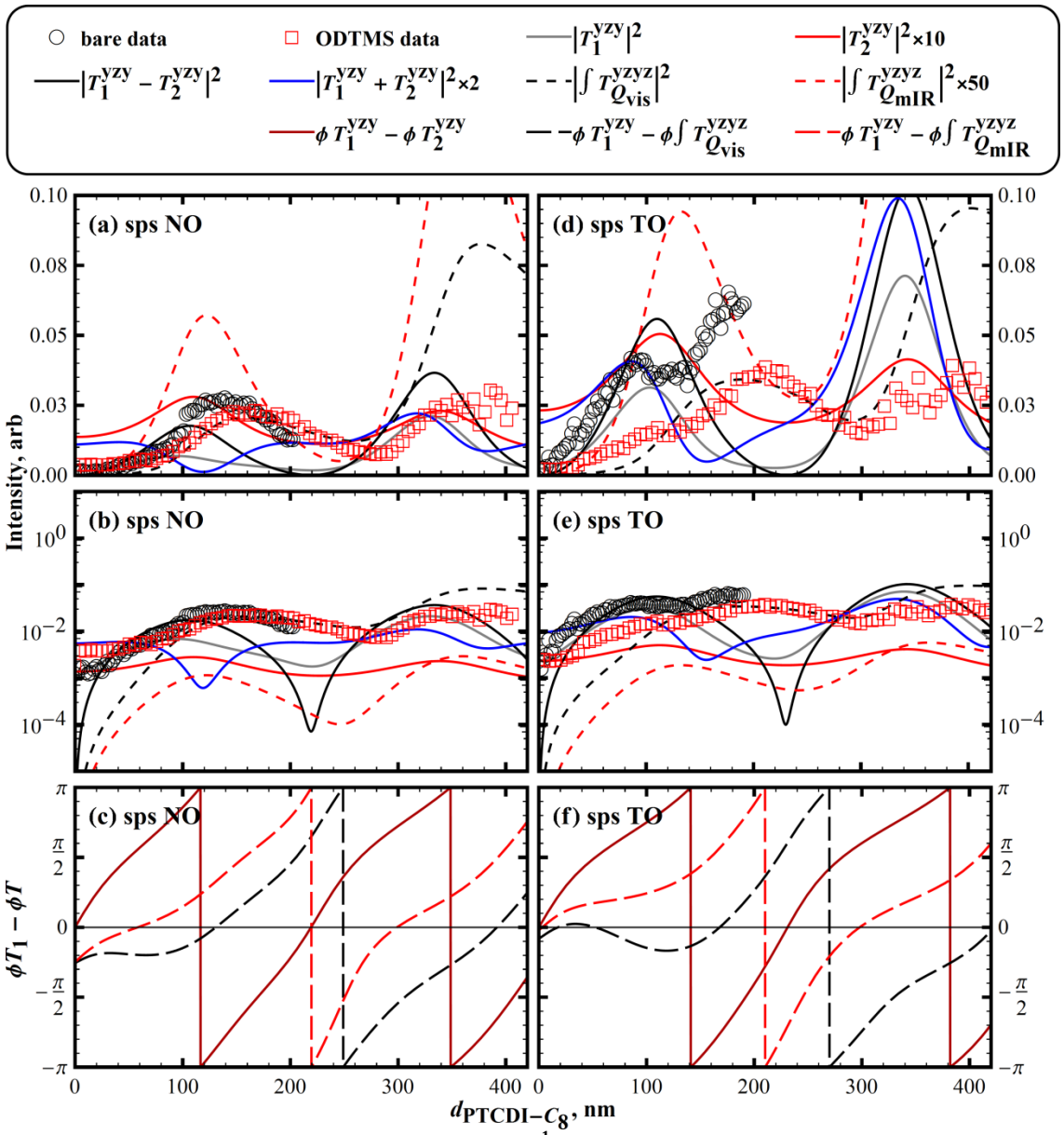

Figure 5-13. VSFG spectral slice around 1660 cm^{-1} showing averaged *sps* intensity data (from 1650 – 1670 cm^{-1}) as a function of PTCDI-C$_8$ thickness from NO and TO substrates. The first row plots show normalized data from both surface preparations (bare black circles, ODTMS red squares) as well as multiple intensity-level terms that may contribute to the overall observed response, scaled as indicated in the legend. The second row shows the same terms (unscaled) on a log$_{10}$ scale The transfer product phase traces in the last row show the phase relationships relative to the outer interfacial transfer product phase. Data and model traces are scaled by the same factors as in Figure 5-12 so they are all on a common scale.

We may also examine the analogous plots for the *sps* experiment, but in this case we investigate the region around the asymmetric mode at ~1660 cm^{-1} (averaged from the region 1640 – 1670 cm^{-1}). Figure 5-13 shows these results with the data and

model traces all scaled by the same factors used in Figure 5-12. We see again that none of the data are described by a buried interface only response. Also, the various interfacial terms are *not* nearly proportional for NO in Figure 5-13(a) as they were in Figure 5-12(a). This gives us more sensitivity to distinguish which case most closely matches the data in the thinnest regions of the wedge thickness. For example, it is apparent that for both surface preparations on NO and TO that the thinnest region <50 nm is most consistent with either opposite polar orientation (black) or a fully outer interfacial response (gray). From this point up to ~140 nm there appears a discrepancy in which interfacial contribution may best describe date from NO and TO. In Figure 5-13(a) it appears that NO is better described by $\left|T_1^{yzy} - T_2^{yzy}\right|^2$ or $\left|T_1^{yzy}\right|^2$ whereas in Figure 5-13(d) TO is more consistent with $\left|T_1^{yzy} + T_2^{yzy}\right|^2$. Beyond 140 nm there is no consistency between the data and any of the interfacial or bulk terms shown in the plots.

The complicated magnitude and phase dependence of the various transfer products shown in Figure 5-13 combined with no evidence that the data clearly follow the trend for any of our "snapshot" plots for a fully interfacial description suggests that bulk contributions are important for the asymmetric mode in the *sps* experiment. We note that in the case of *sps*, the transfer product for quadrupole coupling to the mIR is about an order of magnitude larger than for *ssp*, as we mentioned should be the case in our discussion from Section 5.5.1. Thus, it may be that quadrupolar coupling to the mIR is non-zero and enhanced in the *sps* experiment. From this, the conclusion is the same as for *ssp*, interfacial terms are likely playing a significant role in the intensity

data, but with increased organic thickness we gain sensitivity to the effects from bulk terms.

The analogous plots to Figure 5-12 and Figure 5-13 for the asymmetric and symmetric stretch, respectively (not shown), indicate that all transfer product traces are similar (but not identical, due to differing wavelengths and optical constants). It should be noted that the frequency dependent mIR refractive index can have a large effect on the transfer product traces, especially for experiments that sample the *z*-component of the mIR input field. It was discussed in Chapter 4 how the Kramers-Kronig relation for modes with larger mIR absorption cross sections can have a significant effect on VSFG transfer products.[397] In this section we have selected a single mIR frequency near the center of the symmetric stretch to compute all transfer products. While this is not ideal for quantitative analysis of the data, it is sufficient for the purposes of this section. The goal here has been to introduce the bulk transfer products and provide some evidence that these terms may be present in the experimental data. With the bulk transfer products now fully developed, we move to applying the analysis to the data.

5.5.3 *PTCDI-C_8 Higher Order Response*

While we have attributed any dipole-allowed interfacial response to the imide functional group on one end of the perylene core pointing away from the organic thin film (see Section 5.4.2 and Figure 5-5), PTCDI-C_8 is formally a centrosymmetric molecule (the perylene core belonging to the D_{2h} point group) and each mode of interest (symmetric and asymmetric) may combine symmetrically or antisymmetrically with its pair mode on the opposite end of the molecule to produce both an IR and a Raman active normal mode. The four possible modes are either Raman or IR active, but not

both as is formally required for VSFG in the electric dipole approximation. The IR active modes have been given in Section 5.4.2 and to this we add Raman center frequencies of 1656.5 and 1699.0 cm^{-1} for ν_s and ν_{as}, respectively. The Raman activities of the carbonyl modes in perylene-diimide derivatives are notoriously weak,[414] thus the assigned Raman frequencies are consistent with our own observations from surface-enhanced Raman measurements as well as reported experimental surface-enhanced and resonance-enhanced values. Additionally, estimates from calculations indicate the Raman modes should be slightly blue-shifted relative to the FTIR modes with a larger shift for the symmetric mode.[413,458] The assigned IR and Raman modes are consistent with those results.

VSFG applied to molecules that possess inversion symmetry has attracted attention in recent years and it has been suggested that quadrupolar interactions are likely significant in these systems, with respect to bulk contributions as well as interfacial contributions (to be discussed in Section 5.6).[234,278,381,459–461] In particular, it has been pointed out that the mechanism for quadrupolar coupling to the mIR field should be strongest for the Raman active modes, and quadrupolar coupling to the visible field should be strongest for IR active modes.[278] This is an important consideration for the model and data analysis that follows.

5.5.4 *Model and Fit Details*

With the bulk and interfacial transfer products known, we set up a model using Eqs. (5.3) - (5.5) and simultaneously fit both modes for four gradient datasets for each polarization experiment. The full form of the model for each dataset was

$$\hat{I}_0^{\alpha\beta\gamma} \propto M \sum_{q=s,as} \left| \chi_{1,q,eff}^{(2),ijk} T_{1,q}^{ijk} + \chi_{2,q,eff}^{(2),ijk} T_{2,q}^{ijk} + \chi_{3,NR}^{(2),ijk} T_{3,q}^{ijk} + \chi_{Q_{vis},q}^{(2),ijkz} \int T_{Q_{vis},q}^{ijkz} + \chi_{Q_{mIR},q}^{(2),ijkz} \int T_{Q_{mIR},q}^{ijkz} \right|^2 \tag{5.11}$$

Due to problems with parameter correlations (as discussed in Section 5.4.4) we were unable to reliably include the additional bulk terms into the fitting routine to analyze the full 2D data plots in Figure 5-3 and Figure 5-4. Instead, we simplify the analysis to a single dimension by considering an average of the data over each frequency region of appreciable response for both modes of interest, renormalized to match peak intensities in the 2D plots. While this is not ideal, we justify this simplification from our observations in the last section where we showed the VSFG spectral slices contain many features of the transfer product slices. Further, we ease some of the complications that arise from ignoring the frequency dependent phase by including phase parameters in the fitting routine, and we discuss their physical significance in what follows.

Each transfer coefficient was evaluated in the vicinity of each mode as was presented in the last section. This is indicated in Eq. (5.11) by including subscript q on all transfer products. Using the same considerations detailed in Secton 5.4.3 we fit these slices along the $d_{\text{PTCDI-C}_8}$ coordinate (simultaneously for both modes of a given polarization experiment) to the model given in Eq. (5.11) where each susceptibility factor was floated as a constant complex number for each of the two modes of interest, with the exception of $\chi_{1,eff}^{(2),ijk}$, which was again parameterized as a series of points along the organic thickness axis connected by linear interpolation. We use subscript *eff* on the two organic interfacial susceptibilities (interfaces 1 and 2) to specify that we now consider these effective dipolar susceptibilities. Details of this statement will be made

clear when we address higher order interfacial terms in Section 5.6. Since PTCDI-C_8 is known to assemble identically through the bulk on either surface preparation[95] we set the susceptibilities of both possible bulk contributions ($\chi^{(2),ijkz}_{Q_{vis}}$ and $\chi^{(2),ijkz}_{Q_{mIR}}$) unique for each mode but locked to be identical for all four datasets of a given polarization experiment.

Each susceptibility component in Eq. (5.11) was parameterized with an amplitude, χ, and phase, $\phi\chi$, relative to the outer interfacial term (i.e. $\chi\exp(i\phi\chi)$ with the phase of $\chi^{(2),ijk}_{1,eff}$ set to 0). The phase parameters offset the phase plots in the last rows of Figure 5-10 and Figure 5-11. Inclusion of the phase parameters is meant to account for the sensitivity of the phase difference for nearly identical Lorentzian oscillators. It is well known that even a small split in the center frequency of otherwise identical modes leads to an appreciable phase difference, especially in the region between those modes.[96,395] Further, we have restrictions on how large the difference may be before we must consider a sign change on the susceptibility amplitude. The phase difference between two Lorentzian oscillators with the same amplitude sign computed at the center frequency (maximum in the peak at the intensity level) of the reference oscillator ranges between $\pm\pi/2$, representing a blue or red relative frequency shift. Oscillators with opposite amplitude signs may range from $\pi\pm\pi/2$. Thus, we interpret any phase result that lies outside the range of $\pm\pi/2$ as the result of an oscillator that requires an amplitude sign change. In the results presented next, any phase parameter that resulted in the region between $\pi/2$ and $3\pi/2$ was adjusted by simply adding or subtracting π to bring it within $\pm\pi/2$ accompanied by a change in

the sign on the corresponding amplitude fit result. The signs of the amplitudes normally provide a measure of relative polar orientation of modes within the electric dipole approximation, but more importantly they will be used in the next section to deduce relative magnitudes of higher order interfacial terms.

Every contribution to a given peak, whether it is bulk or interfacial, is likely shifted to varying degrees relative to the center of the outer interfacial contribution (again, even a small shift may produce a large effect on the intensity data). We interpret the shift (and therefore the phase parameter) for the buried interfacial contribution as resulting from a difference in the buried interfacial environment relative to the outer interface. We infer the shift in the bulk contributions as also being related to a different "bulk" environment, but these are also shifted relative to one another due to each coupling stronger to either the FTIR or Raman active mode. That is, the center frequencies for each of the bulk contributions from quadrupolar coupling to the visible and mIR are not identical, as discussed in Section 5.5.3, and therefore do not share a common phase parameter.

A nonresonant amplitude at the SiO_2/Si interface was assigned a static value in the same way as Section 5.4.3, based on results from fitting a region of the data outside of vibrational resonances (around 1740 cm^{-1}). In this analysis where we incorporate bulk terms, we now include the nonresonant response for the *sps* model. All nonresonant results are included in the tables below.

5.5.5 *Fit Results and Discussion*

Figure 5-14 and Figure 5-15 show data slices and fits for *ssp* and *sps*, respectively, including results for the outer interfacial susceptibility (green dots

connected by green lines). All other fit parameters and static contributions are presented in Table 5-4 and

Table 5-5. Again, we find that even with the constraints imposed by the simultaneous fitting routine that we have remarkable agreement between model and data. It is especially noteworthy since our data treatment effectively averages over the dependence on frequency through the vicinity of each mode, indicating that this procedure provides a simplified way to begin to analyze possible bulk contributions from VSFG applied to thin film systems. We point out that even in Figure 5-15(b), where there is a significant dip in response at around 130 nm for TO that is not present in any other data, that the model captures the feature by response from the outer interface that is nearly constant and also consistent with the other results for the outer contribution. That is, there was no need for the parameterization of the outer mode to vary in such a way so as to account for this feature through parameter correlations; it is attributable to thin film interference effects described by the thin film model. We find significant improvements for the description of *sps* data for ν_{as} from this simplified model (Figure 5-15(b)) relative to the bottom row results for the same mode in Figure 5-8. Also, we see that bulk terms can be incorporated into the NO and NO-ODTMS *ssp* substrate models for data that was otherwise described quite well by interface-only contributions (see Figure 5-12 and the discussion in Section 5.5.2).

We have also applied this simplified routine to analyze the data without bulk terms and have found that the interfacial results are consistent with the full 2D plot analysis provided in Section 5.4.4. Most notably, the outer interfacial response contains a much larger feature in the vicinity of 200 – 300 nm for both modes and both

polarization experiments. Also, when bulk terms are eliminated, the results for the outer interfacial contribution in Figure 5-15(b) vary in a way that is clearly accounting for the dip in the data from TO and leads to a less physically meaningful result.

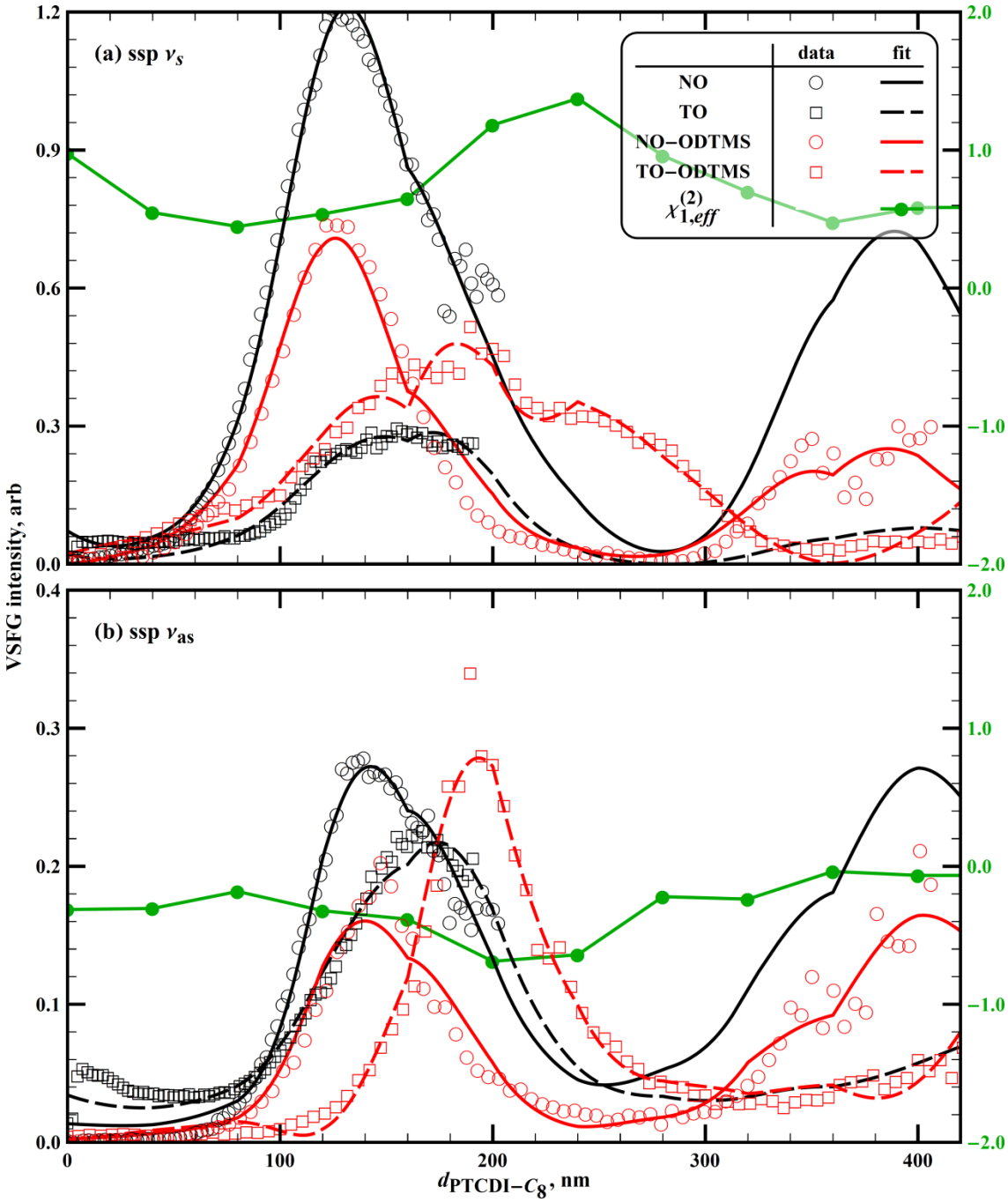

Figure 5-14. Data and fit results for *ssp* slice from (a) the symmetric imide carbonyl stretch around 1700 cm^{-1} and (b) the asymmetric mode around 1660 cm^{-1}. Results for the outer interfacial contribution (green) are scaled on the right, all others are scaled on the left.

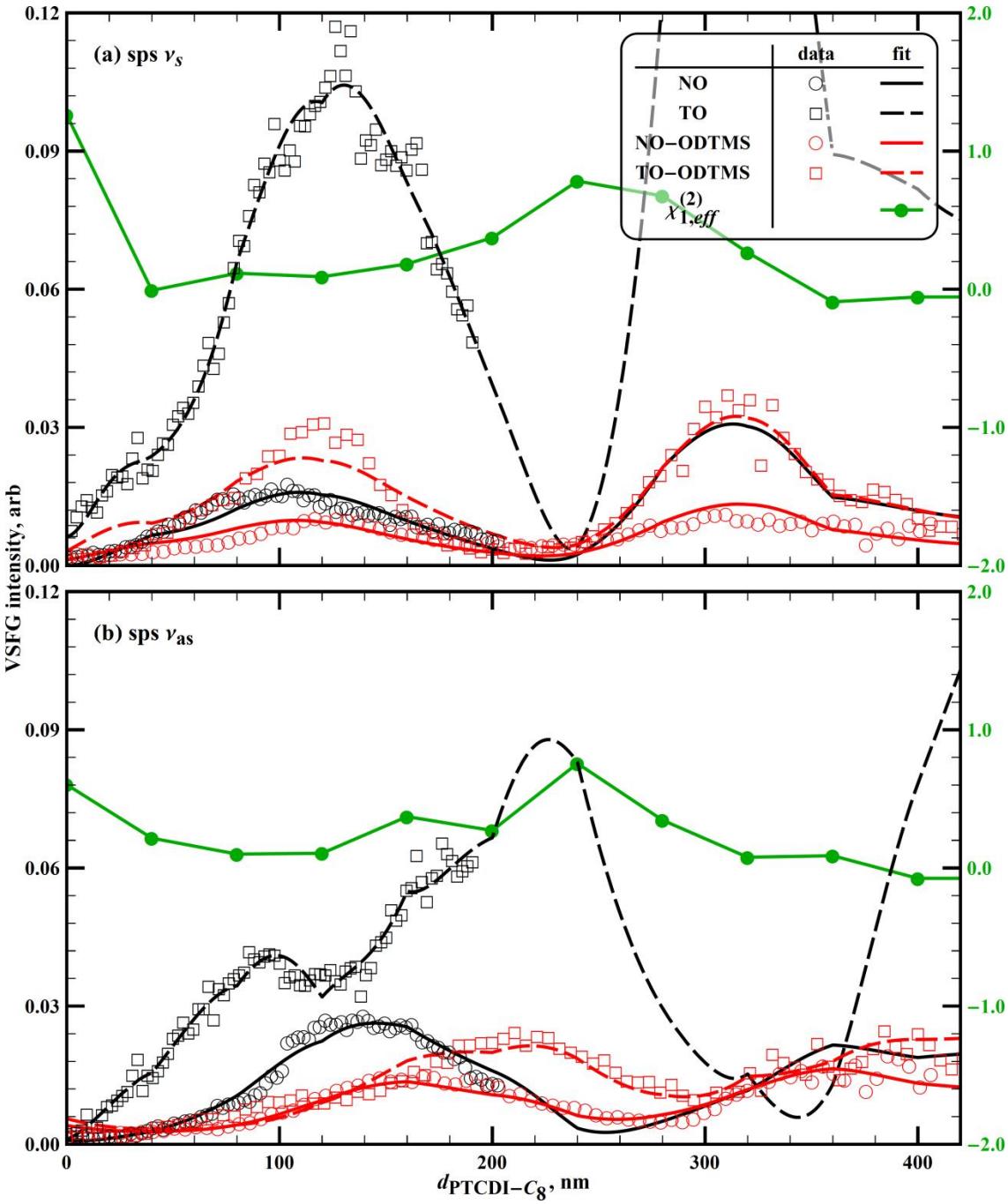

Figure 5-15. Data and fit results for *sps* slice from (a) the symmetric imide carbonyl stretch around 1700 cm^{-1} and (b) the asymmetric mode around 1660 cm^{-1}. Results for the outer interfacial contribution (green) are scaled on the right, all others are scaled on the left.

Table 5-4. Parameter fit results to *ssp* data slice for the symmetric and asymmetric modes. Quantities in italics indicate static parameters (not floated).

		NO	TO	NO-ODTMS	TO-ODTMS
shared parameters	M	*1*	0.33	1.10	2.20
	$\chi^{(2),yyz}_{3,NR}$	*-1.3*	*8.1*	*-2.3*	*5.0*
	$\phi\chi^{(2),yyz}_{3,NR}$	-0.45	-1.09	shared with bare substrates	
ν_s	$\chi^{(2),yyz}_{2,eff}$	-2.69		-0.65	
	$\phi\chi^{(2),yyz}_{2,eff}$	-1.25		0.44	
	$\chi^{(2),yyzz}_{Q_{mlR}}$		-2.80		
	$\phi\chi^{(2),yyzz}_{Q_{mlR}}$		1.20		
	$\chi^{(2),yyzz}_{Q_{vis}}$		-0.094		
	$\phi\chi^{(2),yyzz}_{Q_{vis}}$		0.38		
ν_{as}	$\chi^{(2),yyz}_{2,eff}$	2.91		-0.51	
	$\phi\chi^{(2),yyz}_{2,eff}$	-1.44		-0.55	
	$\chi^{(2),yyzz}_{Q_{mlR}}$		-7.81		
	$\phi\chi^{(2),yyzz}_{Q_{mlR}}$		0.44		
	$\chi^{(2),yyzz}_{Q_{vis}}$		0.16		
	$\phi\chi^{(2),yyzz}_{Q_{vis}}$		-0.64		

Table 5-5. Parameter fit results to *sps* data slice for the symmetric and asymmetric modes. Quantities in italics indicate static parameters (not floated).

		NO	TO	NO-ODTMS	TO-ODTMS
shared parameters	M	*1*	4.8	0.17	0.29
	$\chi^{(2),yzy}_{3,NR}$	*0.35*	*0.39*	*0.28*	*0.35*
	$\phi\chi^{(2),yzy}_{3,NR}$	-3.50	-2.05	shared with bare substrates	
ν_s	$\chi^{(2),yzy}_{2,eff}$	-0.83		-2.03	
	$\phi\chi^{(2),yzy}_{2,eff}$	0.08		0.36	
	$\chi^{(2),yzyz}_{Q_{mlR}}$		-0.85		
	$\phi\chi^{(2),yzyz}_{Q_{mlR}}$		0.93		
	$\chi^{(2),yzyz}_{Q_{vis}}$		0.11		
	$\phi\chi^{(2),yzyz}_{Q_{vis}}$		1.36		
ν_{as}	$\chi^{(2),yzy}_{2,eff}$	-0.68		-2.66	
	$\phi\chi^{(2),yzy}_{2,eff}$	0.02		-1.51	
	$\chi^{(2),yzyz}_{Q_{mlR}}$		2.76		
	$\phi\chi^{(2),yzyz}_{Q_{mlR}}$		1.22		
	$\chi^{(2),yzyz}_{Q_{vis}}$		0.79		
	$\phi\chi^{(2),yzyz}_{Q_{vis}}$		-0.49		

It is significant that following the routine outlined here that all outer interfacial responses have an improved physical interpretation, leading to confidence in the extracted parameters. In all four plots of Figure 5-14 and Figure 5-15, we see the magnitude of the outer interfacial response starts high at the thinnest edge of the wedge and tails off to a nearly constant value by 100 nm. Again, this is consistent with increased roughness at the outer interface leading to broadening of the average polar orientation and a reduction in VSFG response. The feature around 200 -300 nm that we noted in the electric dipole approximation analysis (Section 5.4.4) is drastically reduced in all four plots by inclusion of bulk terms. This more reasonable result combined with the exceptional agreement between data and model is our primary evidence that bulk contributions are significant in this system.

From Table 5-4 and Table 5-5 we see that for both modes and both polarization experiments that each $\left|\chi_{Q_{mIR}}^{ijkm}\right|$ is comparable or larger than the magnitudes of the corresponding interfacial response results and that $\left|\chi_{Q_{vis}}^{ijkm}\right| < \left|\chi_{Q_{mIR}}^{ijkm}\right|$ by as much as an order of magnitude or more. The $\chi_{Q_{mIR}}^{ijkm}$ interaction involves a resonant electric quadrupole transition followed by an anti-stokes Raman scattering event.[278] While the overall process involves both transition moments, and certainly depends on anisotropy, our results for $\chi_{Q_{mIR}}^{ijkm}$ roughly match the relative Raman activity for these two modes.[413] The $\chi_{Q_{vis}}^{ijkm}$ interaction involves a resonant IR transition followed by a nonresonant quadrupolar Raman interaction with selection rules identical to hyper-Raman scattering (weaker than Raman).[278,459] Quadrupolar coupling to the visible is expected to be smaller due to this higher order nonresonant process.

From our qualitative observations in Section 5.3 we noted that the peak intensity for ν_{as} occurs at larger PTCDI-C_8 thicknesses relative to ν_s for both *ssp* and *sps*, and this is clearly evident in the data plots of Figure 5-14 and Figure 5-15. Also, in Section 5.5.2 we noted that the $d_{\text{PTCDI-C}_8}$ axis appeared off by about 10 nm relative to the purely interfacial transfer product description of the data. While the interferences between contributing source terms are very complicated, the parameter results in Table 5-4 and Table 5-5 show that ν_{as} has larger bulk contributions due to both $\left|\chi_{Q_{vis}}^{(2),ijkm}\right|$ and $\left|\chi_{Q_{mir}}^{(2),ijkm}\right|$ for both polarization experiments. Quadrupolar coupling to the mIR is especially large for ν_{as}. From Figure 5-12 and Figure 5-13we see the bulk transfer products for both the visible and mIR contain oscillations that have peak intensities shifted to larger organic thicknesses relative to the interfacial "snapshot" traces, thus causing the detected peaks to shift in the same direction. They are especially shifted for $\left|\int T_{Q_{mIR}}^{(2),ijkm}\right|$ in *ssp* and $\left|\int T_{Q_{vis}}^{(2),ijkm}\right|$ in *sps*. We point out that when comparing various modes from plots such as those obtained in Figure 5-3 and Figure 5-4 that the observation of relative peak intensity maxima occurring at thicknesses larger than predicted by interface-only response is an indication of significant bulk contributions. Larger shifts indicate larger bulk response relative to the interfacial contributions of a given mode.

It is interesting to point out that the magnitude of $\chi_{Q_{mIR}}^{ijkm}$ is on the same order for *sps* as for the *ssp* experiment but the mIR quadrupolar coupling term in Eq. (5.11) is more favorable for *sps* since $\left|\int T_{Q_{mIR}}^{yyzz}\right|$ is about an order of magnitude larger (see Figure 5-7 and Figure 5-8). It is important to remember that, although the interfacial and bulk

susceptibilities extracted from the fits indicate similar magnitudes, the full contribution to the detected signal for each source depends on the product of the response and its associated transfer product, which is a function of both thin film thicknesses. It is the $T\chi$ terms that determine the relative importance of interfacial and bulk contributions. For instance, we find for our results that at thicknesses less than 20 nm, in most cases the bulk terms are 1 – 3 orders of magnitude smaller than the interfacial terms but at larger thicknesses they may be comparable or larger by as much as an order of magnitude or more. Careful consideration for thin film system geometry can help minimize bulk contributions. For this system it is only at the thinnest end of the wedge where the bulk terms become small due to their transfer products becoming small relative to the interfacial transfer products. However, a relative difference of even 3 orders of magnitude may not translate to a negligible bulk contribution for quantitative separation of the various VSFG sources due to cross terms with the interfacial contributions.

The extracted higher order terms indicate that quadrupolar coupling is particularly favorable for this system. In light of the symmetry of this centrosymmetric molecule combined with its ordered terraced packing it is conceivable that PTCDI-C_8 thin films are more susceptible, so to speak, to higher order interactions. It has been pointed out that there are some physical conditions for which quadrupolar coupling should be more favorable. Systems with oppositely oriented pairs of polar atomic groups that are in comparable proximity to the average molecular layer thickness, or when the size of the functional group under interrogation is comparable in size to molecular dimensions are such circumstances that may lead to significant quadrupolar

response from the bulk.[374] The vapor deposited PTCDI-C_8 thin film system is subject to both conditions. Furthermore, evidence for higher order contributions for other centrosymmetric molecules has been mounting in recent years.[234,278,381,459–461]

5.5.6 *Additional Comments*

We consider another possible bulk term resulting from coupling of the electric quadrupolar polarization $\ddot{Q}^{(2)}$ to the emitted field $E_{Q_P}^{(2),\alpha}$ which has the form[235]

$$\begin{aligned} E_{Q_P}^{(2),\alpha} &= \int_{d_{PTCDI-C_8}} \vec{t}_{z,0,(i,\alpha)}^{\,VSFG} \left[\nabla \cdot \ddot{Q}^{(2)}(z)\right]^{ijlm} dz \\ &= \int_{d_{PTCDI-C_8}} \vec{t}_{z,0,(i,\alpha)}^{\,VSFG} \left[\frac{\partial \chi_{Q_P}^{ijlm} \vec{t}_{0,z(\beta,j)}^{\,vis} \vec{t}_{0,z(\gamma,k)}^{\,mIR}}{\partial m}\right] dz \end{aligned} \tag{5.12}$$

where the integrand can be expressed as

$$\vec{t}_{z,0,(i,\alpha)}^{\,VSFG} \left[\frac{\partial \chi_{Q_P}^{ijlm} \vec{t}_{0,z(\beta,j)}^{\,vis} \vec{t}_{0,z(\gamma,k)}^{\,mIR}}{\partial m}\right] = \left(T_{Q_{vis}}^{ijkm} + T_{Q_{mIR}}^{ijkm}\right) \chi_{Q_P}^{ijlm} \tag{5.13}$$

Assuming no spatial dependence on $\chi_{Q_P}^{ijlm}$ through the bulk of the film, it is easy to arrive at the final relation in Eq. (5.13), which says that VSFG emitted from this source term contributes in the same way and equally to electric quadrupolar coupling to the input fields presented in this section ($T_{Q_{vis}}^{ijkm}$ and $T_{Q_{mIR}}^{ijkm}$ are the quadrupolar transfer products introduced in Eq. (5.5)). That is, the response attributed to $\chi_{Q_{vis}}^{ijlm}$ and $\chi_{Q_{mIR}}^{ijlm}$ discussed in this section may contain some contribution from coupling of the emitted field to $\ddot{Q}^{(2)}$ Our fit results indicate that $\chi_{Q_{mIR}}^{ijkm} > \chi_{Q_{vis}}^{ijkm}$ for both *ssp* and *sps* so that contributions from $\chi_{Q_P}^{ijlm}$ are not dominating both higher order terms (else the results for electric quadrupole coupling to input fields would be similar in amplitude).

While we have determined that bulk contributions are likely important in these experiments for both modes of interest, it is important to point out that the data *cannot* be fit without interfacial terms. In the next section we analyze the interfacial results and present evidence that they are likely a result of both dipolar and higher order interactions.

5.6 INTERFACIAL CONTRIBUTIONS

It is well known that the dipole approximation for interfacial VSFG depends primarily on two factors: the response is resonantly enhanced (there are VSFG active modes at the interface) and that there is significant polar orientation of those modes at the interface. The literature is laden with discussion of possible higher order contributions to the interfacial response, which is important when considering the results for the interfacial susceptibilities. Quantitative molecular orientation calculations can be performed only if the dipolar interaction can be separated from higher order terms.

In particular, and as mentioned in Section 5.5.1, the consequence of the discontinuity of the normal component for any input field results in a large field variation over the thickness of the interface so that higher order response is possible through quadrupolar coupling to that very large field gradient.[234,373] It has also been pointed out that, just as the refractive index changes abruptly from one material to another, there is also a large spatial variation in the susceptibility at the boundary. This can be expressed in Eq. (5.12) where the integration is performed over just the interfacial thickness and now $\chi_{Q_P}^{ijlm}$ *is* spatially varying from the bulk value to 0 with

transition from the nonlinear medium to the VSFG inactive (linear) medium. Analysis of this effect leads to contributions from the quadrupolar polarization ($\ddot{Q}^{(2)}$) to the emitted field from the organic interface that now contains a bulk response that is inseparable from the interfacial response.[235,373,459] However, as we concluded in Section 5.5.6, $\chi_{Q_P}^{ijlm}$ is likely smaller as compared to the interfacial susceptibility for this system. Also, since the susceptibility portion of electric quadrupolar coupling to the input fields is expected to be on the same order at the interface as for the bulk, but its contribution then enhanced by interaction with a much larger field gradient, we expect quadrupolar coupling to the input fields at the interface to be much larger than contributions from $\ddot{Q}^{(2)}$. Thus, in this section we consider higher order interfacial terms that involve electric quadrupolar coupling to the input field that contains the discontinuous *z*-component and we do not consider contributions from $\ddot{Q}^{(2)}$. These interactions are described by fourth rank tensors.

5.6.1 *Electric Quadrupolar Coupling to Large Interfacial Field Gradients*

In general, there are 8 nonzero elements of fourth rank tensors in the presence of a $C_{\infty,v}$ symmetry axis (as at a planar interface of isotropic materials). If we consider only those terms that involve the normal electric field component and derivatives with respect to the z-axis, there is only a single term that contributes for each polarization experiment. They carry the same indices as those detailed for the bulk response in the last section (*yyzz* for the *ssp* experiment and *yzyz* for the *sps* experiment).

$$E_{v,Q_{mIR}}^{(2),ssp} = \chi_{v,Q_{mIR}}^{(2),yyzz} \vec{t}_{v,0,(y,s)}^{VSFG} \overleftarrow{t}_{0,v(s,y)}^{vis} \left[\frac{\partial \overleftarrow{t}_{0,v(p,z)}^{mIR}}{\partial z} \right]_{\text{interface } v} \tag{5.14}$$
$$= \chi_{v,Q_{mIR}}^{(2),yyzz} T_{v,Q_{mIR}}^{yyzz}$$

$$E_{v,Q_{vis}}^{(2),sps} = \chi_{v,Q_{vis}}^{(2),yzyz} \vec{t}_{v,0,(y,s)}^{VSFG} \left[\frac{\partial \overleftarrow{t}_{0,v(p,z)}^{vis}}{\partial z} \right]_{\text{interface } v} \overleftarrow{t}_{0,v(s,y)}^{mIR} \tag{5.15}$$
$$= \chi_{v,Q_{vis}}^{(2),yzyz} T_{v,Q_{vis}}^{yzyz}$$

Here $E_{v,Q_{mIR}}^{(2),ssp}$ indicates the electric field emitted from interface v due to electric quadrupolar coupling to the mIR in the *ssp* experiment and in the same way $E_{v,Q_{vis}}^{(2),sps}$ is the electric field emitted from interface v due to quadrupolar coupling to the visible field in the *sps* experiment. The interfacial quadrupolar susceptibilities $\chi_{v,Q_{mIR/vis}}^{(2),ijkm}$ each have an associated interfacial quadrupolar transfer coefficient $T_{v,Q_{mIR/vis}}^{(2),ijkm}$ that involves a field derivative computed over just the interfacial layer.

Thus, the full form of the interfacial response can be written as a sum of two interfaces, each with a dipole-allowed term and a single higher order term due to field discontinuity.

$$E_{\text{interfacial}}^{(2),ssp} = \left(\chi_1^{(2),yyz} T_1^{yyz} + \chi_{1,Q_{mIR}}^{(2),yyzz} T_{1,Q_{mIR}}^{yyzz} \right) + \left(\chi_2^{(2),yyz} T_2^{yyz} + \chi_{2,Q_{mIR}}^{(2),yyzz} T_{2,Q_{mIR}}^{yyzz} \right) \tag{5.16}$$

$$E_{\text{interfacial}}^{(2),sps} = \left(\chi_1^{(2),yzy} T_1^{yzy} + \chi_{1,Q_{vis}}^{(2),yzyz} T_{1,Q_{vis}}^{yzyz} \right) + \left(\chi_2^{(2),yzy} T_2^{yzy} + \chi_{2,Q_{vis}}^{(2),yzyz} T_{2,Q_{vis}}^{yzyz} \right) \tag{5.17}$$

The normal component input field profile is certainly complicated at the interface, but we can perform a simplified analysis of $T_{v,Q_{vis/mIR}}^{ijkm}$ using some assumptions. We present the analysis for the *ssp* experiment of Eq. (5.14) but what follows applies equally well to the *sps* experiment of Eq. (5.15). We start by writing out $\overleftarrow{t}_{0,z(p,z)}^{mIR}$ in polar

form and then the derivative in brackets leads to an expression of the form from Eq. (5.10) with $\exp\left(i\phi t^{mIR}_{0,v,(p,z)}\right)=\exp\left(ik_z^{mIR}z\right),$ to within a known constant phase factor.

$$\frac{\partial\left|\vec{t}^{\,mIR}_{0,v(p,z)}\right|\exp\left(i\phi t^{mIR}_{0,v,(p,z)}\right)}{\partial z}=\left[ik_z^{mIR}\left|\vec{t}^{\,mIR}_{0,v(p,z)}\right|+\frac{\partial\left|\vec{t}^{\,mIR}_{0,v(p,z)}\right|}{\partial z}\right]\exp\left(i\phi t^{mIR}_{0,v,(p,z)}\right) \tag{5.18}$$

Of the two terms in brackets it should be the case that $ik_z^{mIR}\left|\vec{t}^{\,mIR}_{0,v(p,z)}\right|\ll\partial_z\left|\vec{t}^{\,mIR}_{0,v(p,z)}\right|$ because of the abrupt change in the field magnitude. The form of $\left|\vec{t}^{\,mIR}_{0,v(p,z)}\right|$ is complicated but will follow a continuous path through the boundary in order to connect the amplitudes on either side. A very simple approximation considers a linear change through the interface where we connect the field magnitudes on the z^+ and z^- side of the boundary over the thickness of the nonlinear interfacial layer $d_{\text{interface }v}$. so that

$$\frac{\partial\left|\vec{t}^{\,mIR}_{0,v}\right|}{\partial z}=\frac{\left|\vec{t}^{\,mIR}_{0,v^+}\right|-\left|\vec{t}^{\,mIR}_{0,v^-}\right|}{d_{\text{interface }v}} \tag{5.19}$$

Now, upon inspection of Figure 5-10 we can see that for interface 1, $\left|\vec{t}^{\,mIR}_{0,1^+}\right|-\left|\vec{t}^{\,mIR}_{0,1^-}\right|>0$ and for interface 2, $\left|\vec{t}^{\,mIR}_{0,2^+}\right|-\left|\vec{t}^{\,mIR}_{0,2^-}\right|<0.$ Thus, when Eq. (5.19) is inserted into Eq. (5.14) (remembering to pick up the phase factor from Eq. (5.18)), and the analogous expressions for the visible are inserted into Eq. (5.15), the quadrupole transfer coefficient results in a π phase shift (sign change) on the quadrupolar coupling term of interface 2 relative to the same term at interface 1. We also see that the quadrupolar transfer products are related to the dipolar interfacial transfer products through a simple

scaling factor (remembering that $\partial_z \left| \overleftarrow{t}_{0,v}^{vis/mIR} \right|$ is just a real number as indicated in Eq. (5.19)). The relations are

$$T_{1,Q_{mIR}}^{yyzz} = \frac{\left| \partial_z \left| \overleftarrow{t}_{0,1}^{mIR} \right| \right|}{\left| \overleftarrow{t}_{0,1}^{mIR} \right|} T_1^{yyz} \tag{5.20}$$

$$T_{2,Q_{mIR}}^{yyzz} = -\frac{\left| \partial_z \left| \overleftarrow{t}_{0,2}^{mIR} \right| \right|}{\left| \overleftarrow{t}_{0,2}^{mIR} \right|} T_2^{yyz} \tag{5.21}$$

$$T_{1,Q_{vis}}^{yzyz} = \frac{\left| \partial_z \left| \overleftarrow{t}_{0,1}^{vis} \right| \right|}{\left| \overleftarrow{t}_{0,1}^{vis} \right|} T_1^{yzy} \tag{5.22}$$

$$T_{2,Q_{vis}}^{yzyz} = -\frac{\left| \partial_z \left| \overleftarrow{t}_{0,2}^{vis} \right| \right|}{\left| \overleftarrow{t}_{0,2}^{vis} \right|} T_2^{yzy} \tag{5.23}$$

We point out that, as long as the effective interfacial thickness does not change with the organic thin film thickness (especially for the outer interface), these scaling factors are constant with $d_{\text{PTCDI-C}_8}$ since the magnitude and its derivative through the interface are proportional (i.e. $\partial_z \left| \overleftarrow{t}_{0,v} \right| \propto \left| \overleftarrow{t}_{0,v} \right|$, numerically verified for both input beams).

We can absorb the scaling factors on the quadrupolar transfer products into the definitions of the electric quadrupolar susceptibilities (indicated by a hat in Eqs. (5.26) - (5.29)), but we will factor out the sign and rewrite Eqs. (5.16) and (5.17) using effective interfacial susceptibilities:

$$E_{\text{interfacial}}^{(2),ssp} = \chi_{1,eff}^{(2),yyz} T_1^{yyz} + \chi_{2,eff}^{(2),yyz} T_2^{yyz} \tag{5.24}$$

$$E_{\text{interfacial}}^{(2),sps} = \chi_{1,eff}^{(2),yzy} T_1^{yzy} + \chi_{2,eff}^{(2),yzy} T_2^{yzy} \tag{5.25}$$

with

$$\chi_{1,eff}^{(2),yyz} = \chi_{1}^{(2),yyz} + \hat{\chi}_{1,Q_{mIR}}^{(2),yyzz} \tag{5.26}$$

$$\chi_{2,eff}^{(2),yyz} = \chi_{2}^{(2),yyz} - \hat{\chi}_{2,Q_{mIR}}^{(2),yyzz} \tag{5.27}$$

$$\chi_{1,eff}^{(2),yzy} = \chi_{1}^{(2),yzy} + \hat{\chi}_{1,Q_{vis}}^{(2),yzyz} \tag{5.28}$$

$$\chi_{2,eff}^{(2),yzy} = \chi_{2}^{(2),yzy} - \hat{\chi}_{2,Q_{vis}}^{(2),yzyz} \tag{5.29}$$

It is instructive to compare the forms of Eqs. (5.24) and (5.25) with Eq. (5.3) to see that the functional form for the two interfaces are the same. Eqs. (5.26) - (5.29) show that the effective interfacial response ($\chi_{v,eff}^{(2),ijk}$ from Eq. (5.11)) can be expressed as the sum of the dipolar interaction and the quadrupolar interaction that *behaves* like the dipolar susceptibility in the presence of the $C_{\infty,v}$ symmetry at the interface. That is, although the sign of the fourth rank tensors are not subject to reversal upon inversion of the *z*-axis (as with the dipolar response), the field gradients cause a sign change in this system. The new definition of the electric quadrupolar susceptibilities contain both the intrinsic electric quadrupolar response at the interface (small) as well as effects from the field gradients (large, as can be seen for the mIR in the *ssp* experiment in Figure 5-10 and the visible in the *sps* experiment in Figure 5-11) so that the interfacial higher order susceptibilities $\hat{\chi}_{v,Q_{vis/mIR}}^{(2),ijkm}$ may be of comparable magnitude *or larger than* the interfacial electric dipole susceptibilities.

In this approximation we will analyze possibilities for the relative contributions from the two terms contained in $\chi_{v,eff}^{(2),ijk}$ in Eqs. (5.26) - (5.29) in order to rationalize the fit results for the interfacial response in Section 5.5. First, we consider all susceptibilities as singly resonant so that they have real amplitudes. The first term in

each equation is the electric dipole term that has an independent response at each interface ($\left|\chi_2^{(2),ijk}\right| \neq \left|\chi_1^{(2),ijk}\right|$). Even with unequal magnitude, we specify that the amplitude sign is necessarily opposite at each interface due to the inversion symmetry present in the PTCDI-C_8 molecule (see Figure 5-1). As discussed in Section 5.4.2, for electric dipolar response it must be the case that molecular inversion symmetry is broken at the interface so that only the imide carbonyl groups at one end of the molecular layer at each interface pointing away from the organic thin film (Figure 5-5) contribute to the electric dipolar response. The second terms are due to discontinuity of the input field whose normal component is involved in the interaction. The fourth rank elements $\hat{\chi}_{v,Q_{vis/mIR}}^{(2),ijkl}$ are not subject to sign change upon inversion of the *z*-axis so that, while the interfaces may have unequal magnitudes for a given vibrational mode, they should generally have the same sign. Next, we discuss evidence in the data that suggests that although there are likely appreciable interfacial dipolar terms present, there are also higher order terms so that the dipole approximation may not be an appropriate description for the interfacial response from this system.

5.6.2 *Evidence for Higher Order Interfacial Response*

The presence of both an electric dipole allowed response as well as electric quadrupolar coupling to input fields within the effective interfacial susceptibility leads to the possibility of fairly complicated response at the outer interface as a function of PTCDI-C_8 thickness. Whereas we might expect that the dipole allowed interaction magnitude should asymptotically decrease to some small number due to increased surface roughness (broadening of the net polar orientation distribution), the

interpretation for how bulk-like interfacial terms should change is less clear. Electric quadrupolar coupling is sometimes referred to as a "nonlocal" effect in that the interactions are not confined to a single molecule as the smallest volume element in condensed phases (as in the way we think of dipole-type interactions), rather, there may be cooperative interactions so that groups of molecules may be responsible for the overall higher order interfacial terms.[234,374] A simple example is given by considering the electric quadrupolar interaction with a single molecule versus a dimer, trimer, etc. The structures of such groups are not well defined so that even as the morphology at the outer interface may change with thickness, the active volume units may change depending on molecular organization. That is, in one interfacial film morphology it may be that single molecules provide the dominating electric quadrupolar response and in a different morphology it may be groups of molecules.

The thickness dependent response of the two possible contributions from an interface may be complicated; however, we can investigate the relative magnitudes of electric dipole response to electric quadrupole response by considering just the sign of the susceptibilities from the fit results in Section 5.5.5. We will confine our analysis for the outer interfacial contribution to the region <150 nm for all fit results. The fitting routine in this region was more constrained by data for all surface preparations. Our analysis will proceed by considering the sign of each susceptibility contribution using three constraints: (1) the dipolar contribution must have opposite signs at each interface, (2) the sign of the interfacial quadrupolar interaction should match the sign of the bulk contribution from the fit results, and (3) the sign of the effective interfacial susceptibilities from the fit results must be obtainable by the relations between electric

dipole and electric quadrupolar susceptibilities given in Eqs. (5.26) - (5.29). Using these conditions we have determined for each mode in both experiments the relative magnitude and sign of each term in the effective susceptibilities. The results are presented in

Table 5-5. The last two columns of the table give the relative magnitude of the input field dipolar and quadrupolar susceptibilities where we have replaced the symbol χ by the sign of the corresponding term. We point out that, with the exception of ν_{as} for *ssp*, the fit routine always resulted in a common $\text{sign}\left[\chi^{(2),ijk}_{2,eff}\right]$ for both bare and ODTMS functionalized SiO_2 interfaces so that the same analysis applies to both surface preparations.

Table 5-6. Summary results of the sign analysis for the relative interfacial contributions from the electric dipolar and electric quadrupolar response to the effective surface susceptibility.

		Fit Results			Conditions Satisfying $\text{sign}\left[\chi^{(2),ijk}_{v,eff}\right]$:	
Experiment	Mode	$\text{sign}\left[\chi^{(2),ijk}_{1,eff}\right]$	$\text{sign}\left[\chi^{(2),ijk}_{2,eff}\right]^a$	$\text{sign}\left[\hat{\chi}^{(2),ijkm}_{Q_{mIR/vis}}\right]$	$\chi^{(2),ijk}_{1} + \hat{\chi}^{(2),ijkm}_{1,Q_{mIR/vis}}$	$\chi^{(2),ijk}_{2} - \hat{\chi}^{(2),ijkm}_{2,Q_{mIR/vis}}$
ssp	ν_s	+	−	−	$\left\|+\right\|^{(2),yyz}_{1} > \left\|-\right\|^{(2),yyzz}_{1,Q_{mIR}}$	$\left\|-\right\|^{(2),yyz}_{2} > \left\|-\right\|^{(2),yyzz}_{2,Q_{mIR}}$
	ν_{as}	−	+ (bare) − (ODTMS)	−	$\left\|+\right\|^{(2),yyz}_{1} < \left\|-\right\|^{(2),yyzz}_{1,Q_{mIR}}$	$\left\|-\right\|^{(2),yyz}_{2} < \left\|-\right\|^{(2),yyzz}_{2,Q_{mIR}}$ $\left\|-\right\|^{(2),yyz}_{2} > \left\|-\right\|^{(2),yyzz}_{2,Q_{mIR}}$
sps	ν_s	+	−	+	$\left\|-\right\|^{(2),yzy}_{1} < \left\|+\right\|^{(2),yzyz}_{1,Q_{vis}}$	$\left\|+\right\|^{(2),yzy}_{2} < \left\|+\right\|^{(2),yzyz}_{2,Q_{vis}}$
	ν_{as}	+	−	+	$\left\|-\right\|^{(2),yzy}_{1} < \left\|+\right\|^{(2),yzyz}_{1,Q_{vis}}$	$\left\|+\right\|^{(2),yzy}_{2} < \left\|+\right\|^{(2),yzyz}_{2,Q_{vis}}$

An example analysis can be performed for the symmetric stretch in the *ssp* experiment. The fit results in Figure 5-12(a) indicate that the sign of the contribution from interface 1 ($\text{sign}\left[\chi^{(2),yyz}_{1,eff}\right]$) is positive at all thicknesses, whereas Table 5-4 shows

$\text{sign}\left[\chi_{2,eff}^{(2),ijk}\right]$ and $\text{sign}\left[\hat{\chi}_{Q_{mIR}}^{(2),yyzz}\right]$ are both negative. In order to arrive at the overall signs for the effective interfacial susceptibilities, it must be that the dipolar interaction $\chi_{v}^{(2),yyz}$ is positive (negative) at the outer (inner) interface and that the magnitude of the dipole term is larger than the mIR quadrupolar coupling term at both interfaces. This is expressed in the last two columns of Table 5-6.

The table results indicate that there are various conditions for which either the electric dipole interactions or quadrupolar couplings may dominated the effective interfacial response. Interpreting the connection between the results in Table 5-6 and the average molecular orientation at each interface may be ambiguous as we cannot quantify the individual absolute dipolar and quadrupolar contributions; we have information only about their relative magnitudes. Nevertheless, we can use the information we have and present a physical picture that is consistent with the sign analysis and parameter fit results from the last section. We begin with a discussion on important factors affecting the relative interfacial contributions.

It is likely that $\left|\chi_{v}^{(2),ijk}\right|$ is comparable to $\left|\hat{\chi}_{v,Q_{mIR/vis}}^{(2),ijkm}\right|$ in all cases but their relative magnitudes depend on the molecular orientation leading to cases where one or the other contribution is largest. Since we have absorbed the effects of the large input field interfacial gradient into $\hat{\chi}_{v,Q_{mIR/vis}}^{(2),ijkm}$, its magnitude will also depend on the dielectric environment. It has been pointed out that, for single interface systems, in the limit that the indices of the bulk materials are matched on either side of an interface (e.g. interface of ice and water), the gradient becomes zero and there can be no interfacial quadrupolar coupling to the input beams.[171] This has been used to demonstrate whether the major

interfacial contribution is due to symmetry breaking (dipolar interaction) or gradient coupling (quadrupolar interaction) by varying the material (refractive index) adjacent to the nonlinear interface.[234] In the thin film geometry, the result of index matching within the thin film layers is that the interfacial gradient becomes matched to the nonzero bulk gradient (Section. 5.5) so that quadrupolar coupling is still possible but the interfacial terms will be on the order of the same quantities in the bulk, but integrated over a much smaller volume. For our system, the bulk indices on either side of interface 2 (PTCDI-C_8 − SiO_2) are more closely matched than for interface 1 (PTCDI-C_8 − Air) as can be seen in Figure 4-2.[397] This manifests as a smaller jump in the discontinuous input field magnitudes at the buried interface in Figure 5-10 and Figure 5-11. Thus, the results for the relative magnitudes at the buried interface in Table 5-6 are subject to consideration for the smaller discontinuity at that interface leading to smaller quadrupolar coupling terms relative to the outer interfacial higher order contributions.

Molecular orientation is certainly playing a significant role in the results for $\chi_{v,eff}^{(2),ijk}$ as well. The dipolar terms for each mode provide a straightforward connection between average polar orientations of modes; whereas the quadrupolar (nonlocal) interactions depend on molecular structure as well but in a more complicated way. The symmetric and asymmetric dipolar interactions provide orthogonal measures of orientation of the perylene core that can ideally be used to deduce average molecular orientation as discussed in Section 5.4.2. In the limit that the quadrupolar coupling terms are insensitive to molecular orientation at the interface, the effective surface susceptibilities for each experiment should vary as depicted in Figure 5-6. For tilt along the long axis of the perylene core, the *ssp* contribution for ν_s will be largest for

molecules standing completely upright (*sps* should be zero in the limit they are completely upright). For tilt along the short axis, the *sps* contribution for ν_{as} will be maximal for molecules that have no tilt (that is, when the short axis is parallel to the substrate plane, then *ssp* will be minimal). With this discussion we move to detailing a physical picture for molecular orientation at each of the interfaces of the organic thin film. We begin with the buried interface.

5.6.2.1 SiO_2 – PTCDI-C_8 Interface

The sign analysis results for the buried interface in Table 5-6 show that the electric dipole contribution always dominates the *ssp* response of ν_s, whereas for ν_{as} the dipole interaction is larger for ODTMS substrates and quadrupolar coupling to the mIR is larger for bare SiO_2. This is consistent with a high degree of polar orientation along the long axis of the perylene core for both substrate surface preparations leading to a large dipole contribution from ν_s. At the same time, the relative twist along the long axis (tilt of the short axis) may be minimal for bare SiO_2 leading to a situation where the higher order term is larger and vice versa for ODTMS. The sign analysis for the buried interfacial response from the *sps* experiment results in a larger visible quadrupolar coupling term in all cases. This may be due to large quadrupolar coupling to the visible or small dipolar interactions. In either case, we can use the information obtained from the sign analysis combined with the relative magnitudes of the effective susceptibilities obtained from the fits to deduce the relative dipolar contribution for both substrate surface preparations.

We return to the results in Table 5-4 and

Table 5-5 and make some qualitative statements about any differences in molecular orientation at the buried interface for bare SiO_2 and ODTMS treated substrates. Again, if we consider that the higher order terms at each interface are relatively insensitive to molecular orientation, and that the optical constants of the ODTMS SAM do not significantly alter the interfacial field gradient relative to bare SiO_2, we can compare the relative magnitudes of the interfacial dipolar contribution for both modes on each substrate surface preparation. For instance, since we have deduced that $\left|-\right|_2^{(2),yyz} > \left|-\right|_{2,Q_{mIR}}^{(2),yyzz}$ for ν_s and we see from Table 5-4 that $\left|\chi_{2,eff}^{(2),yyz}\right|$ is larger for ODTMS versus bare, we conclude that ODTMS has a larger dipolar contribution for this mode. These relations can be deduced for the remaining cases and the results are collected in Table 5-7. We find that the ODTMS surface preparation results in the first monolayer of PTCDI-C_8 standing more upright but with more tilt across the short axis of the perylene core relative to the first monolayer on ODTMS functionalized SiO_2. This is consistent with XRR and AFM measurements on a similar molecule (5 carbon chain version of PTCDI) where it was found that the initial layer grown on bare SiO_2 is thinner than the same layer on an alkyl-SAM modified substrate, consistent with an interfacial organic phase that is more reclined along the long axis.[103] A similar finding was reported for GIXD data from PTCDI-C_8 thin films grown on SiO_2 under conditions similar to ours where the initial monolayer phase was thinner than the bulk terraces.[95] Our previous *ssp* study of very thin films of PTCDI-C_8 on the same substrate surface preparations concluded that the interfacial monolayer phase on bare SiO_2 were subject to reorganization to an even more reclined phase upon thermal annealing.[96] In that study we were not able to deduce the relative amount of tilt between the two surface

preparations prior to thermal annealing, only that there was a change due to thermal annealing. Also, analysis of the relative average tilt along the short axis was hindered by low S/N for ν_{as} in that study. Here we provide evidence that there is indeed a difference on these two surface preparations. This result has important implications for charge mobility performance in PTCDI-C_8 oFETs.

Table 5-7. Summary results for analysis of the substrate preparation with the larger dipolar response at the buried interface.

experiment	mode	substrate prep with larger $\chi_2^{(2),ijk}$ contribution
ssp	ν_s	ODTMS
	ν_{as}	ODTMS
sps	ν_s	bare
	ν_{as}	bare

5.6.2.2 PTCDI-C_8 – Air Interface

There are a couple features to point out from the thickness dependent response of the outer interfacial contributions in Figure 5-14 and Figure 5-15. First, as noted in the Section 5.5.5, the feature present in the dipole approximation at around 200 – 300 nm is significantly diminished, indicating that inclusion of bulk terms is important for thicker films due to this physically more meaningful result. By extension, higher order interfacial terms are likely important. For thicknesses <100 nm, we see that in most cases there is a rapid decrease in $\left|\chi_{2,eff}^{(2),ijk}\right|$, with the exception of Figure 5-15(b) where the magnitude changes in the same way but much more gradually. This result is likely a circumstance related to difficulties with accounting for the nonresonant response to be discussed in Section 5.7.2. Nevertheless, the changes in the effective susceptibility at the outer interface can be rationalized as in Section 5.4.4 by considering how the dipolar

contribution changes with increased organic thickness. For instance, the decrease in $\left|\chi_{1,eff}^{(2),ijk}\right|$ for the symmetric mode in both experiments is consistent with the loss of dipolar contribution and can be interpreted as an increase in surface roughness leading to broadening of the average polar orientation distribution of molecules at the outer interface. As before, we cannot separate broadening effects from changes in the orientational distribution so that a similar analysis performed on the buried interface in the last section is not possible for the outer organic interface. However, we can now provide an explanation for a feature noted in the outer interface-only analysis performed in Section 5.4.4. A sign change in the outer interfacial response may now be interpreted as a change in the relative contribution from the dipolar and quadrupolar interactions. From Table 5-6 we see that loss of dipolar response will in all cases change the sign of the outer interfacial effective susceptibility.

5.7 OTHER EFFECTS

The constrained model reported in Section 5.4 performed remarkably well for predicting major features in the detected signal intensity in most cases, indicating the signals are primarily due to interfacial response. Then, in Sections 5.5 and 5.6 we expanded the thin film model and data analysis to include higher order responses in the detected signal. This allowed for separating and extracting a qualitative picture of molecular structure at the buried interface. While we see this work as a significant step in the direction of solving the two-interface problem of VSFG applied to organic thin film systems, it is important to point out that the analysis of various VSFG source terms is semi-quantitative at best. Quantitative analysis of the various source terms was not

possible for several reasons. Here we point out some additional effects that may have a significant impact on the detected signal intensity and fitting results. The goal in this section is to highlight possible complicating factors and present some suggestions for improving on this work.

5.7.1 *Experimental*

There were primarily two experimental aspects that led to ambiguity in the data interpretation. They are related to sample preparation and axes calibration. While we made every effort to produce pristine wedged samples, there were a number of factors that were out of our experimental control. These can be generally divided into nonidealities with the substrate surface preparation prior to organic deposition and nonidealities in the wedges themselves. Frequency calibration issues had to do with compounding errors from wavelength calibration for the 800 nm characterization as well as the SFG wavelength axis, and the thickness axis was subject to errors from our SE characterization from Section 5.2.3.

The substrates presented a challenge in terms of preparing homogeneous surfaces over relatively large areas, especially for the ODTMS functionalized substrates. Any heterogeneity along the VSFG raster can change the molecular orientation of PTCDI-C_8 at the buried interface and may translate to a change at the outer interface as well. While visual inspection indicated no obvious surface heterogeneity along the raster direction, microscopic surface heterogeneity was still possible. Thus, the ideal case of a constant response from the buried interface at all raster points along the gradient may not be valid. To further highlight this possibility, one needs only to consider VSFG microscopy studies to illustrate that spatial

heterogeneity is possible in any VSFG measurement on various length scales.[284,285] In fact, we have observed for other samples of PTCDI-C_8 thin films that the VSFG intensity data may be consistent across multiple raster spots for a single thin film thickness (and over a much smaller area) but may occasionally vary from spot to spot. While the origins of these variations are not known, their presence articulates the exquisite interfacial sensitivity of VSFG. Spatial heterogeneity is likely present to some degree in all datasets in Figure 5-3 and Figure 5-4. The additional step of functionalizing the surface with ODTMS increases this possibility and may be partially responsible for the bumps in the outer mode amplitudes above 200 nm in Figure 5-9, Figure 5-14, and Figure 5-15. That is, since data in this region are only from ODTMS substrates, any nonidealities in the surface preparation are more likely to present themselves in the fit results through parameter correlations. Future studies will need to focus on characterizing any surface heterogeneity or aim for characterizing individual spots by acquiring richer datasets. More will be said about possible data acquisition improvements in Section 5.7.1.

Vapor depositing the organic wedge provided the advantage of producing the linear thickness gradient needed for this study (as opposed to other organic thin film deposition techniques such as spin casting from solution); however, there are some issues that accompany this procedure. The 2-dimensional terraces formed by vapor deposited PTCDI-C_8 leads to mesa structuring, or incomplete islanding, at the outer interface that increases with organic thickness.[95,103] Topographical AFM images from samples prepared with PTCDI-C_8 deposited at 100 °C on NO substrates are shown Figure 5-16. A 2×2 μm image of an 8 nm film is inset in a 5×5 μm image of a 200 nm

film and both share the same vertical scale. The images reveal the presence of 2 – 3 incomplete layers for the 8 nm film (RMS roughness on the order of 1 – 2 nm),[96] whereas the image from the 200 nm film shows up to 10 or more incomplete layers (RMS on the order of 5 nm) and a substantially different surface morphology, showing needle-like islands.

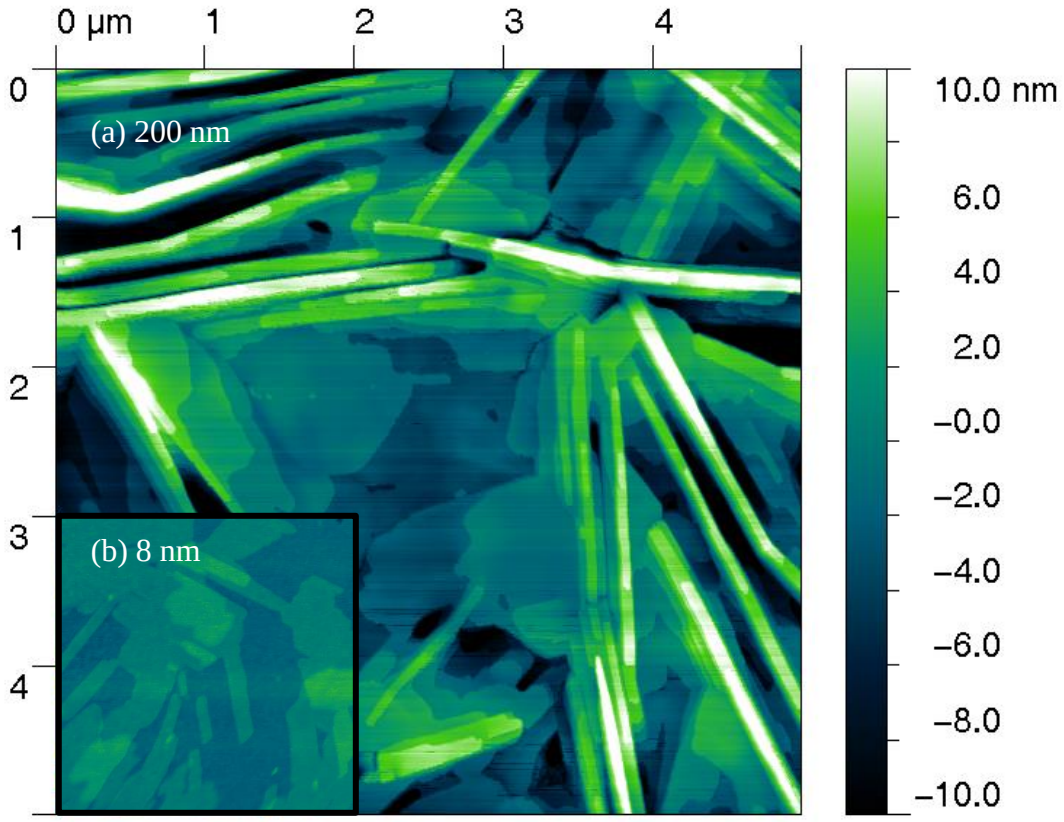

Figure 5-16. Topographical AFM images of PTCDI-C_8 vapor deposited on NO substrates heated to 100 °C during the deposition. The outer interfacial topography is shown for (a) 5×5 µm of a 200 nm film and (b) is an inset 2×2 µm image of an 8 nm film.[i] Images share a common vertical scale.

The change in roughness and morphology at the outer interface at larger thicknesses is likely to lead to a VSFG response that behaves in a complicated way as a function of organic thickness. The consequence of this could also be in a density

[i] I thank Z. Sohrabpour for collecting AFM images from the 200 nm film.

gradient through the film (as indicated in the SE analysis in Section 5.2.3) that would complicate the analysis of bulk contributions as well as the computation of the transfer products. The SE analysis indicated the index may be graded to some small extent, especially for thicknesses >150 nm. Thus, the assumption that the deposited thin film wedges were linear with constant density through the bulk is an approximation that breaks down at the thicker end of the 400 nm wedges. A small nonlinearity in the thickness axis may have an appreciable effect on extracted parameters.

The calibration for the frequency axis was subject to some error. We estimate the error to be ±4 cm^{-1} due to compounding errors from calibration at the VSFG and visible wavelengths. Even an error this small can have an impact on extracted parameters when tying parameters together across multiple datasets. Thus we point out the necessity of a highly accurate wavelength calibration when performing simultaneous data fits. In addition, the frequency dependent refractive index of PTCDI-C_8 obtained from mIR SE[397] resulted in Gaussian oscillators with mode centers that did not match exactly the bulk center frequencies observed from FTIR of nearly identical samples. FTIR center for the ν_s was +3 cm^{-1} while ν_{as} was -2 cm^{-1}. We have shown that the mIR refractive index results in transfer products that vary appreciably through the vicinity of each vibrational mode so that fit results depend considerably on consistency between the refractive index and experimental frequency axes.[397] The difference is likely due to a couple effects. The FTIR analysis does not take into account thin film interference effects that may shift an oscillator's apparent center as a function of film thickness, and the mIR SE data analysis was subject to some errors due to evidence of other effects such as a graded index and optical anisotropy. Another factor that has not

been considered is the possibility for nonlinear effects for all refractive indices.[462] Since VSFG is a pulsed laser experiment, these third order effects are also possible.

Another consequence of variable film morphology with thickness is the possibility for a more complicated bulk response. Quadrupolar coupling is expected to be decreased in isotropic materials relative to well-ordered terraces[374] so that there is likely some variation in $\chi_{Q_{vis}}^{(2),ijkm}$ and $\chi_{Q_{mIR}}^{(2),ijkm}$ through the bulk of the organic. The largest bulk contributions should be present in the first well-ordered terraced layers so that the fit result may be underestimating the bulk contribution at the thinnest end of the organic wedge. On the other hand, the bulk transfer products tend to decrease very rapidly in this region (see Figure 5-10 and Figure 5-11) so that these terms may be negligible at thin organic thicknesses. In either case, bulk contributions may not be the only complicating factor in the detected response. Next we discuss the vibrationally nonresonant susceptibility.

5.7.2 *Nonresonant Susceptibility*

One of the largest factors confounding our data analysis was the observation of an appreciable nonresonant response, especially in the *ssp* measurements but also observable in the *sps* data. Generally speaking, since any nonresonant term is, by definition, not resonantly enhanced its source may be from a number of possible interfacial or bulk responses. Since a detailed understanding of the nonresonant response is typically not necessary for VSFG measurements, it is standard practice to combine all interfacial and bulk terms into a single effective susceptibility. This poses a problem for multilayer thin film systems where we must calculate the thickness

dependent nonresonant amplitude (magnitude and phase) using transfer products from the thin film model. The transfer products are different depending on which interfaces or which bulk media are acting as source terms.

We found that characterizing the source of the nonresonant response was problematic. The simple model we used was based on assigning nonresonant susceptibilities to each substrate by fitting a region around 1740 cm^{-1}, presumably outside of any vibrational response, assuming the total SFG response is due to a nonresonant contribution at the Si–SiO_2 interface. The response was floated as a real constant value so that all dependence on organic thickness was contained in T_3^{ijk}. Agreement between the model and intensity data were satisfactory for all *sps* data and for *ssp* from NO substrates, but only marginal for *ssp* from TO substrates. This is an indication that out assumptions are not valid. The tails of the Lorentzian oscillators used to describe our vibrational resonances covered our entire spectral window and had a non-negligible effect on the small nonresonant response. Also, our conjecture that the response is strictly from the Si-SiO_2 interface may not be a complete description of the nonresonant susceptibility. We also evaluated the inclusion of bulk terms from the oxide layer for TO substrates but this resulted in only minimal improvement. We attempted to parameterize the nonresonant simultaneously with the resonant fit but this always resulted in unphysical results where resonances became quite wide and the total nonresonant contribution was obviously too large in areas of minimal vibrational response. Without knowing the sources of the nonresonant response, we may always deduce how the magnitude varies with thickness by considering spectral regions free of vibrational resonances, but we still have no phase information. Fitting the nonresonant

response to multiple source terms (Eq. (5.11)) in these regions was ambiguous because of low S/N and issues with being in regions that are not truly free of vibrationally resonant response so that even if we recovered a better fit at the intensity level, the overall phase of the nonresonant contribution was still questionable. Then, in regions of large vibrational response, the interferences between resonant and nonresonant responses were not well described, which had a significant impact on modeled signal intensity.

Inclusion of the simple model of $\chi_{NR}^{(2)}$ from the Si–SiO_2 interface in the fitting routines served to improve the fits in some areas, while degrading agreement in others. In the end, we chose to use the Si–SiO_2 model in order to retain a simpler model. Our assumption was that the parameterization of the outer interfacial resonant amplitudes would, at least partly, absorb this deficiency through parameter correlations leading to more reliable results for the buried interfaces, our primary concern. This is admittedly not ideal; however, we believe that the problem of the nonresonant response does not deter from the main goal of this work: to provide experimental evidence that optical interference effects are certainly very important for VSFG applied to thin film systems and that the thin film interference model provides a good description of both interfacial was well as bulk resonant contributions. A greater understanding of the nonresonant susceptibility is critical to better parameterize this source term and separate the effect it has on the resonant data. Some options for dealing with this problem may be to explore ways to suppress the nonresonant response or obtain phase information using heterodyne-detection.[279,292,463,464]

5.7.3 *Final Comments*

Our ultimate goal is for quantification of the various source terms contributing to the total VSFG response from organic thin film systems. We acknowledge that this is a formidable task that, if it is to be reached, will be attained incrementally. To that end, we provide here some immediate steps to improve upon this work. First, parameter correlations are always going to be an issue when parameterizing data at the electric field level (as opposed to at the intensity level) due to the complicated ways in which different source terms may interfere constructively or destructively. This is a significant source of ambiguity. Reducing parameter correlations can only be done with more (and more reliable) information. Simultaneous fits to multiple datasets is very useful for constraining the fit routine, however, the first suggestion we have is to minimize the number of different physical spots from which data are to be obtained for a fit set. While this is counter to the idea of getting more information it is a significant step for obtaining reliable information by minimizing sample to sample differences since VSFG is extremely sensitive to variations at interfaces. The wedge system used in this work offered the advantage of the measurement being performed in ambient conditions (as opposed to a special cell designed to simultaneously measure VSFG on a single spot while vapor depositing the organic);[313,354] however, a major drawback was that we had to make measurements over many spots, not to mention the extensive time needed for data collection. The next suggestion is for a highly accurate wavelength calibration. Even seemingly small differences of only a wavenumber or two can translate into significant differences in the model description of the data. In particular, agreement between the mIR refractive index of the organic and the down-converted

mIR frequency axis of the VSFG data is crucial in order to correctly capture any rapid fluctuations in the transfer products in the vicinity of the mode centers. This is especially true for the *ssp* experiment as discussed in Section 4.3.1.[397]

If we are to suggest taking data from fewer spots then we must supplement with suggestions for obtaining more information from a given spot. Some experimentally viable ideas include mixed polarization experiments to gain phase information from fields generated by different polarization combinations. A carefully planned experiment using a tunable narrowband visible pulse could be used to obtain essentially the same VSFG susceptibility spectrum at different sum frequencies. By modeling the transfer products while constraining the susceptibility parameters we could have a very sensitive way to reduce parameter correlations during simultaneous fits. Multiple input angles could also be used in conjunction with proper modeling of the transfer coefficients but must also account for any variation in beam overlap. Finally, heterodyne detected or time domain experiments could be used to extract phase information from a given measurement, providing another constraint for data fitting routines.[279,292,463,464] These alternate data collection schemes for a single sample offer another advantage in that one may choose to work with a sample with optimized thin film thicknesses for very high S/N (e.g. at any of the maxima in Figure 5-3 and Figure 5-4), which can reduce data collection times considerably. Finally, a careful analysis of how susceptibility elements must be related through the microscopic hyperpolarizabilities (Section 1.3.2.8) could provide additional constraints for modeling the sample response from different polarization experiments.[427]

5.8 CONCLUSION

In this chapter we have provided compelling experimental evidence that the thin film interference model gives a complete description of optical interference effects present in interfacial nonlinear spectroscopy applied to thin film systems composed of more than a single thin film layer. Further, we have extended the interfacial model to include optical interference effects present in bulk terms. We used wedged samples and a constrained fitting model to describe our intensity data by parameterizing the sample response (susceptibilities) while using known experimental parameters to simply calculate transfer product (optical interference) effects. The results indicate that this is a step toward quantitative separation of interfacial contributions and that higher order terms are likely important for this system. In fact, we have shown that using the optical interference model that the thin film geometry offers a unique method for quantifying and separating various source terms to the total VSFG signal.

While we have concluded that bulk contributions are likely playing a role in the detected signal, it is important to emphasize that the data cannot be described well without interfacial contributions. However, we have provided evidence that higher order *interfacial* terms are likely present as well, but we were not able to quantitatively separate these from the electric dipole response. This hinders a detailed interfacial structural analysis. Nevertheless, we have presented an analysis based on the sign of the resulting resonant amplitudes that provides a physical picture of molecular structure at each interface of the organic film and that accounts for effects from possible higher order interfacial terms. The results of this analysis are consistent with a smaller electric quadrupolar contribution from the buried interface that is likely due to a smaller field

gradient across that interface due to closer index matching between adjacent materials. That is, the buried interface with which we are primarily concerned is closer to satisfying the electric dipole approximation.

The factors that have the largest influence on detected signal intensity as a function of thin film thickness are due to transfer product (optical interference) effects for both interfacial as well as bulk terms. It is interesting to note that the initial rise in the experimental intensity data happens in the range of PTCDI-C_8 thicknesses commonly used in organic semiconducting devices such as oLEDs and oFETs, from very thin to roughly 100 nm. If the experiment had only sampled those thicknesses, it would have been easy to erroneously assign such a trend to a completely bulk contribution. Or, if the experiment had sampled a thinner region with more signal intensity and compared with an experiment that sampled a much thicker film in a region with less signal intensity, the erroneous conclusion may be that there are no bulk contributions and that signal loss for thicker films is due to absorption of the mIR through the bulk. Here we have shown that thin film optical interference effects must be reliably accounted for in order to separate various source terms to the detected signal intensity.

We consider this work a step in the direction of the difficult task of quantitative separation of interfacial responses of VSFG on organic thin film multilayer systems. The extension of the model to include bulk terms due to quadrupolar coupling to the input fields can be further developed in a straightforward way to describe other possible bulk terms of the same order such as magnetic dipole coupling of the input fields to the nonlinear source electric dipole polarization as well as coupling of the quadrupolar and

magnetic dipolar nonlinear polarization to emitted fields.[235] Analysis of the transfer products associated with these types of interactions and identifying systems where they may play an important role are goals for future studies.

[i] This work was supported by the National Science Foundation under Award Number DMR-1006386. Parts of this work were also carried out in the Characterization Facility, University of Minnesota, which receives partial support from the NSF through the MRSEC program.

6 Prequel: Molecular Structure ↔ Device Function Efforts

"Basic research is when I am doing what I don't know what I am doing"

-Wernher von Braun

CHAPTER SUMMARY

This chapter provides a retrospective view of all pertinent unpublished work performed over the course of my graduate work. All experiments detailed here were completed prior to the work reported in Chapters 2 – 5. The significance of this early work is in describing important advances in developing the VSFG spectrometer into a sensitive instrument for studying organic thin film systems and experiences with *in situ* studies on PTCDI-C_8 oFETs, as well as electrically characterizing oFETs made with different processing conditions. All efforts were aimed at deducing correlations in the molecular structure ↔ device function relationship. The conclusion from this early work is that improvements are needed to obtain unique electrical characteristics for different fabrication procedures and that VSFG data modeling must include optical interference effects to further constrain data fitting routines. The latter issue became the primary focus of this dissertation. In hindsight, some of the peculiarities of these early efforts make some sense in the context of thin film interference, and should perhaps be revisited from that perspective by a future student of the project.

6.1 INTRODUCTION

In the course of any graduate work there are numerous experiments performed which were important for the direction that the project ultimately took but, for various reasons, are never officially reported. The purpose of this final chapter is to highlight some of the key experiments that were performed to get the new VSFG spectrometer up and running as well as some of the work done with *in situ* VSFG measurements on oFETs and electrical characterization as a function of time. These experiments are what ultimately led to the primary focus being on the problem of two-interfaces and optical interferences in VSFG applied to thin film multilayer systems.

In the beginning, the idea was to measure resonant VSFG from oFETs with applied gate bias and monitor a change in the response as correlated with a structural change (presumably) at the buried interface to see if there was evidence for molecular rearrangement. This was the procedure for our work in the alkyl region of P3HT oFETs[25] where we concluded that the changed VSFG response could be accounted for by the vibrationally nonresonant response due to charge accumulation. The vibrational resonances (and therefore molecular structure) remained unchanged at all biases. For PTCDI-C_8 devices, the focus has remained on the imide carbonyl stretching modes (symmetric and asymmetric) because they were expected to report on the orientation of the planar perylene core of the molecule (see Section 2.2 and 5.4.2). Early thoughts were that those modes would also be very sensitive to charge injection. While we have never observed a formally anionic VSFG active mode due to charge carrier localization as has been reported,[465] Section 6.3.3.5 details a simple procedure for modeling VSFG sensitivity to partial charges due to electron delocalization.

A large difference between our work in the alkyl region of P3HT oFETs and the imide stretching region of PTCDI-C_8 oFETs was in our experiences with fitting the vibrational resonances. Whereas with P3HT, a single interface model was sufficient to capture all features of the data, in almost all cases the imide modes had response lineshapes that could not be fit with a single Lorentzian oscillator or even Voigt lineshape.[238] In order to capture the response, each peak needed to be fit with two closely spaced oscillators, which is consistent with contributions from two chemically distinct interfaces of the thin film. The earliest experiments on PTCDI-C_8 (detailed in Section 6.2) provided evidence for the two-interface and optical interference effects that this young project had not yet considered. These experiences led to the conclusion that the two-interface problem combined with multilayer optical interference effects were important features in VSFG experimental data from PTCDI-C_8 oFETs.

The general project goal that was laid out from when I first joined the Massari Research Group has remained unchanged. It has always been the goal to use VSFG to study the active interfaces in oFETs. These are inherently buried interfaces within multilayer thin film structures. The major contribution of this dissertation is a subset of that original idea that is extensible to other systems: modeling the multiple-interface and multilayer optical interference effects in surface-specific coherent nonlinear optical spectroscopies applied to thin film systems composed of an arbitrary number of layers. This chapter highlights some of the obstacles and key experiments leading up to the major contribution; from the early issues with detection efficiencies, through *in situ* VSFG studies of oFETs with applied gate bias and as a function of electrical cycling over time. The final section is devoted to discussing electrical characterization of

PTCDI-C_8 oFETs with various processing conditions where it turned out to be very difficult to discern any obvious differences in electrical characteristics.

6.2 VSFG EARLY WORK

6.2.1 *N-Alkane Thiol SAM on Gold: PMT vs. CCD*

The earliest VSFG work was aimed at simply obtaining vibrationally resonant sum frequency generation with large enough S/N. The original sample was a model system of an alkane SAM on a gold substrate that had previously been studied with VSFG.[238,466–468] In the first versions of the VSFG spectrometer, the detection system scanned wavelengths using a monochromator, photomultiplier tube (PMT), and gated integrator. The experimental setup was greatly enhanced with the purchase of the liquid nitrogen cooled CCD (Spec-10, Princeton Instruments) that allowed for multiplex detection with much greater sensitivity. The quantum efficiencies (QE's) of PMTs are actually quite low, the best QE's are around 25% but most fall in the 10-20% QE range. The CCD has >90% QE in the VSFG spectral ranges of interest.

As an example of the improvements in detection system, a SAM of 1-octadecanethiol (ODSH) on gold substrate was prepared and VSFG was measured in the alkyl stretching region. Figure 6-1 shows *ppp* VSFG data obtained with the old PMT and monochromator scanning method (red circles) and the newly acquired CCD (black circles). The wavelength axis is not accurately calibrated and each spectrum has been normalized to each respective maximum data point. The important feature here is that the low S/N observed in the PMT data took ~19 hrs to complete whereas the CCD, with much higher S/N, was set up with only a 10 min integration time. In the CCD data

there are prominent vibrational resonances beating against the large nonresonant gold background, whereas in the PMT data the S/N is so poor there are no obvious vibrational resonances. The nonresonant response takes on the Gaussian shape of the mIR pulse power spectrum.

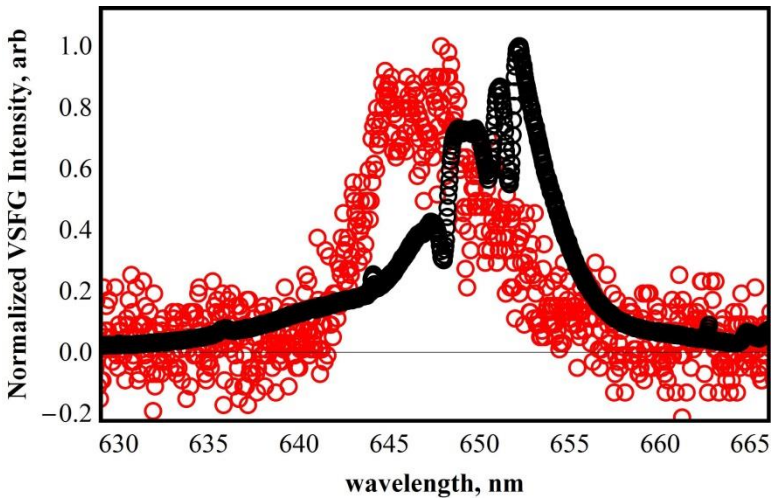

Figure 6-1. VSFG spectra of ODSH SAM on gold substrate taken with the *ppp* polarization combination. The black circles are normalized data taken with the newly acquired CCD with a 10 minute integration time. The red circles are data from the same sample taken with the old PMT and monochromator setup, which took ~19 hrs to complete. The wavelength axis is not accurately calibrated.

With the CCD detector, spectra that took many hours with poor S/N could now be obtained in a matter of seconds to minutes with much greater sensitivity. This experimental improvement was the single most important enhancement to move forward with the major project goal of studying organic thin film systems.

The struggles with the early detection system resulted in teaching the importance of a high degree of experimental control. With such low S/N it taught us to pay very careful attention to all details such as beam characteristics (tuning, timing, spectral width, chirp, focus), spot sizes at the sample, and finer points in the detection system such as signal collection and pointing, focus at the detector, and calibration.

These experiences have led to our group being able to collect data at higher S/N with smaller beam energies when using the CCD detector.

6.2.2 *Early Indication of Two Interfaces*

After the sensitivity of the CCD had been demonstrated, the project moved immediately to studying organic semiconducting thin film systems. The earliest work on PTCDI-C_8 began by using silicon wafers with a 200 nm thermally grown oxide layer (full specifications of these wafers are included in the Appendix). The choice of organic was motivated by the fact that others in the department and elsewhere had been studying that particular molecule and that it is readily available from standard chemical suppliers.[50,103,407,465] There was much already known about PTCDI-C_8 thin film structure, as detailed in Section 2.2, and this was expected to corroborate VSFG data analysis. One of the earliest experiments on PTCDI-C_8 was designed to test for any in-plane anisotropy of the sample, but as is often the case, a wholly different phenomenon turned out to be the major observation.

PTCDI-C_8 oFETs where fabricated on silicon wafers with 200 nm thermal oxide. Sample preparation is detailed in the Appendix for preparing bottom contact FET electrodes using photolithography. Four FETs were broken from the prepared wafer and PTCDI-C_8 was vapor deposited in the Frisbie group lab. The vapor deposition was performed under high vacuum (10^{-6} Torr) with the substrate FETs heated to 50 °C. The deposition was maintained at a constant rate of 0.1 Å/s up to a total thickness of 20 nm.

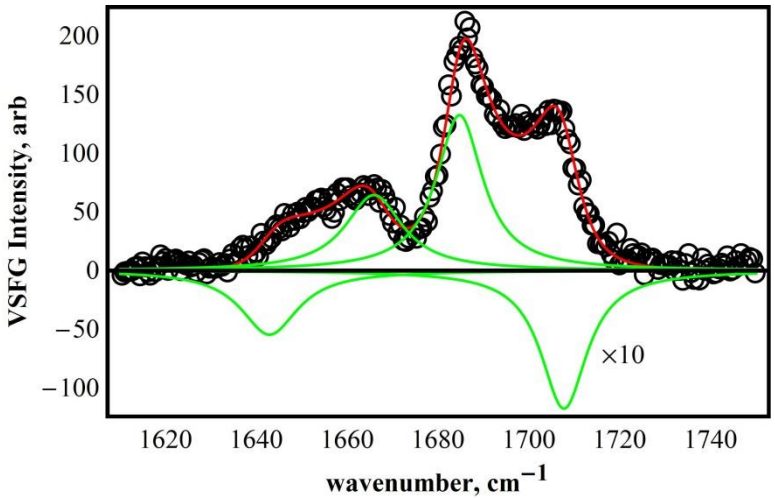

Figure 6-2. VSFG spectrum of the imide C=0 stretching region. Black circles are normalized data, the red line is the fit, and green lines show the imaginary part of the individual Lorentzian contributions scaled by 10.

In-plane anisotropy was tested by mounting a sample on a stage with azimuthal rotation. VSFG data taken in the imide C=O stretching region at multiple angles indicated no rotational anisotropy, as expected. However, spectra indicated clear double peaks for each of the symmetric and asymmetric modes (assigned in Section 2.4.3). Figure 6-2 shows VSFG data (black circles) taken at the initial azimuthal angle with fit overlaid (red line). The model used to fit the data was a simple sum of four Lorentzian oscillators.

$$I^{VSFG} = \left| \sum_{q=1}^{4} \frac{A_q}{\bar{\omega}_q - \omega_{IR} - i\Gamma_q} \right|^2 \tag{5.30}$$

The imaginary parts of the individual Lorentzian oscillators are also included in the figure scaled by 10 (green lines). The fitting routine had the widths locked between the two higher frequency modes and the two lower frequency modes. The center frequency differences $\delta\omega$ between higher and lower energy peaks for each mode were locked to be the same. The parameter fit results are shown in Table 6-1.

Table 6-1. Parameter fit results for Figure 6-2.

q	1	2	3	4
A_q (arb)	-42.0	49.5	82.4	-73.2
Γ_q (cm^{-1})	7.7		6.2	
$\bar{\omega}_q$ (cm^{-1})	1642.8	1642.8+ $\delta\bar{\omega}$	1684.7	1684.7+ $\delta\bar{\omega}$
$\delta\bar{\omega}$ (cm^{-1})	23.0			

These results are among the earliest data taken on PTCDI-C_8 oFETs and one of the few instances in which experimental data clearly indicated that each of the symmetric and asymmetric modes is bimodal. In terms of the two-interface model, this can be interpreted as each vibrational mode resulting from contributions from each interface where the interfacial contributions have opposite polar orientation leading to opposite sign on A. It is important to note that these data cannot be fit with modes with the same polar orientation and that this is significant because it indicates that VSFG is sensitive to the imide modes on one end of the PTCDI-C_8 molecule, the ends that point away from the organic thin film at each interface. These are the true interfacial functional groups. The frequency difference can be thought of as due to the different chemical environments at the buried SiO_2 interface versus the outer air boundary. However, a frequency difference of 23 cm^{-1} is rather large and highly unlikely. It is unclear why this particular measurement indicated such a large splitting between interfacial modes. It may be due to several causes, one of which may be due to a lack of consideration for optical interferences in this thin film system so that this very simple model must make up for deficiencies in the parameter assumptions.

Several months later, VSFG data were retaken on these samples, but biases had been applied in the interim. In that same set of experiments, new samples prepared from the same 200 nm thermal oxide wafer but with PTCDI-C_8 deposited to a thickness

of 40 nm were also measured. VSFG data did not indicate clear bimodal behavior in the intensity data (*ppp* and *ssp*) for either the old 20 nm samples after applied bias or the new 40 nm samples. One difference between the earlier data and the new data was in the source of the visible input pulse. In the earlier work shown in Figure 6-2, the full output of the regen (~1.2 W) was used for the VSFG experiment with about 450 mW used for generating the mIR while the remaining power (~750 mW) was spectrally narrowed in the 4f pulse shaper to give the visible pulse used in the experiment. In the later experiments, the MPA had been constructed (detailed in Section 2.3.5.1). It is not clear if or why this could have had some effect on the data since the original observation of bimodal response was never redone without applied bias.

Following this early work, the project moved to using 300 nm thermal oxide wafers because electrical characterization of oFETs prepared on 200 nm oxide were plagued with gate electrode leak currents. At the time, it was not clear the importance of optical interference effects on VSFG data. Since moving to the 300 nm oxide, unimodal intensity data for each C=O stretch has been the norm with bimodal hints observed intermittently; usually as a result of applied biases. It is interesting to consider these results in retrospect since data modeling with clear bimodal behavior is constrained for the two-interface model far better than unimodal VSFG peaks. Also, considering slices at 200 nm in the simulation plots in Chapter 4 indicates unique sensitivity to organic thickness relative to the native oxide and 300 nm oxide wafers used in Chapter 5. It may be useful for future work on VSFG data obtained from oFETs to return to the 200 nm oxide wafers.

6.2.3 *Search for Bulk Contributions*

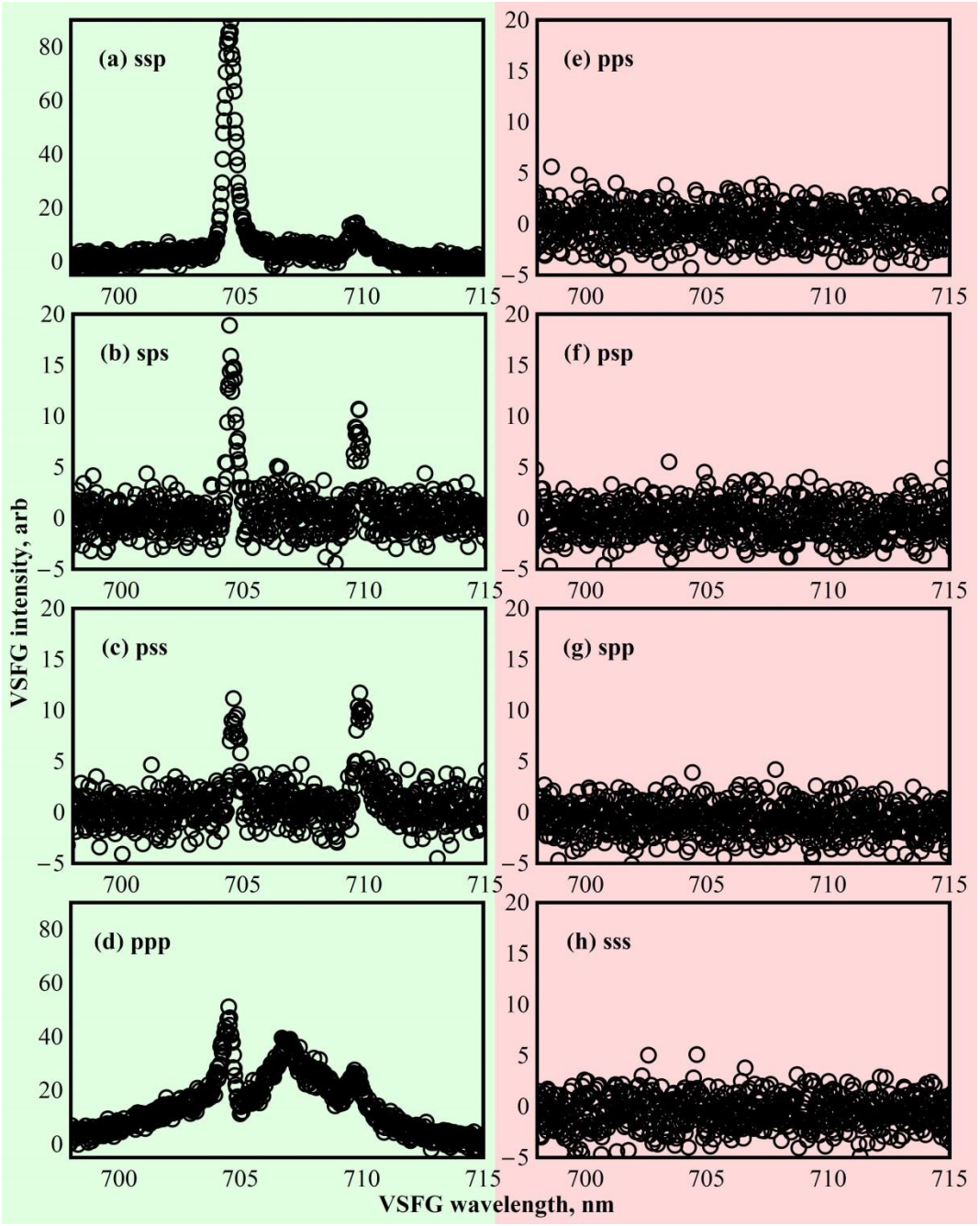

Figure 6-3. All possible polarization combination experimental data. (a) – (d) show dipole-allowed experiments while (e) – (h) show dipole forbidden data. The mode around 705 nm is the symmetric stretch, while the peak around 710 nm is a mode of the perylene ring.

The next experiments on PTCDI-C_8 were aimed at looking for evidence of any bulk contributions to the vibrationally resonant SFG. As a starting point, it was

conjectured that we could rule *in* bulk contribution if one of the forbidden polarization combinations was nonzero (all combinations *not* contained in Table 1-1). Thus, one oFET with a 40 nm organic thin film on a 300 nm thermal oxide wafer was subject to all possible polarization combinations, with the mIR tuned to the imide C=O stretching region. Figure 6-3 shows the results of all eight experiments. Only dipole-allowed experiments (Figure 6-3(a)-(d)) showed any vibrationally resonant response while all dipole-forbidden experiments (Figure 6-3(e)-(h)) were VSFG silent. Thus, we concluded from this that higher order bulk terms could not be ruled *in*, although they could not necessarily be ruled *out* since they may still contribute to the dipole-allowed polarization experiments.

6.2.4 *Early Indication of Optical Interference*

The conclusion from forbidden polarization experiments suggested that further testing was needed in order to determine if bulk terms were important in the VSFG intensity level data. An experiment was designed in which multiple thicknesses of PTCDI-C_8 were deposited on silicon wafers with a 2 nm native oxide. Thicknesses of the organic spanned a range of 20 – 200 nm. The raw data with backgrounds subtracted of VSFG measured with the *ssp* polarization combination are shown in Figure 6-4. It was thought that if bulk contributions were important, the signal intensity should grow quadratically with thickness. The reasoning behind this flawed assumption is described in Section 1.3.2.4 and is the result of expanding the expression that describes bulk contributions from very large crystals around zero thickness and truncating at the first nonzero (quadratic) term. The problem with that approach is that thin film interferences are not considered.

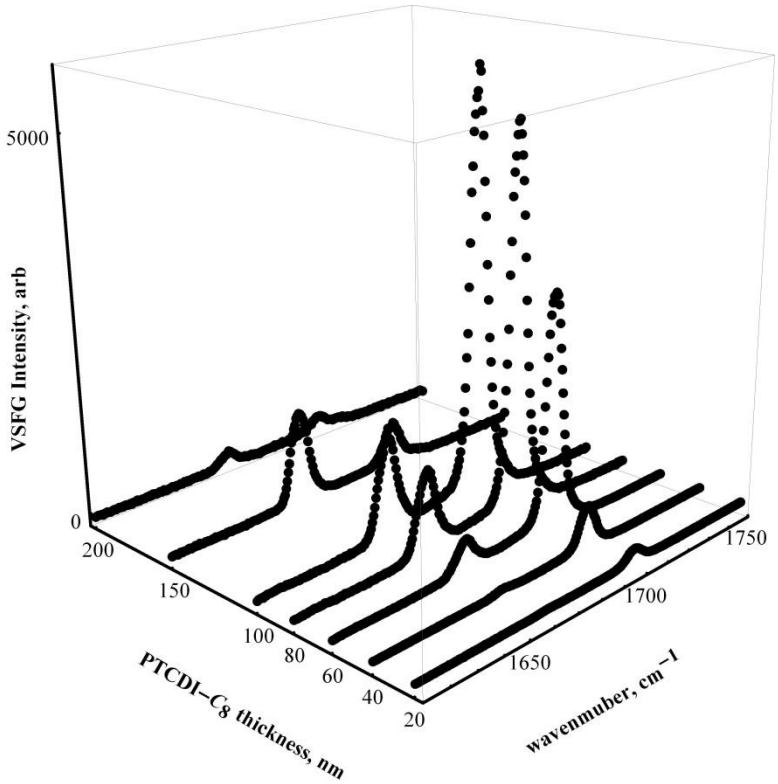

Figure 6-4. *ssp* VSFG thickness study of PTCDI-C_8 deposited on Si wafer with 2 nm native oxide.

At the time, we were not thinking too much of optical interference effects so that as data were coming out it appeared there was a clear, very dramatic, rise in signal intensity for the symmetric mode at 1700 cm^{-1} up to a thickness of 100 nm that seemed to suggest very strong bulk response, but at 150 and then 200 nm the signal intensity dropped suddenly. Also, the relative intensity of the symmetric and asymmetric mode seemed to change with thickness. The reason for these observations was not clear at the time.

The notable intensity changes with organic thickness were eventually interpreted as arising from optical interference effects, and so began the work described in the previous chapters of this dissertation. It became clear that the two-interface problem associated with organic thin films and VSFG combined with optical interference effects

was an area that had had some attention in the literature (detailed in Section 1.3.1.6), but that the issues associated with SFG and SHG applied to systems composed of more than a single thin film layer have been largely ignored. This became the major focus of this thesis project since the goal was to characterize molecular structure at the buried interface of oFETs. These are inherently two-interface and multilayer thin film structures.

6.3 *IN SITU* VSFG OFET STUDIES

One of the earliest attempts at quantifying how oFET electrical performance was dependent on molecular structure was to look for changes in VSFG response with applied gate bias. However, as PTCDI-C_8 is generally considered an n-type organic semiconductor, the mobile charge carriers are electrons which make these devices susceptible to oxidation from environmental oxygen and water. It was immediately clear that the experiment would need a special cell designed to eliminate environmental effects on device performance.

6.3.1 *VSFG Vacuum Cell Details*

A vacuum cell suitable for placement in the VSFG spectrometer was designed by us and fabricated by the physics machine shop at the University of Minnesota. A full schematic drawing showing all features and dimensions is presented in Figure 6-5. The cell includes windows for input and generated beams and three vacuum ports: one for actively pumping on, a second for an electrical feedthrough to make connections to oFETs under study, and a third for a vacuum pressure gauge. This allowed for applied

biases with *in situ* VSFG studies under high vacuum. Samples were loaded by purging

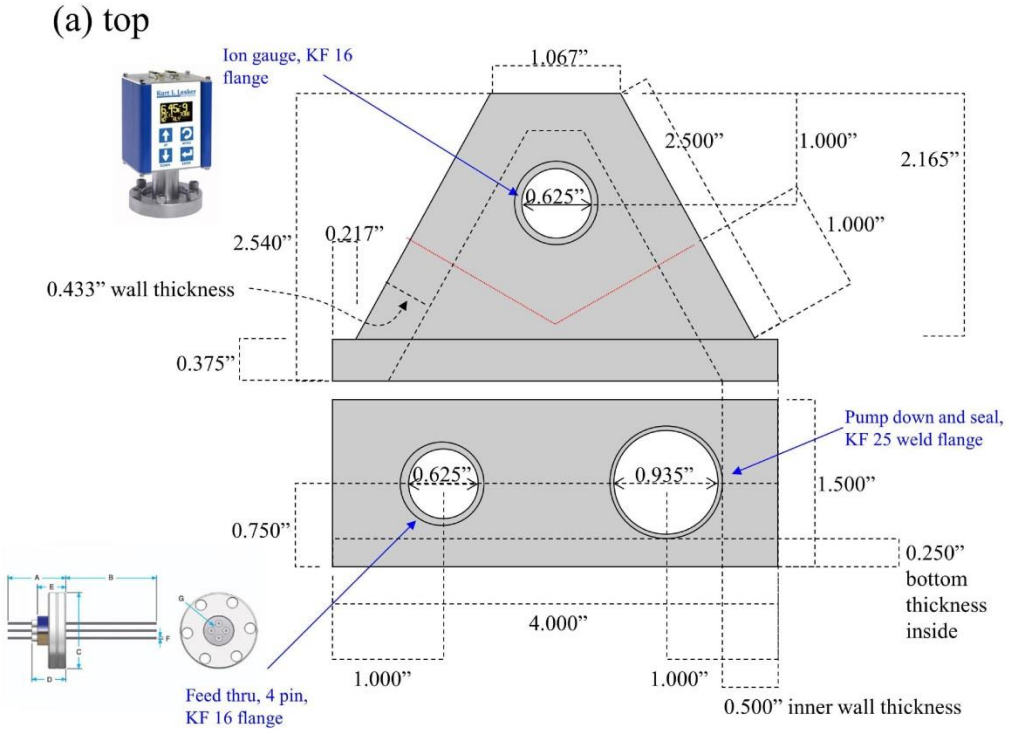

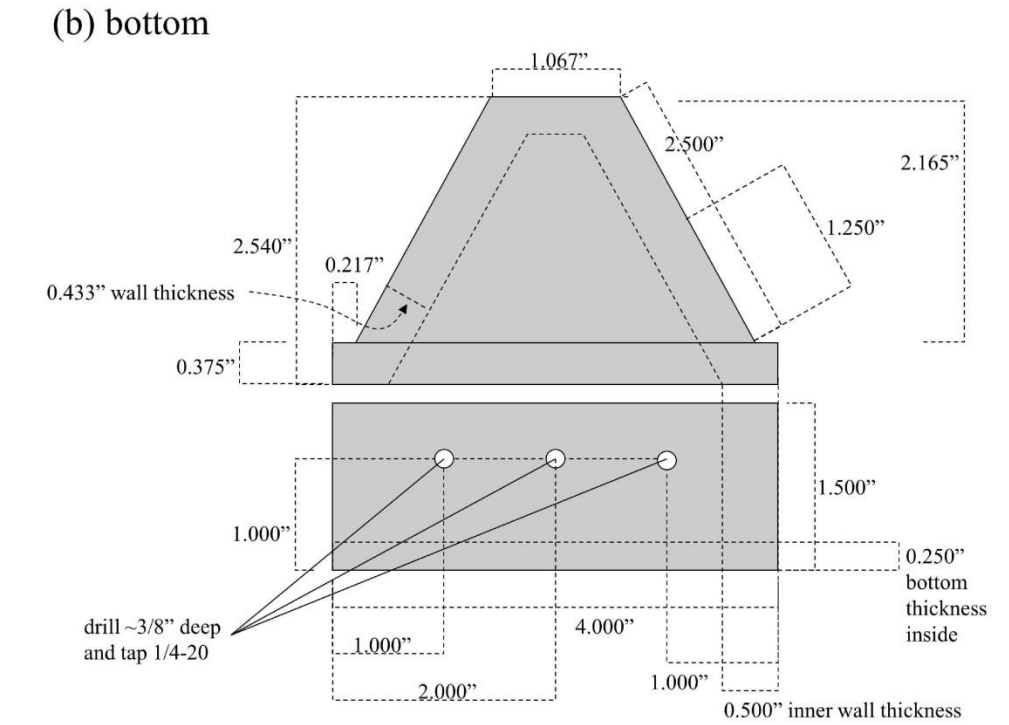

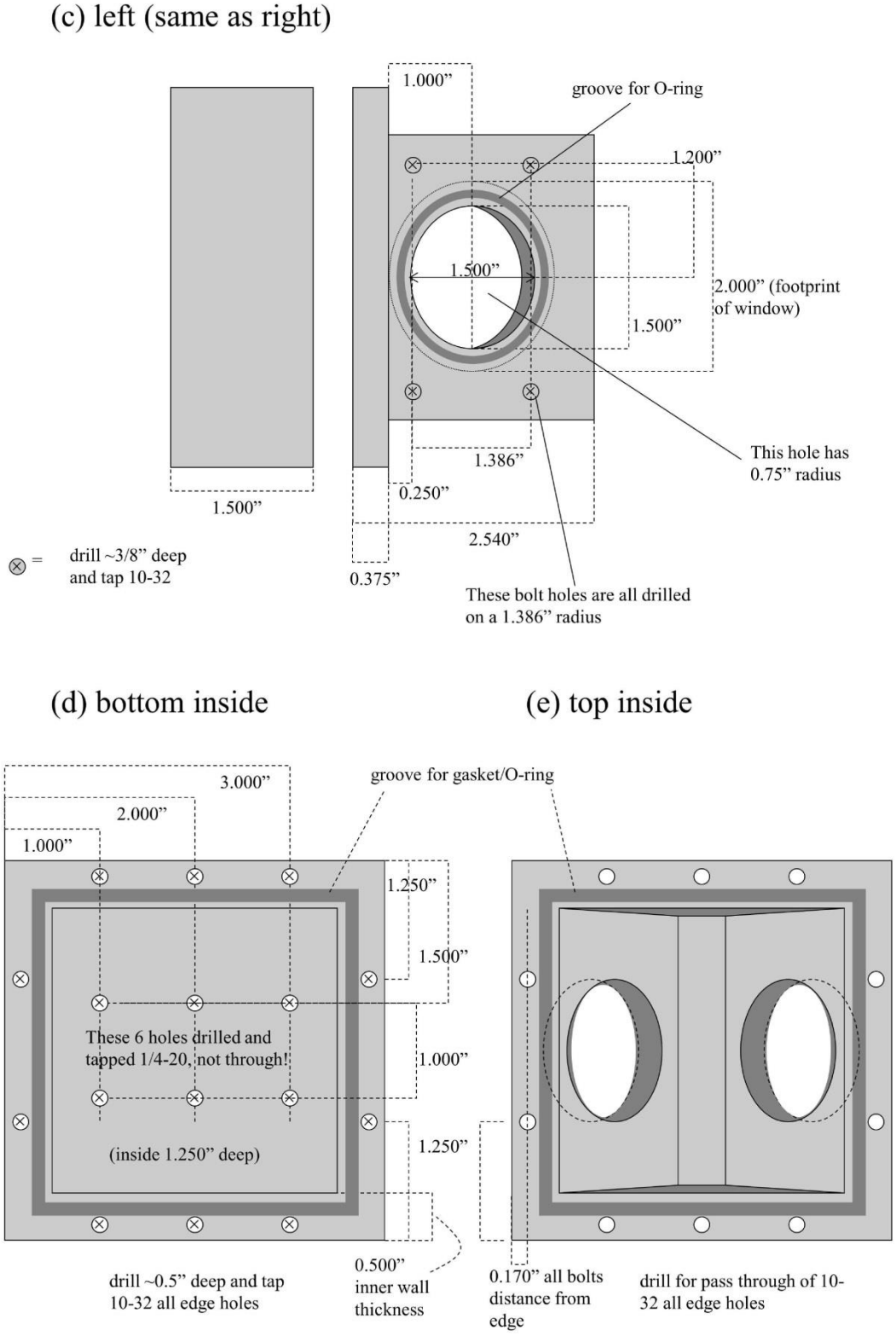

Figure 6-5. Full schematic drawing of the VSFG vacuum cell showing views from (a) top, (b) bottom, (c) left (same as right), (d) inside the bottom section, and (e) inside the top section.

the vacuum cell with nitrogen and removing the top section (Figure 6-5(e)) for access to the sample holder magnetic mount situated in the bottom section (Figure 6-5(d)). The vacuum cell was modified later by placing a window in the center of the top section (Figure 6-5(e)) to allow for the use of the quadrant photodiode (QPD) positioning system detailed in Section 5.2.2.

6.3.2 *VSFG with Applied Gate Bias*

6.3.2.1 Initial *ppp* Studies

In the first VSFG measurements using the vacuum cell, a 40 nm PTCDI-C_8 thin film deposited on a 300 nm SiO_2 bottom contact FET substrate (1 mm × 1 mm channel dimensions, see Figure 1-1) was measured with the *ppp* polarization combination with several gate biases applied for accumulation mode (accumulation of electrons in the channel where VSFG was being measured). A simple circuit diagram in Figure 6-6 shows the electrical connections during the experiment where we monitored for any significant gate current leakage I_G as indicated in the diagram. VSFG was measured in the center of the channel and the vacuum cell pressure during measurement was 10^{-5} Torr.

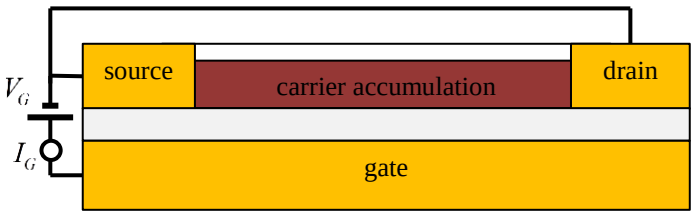

Figure 6-6. Simple circuit diagram showing electrical connections during VSFG study with applied gate bias.

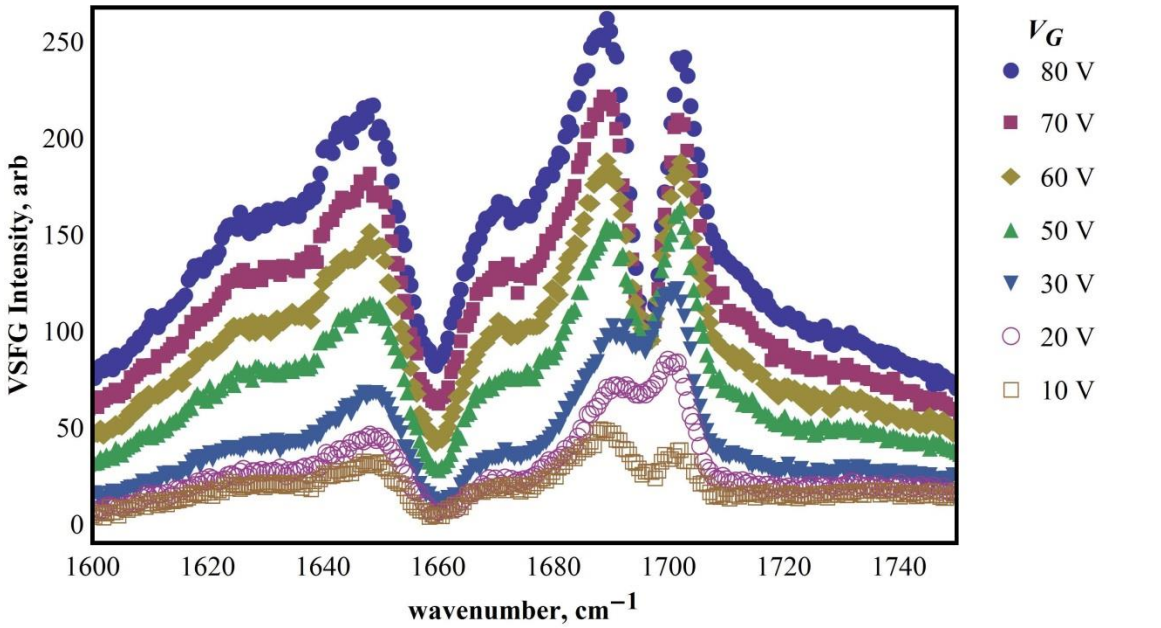

Figure 6-7. VSFG (*ppp*) raw data measured on PTCDI-C_8 oFET under electron accumulation.

Figure 6-7 shows the results of the experiment. There are several features present in the data. First, there is a vibrationally nonresonant background that takes on the profile of the mIR power spectrum and increases with increased gate bias. The symmetric stretch (~1700 cm^{-1}) is bimodal at all biases and the asymmetric mode (~1660 cm^{-1}) is derivative-like. The interference between the vibrational resonances with each other and the nonresonant background produces spectra that are fairly complex. The *ppp* experiment turns out to be very sensitive to charge carrier injection and is the basis for our work on monitoring charge accumulation in P3HT oFETs.[25]

Between each scan shown in Figure 6-7 the gate bias was set to zero and VSFG data was collected. Figure 6-8 shows the spectra. It is apparent that the vibrationally nonresonant background persists even after removal of the accumulation voltage and that the effect is more pronounce for higher accumulation voltages. The lingering vibrationally nonresonant response in the 0 V data has been attributed to trapped charges that create states in what is referred to, in a general sense, as the polaron band

of charged organic semiconductors.[465,469,470] Another possible contribution is from third order DC field response created by the trapped charges at the interface.[25,341,348]

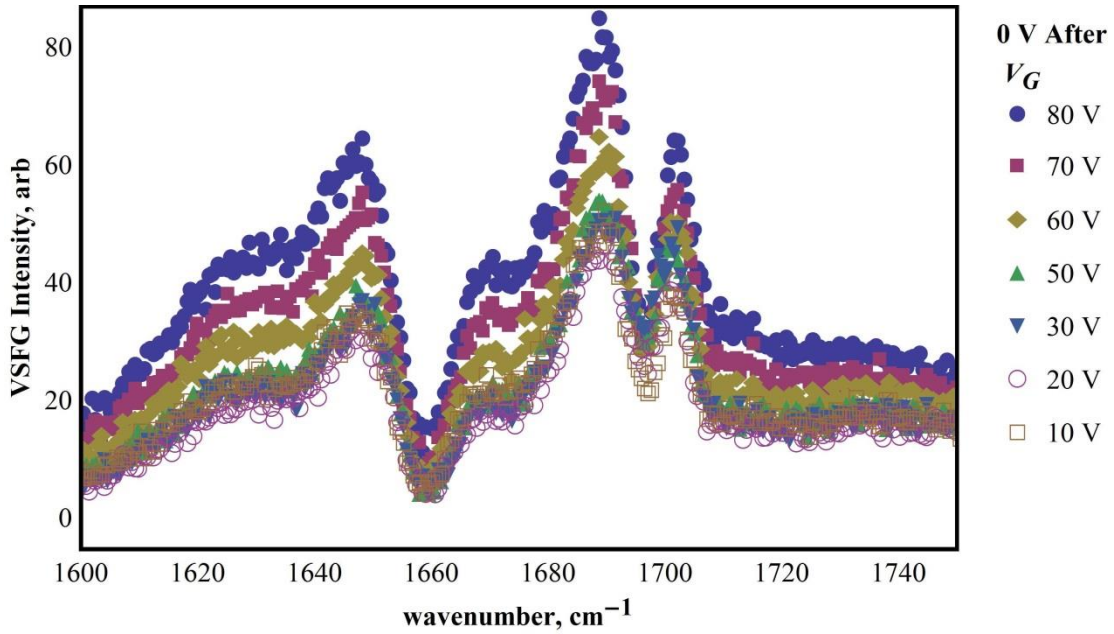

Figure 6-8. VSFG (*ppp*) taken with V_{Gate} = 0 after each gate bias scan in Figure 6-7.

The results from Figure 6-8 highlight one of the complicating factors when performing these *in situ* VSFG experiments. Often the VSFG data are not collected under steady-state charge carrier concentration because the kinetics of concentration changes are often much slower (minutes to hours or even days) than the time frame of a given VSFG experiment. An important lesson learned in these early gate bias studies was that one must be careful when comparing data taken under the same instantaneous conditions because the sample bias history often plays a prominent role in the detected signal intensity.

6.3.2.2 Refined *ssp* Studies

After the initial experiments in the vacuum cell it became clear the importance of applied bias history on VSFG data. Another study was then conducted that was

designed to give finer control over the applied biases. The goal was still to use VSFG to observe if gate bias stress effects possibly perturb molecular structure in the accumulation region. From the earlier work we learned that data interpretation of the *ppp* experiment was fairly complicated. Thus, we moved to taking *ssp* VSFG data because it was less sensitive to the vibrationally nonresonant polaron response and it samples a single element of the second order susceptibility (see Table 1-1). We also opted for thinner 8 nm PTCDI-C_8 films to minimize optical phase shifts through the organic layer. Again, the goal was to simplify data interpretation.

The experiment used a variety of sample conditions. PTCDI-C_8 oFETs were fabricated from 300 nm thermal oxide FET substrates (photolithography detailed in the Appendix) with two accumulation channel surface preps (RCA cleaned bare SiO_2 and ODTMS SAM functionalized, see Section 2.3.2) and two substrate temperatures (30 and 100 °C) during the 8 nm thin film deposition. At least four samples of each type were prepared and duplicates of this sample set were made, which were then post-annealed at 110 °C for 1 hour in air. The total number of samples was 4 each × 2 surface preps × 2 deposition temperatures × 2 post processing (unannealed and annealed) = 32 total oFETs.

Every sample that went into the VSFG vacuum cell was *intended* to be subjected to the same gate voltage and VSFG data cycle so that they would all have the same bias history. The experiment was set up to measure VSFG before any applied gate bias, and then follow the order of 0, -80, -10, 0, 10, 20, 30, 40, 50, 80, 100, 0, -80, 0 V. The experiment ran automatically with a custom LabVIEW program written to computer control the sequence of data collection steps. ZnO reference spectra were collected

before and after each sample voltage cycle experiment in order to normalize the data (detailed in Section 2.3.5.2 and 5.2.2). An example full data set for a sample oFET of PTCDI-C_8 deposited on a bare SiO_2 FET substrate at 100 °C is shown in Figure 6-9.

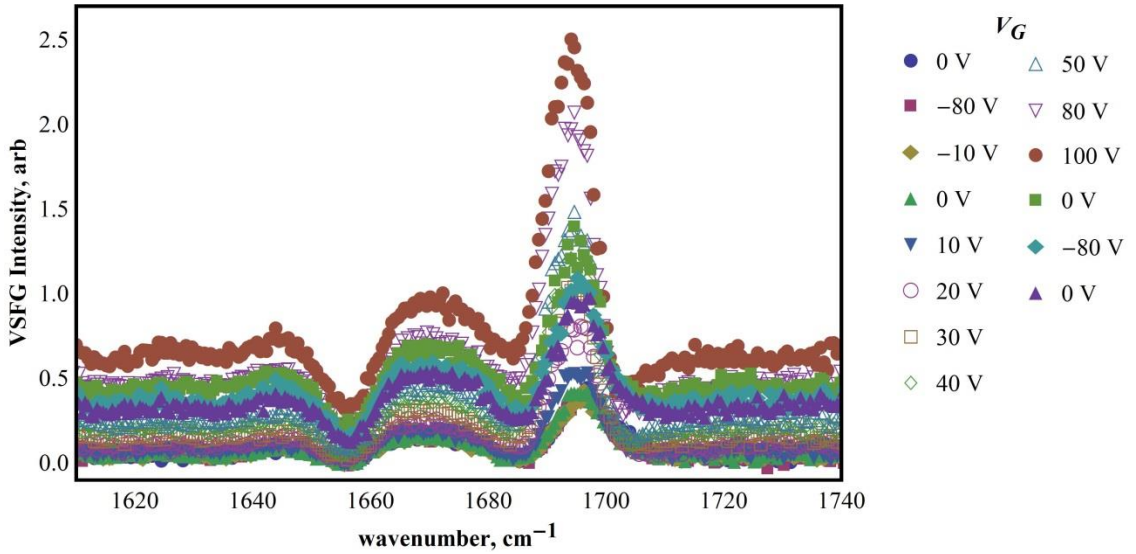

Figure 6-9. Reference normalized *ssp* VSFG data for 8 nm PTCDI-C_8 oFET (300 nm thermal oxide) deposited at 100 °C substrate temperature for every voltage in the gate bias experiment.

The spectra are clearly less complex than the previous *ppp* data with an obvious peak for the symmetric mode and a dip for the asymmetric mode. There is no discernable bimodal behavior for either vibrational resonance. The vibrationally nonresonant background is still present but smaller than the *ppp* data in Figure 6-7. It increases with increased accumulation voltage.

The experiment was tedious with each sample taking about 12 hours to complete. At that time, the QPD sample positioning system (Section 5.2.2) had not been built yet so that each sample that was loaded into the vacuum cell had to be realigned for the signal to point correctly into the detection system. Spectra were collected as an average of a series of five 4 minute date frames with 4 minute background frames (mIR beam blocked) taken in between each data frame (this detail is

important for the next section). When data collection was started by LabVIEW, it was noted that sometimes the Keithley 617 electrometer reading the gate current leakage (Figure 6-6) would become set to read voltage at the beginning of data collection due to a glitch in the LabVIEW software. For most samples where this happened, it was manually changed back to read current at various points during the experiment (as soon as it was realized the setting was not correct) without realizing until later that this had a dramatic effect on the data. By setting the read mode to voltage, the circuit would effectively drop the entire gate potential over the electrometer so that until the read mode was manually changed back to current there was no gate bias applied to the device itself (see Figure 6-6). This certainly undermined one of the primary design features of the experiment, leading to not all samples having the same applied bias history. Nevertheless, there were some interesting observations gleaned from these efforts.

6.3.2.2.1 Hole Injection in ODTMS Devices

While the experiment did not go as planned, there were some new and notable observations made that can be generalized to each sample type. It was observed that for the initial depletion gate biases (-80 and -10 V) the VSFG response depended on surface preparation but not on substrate temperature during deposition or post-annealing. For bare SiO_2 devices there was essentially no difference between the first four applied gate biases (0, -80, -10, and 0 V) but for ODTMS devices there was a change with depletion (or hole injection). Exemplary data for two samples are shown in Figure 6-10. Both devices had PTCDI-C_8 deposited with substrate temperature of 100 °C but the same

trends were observed for 30 °C devices with and without thermal annealing. In Figure 6-10(a) there is no discernible change in the VSFG response among the applied biases whereas in Figure 6-10(b) there is a dramatic increase in signal intensity, but only for the symmetric mode.

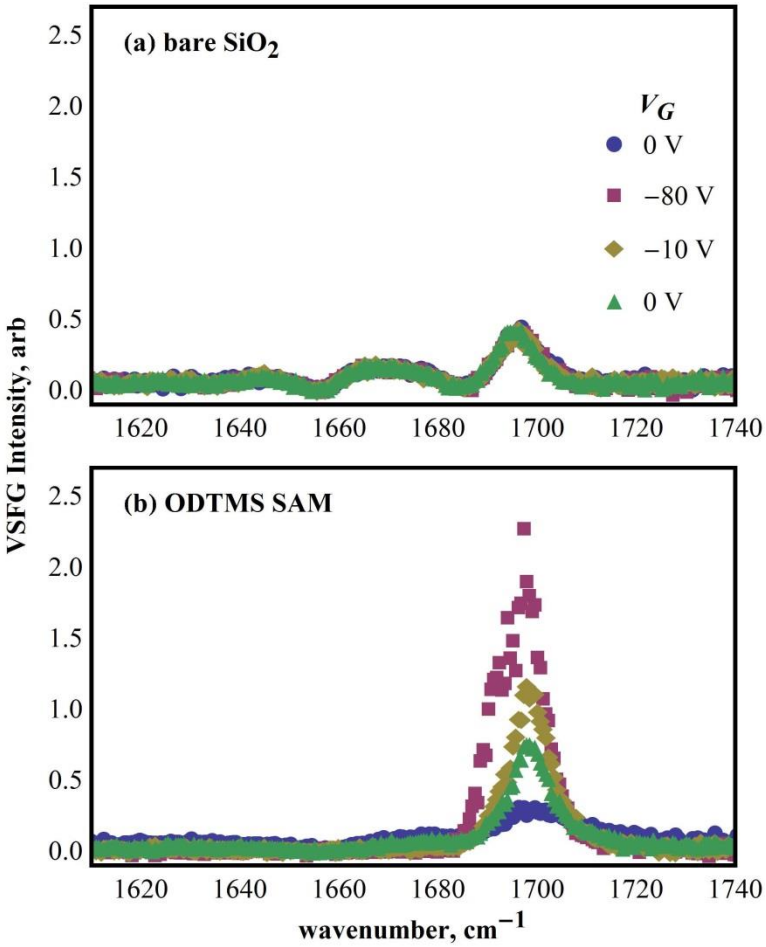

Figure 6-10. VSFG data from initial depletion gate biases for a (a) bare silica oFET and a (b) ODTMS substrate prep. Both had PTCDI-C_8 deposited at 100 °C substrate temperature.

The dramatic change in response for the symmetric mode suggests depletion biases were indeed affecting the organic in the ODTMS device, but it is not clear exactly how. Depletion biases inject holes into the organic accumulation region which directly affect the HOMO. One explanation is that the symmetric mode is strongly coupled to the HOMO electronic state so that it is very sensitive to changes in the

electronic configuration, but somehow holes do not contribute a polaron band nor any third order DC field response since there is no change in the spectra at vibrationally nonresonant frequencies. Further, it is not clear why the higher surface energy bare SiO_2 device was not susceptible to hole injection or why the lower surface energy ODTMS device allowed for it. The experiment may have had some issues, but for the devices that could be confirmed to have been exposed to all intended gate biases, this phenomenon was always observed.

6.3.2.2.2 Variable Kinetics of Hole Injection

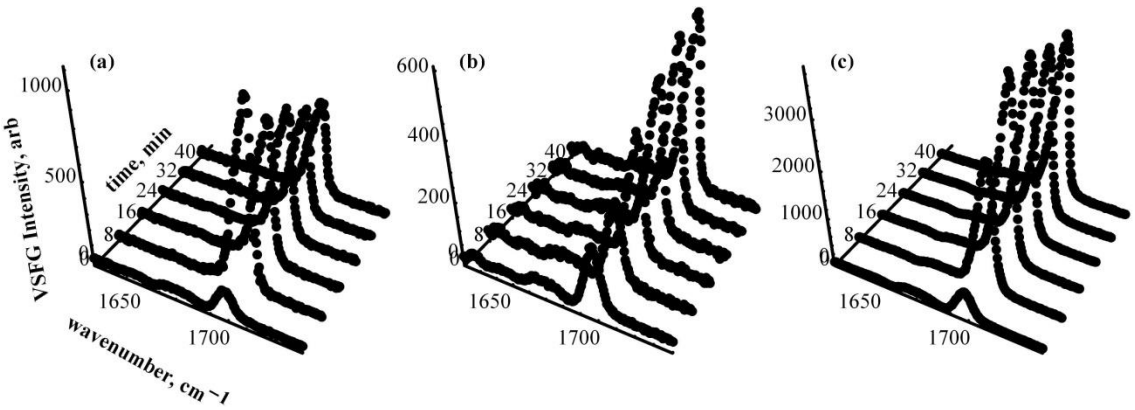

Figure 6-11. Individual data frames for the initial -80 V_G bias experiment for ODTMS channel surface preps. (a) and (b) had 8 nm PTCDI-C_8 deposited at 100 °C substrate temperature and (c) was deposited at 30 °C and post-annealed at 110 °C in air.

Whatever the reason ODTMS devices were susceptible to hole injection, it was also observed that the kinetics for that process were generally slow and exhibited bidirectional behavior as observed from the change in the symmetric peak on several samples. Figure 6-11 shows for three different samples the individual data frames for the initial -80 V_G bias. These are plotted as a function of time for each of the five frames that are averaged to produce the corresponding spectrum in Figure 6-10. The frames at 0 minutes are the initial VSFG spectra taken at 0 V_G (all 5 frames averaged).

All data have not been normalized but the individual absolute scales are expected to be self-consistent. The samples are ODTMS devices with 8 nm of PTCDI-C_8 deposited at 100 °C (Figure 6-11(a) and (b)) and one deposited at 30 °C and post annealed at 110 °C in air (Figure 6-11(c)). All samples have been confirmed to have had biases applied correctly as the original experiment intended. It is clear that the change in response always increases relative to the 0 V_G data and the spectra can increase (Figure 6-11(a)) or decrease (Figure 6-11(b)) with time, or that it can initially increase and then decrease (Figure 6-11(c)) over the course of collecting the five data frames. The kinetics shown in the figure indicates that there is large sample to sample variability since data acquisition and applied bias were timed very precisely by the LabVIEW program (to well within 1 second). So the various observed kinetics are real and present another confounding factor when attempting to analyze VSFG data with applied gate bias.

6.3.2.2.3 Data Modeling With Accumulation Gate Bias

While charge carrier concentration kinetics and the different ways in which different carrier species affect the sample VSFG response are processes that complicate data interpretation, the timeframe of kinetics were different for mobile electrons versus immobile holes. Generally, it was observed that application of accumulation biases (accumulation of electons for this n-type molecule) resulted in apparently instantaneous changes to the VSFG response, whereas hole injection (or removal of accumulated electrons from the channel) were kinetically slow and on the order of, or slower than, the time frame of the VSFG experiment. With that information we returned to this data set some time later, after the development of the multilayer interference model

described in the previous chapters. We decided to model one of the sets of data for accumulation voltages in order to discern the possible cause of the changed response.

In Figure 6-9 it is apparent that the symmetric mode becomes slightly red-shifted with increased gate bias. We postulated that electron injection should affect the vibrational frequencies of the modes at the inner interface as the bond order is lowered by delocalized electron accumulation in the perylene ring system. One sample was chosen and the model was set up to simultaneously fit all accumulation voltages. The full multilayer interference model was used to fit the data and a vibrationally nonresonant contribution at the Si/SiO_2 interface was included to account for the response at vibrationally nonresonant frequencies.

Figure 6-12(a) shows the data and resulting fit (b) for the gate biases considered for an 8 nm PTCDI-C_8 oFET deposited at 30 °C on a 300 nm thermal oxide FET substrate and post-annealed at 110 °C. Table 6-2 shows all symmetric mode parameter results that were constant for all biases. The fitting routine locked all resonant parameters to be the same at all gate biases and the widths to be the same for the symmetric and asymmetric mode (but different at interface 1 vs. 2) with the exception of the center frequencies of the buried interfacial modes which were allowed to float freely. We focus our analysis on the higher S/N of the symmetric stretch (center frequency result shown in Figure 6-12(c) as well as the nonresonant response in Figure 6-12(d).

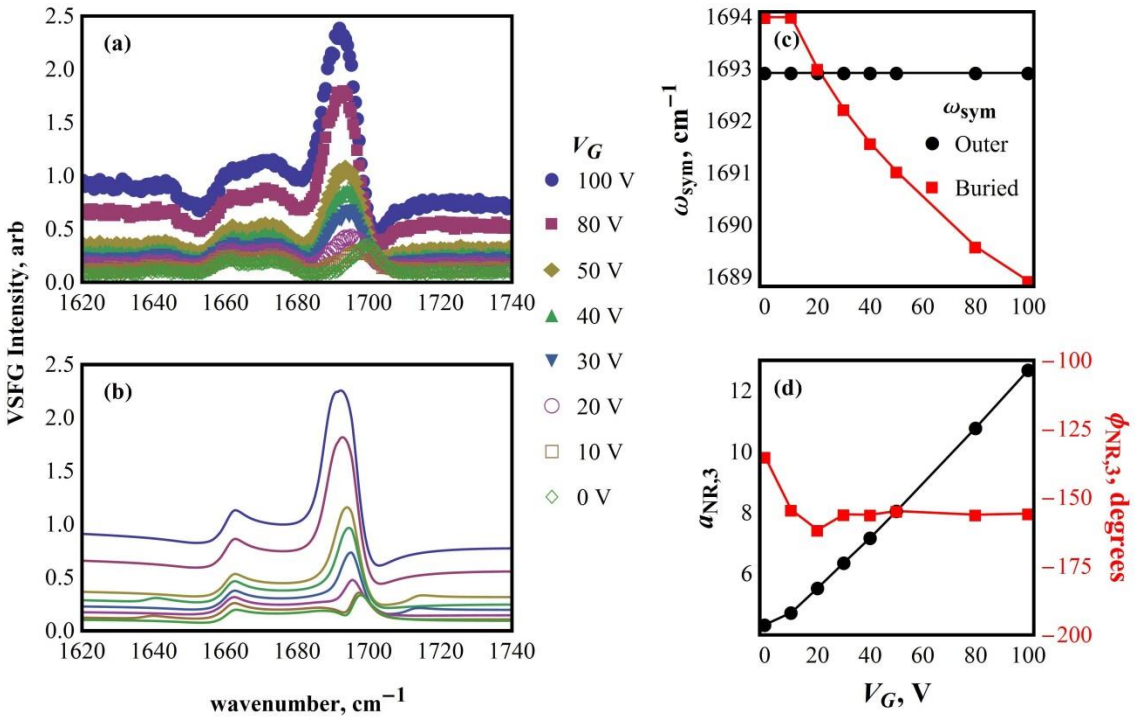

Figure 6-12. (a) VSFG data and (b) fit result for an 8 nm PTCDI-C_8 oFET deposited at 30 °C on a 300 nm thermal oxide FET and post annealed at 110 °C. Plot (c) shows fit results for the center frequency of the symmetric mode and (d) are results for the vibrationally nonresonant contribution at the Si/SiO_2 (third) interface.

Table 6-2. Fit results for the bias-independent parameters for the C=O imide symmetric stretch from the accumulation gate bias study.

Interface	1	2
A_{sym} (arb)	-43.4	33.4
Γ_{sym} (cm^{-1})	4.3	3.8

The fit functions show reasonable agreement between the model and data. This result indicates that a simple frequency shift and increased vibrationally nonresonant contribution are all that is needed to explain the changed VSFG response with applied gate bias. The fit results reveal that the inner symmetric mode center frequency red-shifts with higher accumulation voltages as we would expect with increased electron density since they fill the LUMO, which is an antibonding orbital in conjugated organic ring systems. While the fit results indicate the red-shift is nonlinear, the increase in the

nonresonant response appears linear at higher accumulation biases. A detailed analysis of why this may occur is outside this scope but, it is apparent that this procedure could be used as a sensitive probe to charge carrier concentration and kinetics at the buried interface in active oFET devices.

The fitting routine results are certainly interesting and convincing; however, they are a consequence of the preconceived notion of what was affecting the VSFG response and the subsequent choice of how the model was set up. Other modeling schemes have indicated that, instead of a frequency shift, the amplitudes (Eq. (5.30)) of the modes at the buried interface (and perhaps even the outer interface for these 8 nm thin films) may change with gate bias. The amplitude change may be due to molecular rearrangement, a change in the intrinsic response of molecules with otherwise unchanged orientation (e.g. becoming doubly or triply resonant), or just simply a result of changed transfer products (local fields) due to the presence of a charged sheet at the buried interface. Recall that in Section 1.3.2 the theory of SFG is established with Maxwell's equations by considering no free charges or currents at any interface. This is certainly no longer true for oFETs under accumulation. In order to uniquely identify the underlying mechanisms affecting the VSFG response, more work is necessary to expand the model to include charged interfaces as well as cleverly designed experiments to test new theories.

6.3.3 *VSFG Device Lifetime Experiment*

6.3.3.1 Experiment Details

As issues with data interpretation of VSFG applied to oFET devices under accumulation became more apparent, a new experiment was designed in order to test if VSFG could detect any molecular rearrangement over the lifetime of devices subjected to electrical cycling. The key difference of this experiment is that VSFG was measured *between* voltage scans, i.e. with no applied biases. The experiment was set up to collect *ssp* VSFG data between a number of $I_D - V_G$ curves (transfer characteristics, Section 1.2.2.1) within the vacuum cell. The full sequence of data collection was

$$\left[\text{VSFG} \rightarrow \left(I_D - V_G\right)_2 \rightarrow \text{VSFG} \rightarrow \left(I_D - V_G\right)_{10}\right]_n \tag{5.31}$$

looped *n* times for at least a day of data collection, all controlled automatically by LabVIEW. This allowed us to track the electrical parameters of mobility and threshold voltage over time as well as any changes in VSFG response. The device contacts were all set to ground during VSFG data collection. The $I_D - V_G$ curves were performed in the saturation regime with $V_D = 100$ V and V_G scanned from -10 to at least 100 V in steps of 1 V in the forward direction followed immediately by the reverse direction. Each electrical scan took about 20 minutes. The VSFG data acquisition was set up with 6 minute integration frames with 6 minute background frames (mIR blocked) and 5 frames averaged for a total acquisition time of 1 hour per VSFG spectrum. ZnO reference spectra were collected just before the loop in Eq. (5.31) was started and just after it was stopped.

The samples were devices with 1 mm × 1 mm channel dimensions (see Figure 1-1) prepared on RCA cleaned substrates (Section 2.3.2) with PTCDI-C_8 vapor deposited at 0.1 Å/s to a thickness of 8 nm and substrate temperatures of 30 °C and 100 °C. An additional step of post-annealing the FET substrate at 250 °C for 15 minutes on a hot plate prior to organic deposition was used to cure the metal electrodes. Data were taken on two samples of each substrate temperature. Samples were pumped down in the vacuum cell overnight prior to electrical connections and data acquisition. Experiments were performed at 10^{-5} – 10^{-6} Torr within the VSFG vacuum cell.

Several experimental improvements were also employed during these measurements. The QPD sample positioning system had been constructed by now (Section 5.2.2) and so the vacuum cell described in Section 6.3.1 was modified with a front window to accommodate the normal incident HeNe in the QPD system. This greatly facilitated sample replacement and realignment. Also, it became apparent that the ion gauge mounted on the cell directly above the sample had an effect on the electrical data. That port was capped and the gauge was moved much farther down the vacuum line, away from the sample to where cycling the gauge on and off had no apparent effect on $I-V$ data. It is unclear if the original placement of the ion gauge had any effect on VSFG data described in Sections 6.3.2.1 and 6.3.2.2.

6.3.3.2 Qualitative Observations

An exemplary raw data set for a device with PTCDI-C_8 deposited at 100 °C is shown in Figure 6-13. The time axis is relative to when the experiment was first started so that the initial VSFG scan always corresponds to time 0. It is clear that there is

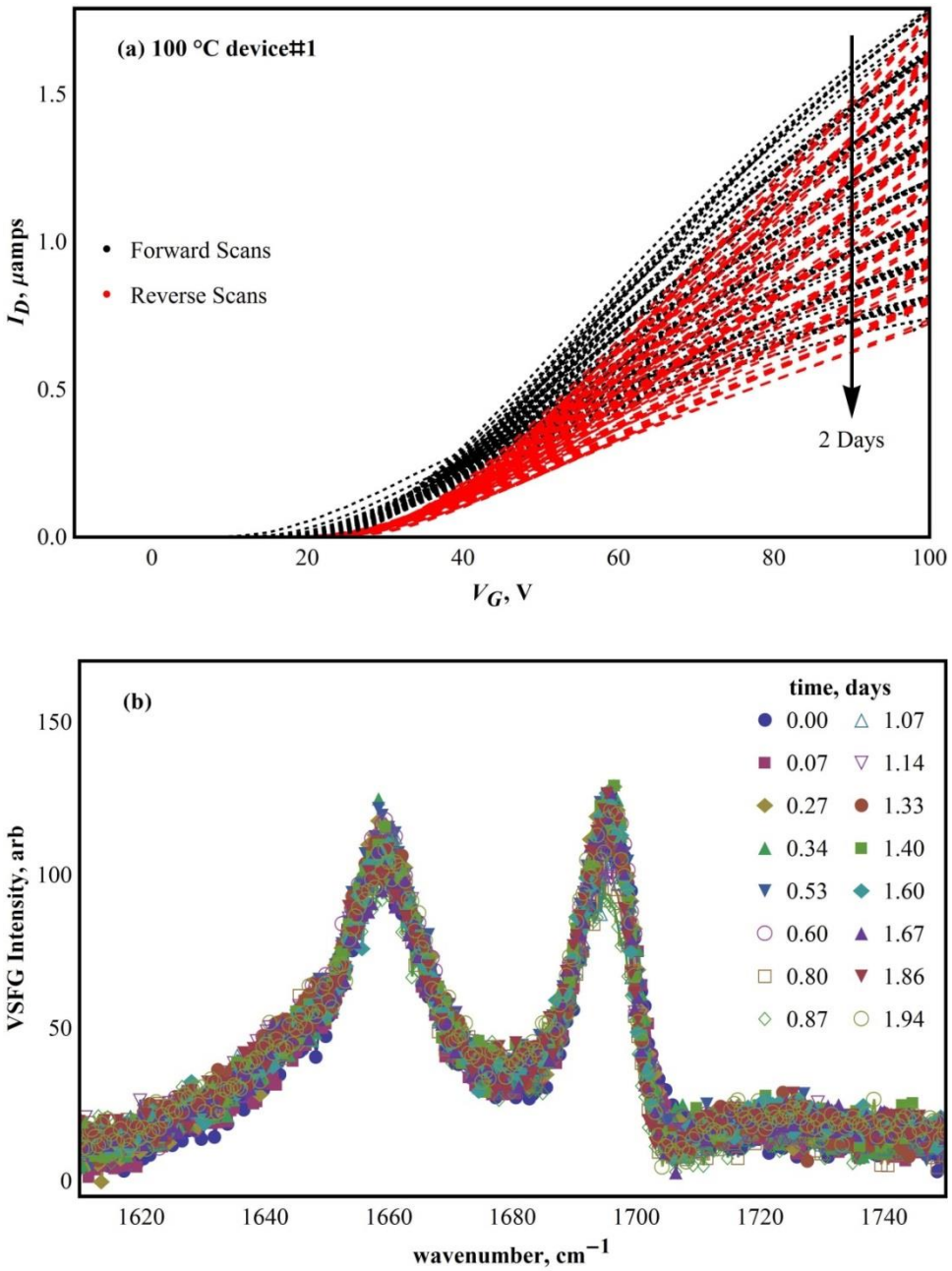

Figure 6-13. Exemplary raw data set for VSFG device lifetime experiment showing how (a) I_D-V_G curves and (b) *ssp* VSFG data change over two days of data collection. Data shown is for a device deposited at 100 °C substrate temperature. The drain bias was 100 V.

significant hysteresis between the forward and reverse electrical scans. The electrical characteristics (Figure 6-13(a)) change significantly over the course of the experiment whereas possible changes in the VSFG data (Figure 6-13(b)) are not obvious. Careful inspection reveals there may be a slight change in the symmetric stretch by the end of

the first day; however, these plots are not normalized by ZnO reference spectra. The reference spectra were collected only prior to data collection and after the experiment loop in Eq. (5.31) was stopped so that we could not account for any fluctuations in laser stability during the experiment. Thus, the VSFG data analysis in the next section is restricted to only the initial and final spectra of a given experiment, where reference normalization was more reliable.

6.3.3.3 Drain Current Breakdown

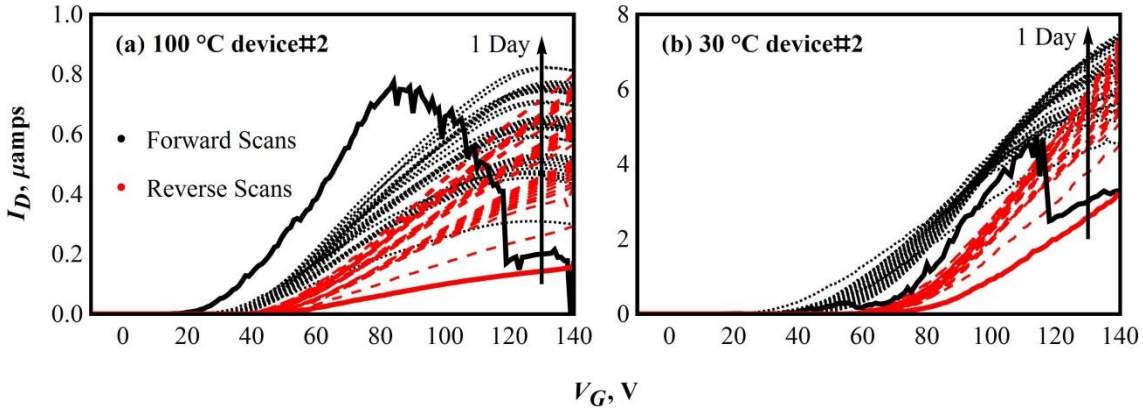

Figure 6-14. Electrical data showing I_D-V_G curves where there is breakdown in the drain current for initial scans (solid lines) and where subsequent scans (dashed) show reversed time dependent behavior relative to Figure 6-13. Data shown is for PTCDI-C_8 oFETs deposited at (a) 100 °C and (b) 30 °C.

The observed electrical data changes with time and the hysteresis between forward and reverse scans are typical for PTCDI-C_8 oFETs with one exception. Often it was found that the initial $I_D - V_G$ scan would reach some gate voltage tolerance where the drain current would break down in the initial forward scan. Subsequence curves would show a reversal of the time dependence observed in Figure 6-13(a). This was observed for devices deposited at both 100 °C (Figure 6-14(a)) and 30 °C (Figure 6-14(b)). Comparison of the electrical data for the two different 100 °C devices in Figure 6-13(a) and Figure 6-14(a) shows that the gate voltage at which drain current

breakdown occurs is dependent on the individual devices and not on specific device processing conditions.

The cause of this phenomenon remains unclear but it highlights another important aspect when interpreting electrical data. Even if the drain current breakdown is not obviously observed in PTCDI-C_8 oFETs, often the initial $I_D - V_G$ scans contain a much higher level of noise than subsequent scans. This suggests that there are some conditioning processes that happen within the channel when accumulation of charge carriers first occurs.

6.3.3.4 Electrical Data Analysis

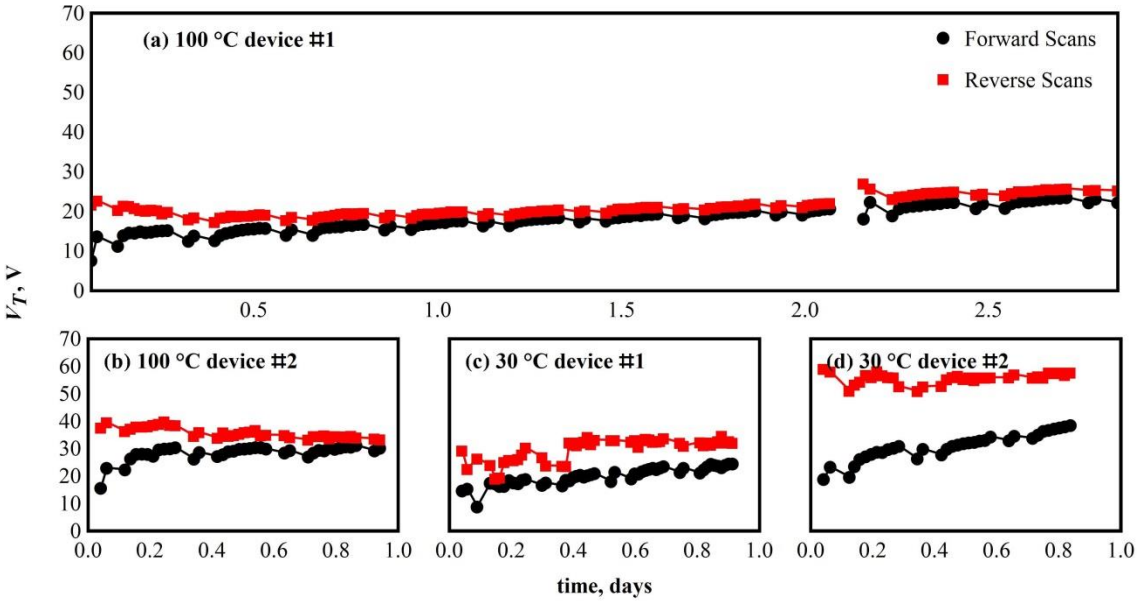

Figure 6-15. Threshold voltages extracted for all 4 devices used in the study.

In order to quantify the electrical data, the scans for all four devices where fit to Eq. (1.8) with the capacitance of the SiO_2 dielectric measured to be 1.2×10^{-8} F/cm^2.[96] The data range used in the fitting routine was the portion of each curve nearest to onset of appreciable drain current and was linear in the $\sqrt{I_D}$ plots (Figure 1-2(b)). The

mobilities and threshold voltages were extracted over the course of the experiments for both the forward and reverse scan directions.

Figure 6-15 shows how the threshold voltages (V_T) varied over the time each device spent in the vacuum cell. The hysteresis between the forward and reverse scans that is apparent in the raw data plots of Figure 6-13(a) and in Figure 6-14 results in different threshold voltages extracted for each scan direction. Hysteresis is smaller for the devices deposited at 100 °C and it appears to be asymptotically approaching no difference in threshold voltage in time for all devices. The reverse scan has higher threshold voltage in all cases and is probably a result of bias stress effects from the forward scan. From these results, the threshold voltages do not appear to be statistically distinct between the two device types used in this study.

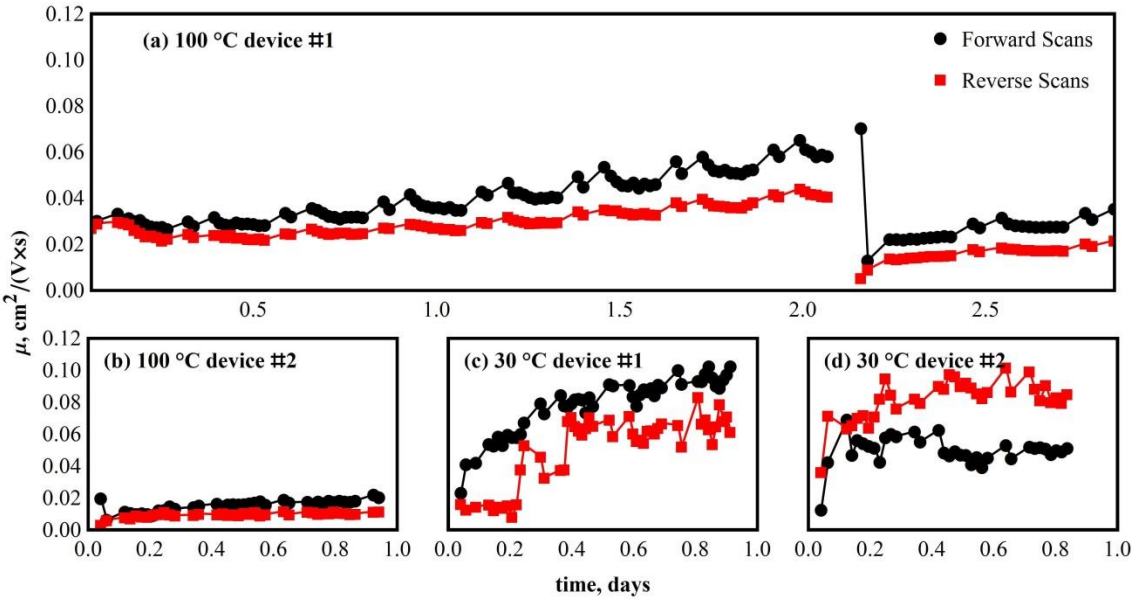

Figure 6-16. Mobilities extracted for all 4 devices used in the study.

Figure 6-16 shows how the mobilities (μ) varied over the time each device spent in the vacuum cell. Again, hysteresis between forward and reverse scans in the raw data result in different mobilities extracted for each scan direction. For 100 °C

devices the hysteresis was smaller and appeared to be diverging with time. The 30 °C devices started with mobilities comparable to the 100 °C devices (~0.02 $cm^2/V \times s$) but dramatically increased in the first portion of the day to a maximum mobility of around 0.1 $cm^2/V \times s$. The 100 °C devices were more constant with time and had lower peak mobilities. Generally, the reverse scans show lower field-effect mobility with the exception of the 30 °C device #2 in Figure 6-16(d).

The break in data at about 2.1 days in Figure 6-15(a) and Figure 6-16(a) shows where a second experiment was performed after the data collected in Figure 6-13. The device was not removed from the vacuum cell when a second round of data collection began. In this experiment, the gate bias was scanned out further to 140 V. Whereas data prior to this new experiment never indicated a breakdown in the drain current for this device, we observed that at around 120 V the drain current collapsed in a manner comparable to the initial forward scans in Figure 6-14 (raw data not shown). Thus, in Figure 6-16(a) the initial forward scan in the new section of data around 2.1 days shows a continuation of the trend seen in the mobility data up to that point, but immediately the reverse scan and all subsequent scans show a drastic reduction in mobility. The threshold voltage at this point in Figure 6-15(a) appears to only produce a hiccup in the data and then continues immediately as it left off from the previous experiment, albeit with a bit larger hysteresis between forward and reverse scans.

The mobilities from the second experiment in Figure 6-16(a) appear to drop to levels similar to the second 100 °C device data in Figure 6-16(b). That device exhibited a tolerance voltage around 100 V in the very first electrical scan performed (Figure 6-14(a)). It is tempting to conclude that once any device is brought beyond its gate bias

tolerance that the charge carriers are somehow immediately less mobile. However, the first oFET of the 30 °C device never experienced this phenomenon (data not shown) whereas the second did (Figure 6-14(b)). The mobilities of these two oFETs are similar in Figure 6-16(c) and (d). At this point the mechanism of the gate bias tolerance and drain current breakdown remains unclear. It may be related to the particular processing conditions used here. A search through the literature indicated that this phenomenon has not yet been reported.

6.3.3.5 VSFG Data Modeling

While it is not evident the cause of the drain current breakdown or what physical changes occur in the conduction channel of the PTCID-C_8 oFETs, it is certain that with or without it the electrical properties of these devices always change over time. From this perspective we looked at the VSFG data to see if it was possible to tell if the response, and therefore possibly the molecular structure, was changing. The data were fit to a two-interface model with a simple transfer product constant (T_2^{ssp}, i.e. this was not calculated using the thin film interference model) applied to the buried (channel) interface and included a constant vibrationally nonresonant contribution.

$$I^{ssp} = \left| \left(\chi^{(2)}_{sym,1} + \chi^{(2)}_{asym,1} \right) + T_2^{ssp} \left(\chi^{(2)}_{sym,2} + \chi^{(2)}_{asym,2} \right) + \chi^{(2)}_{NR} \right|^2 \tag{5.32}$$

The terms in parenthesis are grouped according to interface (1 being the outer and 2 is the inner). Each resonant contribution took the form of a Lorentzian oscillator as in Eq. (5.30). For each of the four samples, we consider only a subset of all the VSFG spectra: the initial scan (prior to any applied bias), the first scan after the first two $I_D - V_G$ curves (see Eq. (5.31)) and the final VSFG scan. The first two datasets were

normalized by the initial ZnO reference spectrum taken just before the beginning of each experiment and the last was normalized by the final reference spectrum taken after each experiment was completed.

In order to assess if our data and model could differentiate changes in response at the buried interface, we set up the fitting routine to test the null hypothesis. To determine if the resonant response could be modeled as *unchanged* over the course of the experiment, the fitting routine was set up to simultaneously fit all 15 spectra. Each sample contained identical resonant parameters for all time points (but unique for each sample). The only parameters that were unique to each time point dataset were the nonresonant susceptibility amplitude $\left|\chi_{NR}^{(2)}\right|$ and the transfer product for spectra other than those taken at time 0. For those, the transfer product was set equal to 1.

It was necessary to further constrain the simultaneous fitting routine because the model over-parameterizes the data (there are 15 parameters per spectrum possible with the model presented in Eq. (5.32)). The phase of the vibrationally nonresonant contribution $(\phi\chi_{NR}^{(2)})$ was set to be identical for all spectra. The resonant widths (Γ) were locked to be identical for each mode at each interface for all datasets. The center frequencies were also locked to be identical for each mode at both interfaces for all datasets so that there were only two floating parameters for the mode center frequencies $(\bar{\omega})$, one each for the symmetric and asymmetric modes. The buried interfacial center frequencies were then manually offset by -7 cm^{-1} for the symmetric mode and -5 cm^{-1} for the asymmetric mode, but still floated with the outer mode center frequencies. The

Table 6-3. Full parameter results for VSFG data fitting. Bold values indicate parameters that were not floated. Units for *A* are arbitrary, Γ and $\bar{\omega}$ are cm^{-1}.

	device:	100 °C #1						100 °C #2			30 °C #1			30 °C #2		
	time (days)	0.00	0.07	2.07	2.12	2.20	2.81	0.00	0.08	0.96	0.00	0.07	0.92	0.00	0.08	0.86
NR	$\lvert\chi^{(2)}_{NR}\rvert$	0.21	0.22	0.28	0.29	0.28	0.28	0.25	0.28	0.32	0.23	0.22	0.29	0.21	0.23	0.37
	$\phi\chi^{(2)}_{NR}$	4.56														
Interface 1	A_{sym}	1.46						3.49			0.97			0.87		
	Γ_{sym}	5.37														
	$\bar{\omega}_{sym}$	1702.28														
	A_{asym}	3.76						3.02			1.61			1.22		
	Γ_{asym}	10.17														
	$\bar{\omega}_{asym}$	1658.37														
Interface 2	T_2^{ssp}	**1.0**	0.98	0.96	0.87	0.91	1.12	**1.00**	1.03	1.20	**1.00**	0.92	0.87	**1.00**	1.18	1.00
	A_{sym}	-2.66						-2.31			-2.19			-1.90		
	Γ_{sym}	6.06														
	$\bar{\omega}_{sym}$	*1695.28*[i]														
	A_{asym}	-0.32														
	Γ_{asym}	3.75														
	$\bar{\omega}_{asym}$ [1]	*1653.37*[ii]														

resonant amplitudes (A) were locked to be identical at each time point for each sample, with one exception. The buried asymmetric amplitude needed to be further constrained to keep it well behaved during the fit because of its relatively small contribution. It was set to be identical for all 15 spectra. The full parameter fit results are presented in Table 6-3.

Figure 6-17 shows the resulting fit plots with data (black circles), model fits (red lines), and the individual imaginary components of the outer interfacial modes (gray and short dashes) and buried modes scaled by transfer products (magenta and long dashes). The model reproduces the data quite well so that it is immediately evident that any apparent differences in the data may be attributed to differences in the nonresonant

[i] **Value locked with -7 cm^{-1} shift from $\bar{\omega}_{sym}$ at interface 1.**

[ii] **Value locked with -5 cm^{-1} shift from $\bar{\omega}_{asym}$ at interface 1.**

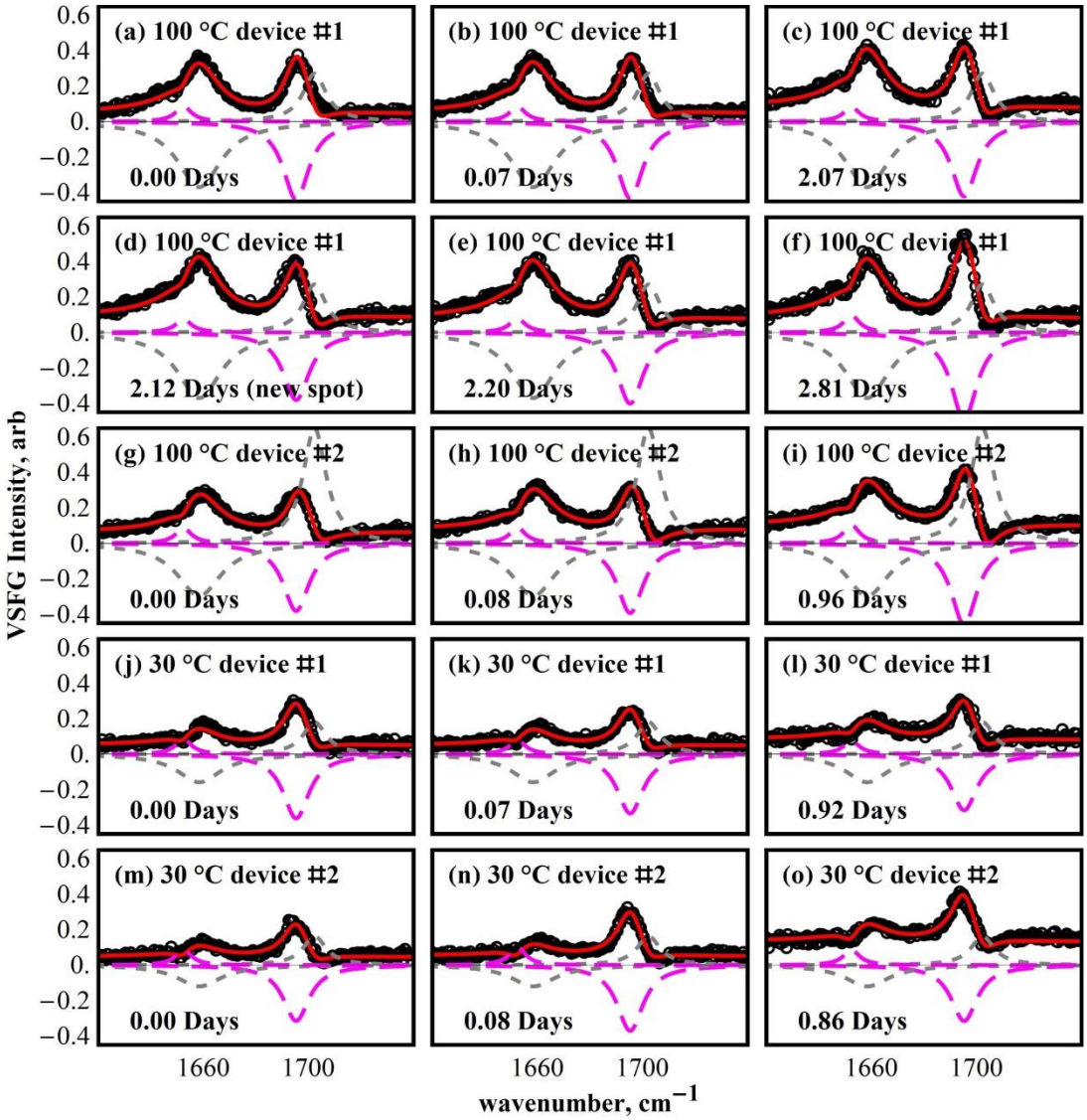

Figure 6-17. Plot results for simultaneous fit to VSFG data for all four samples. Shown are the data (black circles), resulting fits (solid red lines), and the imaginary part of the outer interfacial modes (gray and short dashes) and buried modes scaled by transfer products (magenta and long dashes). The indicated time points match the corresponding time axes in Figure 6-15 and Figure 6-16.

response and changes in the transfer product at the buried interface. Thus, we cannot disprove the null hypothesis, and so any attempt at modeling the data with a different fitting routine that could allow for structural differences (differences in the amplitude parameters) would result in non-unique fit function (this has been done and resulted in model and data agreement similar to Figure 6-17). Therefore, these measurements

cannot discern with certainty if the changes observed in the electrical data (Figure 6-15 and Figure 6-16) have any correlation with changes in molecular ordering or orientation.

While the measurement made here could not unambiguously discern if there were any changes in molecular structure over the course of the experiment, a closer look at the parameter results in Table 6-3 indicates that there likely is some degree of extraneous effects as a result of the chosen fitting routine. Figure 6-18 shows the results for the parameters that were unique to each dataset. In Figure 6-18(a) we see that $\left|\chi_{NR}^{(2)}\right|$ increases for all samples. This signifies that device cycling over time results in higher concentration of trapped charge carriers when the device is turned off. Figure 6-18(b) shows how the transfer products change. It indicates that, relative to time zero, this quantity minimized the fit error by going up or down. We would expect that changes in the local fields at the buried interface (and therefore the transfer product results) should change *in the same direction* with the introduction of trapped charges, i.e. they should all be larger than or smaller than 1 (relative to the scan at time zero, before any applied bias). This is not the case as values vary above and below 1. Also, if the changed transfer products and differences in the nonresonant response are both a result of trapped charges, there should be some functional correlation between them. Figure 6-18(c) indicates no correlation between $\left|\chi_{NR}^{(2)}\right|$ and $\left|T_2^{ssp}\right|$. From this sample set we calculate that the probability of the Pearson coefficient of correlation[471] to be 0 is 87% (i.e. there is an 87% probability that $\left|\chi_{NR}^{(2)}\right|$ and $\left|T_2^{ssp}\right|$ are completely uncorrelated).

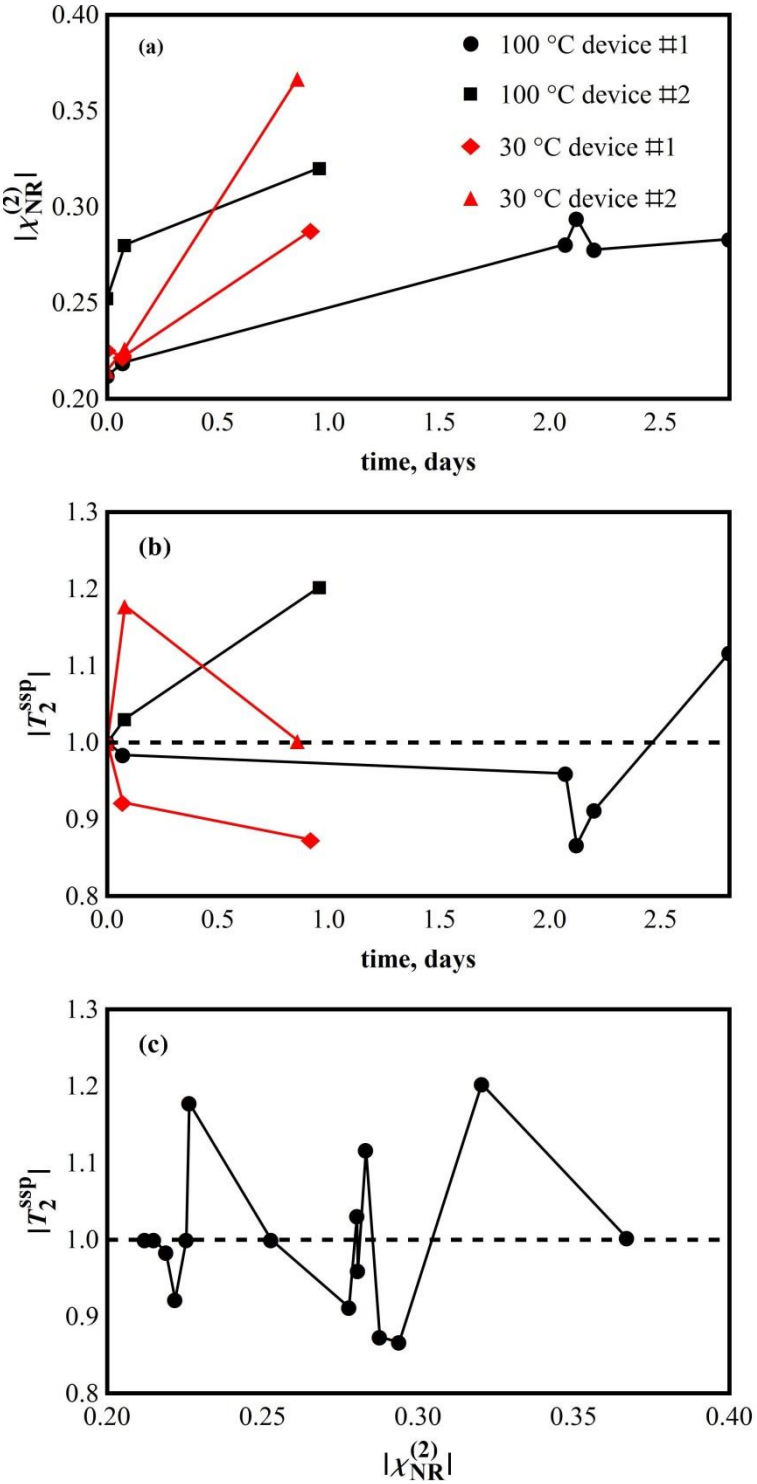

Figure 6-18. Parameter fit results for all devices for (a) $\left|\chi^{(2)}_{NR}\right|$ and (b) $\left|T_2^{ssp}\right|$. The plot in (c) shows how these results are uncorrelated.

The behavior of $\left|\chi_{NR}^{(2)}\right|$ is significantly affected by the fitting routine attempting to capture the response outside of the vibrational resonances, whereas $\left|T_2^{ssp}\right|$ is correlated with the resonant amplitudes through the product in Eq. (5.32). This leads to physically meaningful results in the first case, but less so in the latter. Since the buried asymmetric mode contribution was small, it is likely that the fit parameters are at least partially a result of the routine simply optimizing $\left|T_2^{ssp}\right|$ to make up for the assumption that for each sample A_{sym} is constant over time at the buried interface. If the fit were to be rerun with the roles of A_{sym} at the buried interface and $\left|T_2^{ssp}\right|$ reversed, the resulting plot for the amplitude results would look similar to Figure 6-18(b) but with the opposite trends (i.e. where $\left|T_2^{ssp}\right|$ goes up relative to time zero A_{sym} would go down and vice versa). In this case it is still tricky to find a physical explanation for the resulting variations. This emphasizes some of the difficulties of applying a two-interface model to VSFG data even with constraints on parameters imposed by simultaneous fits. Most often the fit routine parameters are still underdetermined by the data.

The discussion on fitting data is important for future efforts for applying a two-interface model to VSFG data. Experiments need to be designed to help eliminate ambiguities. This was one part of the reason for designing gradient samples in Chapter 5, to provide better constraints on fitting routines with more experimental data as well as a better model for transfer products.

6.4 DEVICE LIFETIME ELECTRICAL CHARACTERISTICS

The final efforts to be presented on PTCDI-C_8 oFETs came as a result of the observed large variations in electrical characteristics making it difficult to discern clear differences for various device processing conditions. Discerning these differences is a key goal in our search for a correlation in the molecular structure ↔ device function relation. While we had some success with devices presented in Section 2.4.8, the majority of the experiences with these oFETs have indicated that there are usually no clear statistical differences in extracted mobilities and threshold voltages for the various fabrication procedures and that this is confounded by the sample bias history dependence of device electrical performance. This is an indication of both the inherent properties of organic semiconducting materials (indeed, it is one reason they are so challenging yet interesting) as well as a sign that perhaps the fabrication processes could be improved.

The oFET fabrication processes varied several conditions and held others constant for all devices considered here. Variations included channel surface prep (RCA cleaned bare SiO_2 and ODTMS SAM functionalized), the substrate temperature when the PTCDI-C_8 was deposited (30 °C and 100 °C), and organic film thicknesses (8 nm and 20 nm). Elements that were constant included bottom gate/bottom contact FET substrates with 2 mm × 1 mm channel dimensions. The electrodes were deposited by photolithography (see Appendix) on wafers with 300 nm thermally grown oxide. The PTCDI-C_8 deposition rate was always adjusted to 0.1 Å/s. In all cases, with one

exception, devices were deposited in the OVD chamber (detailed in Section 2.3.4), transferred out and into air before being reintroduced into vacuum for electrical characterization. $I-V$ curves were always performed at 1×10^{-4} Torr or lower. In most cases, devices were subjected to electrical characterization only during their first time under vacuum, once they were removed and exposed to air they were almost never tested further.

6.4.1 *Saturation Regime*

6.4.1.1 Sorted by PTCDI-C_8 Thickness and Deposition Substrate Temperature

In total there were 50 PTCDI-C_8 oFETs fabricated and electrically characterized. These were typically subjected to multiple I_D-V_G electrical scans (transfer characteristics, Section 1.2.2.1) over the time frame of at least a day (and in some cases up to 2 months). In most cases, the electrical data were collected in the saturation regime with $V_D=10$ V and V_G scanned from at most -10 V to at least 85 V (but more commonly 100 V) in increments of 1 V and in both the forward and reverse directions. Saturation mobilities (μ_{sat}) and threshold voltages (V_T) were then extracted by fitting the linear portion of the $\sqrt{I_D}$ curve to Eq. (1.8) nearest to the onset of appreciable drain current. The capacitance of the dielectric was previously measured to be 1.2×10^{-8} F/cm^2.[96]

Figure 6-19 shows the cumulative results for extracted electrical parameters for all samples subjected to the time dependent experiment. Individual samples are joined by lines and plotted as a function of time elapsed since the organic deposition step of

the oFET fabrication process. Sample types are colored according to organic thickness and substrate temperature during organic deposition. Inset are box-and-whisker charts indicating median values, upper 75% and lower 25% quartile, and maximum and minimum values.

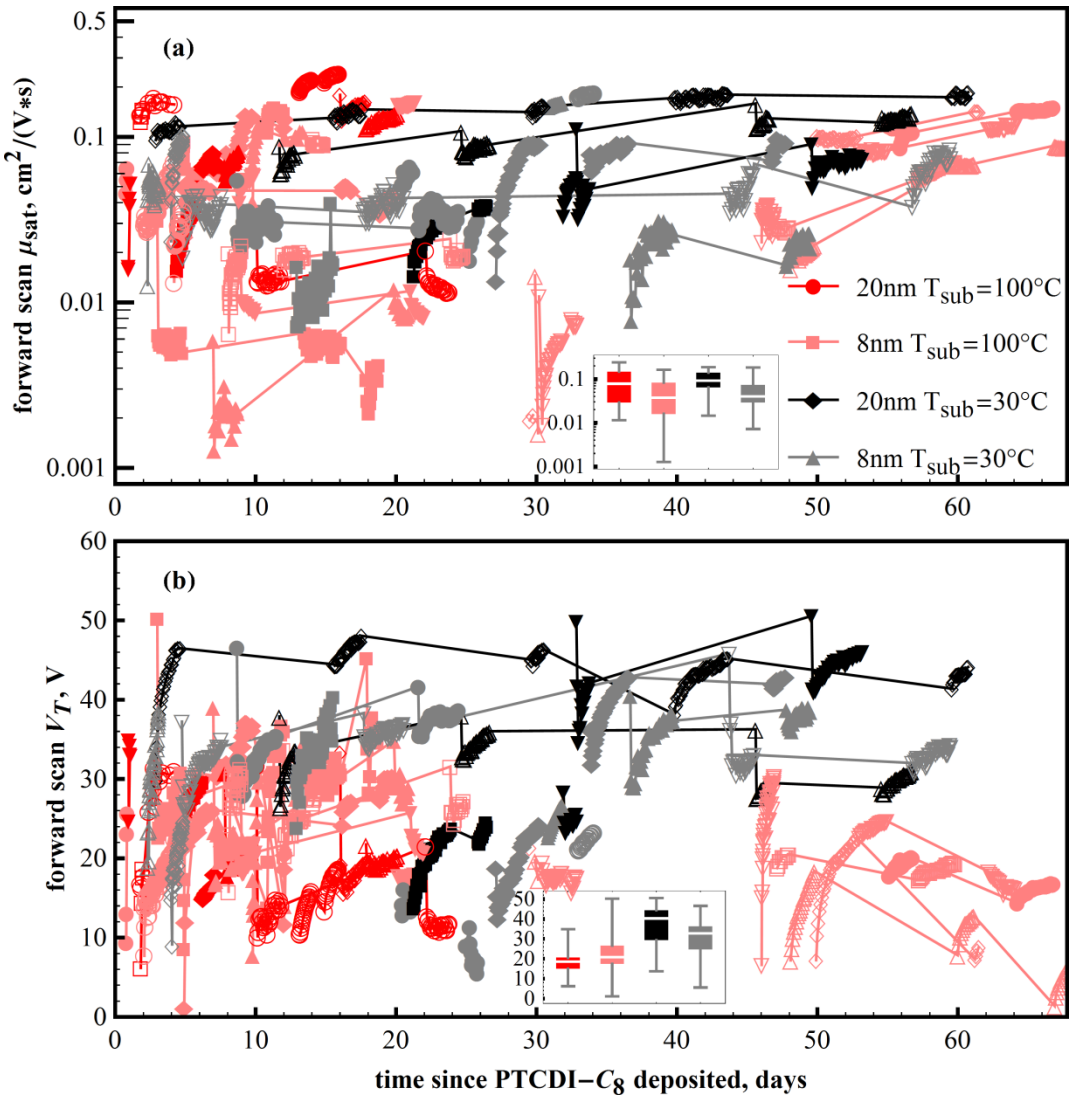

Figure 6-19. Cumulative results for (a) mobilities and (b) threshold voltages extracted from saturation regime transfer characteristics for all devices prepared and tested. The data are colored according to the thickness of the PTCDI-C_8 film and substrate temperature during organic deposition. Each set of markers joined by lines indicates results for a single sample as a function of time since the organic was deposited. Inset are box-and-whisker charts indicating median values, upper 75% and lower 25% quartile, and maximum and minimum values.

We generally observe that there is time dependence for all samples and that there is strong evidence that previous measurements affect current measurements. Again, sample bias history plays a role in the instantaneous experimental conditions and sample response as discussed in Section 6.3. Cases where devices exhibit high mobilities in the first data point relative to all subsequent measurements experienced the drain current breakdown discussed in Section 6.3.3.3. Overall mobilities span more than 2 orders of magnitudes in Figure 6-19(a) and threshold voltages range from near 0 V to over 50 V.

There is at least an order of magnitude spread in extracted mobilities for each sample type categorized in Figure 6-19(a) and a 30 - 40 V spread in extracted threshold voltages in Figure 6-19(b). Under the assumption of normally distributed sample populations, there is no statistical difference between any electrical characteristics for different device preparations. However, looking at the raw data results, there are some trends that should be mentioned. First, it appears in Figure 6-19(a) that all device types may reach peak mobility around 0.1 -0.2 $cm^2/(V*s)$. This maximum is a plateau across all time, some devices reach it sooner and remain there whereas others approach it over time, and some more rapidly than others. At very long times, relative to the initial organic deposition, they are all approaching that maximum with fewer devices found with very low mobilities. Altogether, this suggests the possibility of kinetically very slow changes in the accumulation layer that may be accelerated by electrically cycling the device. What those changes may be are not clear from this look at the data, we will comment further on this in the next section.

The mobility statistics in the inset box-and-whisker chart of Figure 6-19(a) indicate that there is possibly a difference in the population widths for the thinner devices vs. the thicker ones. The thinner devices tend to have similar maxima to the thicker devices but lower minima. This may indicate that the 8 nm organic films are approaching a regime in which field-effect mobility is affected by the absence of excess organic material. This is plausible since 8 nm corresponds to ~4 full monolayers of terraced PTCDI-C_8 in a film that is actually composed of maybe 1 or 2 full buried monolayers with >2 partial layers at the outermost interface.

Finally, in the inset of Figure 6-19(b), threshold voltage statistics indicate that there is perhaps a difference in the means between devices deposited at 100 °C versus those deposited at 30 °C. However, as will be shown next this may be due to data skewing because ODTMS devices were only deposited at the cooler substrate temperature. More discussion on the threshold voltage is included in the next section.

6.4.1.2 Sorted by Substrate Surface Prep: ODTMS vs. Bare SiO_2

Another view of the same data shown in Figure 6-19 is presented in Figure 6-20 where instead the data have been colored according to the FET substrate surface prep (ODTMS vs Bare SiO_2) and PTCDI-C_8 thickness. An important feature is that all ODTMS devices tested had PTCDI-C_8 deposited only at 30 °C, none were ever prepared at the higher substrate temperature.

The mobility data in Figure 6-20(a) reveal that there appears to be less time dependence for the ODTMS devices as compared to the thinner bare devices. The thicker (20 nm) bare devices were sampled over only half the time window and so we

cannot conclude anything about time dependence beyond about 33 days. The slow kinetics of change in the accumulation layer mentioned in Section 6.4.1.1 may be related to our conclusions in Section 2.4.8. There, we found that VSFG data for preannealed as compared to postannealed devices were consistent with previous

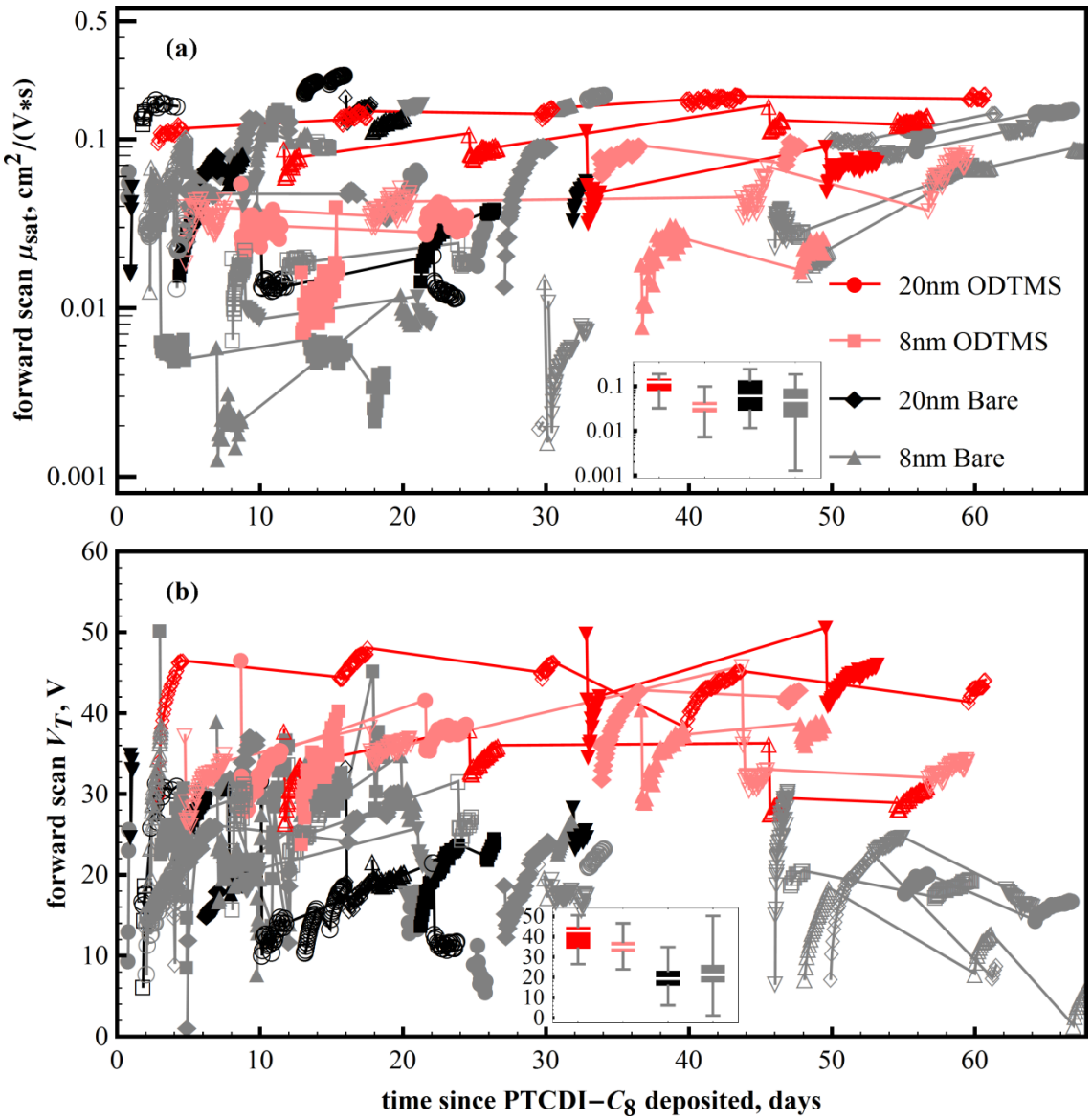

Figure 6-20. Cumulative results for (a) mobilities and (b) threshold voltages extracted from saturation regime transfer characteristics for all devices prepared and tested. The data are colored according to the substrate surface prep (ODTMS vs. bare SiO_2) and thickness of the PTCDI-C_8 film. Each set of markers joined by lines indicates results for a single sample as a function of time since the organic was deposited. Inset are box-and-whisker charts indicating median values, upper 75% and lower 25% quartile, and maximum and minimum values.

findings for PTCDI-C_8 thin film growth. The initial PTCDI-C_8 layer that forms on ODTMS devices is thermodynamically more stable relative to bare SiO_2. We found that the first monolayer on SiO_2 was subject to molecular reorganization to a more reclined phase upon thermally annealing the films but which also lead to increased mobility. Thus, the larger observed time dependence in Figure 6-20(a) for the bare devices may be a result of kinetically very slow changes in the accumulation layer that were otherwise sped up by thermal annealing in the work presented in Chapter 2. These observations have some implications for optimum device performance and functional lifetimes.

The results in Figure 6-20(b) indicate that ODTMS devices typically have higher threshold voltages than bare SiO_2 and that both have values that span more than 20 V. One of the factors that contribute to a higher barrier to charge injection mentioned in Section 1.2.2.2 is a barrier at the interface of the source and/or drain electrodes with the organic semiconductor. These are almost certainly higher for ODTMS devices since the insulating SAM was deposited *after* the electrodes but before PTCDI-C_8 deposition. The higher threshold voltage for ODTMS devices skew the box-and-whisker chart in Figure 6-19(b) for 30 °C devices to apparently higher median values and larger distribution widths since a large portion of that population is from the ODTMS surface preps. The largest variation in V_T is for the 8 nm thicknesses on bare SiO_2 substrate, indicating again that that thickness is probably approaching a limit where a lack of excess PTCDI-C_8 affects device performance. This is seen in the

distribution widths of the mobility data for both substrate preps as well, although to a lesser extent for 8 nm on ODTMS.

The smaller variation in V_T for the thinner ODTMS devices versus the thinner bare devices is likely attributable to the thermodynamic stability of the films on the SAM, whereas the larger mean threshold voltage for the functionalized substrate is a result of our processing conditions. At the time these devices were being fabricated it was thought that the chemistry of SAM formation should select for only the SiO_2 channel and not the gold electrodes. These results indicate that this is not the case and that ODTMS may contribute to barriers at the source and drain. This highlights that every detail of oFET fabrication is important and that future efforts should aim for separating substrate preparation from the electrode and organic film depositions.

6.4.2 *Linear vs. Saturation Regime*

In many of the electrical characterization experiments, the test station software was set to alternate between linear and saturation regime transfer characteristics. The experiments were set up to take a single linear scan followed by a single saturation curve and cycled over at least a day. In most cases, there was a 10 minute waiting period between scans with the device set to ground to allow for any bias stress effects to relax. Again, the gate voltage was scanned from at most -10 V to at least 85 V in 1 V increments and V_D was set to 10 V for the linear regime and 100 V for saturation scans. The saturation scans were fit to Eq. (1.8) as described in the last section and the linear scans were fit to Eq. (1.6) in the linear portion of the $I_D - V_G$ curve. The goal was to

better characterize differences in extracted electrical parameters due to nonidealities as discussed in Section 1.2.2.1.

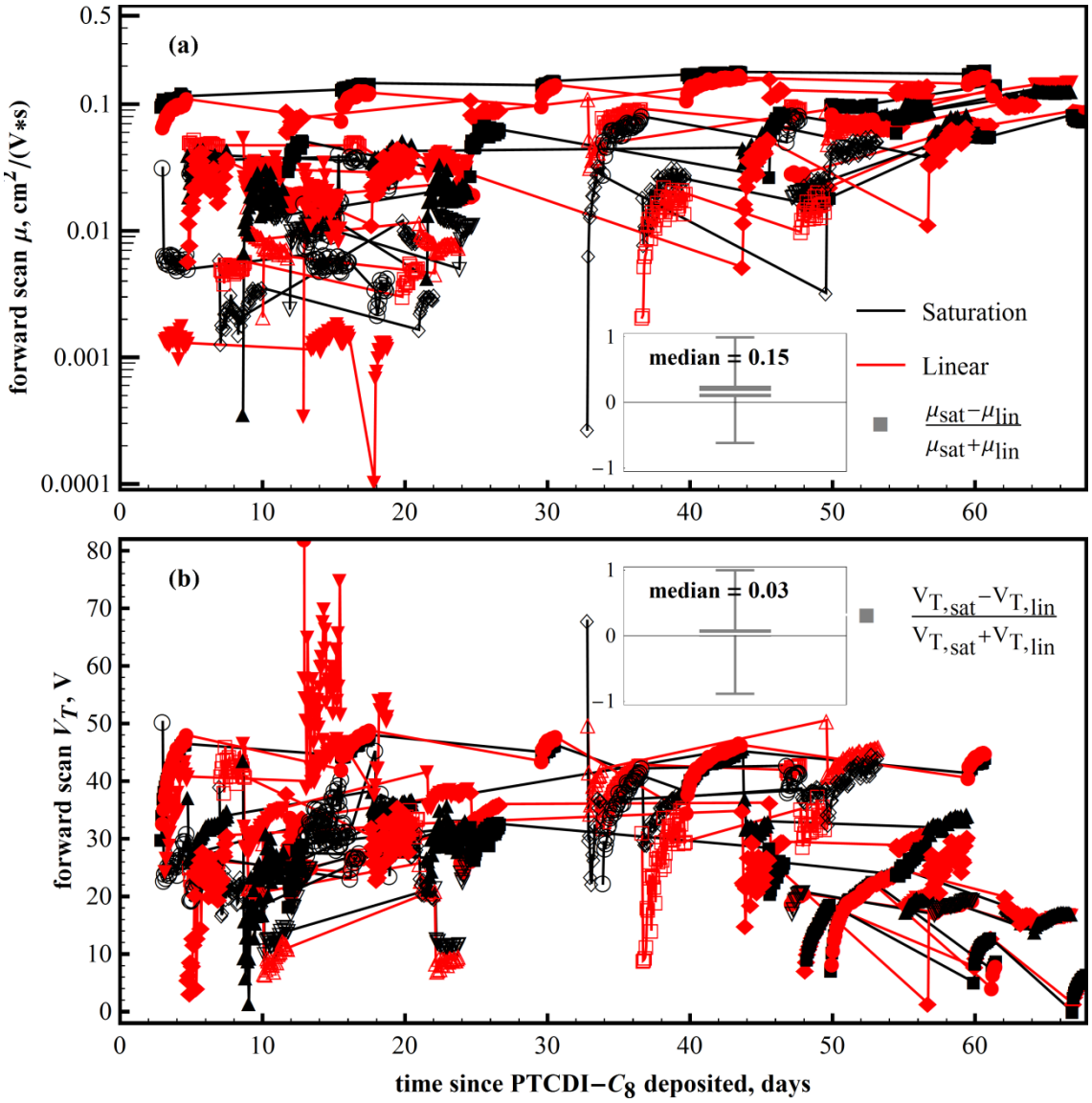

Figure 6-21. Cumulative results for (a) mobilities and (b) threshold voltages for devices that underwent cyclic linear and saturation regime $I_D - V_G$ characterization. Inset are box-and-whisker charts showing the imbalance in the results for each pair of curves.

In Figure 6-21 the results from data modeling are shown. The linear regime results present the same trends as those found in the saturation data, with all results for mobility approaching a ceiling value of ~0.1 – 0.2 $\text{cm}^2/(\text{V*s})$. The same is true for the

threshold voltages of Figure 6-21(b) where the spread in values is essentially constant in time. Inset in each figure is a plot of the difference of sequential results over their sum. That is, for each linear – saturation $I_D - V_G$ data cycle, the resulting pair of mobilities and threshold voltages were used to calculate a measure of the imbalance for each parameter extracted from each regime. Here 0 indicates perfect balance (a line is drawn through each inset at 0) where there is no difference between mobilities or threshold voltages calculated in either regime. Values close to 1 indicate the saturation regime characteristics were much larger than the extracted linear regime parameters, and vice versa for values close to -1.

Median values indicate that, for both mobility and threshold voltage, saturation regime results tend to be higher than the linear regime. A result of 0.15 for mobility indicates that on average $\mu_{\text{sat}} = 1.35\mu_{\text{lin}}$ and a value of 0.03 for threshold voltage corresponds to $V_{T,\text{sat}} = 1.06V_{T,\text{lin}}$. The box in the insets contain all values in the 25% to 75% quartile and the whiskers indicate maximum and minimum values. Clearly the ranges of unbalance for both parameters include much larger values for either regime but the distributions of results are fairly narrow, being a bit larger for mobilities.

The ranges shown in the unbalance are possibly an indication of extraneous effects for those data points approaching ± 1. Data taken in the linear regime were subject to lower overall peak currents, and in some cases this affected the S/N. Also, the dependence of drain voltage on current is quadratic in the ideal derivation of Eq. (1.6). In real devices there may need to be corrections to this to account for nonlinearities in contact barriers and channel resistance, especially for the two different

substrate surface preps used. The differences observed in extracted mobilities combined with the low currents obtained in many of the linear regime scans were the motivation for performing $I_D - V_G$ curves in the saturation regime throughout most of my graduate work .

6.4.3 *Four Point Probe Measurements*

The extracted mobilities and threshold voltages depend on the voltage difference across the channel from source to drain electrode. The assumption that V_D is dropped completely within the channel is equivalent to assuming that the total resistance from source to drain is dominated by the channel resistance. However, it is well known that in some cases barriers at the contact point between source electrode and/or drain electrode and the organic can produce non-negligible contact resistances.[52,99,100] In such cases, the potential experienced by charge carriers within the channel is less than that applied between the source and drain electrode.

One way to extract contact resistance corrected electrical characteristics is by using a four point probe (4PP) geometry FET substrate. In a 4PP-FET, the electrodes are identical to those shown in Figure 1-1(b) but two additional potential sensing contacts are included in the photolithographic mask used to fabricate the source and drain elecrodes. The organic semiconductor is then deposited over the probes so that they are in contact with the accumulation layer at the organic-dielectric interface. A schematic view of a 4PP-oFET device is shown in Figure 6-22.

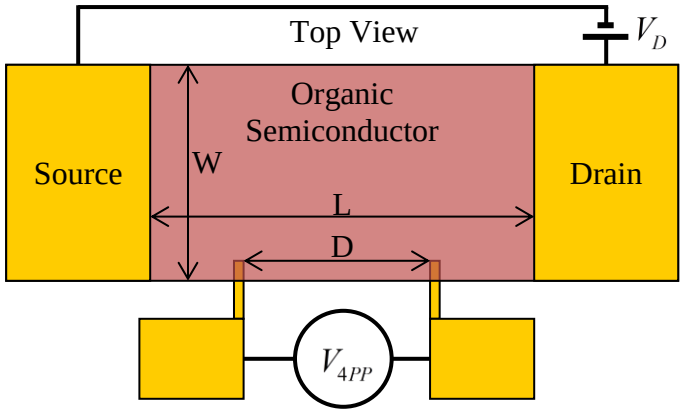

Figure 6-22. Top view of a bottom gate/bottom contact four point probe oFET geometry. The sensing contacts used in this work extended 50 µm into the channel and were 50 µm wide and situated with edges nearest each other at 1/3L and 2/3L so that D = 1/3L The channel dimensions were 2 mm W and 1 mm L.

The 4PP measurement then follows as in the usual linear regime $I_D - V_G$ experiment but with an additional voltmeter detecting the bias across the 4PP sensing contacts (V_{4PP}) with each voltage step. Ideally, the sensed voltage can then be scaled by the ratio of L/D to arrive at the true potential dropped across the channel, effectively removing contact resistance effects. These values can then be used in Eq. (1.6) for each gate voltage to extract contact resistance corrected mobilities and threshold voltages in the appropriate region of the $I_D - V_G$ curve.

Figure 6-23 shows an example of data collection and treatment for each transfer scan performed using 4PP-oFETs. The usual hysteresis is present between the forward (black) and reverse (red) drain current data (empty circles). The V_{4PP} data behave as expected through much of the curve where the device is passing appreciable current between source and drain but falls below zero at subthreshold gate bias. In this region, the conduction channel is not well connected so that describing the 4PP sensed bias here

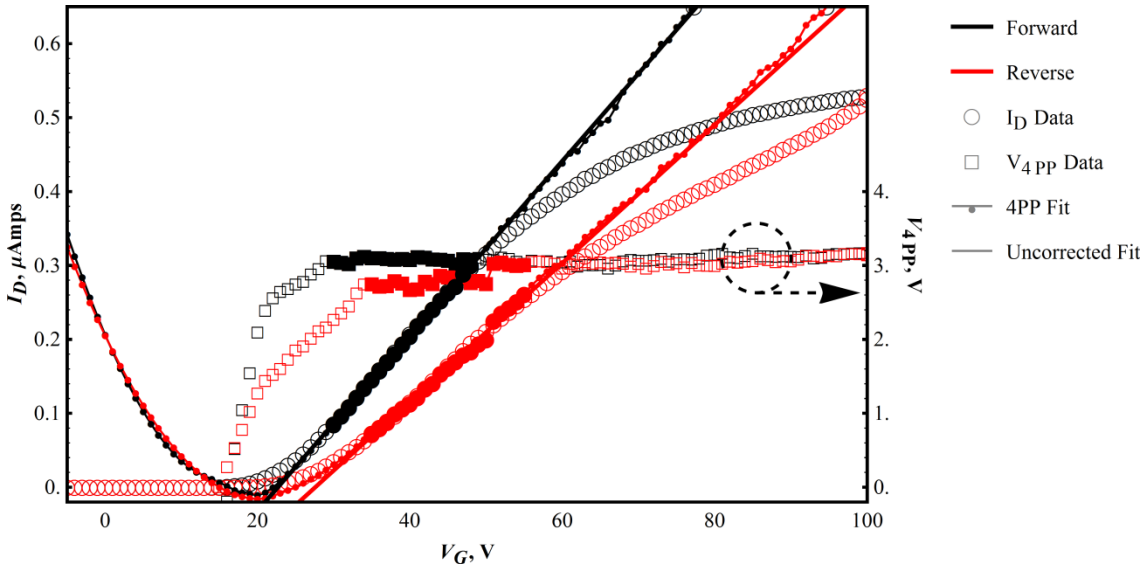

Figure 6-23. Example $I_D - V_G$ curve and fits for the 4PP experiment with $V_D = 10$ V. Gate voltage is scanned in the forward (black) and reverse (red) directions with drain current (empty circles) and V_{4PP} (empty squares) sensed at each step. The data are then fit using the 4PP sensed bias (small joined circles) in the regions of the data indicated by filled circles and squares. They are also fit with the standard model (solid lines) where the applied drain bias is assumed to be dropped fully across the channel (contact resistance is negligible). All curves are scaled on the right except V_{4PP}.

is unnecessary since Eq. (1.6) is not valid (the upward curve in the 4PP fit plots in this region are a direct result of this and have no bearing on results). For each dataset, the linear portion of the curve (solid data markers) was fit to a modified version of Eq. (1.6). The voltage drop across the channel is assumed linear in the linear regime transfer scans so that at each gate voltage V_D is replaced by $3V_{4PP}$ since the sensing probes sampled 1/3 of the channel length.

$$I_D = \frac{W}{L} C_{ox} \mu \left[\left(V_G - V_T \right) \left(3V_{4PP} \right) - \frac{\left(3V_{4PP} \right)^2}{2} \right] \tag{5.33}$$

The data were then fit substituting the gate voltage dependent values of V_{4PP} to extract mobility and threshold voltages for both forward and reverse scans. The data were also fit using the standard model (uncorrected for contact resistance) where the applied drain

bias was $V_D = 10\ \text{V}$ for all scans and samples. For this example we find that uncorrected/corrected mobilities and threshold voltages in the forward scan were $0.0493/0.0536 = 0.92$ and $17.7/18.2 = 0.97,$ respectively, and in the reverse scan they were $0.0390/0.0425 = 0.92$ and $22.6/22.2 = 1.02.$

In most cases the 4PP correction was marginal as compared to the spread in extracted parameter values shown in Figure 6-21 so that it is evident that these devices are dominated by channel resistance. It is clear from the plot of V_{4PP} in Figure 6-23 that the sensed voltage reaches a value very near to 3 1/3 V, exactly the value we would expect for a 10 V drain bias with this 4PP-FET geometry for an ideal device with no contact resistance. Actually, this result is likely due to the non-standard channel dimensions used in this work. By most standards, a 1 mm channel length corresponds to an enormous dimension as compared to typical devices which are usually in the 10's to 100's of microns. In typical devices, the channel resistance is so *small* that it can become comparable to contact resistance. This is typically where efforts are critical for extracting contact-corrected electrical characteristics.

A final note on the 4PP devices should be mentioned. For many of these devices the corrected mobilities were often *lower* than the uncorrected mobilities. It was clear that the bottom contact geometry can lead to intermittent contact between the sensing electrodes and the conduction channel so that the V_{4PP} data were sometimes very erratic. It was especially evident in the ODTMS devices, where again, the ODTMS SAM was applied *after* the electrodes were patterned but before PTCDI-C_8 deposition. Lower corrected mobilities correspond to sensed voltages that, when

multiplied by 3, are larger than the applied drain bias. This observation is likely due to intermittent contact and possibly localized capacitive regions contaminating the sensed voltage reading, leading to unphysical results. Overall, when data collection was well behaved, the 4PP correction was not found to be a relevant procedure for significant improvements for this project.

6.4.4 *Hysteresis*

The last feature to be discussed that is common to all electrical data is the observed drift in electrical parameters over different time scales. The changes observed are generally categorized as either irreversible and continuously changing over the device lifetime (bias stress instability), or short term and reversible effects that lead to periodic structure in the time plots or looping in the bias scans for the forward and reverse directions (hysteresis). Both are considered undesirable memory effects and there is not a sharp distinction between them. These nonidealities are evident in the previous figures in this chapter (e.g. Figure 6-15 or Figure 6-19). While this phenomenon is typical and can be characterized, the origins of memory effects have not been studied extensively.[52] They are generally tied to such factors as device processing conditions, properties of the dielectric, the charge carrier type, and environmental exposure (e.g. oxygen and water).[472–474]

Considering hysteresis in the forward and reverse scans (as can be observed in Figure 6-13(a) or Figure 6-14), it is evident that mobilities and threshold voltages shift for the reverse scans relative to each corresponding forward scan. Figure 6-24 shows the difference between parameters calculated from forward and reverse scans as a function of the forward scan characteristics. Unique markers indicate individual

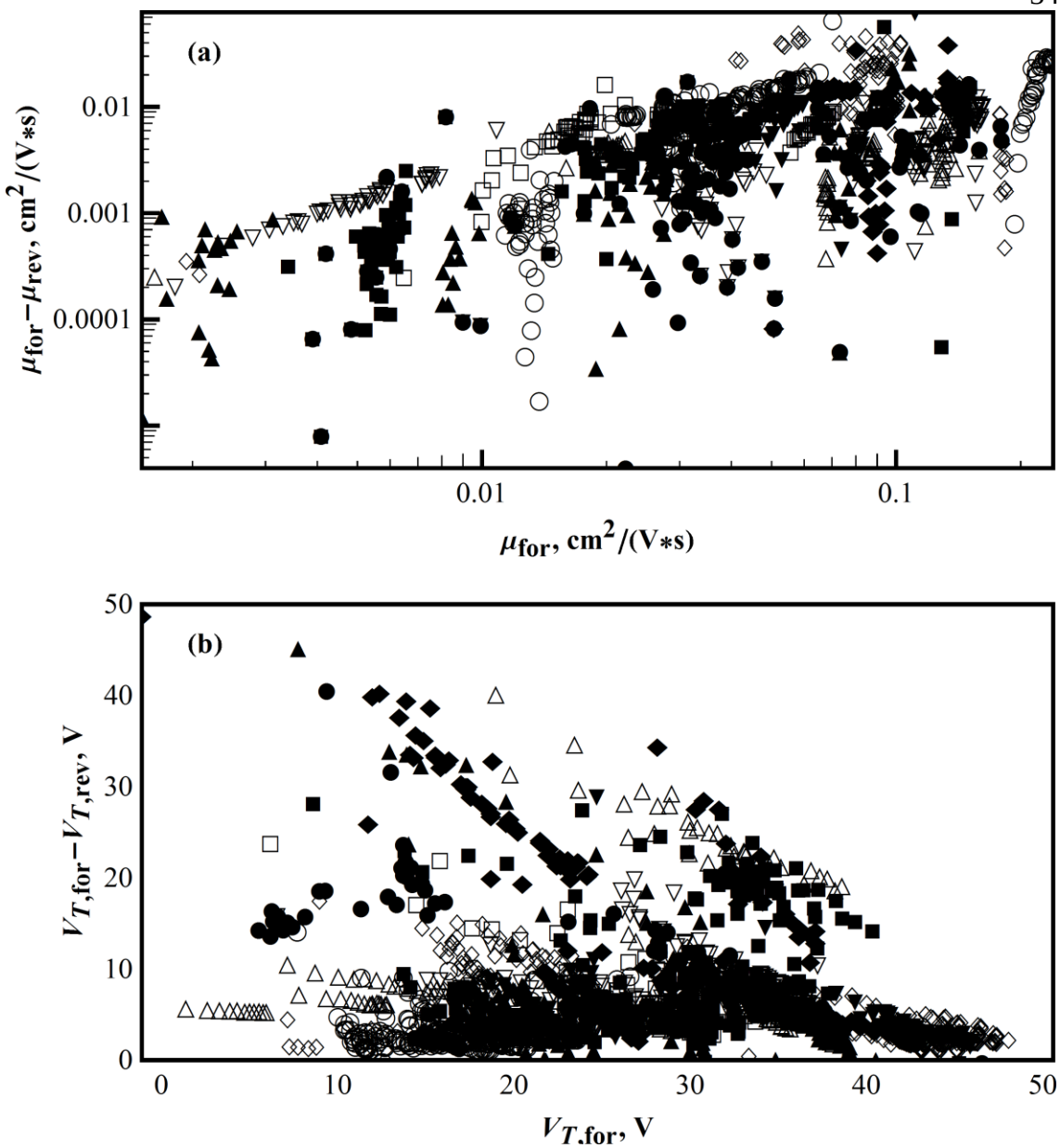

Figure 6-24. Hysteresis between forward and reverse scans for (a) mobility and (b) threshold voltage parameters plotted as a function of forward scan results for all scans performed in the saturation regime. Markers indicate individual samples.

samples. In Figure 6-24(a) it is evident that the mobility difference $(\mu_{for} - \mu_{rev})$ is maximally about an order of magnitude smaller than forward scan mobilities (μ_{for}). Individual sample results indicate that hysteresis may track with changes in forward scan changes (e.g. empty triangles below $\mu_{for} = 0.01$), or may change when forward

scan mobilities remains essential constant (e.g. empty circles around $\mu_{for} = 0.015$). Threshold voltage differences indicate that there is an inclination for all differences to approach ~5 V and that the large differences for any given sample become smaller with larger extracted threshold voltages from the forward scans. In time, however, the threshold voltages calculated from forward scans generally increased (see Figure 6-19(b)) so that hysteresis is also generally increased in time. When taken together, bias stress effects tend to shift threshold voltages higher and create larger hysteresis. Mobilities also tended to increase with time and appear to approach the roof value around 0.1 – 0.2 $cm^2/(V*s)$, but the hysteresis did not always track in the same way.

6.5 CONCLUSION

The early work with applying VSFG to organic semiconducting thin film systems resulted in the construction of a highly sensitive spectrometer capable of integrating hardware and software to obtain very rich datasets. The application of VSFG to oFETs with applied biases or as a function of time and electrical cycling were two areas where large efforts were spent attempting to make correlations in the molecular structure ↔ device function relationship. However, as the project proceeded it became clear that electrical parameter statistics for each device fabrication procedure produced trends depending on device types, but extracted electrical parameters were distributed over large ranges so that population statistics were not unique and had complex time dependences. Extraction of electrical parameters for each device type that can be compared is convoluted by such processes as memory effects and possible organic film relaxation. These effects occur over many different time scales and most

often have different rates that can depend on individual devices or device types. My experiences with oFETs are consistent with the problems outlined in Section 1.2, they are complicate yet interesting.

VSFG data taken on oFETs with applied biases has indicated that the interfacial sensitivity of VSFG is a powerful probe to processes occurring at the active interface. Charge accumulation can be monitored, changes in vibrational resonances can be observed, and distinctions between hole and electron accumulation is clear. The two-interface model can be used to fit VSFG data, providing a method to begin to separate contributions to the detected signal. However, in this chapter the parameters were underdetermined by the data so that they could not be uniquely fit by a two-interface model. This remains a significant difficulty for VSFG data analysis.

Future efforts should focus on obtaining unique device electrical statistics and improved VSFG experiments designed to better determine fit parameters. While utmost care was observed for all fabrication steps on the devices produced in this work, the processes themselves could certainly be improved. For instance, top contact device design using shadow mask deposition could provide a wafer substrate free of any metals when subjected to the RCA cleaning and ODMTS SAM processes. Metal impurities within the oFET channel are known to degrade device performance.[409] Functionalizing the substrate with the SAM before the electrodes would certainly be beneficial for better electrode-organic electrical contact. Strategically designed VSFG experiments are needed to further constrain fit procedures in order to extract unique VSFG parameters.

Contributing to this aspect of VSFG applied to organic semiconducting thin film systems became the primary focus of this thesis work.[i]

[i] I thank C.D. Frisbie research group for use of their physical deposition chamber. This work was supported by the National Science Foundation under Award Number DMR-1006386, by the 3M Corporation Nontenured Faculty Award, and by the University of Minnesota Chemistry First Year Graduate Departmental Fellowship.

Project Conclusion

The chronology of my graduate work is laid out starting with Chapter 6 where I made the choice early on to focus on the latter of two possible directions: improve oFET device fabrication procedures or separate contributions to VSFG data collected from these multilayer thin film systems. Chapters 2 – 5 then detail efforts to that end. Of central importance to the project direction was identifying that VSFG can serve as an ideal experiment for studying buried interfaces in organic thin film systems because it has high interfacial sensitivity and can be applied to a wide variety of systems. In principle, it can be used to deduce molecular structure at any interface accessible by light. An important factor that led to the specific direction of producing the model in Chapter 3 was identifying that the two-interface problem has been largely avoided in the literature, particularly for systems composed of more than a single thin film layer, as outlined in Section 1.3.1.6. It was for that reason that I produced the extensive simulation study of VSFG from the air/PTCDI-C_8/SiO_2/Si stack in Chapter 4 using the multilayer model. The title of my dissertation is *Solving the two-interface problem in vibrational sum frequency generation spectroscopy applied to multilayer thin film systems*, and to that end the efforts put forth in my graduate work have provided a solution in the form of an optical interference model for both interfacial and some possible bulk terms. The VSFG measurements on PTCDI-C_8 thickness gradients in Chapter 5 provide compelling experimental evidence for the model.

My theoretical and experimental results indicate that I have found a solution to the two-interface problem and that I have had success with separating interfacial

contributions to experimental VSFG data; however, it is important to point out that the experimental measurements made throughout this work have not provided enough constraints for unambiguous *quantitative* separation of those contributions. An overarching theme from VSFG data analysis throughout this project has been a problem of parameter correlations in the fitting routines: the parameters are virtually always underdetermined by the data. While the model provides the mathematical theory necessary to describe optical interference effects, there is still work to be done for quantitative VSFG measurements. Some suggestions for immediate improvement on the measurements made in this project are provided in Section 5.7.3.

In the long term, I see generalized coherent nonlinear wave-mixing measurements on thin film systems progressing in the direction of more of an ellipsometric approach in order to extract highly accurate data and additional information (e.g. phase) for all input and generated light beams.[287,288] With the extension of the model to describe optical interferences for higher order bulk terms provided in Chapter 5, it is straightforward to arrive at the analogous bulk transfer products for dipole-allowed interactions such as those encountered in third order experiments applied to isotropic thin film systems (or generally, odd-ordered experiments). In order to quantitatively sort out the multitude of confounding factors, wave-mixing measured in conjunction with the polarization state of the input beams could be used to simultaneous fit linear ellipsometric data for the input beams and compute transfer products for the nonlinear beams. An instrument capable of such measurements could be used to more reliably resolve issues such as optical anisotropy, graded films, and most notably, nonlinear effects on refractive indices so that modeling

could account for possible effects from fluctuations in the input laser beam intensities. To this end, I see my approach to modeling optical interferences as a useful tool for data analysis for nonlinear spectroscopy applied to thin film systems. I consider the broad implications of this project as providing a step towards interface-specific nonlinear spectroscopy becoming a viable and robust tool added to the list of standard techniques for studying interfaces in thin film systems.

Bibliography

(1) Wu, S. *Polymer interface and adhesion*; New York : M. Dekker: New York, NY, 1982.

(2) Rangwalla, H.; Dhinojwala, A. *J. Adhes.* **2004**, *80*, 37–59.

(3) Oscik, J. *Adsorption*; E. Horwood ; Halsted Press: New York, NY, 1982.

(4) Papirer, E. *Adsorption on silica surfaces.*; Dekker: New York, NY, 2000.

(5) Rao, Y.; Comstock, M.; Eisenthal, K. B. *J. Phys. Chem. B* **2006**, *110*, 1727–1732.

(6) Carley, A. F.; Davies, P. R.; Hutchings, G. J.; Spencer, M. S. *Surface chemistry and catalysis*; Kluwer Academic/Plenum Publishers: New York, NY, 2002.

(7) Ma, Z.; Zaera, F. *Surf. Sci. Rep.* **2006**, *61*, 229–281.

(8) Nuzzo, R. G.; Dubois, L. H.; Allara, D. L. *J. Am. Chem. Soc.* **1990**, *112*, 558–569.

(9) Thome, J.; Himmelhaus, M.; Zharnikov, M.; Grunze, M. *Langmuir* **1998**, *14*, 7435–7449.

(10) *Wettability*; Berg, J. C., Ed.; M. Dekker: New York, NY, 1993.

(11) Thompson, B. C.; Fréchet, J. M. J. *Angew. Chemie Int. Ed.* **2008**, *47*, 58–77.

(12) Liu, A.; Zhao, S.; Rim, S.-B.; Wu, J.; Könemann, M.; Erk, P.; Peumans, P. *Adv. Mater.* **2008**, *20*, 1065–1070.

(13) Osikowicz, W.; de Jong, M. P.; Salaneck, W. R. *Adv. Mater.* **2007**, *19*, 4213–4217.

(14) Braun, S.; Salaneck, W. R.; Fahlman, M. *Adv. Mater.* **2009**, *21*, 1450–1472.

(15) Ando, T.; Fowler, A. B.; Stern, F. *Rev. Mod. Phys.* **1982**, *54*, 437–672.

(16) Dodabalapur, A.; Katz, H. E.; Torsi, L.; Haddon, R. C. *Sci.* **1995**, *269* , 1560–1562.

(17) Horowitz, G. *Adv. Mater.* **1998**, *10*, 365–377.

(18) Chesterfield, R. J. R.; McKeen, J. J. C.; Newman, C. R.; Ewbank, P. C.; da Silva Filho, D. A.; Brédas, J.-L.; Miller, L. L.; Mann, K. R.; Frisbie, C. D. *J. Phys. Chem. B* **2004**, *108*, 19281–19292.

(19) Sirringhaus, H. In *Organic Field-Effect Transistors*; Optical Science and Engineering; CRC Press, 2007; pp. 103–137.

(20) Podzorov, V. In *Organic Field-Effect Transistors*; Optical Science and Engineering; CRC Press, 2007; pp. 27–72.

(21) Feller, M.; Chen, W.; Shen, Y. *Phys. Rev. A* **1991**, *43*.

(22) Bain, C. D. *J. Chem. Soc. Faraday Trans.* **1995**, *91*, 1281–1296.

(23) Wilson, P. T.; Briggman, K. A.; Wallace, W. E.; Stephenson, J. C.; Richter, L. J. *Appl. Phys. Lett.* **2002**, *80*, 3084–3086.

(24) Ostroverkhov, V.; Waychunas, G. A.; Shen, Y. R. *Phys. Rev. Lett.* **2005**, *94*, 46102.

(25) Anglin, T. C.; O'Brien, D. B.; Massari, A. M. *J. Phys. Chem. C* **2010**, *114*, 17629–17637.

(26) Jena, K. C.; Covert, P. A.; Hall, S. A.; Hore, D. K. *J. Phys. Chem. C* **2011**, *115*, 15570–15574.

(27) Malinauskas, A. *J. Power Sources,* **2004**, *126*, 214–220.

(28) *Printed organic and molecular electronics*; Gamota, D.; Brazis, P.; Kalyanasundaram, K.; Zhang, J., Eds.; Kluwer Academic: Boston, MA, 2004.

(29) SAMSUNG Introduces World's First Curved OLED TV at CES 2013 http://www.samsung.com/us/news/20352 (accessed 8/29/2013).

(30) LG BEGINS SALES OF WORLD'S FIRST CURVED OLED TV http://www.lgnewsroom.com/newsroom/contents/63430 (accessed 8/29/2013).

(31) Myny, K.; Steudel, S.; Vicca, P.; Genoe, J.; Heremans, P. *Appl. Phys. Lett.* **2008**, *93*, 93303–93305.

(32) Brabec, C. J.; Durrant, J. R. *MRS Bull.* **2008**, *33*, 670–675.

(33) Someya, T.; Pal, B.; Huang, J.; Katz, H. E. *MRS Bull.* **2008**, *33*, 690–696.

(34) Loo, Y.-L.; McCulloch, I. *MRS Bull.* **2008**, *33*, 653–662.

(35) Ashtiani, S. J.; Chaji, G. R.; Nathan, A. *J. Disp. Technol.* **2007**, *3*, 36–39.

(36) Montasser, M. M.; Korzec, D. In *2008 International Conference on Microelectronics*; IEEE, 2008; pp. 437–440.

(37) Pochettino, A. *Atti. R. Accad. Lincei.* **1906**, *15*, 355–363.

(38) Volmer, M. *Ann. der Phys.* **1913**, *345*, 775–796.

(39) Koenigsberger, J.; Schilling, K. *Ann. der Phys.* **1910**, *32*, 179–229.

(40) Akamatu, H.; Inokuchi, H.; Matsunaga, Y. *Nature* **1954**, *173*, 168–169.

(41) Natta, G.; Mazzanti, G.; Corradini, P. *Atti Accad. Naz. Lincei Cl. Sci. Fis. Mat. Nat. Rend. Lincei* **1958**, *25*, 3.

(42) Walatka, V. V; Labes, M. M.; Perlstein, J. H. *Phys. Rev. Lett.* **1973**, *31*, 1139.

(43) Hsu, C.; Labes, M. M. *J. Chem. Phys.* **1974**, *61*, 4640–4645.

(44) *Handbook of organic conductive molecules and polymers*; Nalwa, H. S., Ed.; 4th ed.; Wiley: New York, NY, 1997.

(45) Freund, M. S.; Deore, B. *Self-doped conducting polymers*; Wiley: Hoboken, NJ, 2007.

(46) Chiang, C. K.; Fincher, C. R.; Park, Y. W.; Heeger, A. J.; Shirakawa, H.; Louis, E. J.; Gau, S. C.; MacDiarmid, A. G. *Phys. Rev. Lett.* **1977**, *39*, 1098.

(47) Shirakawa, H.; Louis, E. J.; Epstein, A. J.; MacDiarmid, A. G.; Chiang, C. K.; Heeger, A. J. *J. Chem. Soc. Chem. Commun.* **1977**, 578.

(48) Chiang, C. K.; Druy, M. A.; Gau, S. C.; Heeger, A. J.; Louis, E. J.; MacDiarmid, A. G.; Park, Y. W.; Shirakawa, H. *J. Am. Chem. Soc.* **1978**, *100*, 1013–1015.

(49) Shirakawa, H.; Ito, T.; Ikeda, S. *Makromol. Chemie-Macromolecular Chem. Phys.* **1978**, *179*, 1565–1573.

(50) Newman, C. R.; Frisbie, C. D.; da Silva Filho, D. A.; Brédas, J.-L.; Ewbank, P. C.; Mann, K. R. *Chem. Mater.* **2004**, *16*, 4436–4451.

(51) Horowitz, G. *J. Mater. Res.* **2004**, *19*, 1946–1962.

(52) *Organic field-effect transistors*; Bao, Z.; Locklin, J. J., Eds.; CRC Press: Boca Raton, FL, 2007.

(53) Xie, W.; McGarry, K. A.; Liu, F.; Wu, Y.; Ruden, P. P.; Douglas, C. J.; Frisbie, C. D. *J. Phys. Chem. C* **2013**, *117*, 11522–11529.

(54) Seshadri, K.; Frisbie, C. D. *Appl. Phys. Lett.* **2001**, *78*, 993–995.

(55) Merlo, J. A.; Newman, C. R.; Gerlach, C. P.; Kelley, T. W.; Muyres, D. V; Fritz, S. E.; Toney, M. F.; Frisbie, C. D. *J. Am. Chem. Soc.* **2005**, *127*, 3997–4009.

(56) Horowitz, G.; Hajlaoui, M. E.; Hajlaoui, R. *J. Appl. Phys.* **2000**, *87*, 4456.

(57) Burgi, L.; Sirringhaus, H.; Friend, R. H. *Appl. Phys. Lett.* **2002**, *80*, 2913–2915.

(58) Alexandrov, A.; Ranninger, J. *Phys. Rev. B* **1981**, *23*, 1796.

(59) Monroe, D. *Phys. Rev. Lett.* **1985**, *54*, 146.

(60) Horowitz, G.; Delannoy, P. *J. Appl. Phys.* **1991**, *70*, 469–475.

(61) Arkhipov, V. I.; Emelianova, E. V; Adriaenssens, G. J. *Phys. Rev. B* **2001**, *64*, 125125.

(62) Cordes, H.; Baranovskii, S. D.; Kohary, K.; Thomas, P.; Yamasaki, S.; Hensel, F.; Wendorff, J.-H. *Phys. Rev. B* **2001**, *63*, 94201.

(63) Schmechel, R. *J. Appl. Phys.* **2003**, *93*, 4653.

(64) Schmechel, R.; von Seggern, H. *Phys. Status Solidi* **2004**, *201*, 1215–1235.

(65) Sirringhaus, H. *Adv. Mater.* **2005**, *17*, 2411–2425.

(66) Coropceanu, V.; Cornil, J.; da Silva Filho, D. A.; Olivier, Y.; Silbey, R.; Brédas, J.-L. *Chem. Rev.* **2007**, *107*, 926–952.

(67) Graupner, W.; Leditzky, G.; Leising, G.; Scherf, U. *Phys. Rev. B* **1996**, *54*, 7610.

(68) Werner, A. G.; Blochwitz, J.; Pfeiffer, M.; Leo, K. *J. Appl. Phys.* **2001**, *90*, 123.

(69) Steiger, J.; Schmechel, R.; von Seggern, H. *Synth. Met.* **2002**, *129*, 1–7.

(70) Karl, N.; Marktanner, J.; Stehle, R.; Warta, W. *Synth. Met.* **1991**, *42*, 2473–2481.

(71) Sundar, V. C.; Zaumseil, J.; Podzorov, V.; Menard, E.; Willett, R. L.; Someya, T.; Gershenson, M. E.; Rogers, J. A. *Science* **2004**, *303*, 1644–1646.

(72) Kawanishi, T.; Fujiwara, T.; Akai-Kasaya, M.; Saito, A.; Aono, M.; Takeya, J.; Kuwahara, Y. *Appl. Phys. Lett.* **2008**, *93*, 23303.

(73) Le Comber, P. G.; Spear, W. E. *Phys. Rev. Lett.* **1970**, *25*, 509.

(74) Kawasaki, N.; Ohta, Y.; Kubozono, Y.; Konishi, A.; Fujiwara, A. *Appl. Phys. Lett.* **2008**, *92*, 163307.

(75) Brinkmann, M.; Rannou, P. *Adv. Funct. Mater.* **2007**, *17*, 101–108.

(76) Deman, A.-L.; Erouel, M.; Lallemand, D.; Phaner-Goutorbe, M.; Lang, P.; Tardy, J. *J. Non. Cryst. Solids* **2008**, *354*, 1598–1607.

(77) Todescato, F.; Capelli, R.; Dinelli, F.; Murgia, M.; Camaioni, N.; Yang, M.; Bozio, R.; Muccini, M. *J. Phys. Chem. B* **2008**, *112*, 10130–10136.

(78) Chung, Y.; Verploegen, E.; Vailionis, A.; Sun, Y.; Nishi, Y.; Murmann, B.; Bao, Z. *Nano Lett.* **2011**, *11*, 1161–1165.

(79) Li, H.; Giri, G.; Tok, J. B.-H.; Bao, Z. *MRS Bull.* **2013**, *38*, 34–42.

(80) Marcus, R. A. *J. Chem. Phys.* **1956**, *24*, 966–978.

(81) Marcus, R. A. *Rev. Mod. Phys.* **1993**, *65*, 599–610.

(82) Tolan, M. *X-Ray Scattering from Soft-Matter Thin Films: Materials Science and Basic Research*; Springer Tracts in Modern Physics; Springer: Berlin, Germany, 2000; Vol. 53.

(83) Gibaud, A.; Hazra, S. *Curr. Sci.* **2000**, *78*, 1467–1477.

(84) Rivnay, J.; Mannsfeld, S. C. B.; Miller, C. E.; Salleo, A.; Toney, M. F. *Chem. Rev.* **2012**, *112*, 5488–5519.

(85) Toney, M. F.; Russell, T. P.; Logan, J. A.; Kikuchi, H.; Sands, J. M.; Kumar, S. K. *Nature* **1995**, *374*, 709–711.

(86) Chabinyc, M. L. *Polym. Rev.* **2008**, *48*, 463–492.

(87) Renaud, G.; Lazzari, R.; Leroy, F. *Surf. Sci. Rep.* **2009**, *64*, 255–380.

(88) Porzio, W.; Scavia, G.; Barba, L.; Arrighetti, G.; Milita, S. *Eur. Polym. J.* **2011**, *47*, 273–283.

(89) Hirosawa, I.; Sasaki, N.; Kimura, H. *Jpn. J. Appl. Phys.* **1999**, *38*, L583–L585.

(90) Samant, M. G.; Stöhr, J.; Brown, H. R.; Russell, T. P.; Sands, J. M.; Kumar, S. K. *Macromolecules* **1996**, *29*, 8334–8342.

(91) Stöhr, J.; Samant, M. G.; Cossy-Favre, A.; Díaz, J.; Momoi, Y.; Odahara, S.; Nagata, T. *Macromolecules* **1998**, *31*, 1942–1946.

(92) Weiss, K.; Wöll, C.; Böhm, E.; Fiebranz, B.; Forstmann, G.; Peng, B.; Scheumann, V.; Johannsmann, D. *Macromolecules* **1998**, *31*, 1930–1936.

(93) Cossy-Favre, A.; Díaz, J.; Liu, Y.; Brown, H. R.; Samant, M. G.; Stöhr, J.; Hanna, A. J.; Anders, S.; Russell, T. P. *Macromolecules* **1998**, *31*, 4957–4962.

(94) Chesterfield, R. J.; McKeen, J. C.; Newman, C. R.; Frisbie, C. D.; Ewbank, P. C.; Mann, K. R.; Miller, L. L. *J. Appl. Phys.* **2004**, *95*, 6396–6405.

(95) Krauss, T. N.; Barrena, E.; de Oteyza, D. G.; Zhang, X. N.; Major, J.; Dehm, V.; Würthner, F.; Dosch, H. *J. Phys. Chem. C* **2009**, *113*, 4502–4506.

(96) O'Brien, D. B.; Anglin, T. C.; Massari, A. M. *Langmuir* **2011**, *27*, 13940–13949.

(97) Xu, Z.; Chen, L.-M.; Yang, G.; Huang, C.-H.; Hou, J.; Wu, Y.; Li, G.; Hsu, C.-S.; Yang, Y. *Adv. Funct. Mater.* **2009**, *19*, 1227–1234.

(98) Ito, Y.; Virkar, A. A.; Mannsfeld, S.; Oh, J. H.; Toney, M.; Locklin, J.; Bao, Z. *J. Am. Chem. Soc.* **2009**, *131*, 9396–9404.

(99) Frisbie, C. D.; Panzer, M. In *Organic Field-Effect Transistors*; Optical Science and Engineering; CRC Press, 2007; pp. 139–157.

(100) Pesavento, P. V; Puntambekar, K. P.; Frisbie, C. D.; McKeen, J. C.; Ruden, P. P. *J. Appl. Phys.* **2006**, *99*, 94504–94510.

(101) Puntambekar, K.; Dong, J.; Haugstad, G.; Frisbie, C. D. *Adv. Funct. Mater.* **2006**, *16*, 879–884.

(102) Pratontep, S.; Brinkmann, M.; Nüesch, F.; Zuppiroli, L. *Phys. Rev. B* **2004**, *69*, 165201.

(103) Petit, M.; Hayakawa, R.; Wakayama, Y.; Chikyow, T. *J. Phys. Chem. C* **2007**, *111*, 12747–12751.

(104) Chabinyc, M. L.; Salleo, A.; Wu, Y.; Liu, P.; Ong, B. S.; Heeney, M.; McCulloch, I. *J. Am. Chem. Soc.* **2004**, *126*, 13928–13929.

(105) Germack, D. S.; Chan, C. K.; Hamadani, B. H.; Richter, L. J.; Fischer, D. A.; Gundlach, D. J.; DeLongchamp, D. M. *Appl. Phys. Lett.* **2009**, *94*, 233303.

(106) Majewski, L. A.; Grell, M. *Synth. Met.* **2005**, *151*, 175–179.

(107) Panzer, M. J.; Newman, C. R.; Frisbie, C. D. *Appl. Phys. Lett.* **2005**, *86*, 103503.

(108) Tripathi, A. K.; Heinrich, M.; Siegrist, T.; Pflaum, J. *Adv. Mater.* **2007**, *19*, 2097–2101.

(109) Che, C.-M.; Xiang, H.-F.; Chui, S. S.-Y.; Xu, Z.-X.; Roy, V. A. L.; Yan, J. J.; Fu, W.-F.; Lai, P. T.; Williams, I. D. *Chem. – An Asian J.* **2008**, *3*, 1092–1103.

(110) Cheng, H. L.; Chou, W. Y.; Kuo, C. W.; Wang, Y. W.; Mai, Y. S.; Tang, F. C.; Chu, S. W. *Adv. Funct. Mater.* **2008**, *18*, 285–293.

(111) Cho, J. H.; Lee, J.; He, Y.; Kim, B. S.; Lodge, T. P.; Frisbie, C. D. *Adv. Mater.* **2008**, *20*, 686–690.

(112) Maiman, T. H. *Nature* **1960**, *187*, 493–494.

(113) Collins, R. J.; Nelson, D. F.; Schawlow, A. L.; Bond, W.; Garrett, C. G. B.; Kaiser, W. *Phys. Rev. Lett.* **1960**, *5*, 303–305.

(114) Franken, P. A.; Hill, A. E.; Peters, C. W.; Weinreich, G. *Phys. Rev. Lett.* **1961**, *7*, 118–119.

(115) Bass, M.; Franken, P. A.; Hill, A. E.; Peters, C. W.; Weinreich, G. *Phys. Rev. Lett.* **1962**, *8*, 18.

(116) Giordmaine, J. A. *Phys. Rev. Lett.* **1962**, *8*, 19–20.

(117) Maker, P. D.; Terhune, R. W.; Nisenoff, M.; Savage, C. M. *Phys. Rev. Lett.* **1962**, *8*, 21–22.

(118) Lax, B.; Mavroides, J. G.; Edwards, D. F. *Phys. Rev. Lett.* **1962**, *8*, 166–168.

(119) Terhune, R. W.; Maker, P. D.; Savage, C. M. *Phys. Rev. Lett.* **1962**, *8*, 404–406.

(120) Armstrong, J. A.; Bloembergen, N.; Ducuing, J.; Pershan, P. S. *Phys. Rev.* **1962**, *127*, 1918–1939.

(121) Bloembergen, N.; Pershan, P. S. *Phys. Rev.* **1962**, *128*, 606–622.

(122) Pershan, P. S. *Phys. Rev.* **1963**, *130*, 919–929.

(123) Adler, E. *Phys. Rev.* **1964**, *134*, A728–A733.

(124) Jha, S. S. *Phys. Rev. Lett.* **1965**, *15*, 412–414.

(125) Jha, S. S. *Phys. Rev.* **1965**, *140*, A2020–A2030.

(126) Bloembergen, N.; Shen, Y. R. *Phys. Rev.* **1966**, *141*, 298–305.

(127) Brown, F.; Parks, R. E.; Sleeper, A. M. *Phys. Rev. Lett.* **1965**, *14*, 1029–1031.

(128) Brown, F.; Parks, R. E. *Phys. Rev. Lett.* **1966**, *16*, 507–509.

(129) Sonnenberg, H.; Heffner, H. *J. Opt. Soc. Am.* **1968**, *58*, 209.

(130) Bloembergen, N.; Chang, R. K.; Lee, C. H. *Phys. Rev. Lett.* **1966**, *16*, 986–989.

(131) Wang, C. C.; Duminski, A. N. *Phys. Rev. Lett.* **1968**, *20*, 668–671.

(132) Ducuing, J.; Bloembergen, N. *Phys. Rev. Lett.* **1963**, *10*, 474–476.

(133) Wang, C. C. *Phys. Rev.* **1969**, *178*, 1457–1460.

(134) Bloembergen, N.; Chang, R. K.; Jha, S. S.; Lee, C. H. *Phys. Rev.* **1968**, *174*, 813–822.

(135) Brown, F.; Matsuoka, M. *Phys. Rev.* **1969**, *185*, 985–987.

(136) Rudnick, J.; Stern, E. A. *Phys. Rev. B* **1971**, *4*, 4274–4290.

(137) Wang, C. S.; Chen, J. M.; Bower, J. R. *Opt. Commun.* **1973**, *8*, 275–279.

(138) Sommerfeld, A. *Ann. der Phys.* **1909**, *333*, 665–736.

(139) Simon, H. J.; Mitchell, D. E.; Watson, J. G. *Phys. Rev. Lett.* **1974**, *33*, 1531–1534.

(140) Simon, H. J.; Mitchell, D. E.; Watson, J. G. *Opt. Commun.* **1975**, *13*, 294–298.

(141) De Martini, F.; Shen, Y. *Phys. Rev. Lett.* **1976**, *36*, 216–219.

(142) Simon, H. J.; Guha, J. K. *Opt. Commun.* **1976**, *18*, 391–394.

(143) DeMartini, F.; Giuliani, G.; Mataloni, P.; Palange, E.; Shen, Y. R. *Phys. Rev. Lett.* **1976**, *37*, 440–443.

(144) Chen, Y. J.; Burstein, E. *Nuovo Cim. B Ser. 11* **1977**, *39*, 807–816.

(145) Simon, H. J.; Benner, R. E.; Rako, J. G. *Opt. Commun.* **1977**, *23*, 245–248.

(146) DeMartini, F.; Colocci, M.; Kohn, S. E.; Shen, Y. R. *Phys. Rev. Lett.* **1977**, *38*, 1223–1226.

(147) Fukui, M.; Stegeman, G. I. *Solid State Commun.* **1978**, *26*, 239–241.

(148) Fukui, M.; So, V. C. Y.; Sipe, J. E.; Stegeman, G. I. *J. Phys. Chem. Solids* **1979**, *40*, 523–530.

(149) De Martini, F.; Ristori, P.; Santamato, E.; Zammit, A. *Phys. Rev. B* **1981**, *23*, 3797–3804.

(150) Marschall, N.; Fischer, B. *Phys. Rev. Lett.* **1972**, *28*, 811–813.

(151) Boardman, A. D. *Electromagnetic surface modes*; Wiley: New York, NY, 1982; p. 725.

(152) *Surface Polaritons: Electromagnetic Waves at Surfaces and Interfaces*; Agranovich, V. M.; Mills, D. L., Eds.; North-Holland: New York, 1982; pp. 629 & 661.

(153) Chen, J. M.; Bower, J. R.; Wang, C. S.; Lee, C. H. *Opt. Commun.* **1973**, *9*, 132–134.

(154) Chang, R. K.; Furtak, T. E. *Surface enhanced Raman scattering*; Plenum Press: New York, NY, 1982.

(155) Chen, C. K.; de Castro, A. R. B.; Shen, Y. R. *Phys. Rev. Lett.* **1981**, *46*, 145–148.

(156) Chen, C. K.; Heinz, T. F.; Ricard, D.; Shen, Y. R. *Chem. Phys. Lett.* **1981**, *83*, 455–458.

(157) Chen, C. K.; Heinz, T. F.; Ricard, D.; Shen, Y. R. *Phys. Rev. Lett.* **1981**, *46*, 1010–1012.

(158) Heinz, T. F.; Chen, C. K.; Ricard, D.; Shen, Y. R. *Chem. Phys. Lett.* **1981**, *83*, 180–182.

(159) Shen, Y. R. *John Wiley Sons* **1984**, *32*, 0.

(160) Heinz, T. F.; Chen, C. K.; Ricard, D.; Shen, Y. R. *Phys. Rev. Lett.* **1982**, *48*, 478–481.

(161) Tom, H. W. K.; Mate, C. M.; Zhu, X. D.; Crowell, J. E.; Heinz, T. F.; Somorjai, G. A.; Shen, Y. R. *Phys. Rev. Lett.* **1984**, *52*, 348–351.

(162) Tom, H. W. K.; Mate, C. M.; Zhu, X. D.; Crowell, J. E.; Shen, Y. R.; Somorjai, G. A. *Surf. Sci.* **1986**, *172*, 466–476.

(163) Richmond, G. L. *Surf. Sci.* **1984**, *147*, 115–126.

(164) Tom, H. W. K.; Heinz, T. F.; Shen, Y. R. *Phys. Rev. Lett.* **1983**, *51*, 1983–1986.

(165) Guidotti, D.; Driscoll, T. A.; Gerritsen, H. J. *Solid State Commun.* **1983**, *46*, 337–340.

(166) Driscoll, T. A.; Guidotti, D. *Phys. Rev. B* **1983**, *28*, 1171–1173.

(167) Shank, C. V; Yen, R.; Hirlimann, C. *Phys. Rev. Lett.* **1983**, *51*, 900–902.

(168) Heinz, T. F. *J. Vac. Sci. Technol. B Microelectron. Nanom. Struct.* **1985**, *3*, 1467.

(169) Heinz, T. F.; Loy, M. M. T.; Thompson, W. A. *Phys. Rev. Lett.* **1985**, *54*, 63–66.

(170) Shen, Y. R. *J. Vac. Sci. Technol. B Microelectron. Nanom. Struct.* **1985**, *3*, 1464–1466.

(171) Guyot-Sionnest, P.; Chen, W.; Shen, Y. R. *Phys. Rev. B* **1986**, *33*, 8254–8263.

(172) Richmond, G. L.; Robinson, J. M.; Shannon, V. L. *Prog. Surf. Sci.* **1988**, *28*, 1–70.

(173) Heinz, T. F.; Tom, H. W. K.; Shen, Y. R. *Phys. Rev. A* **1983**, *28*, 1883–1885.

(174) Reider, G. A.; Schmidt, A. J.; Marowsky, G. *Opt. Commun.* **1983**, *47*, 223–225.

(175) Girling, I. R.; Cade, N. A.; Kolinsky, P. V; Earls, J. D.; Cross, G. H.; Peterson, I. R. *Thin Solid Films* **1985**, *132*, 101–112.

(176) Marowsky, G.; Gierulski, A.; Dick, B. *Opt. Commun.* **1985**, *52*, 339–342.

(177) Dick, B.; Gierulski, A.; Marowsky, G.; Reider, G. A. *Appl. Phys. B* **1985**, *38*, 107–116.

(178) Chen, Z.; Chen, W.; Zheng, J.; Wang, W.; Zhang, Z. *Opt. Commun.* **1985**, *54*, 305–310.

(179) Di Lazzaro, P.; Mataloni, P.; De Martini, F. *Chem. Phys. Lett.* **1985**, *114*, 103–108.

(180) Van Wyck, N. E.; Koenig, E. W.; Byers, J. D.; Hetherington III, W. M. *Chem. Phys. Lett.* **1985**, *122*, 153–156.

(181) Khanarian, G. *Thin Solid Films* **1987**, *152*, 265–274.

(182) Marowsky, G.; Steinhoff, R.; Reider, G. A.; Erdmann, D.; Dorsch, D. *Opt. Commun.* **1987**, *63*, 109–113.

(183) Epperlein, D.; Dick, B.; Marowsky, G.; Reider, G. A. *Appl. Phys. B* **1987**, *44*, 5–10.

(184) Felderhof, B. U.; Marowsky, G. *Appl. Phys. B* **1987**, *44*, 11–17.

(185) Girling, I. R.; Cade, N. A.; Kolinsky, P. V; Jones, R. J.; Peterson, I. R.; Ahmad, M. M.; Neal, D. B.; Petty, M. C.; Roberts, G. G.; Feast, W. J. *J. Opt. Soc. Am. B* **1987**, *4*, 950–954.

(186) Marowsky, G.; Chi, L. F.; Möbius, D.; Steinhoff, R.; Shen, Y. R.; Dorsch, D.; Rieger, B. *Chem. Phys. Lett.* **1988**, *147*, 420–424.

(187) Marowsky, G.; Steinhoff, R.; Chi, L. F.; Hutter, J.; Wagnière, G. *Phys. Rev. B* **1988**, *38*, 6274–6278.

(188) Marowsky, G.; Steinhoff, R. *Opt. Lett.* **1988**, *13*, 707–709.

(189) Zhu, X. D.; Shen, Y. R.; Carr, R. *Surf. Sci.* **1985**, *163*, 114–120.

(190) Rasing, T.; Shen, Y. R.; Kim, M. W.; Valint Jr., P.; Bock, J. *Phys. Rev. A* **1985**, *31*, 537–539.

(191) Rasing, T.; Shen, Y. R.; Kim, M. W.; Grubb, S. *Phys. Rev. Lett.* **1985**, *55*, 2903–2906.

(192) Berkovic, G.; Rasing, T.; Shen, Y. R. *J. Chem. Phys.* **1986**, *85*, 7374–7376.

(193) Guyot-Sionnest, P.; Hsiung, H.; Shen, Y. R. *Phys. Rev. Lett.* **1986**, *57*, 2963–2966.

(194) Hicks, J. M.; Kemnitz, K.; Eisenthal, K. B.; Heinz, T. F. *J. Phys. Chem.* **1986**, *90*, 560–562.

(195) Kemnitz, K.; Bhattacharyya, K.; Hicks, J. M.; Pinto, G. R.; Eisenthal, B.; Heinz, T. F. *Chem. Phys. Lett.* **1986**, *131*, 285–290.

(196) Bhattacharyya, K.; Sitzmann, E. V; Eisenthal, K. B. *J. Chem. Phys.* **1987**, *87*, 1442–1443.

(197) Rasing, T.; Stehlin, T.; Shen, Y. R.; Kim, M. W.; Valint P., J. *J. Chem. Phys.* **1988**, *89*, 3386–3387.

(198) Grubb, S. G.; Kim, M. W.; Rasing, T.; Shen, Y. R. *Langmuir* **1988**, *4*, 452–454.

(199) Goh, M. C.; Hicks, J. M.; Kemnitz, K.; Pinto, G. R.; Heinz, T. F.; Eisenthal, K. B.; Bhattacharyya, K. *J. Phys. Chem.* **1988**, *92*, 5074–5075.

(200) Bhattacharyya, K.; Castro, A.; Sitzmann, E. V; Eisenthal, K. B. *J. Chem. Phys.* **1988**, *89*, 3376–3377.

(201) Rasing, T.; Huang, J.; Lewis, A.; Stehlin, T.; Shen, Y. R. *Phys. Rev. A* **1989**, *40*, 1684–1687.

(202) Cynthia Goh, M.; Eisenthal, K. B. *Chem. Phys. Lett.* **1989**, *157*, 101–104.

(203) Castro, A.; Ong, S.; Eisenthal, K. B. *Chem. Phys. Lett.* **1989**, *163*, 412–416.

(204) Murphy, D. V; Von Raben, K. U.; Chen, T. T.; Owen, J. F.; Chang, R. K.; Laube, B. L. *Surf. Sci.* **1983**, *124*, 529–546.

(205) Corn, R. M.; Romagnoli, M.; Levenson, M. D.; Philpott, M. R. *J. Chem. Phys.* **1984**, *81*, 4127–4132.

(206) Chen, T. T.; Von Raben, K. U.; Murphy, D. V; Chang, R. K.; Laube, B. L. *Surf. Sci.* **1984**, *143*, 369–390.

(207) Voss, D. F.; Nagumo, M.; Goldberg, L. S.; Bunding, K. A. *J. Phys. Chem.* **1986**, *90*, 1834–1838.

(208) Marshall, C. D.; Korenowski, G. M. *J. Chem. Phys.* **1986**, *85*, 4172–4180.

(209) Biwer, B. M.; Pellin, M. J.; Schauer, M. W.; Gruen, D. M. *Surf. Sci.* **1986**, *176*, 377–396.

(210) Campbell, D. J.; Corn, R. M. *J. Phys. Chem.* **1987**, *91*, 5668–5673.

(211) Furtak, T. E.; Miragliotta, J.; Korenowski, G. M. *Phys. Rev. B* **1987**, *35*, 2569–2572.

(212) Marshall, C. D.; Korenowski, G. M. *J. Phys. Chem.* **1987**, *91*, 1289–1292.

(213) Campbell, D. J.; Corn, R. M. *J. Phys. Chem.* **1988**, *92*, 5796–5800.

(214) Miragliotta, J.; Furtak, T. E. *Phys. Rev. B* **1988**, *37*, 1028–1030.

(215) Biwer, B. M.; Pellin, M. J.; Schauer, M. W.; Gruen, D. M. *Langmuir* **1988**, *4*, 121–127.

(216) Robinson, J. M.; Richmond, G. L. *Chem. Phys.* **1990**, *141*, 175–188.

(217) Zhu, X. D.; Suhr, H.; Shen, Y. R. *Phys. Rev. B* **1987**, *35*, 3047–3050.

(218) Hunt, J. H.; Guyot-Sionnest, P.; Shen, Y. R. *Chem. Phys. Lett.* **1987**, *133*, 189–192.

(219) Guyot-Sionnest, P.; Superfine, R.; Hunt, J. H.; Shen, Y. R. *Chem. Phys. Lett.* **1988**, *144*, 1–5.

(220) Superfine, R.; Guyot-Sionnest, P.; Hunt, J. H.; Kao, C. T.; Shen, Y. R. *Surf. Sci.* **1988**, *200*, L445–L450.

(221) Harris, A. L.; Chidsey, C. E. D.; Levinos, N. J.; Loiacono, D. N. *Chem. Phys. Lett.* **1987**, *141*, 350–356.

(222) Harris, A. L.; Levinos, N. J. *J. Chem. Phys.* **1989**, *90*, 3878–3879.

(223) Guyot-Sionnest, P.; Hunt, J. H.; Shen, Y. R. *Phys. Rev. Lett.* **1987**, *59*, 1597–1600.

(224) Heinz, T. F. Nonlinear Optics of Surfaces and Interfaces, University of California, Berkeley, 1982.

(225) Ye, P.; Shen, Y. R. *Phys. Rev. B* **1983**, *28*, 4288–4294.

(226) Apell, P. *Phys. Scr.* **1983**, *27*, 211.

(227) Chen, C. K.; Heinz, T. F.; Ricard, D.; Shen, Y. R. *Phys. Rev. B* **1983**, *27*, 1965–1979.

(228) Dick, B. *Chem. Phys.* **1985**, *96*, 199–215.

(229) Shen, Y. R. *Annu. Rev. Mater. Sci.* **1986**, *16*, 69–86.

(230) Felderhof, B. U.; Marowsky, G. *Appl. Phys. B* **1987**, *43*, 161–166.

(231) Sipe, J. E. *J. Opt. Soc. Am. B* **1987**, *4*, 481.

(232) Mazely, T. L.; Hetherington III, W. M. *J. Chem. Phys.* **1987**, *86*, 3640–3647.

(233) Guyot-Sionnest, P.; Shen, Y. R.; Heinz, T. F. *Appl. Phys. B Photophysics Laser Chem.* **1987**, *42*, 237–238.

(234) Guyot-Sionnest, P.; Shen, Y. R. *Phys. Rev. B* **1987**, *35*, 4420–4426.

(235) Guyot-Sionnest, P.; Shen, Y. R. *Phys. Rev. B* **1988**, *38*, 7985–7989.

(236) Shen, Y. R. *Annu. Rev. Phys. Chem.* **1989**, *40*, 327–350.

(237) Heinz, T. F. In *Nonlinear Surface Electromagnetic Phenomena*; Ponath, H.-E.; Stegeman, G. I., Eds.; North-Holland: New York, NY, 1991; pp. 353–416.

(238) Bain, C. D.; Davies, P. B.; Ong, T. H.; Ward, R. N.; Brown, M. A. *Langmuir* **1991**, *7*, 1563–1566.

(239) Hirose, C.; Akamatsu, N.; Domen, K. *J. Chem. Phys.* **1992**, *96*, 997–1004.

(240) Hirose, C.; Akamatsu, N.; Domen, K. *Appl. Spectrosc.* **1992**, *46*, 1051–1072.

(241) Bedeaux, D.; Vlieger, J. *Physica* **1973**, *67*, 55–73.

(242) Bloembergen, N. *Appl. Phys. B* **1999**, *68*, 289–293.

(243) Miranda, P. B.; Shen, Y. R. *J. Phys. Chem. B* **1999**, *103*, 3292–3307.

(244) Superfine, R.; Huang, J. Y.; Shen, Y. R. *Phys. Rev. Lett.* **1991**, *66*, 1066–1069.

(245) Du, Q.; Superfine, R.; Freysz, E.; Shen, Y. R. *Phys. Rev. Lett.* **1993**, *70*, 2313–2316.

(246) Eisenthal, K. B. *Chem. Rev.* **1996**, *96*, 1343–1360.

(247) Wolfrum, K.; Graener, H.; Laubereau, A. *Chem. Phys. Lett.* **1993**, *213*, 41–46.

(248) Zhang, D.; Gutow, J. H.; Eisenthal, K. B.; Heinz, T. F. *J. Chem. Phys.* **1993**, *98*, 5099–5101.

(249) Du, Q.; Freysz, E.; Shen, Y. R. *Phys. Rev. Lett.* **1994**, *72*, 238–241.

(250) Du, Q.; Freysz, E.; Shen, Y. R. *Sci.* **1994**, *264* , 826–828.

(251) Sefler, G. A.; Du, Q.; Miranda, P. B.; Shen, Y. R. *Chem. Phys. Lett.* **1995**, *235*, 347–354.

(252) Stanners, C. D.; Du, Q.; Chin, R. P.; Cremer, P.; Somorjai, G. A.; Shen, Y.-R. *Chem. Phys. Lett.* **1995**, *232*, 407–413.

(253) Scatena, L. F.; Brown, M. G.; Richmond, G. L. *Sci.* **2001**, *292* , 908–912.

(254) Huang, J. Y.; Wu, M. H. *Phys. Rev. E* **1994**, *50*, 3737–3746.

(255) Baldelli, S.; Schnitzer, C.; Shultz, M. J.; Campbell, D. J. *J. Phys. Chem. B* **1997**, *101*, 10435–10441.

(256) Baldelli, S.; Schnitzer, C.; Jane Shultz, M.; Campbell, D. J. *Chem. Phys. Lett.* **1998**, *287*, 143–147.

(257) Corn, R. M.; Higgins, D. A. *Chem. Rev.* **1994**, *94*, 107–125.

(258) Benjamin, I. *Annu. Rev. Phys. Chem.* **1997**, *48*, 407–451.

(259) Richmond, G. L. *Anal. Chem.* **1997**, *69*, 536A–543A.

(260) Walker, R. A.; Gruetzmacher, J. A.; Richmond, G. L. *J. Am. Chem. Soc.* **1998**, *120*, 6991–7003.

(261) Zhang, D.; Gutow, J.; Eisenthal, K. B. *J. Phys. Chem.* **1994**, *98*, 13729–13734.

(262) Wolfrum, K.; Löbau, J.; Laubereau, A. *Appl. Phys. A* **1994**, *59*, 605–610.

(263) Zhang, D.; Gutow, J. H.; Eisenthal, K. B. *J. Chem. Soc. Faraday Trans.* **1996**, *92*, 539–543.

(264) Shi, X.; Borguet, E.; Tarnovsky, A. N.; Eisenthal, K. B. *Chem. Phys.* **1996**, *205*, 167–178.

(265) Radüge, C.; Pflumio, V.; Shen, Y. R. *Chem. Phys. Lett.* **1997**, *274*, 140–144.

(266) Miranda, P. B.; Pflumio, V.; Saijo, H.; Shen, Y. R. *Chem. Phys. Lett.* **1997**, *264*, 387–392.

(267) Wolfrum, K.; Löbau, J.; Birkhölzer, W.; Laubereau, A. *Quantum Semiclassical Opt. J. Eur. Opt. Soc. Part B* **1997**, *9*, 257–267.

(268) Baldelli, S.; Schnitzer, C.; Shultz, M. J.; Campbell, D. J. *J. Phys. Chem. B* **1997**, *101*, 4607–4612.

(269) Miranda, P. B.; Pflumio, V.; Saijo, H.; Shen, Y. R. *J. Am. Chem. Soc.* **1998**, *120*, 12092–12099.

(270) Baldelli, S.; Schnitzer, C.; Shultz, M. J. *J. Chem. Phys.* **1998**, *108*, 9817–9820.

(271) Pohle, W.; Saβ, M.; Selle, C.; Wolfrum, K.; Löbau, J. *Vib. Spectrosc.* **1999**, *19*, 321–327.

(272) Baldelli, S.; Schnitzer, C.; Campbell, D. J.; Shultz, M. J. *J. Phys. Chem. B* **1999**, *103*, 2789–2795.

(273) Eisenthal, K. B. *Annu. Rev. Phys. Chem.* **1992**, *43*, 627–661.

(274) Bell, G. R.; Bain, C. D.; Ward, R. N. *J. Chem. Soc. Faraday Trans.* **1996**, *92*, 515–523.

(275) Shen, Y. R. *Solid State Commun.* **1997**, *102*, 221–229.

(276) Buck, M.; Himmelhaus, M. *J. Vac. Sci. Technol. A Vacuum, Surfaces, Film.* **2001**, *19*, 2717–2736.

(277) Ji, N.; Ostroverkhov, V.; Chen, C.-Y.; Shen, Y.-R. *J. Am. Chem. Soc.* **2007**, *129*, 10056–10057.

(278) Matsuzaki, K.; Nihonyanagi, S.; Yamaguchi, S.; Nagata, T.; Tahara, T. *J. Phys. Chem. Lett.* **2013**, *4*, 1654–1658.

(279) Stiopkin, I. V; Jayathilake, H. D.; Bordenyuk, A. N.; Benderskii, A. V. *J. Am. Chem. Soc.* **2008**, *130*, 2271–2275.

(280) Flörsheimer, M.; Brillert, C.; Fuchs, H. *Langmuir* **1999**, *15*, 5437–5439.

(281) Flörsheimer, M.; Brillert, C.; Fuchs, H. *Mater. Sci. Eng. C* **1999**, *8–9*, 335–341.

(282) Hoffmann, D. M. P.; Kuhnke, K.; Kern, K. *Rev. Sci. Instrum.* **2002**, *73*, 3221–3226.

(283) Kuhnke, K.; Hoffmann, D. M. P.; Wu, X. C.; Bittner, A. M.; Kern, K. *Appl. Phys. Lett.* **2003**, *83*, 3830–3832.

(284) Cimatu, K.; Moore, H. J.; Lee, T. R.; Baldelli, S. *J. Phys. Chem. C* **2007**, *111*, 11751–11755.

(285) Cimatu, K. A.; Baldelli, S. *J. Phys. Chem. C* **2009**, *113*, 16575–16588.

(286) Smith, K. A.; Conboy, J. C. *Anal. Chem.* **2012**, *84*, 8122–8126.

(287) Begue, N. J.; Moad, A. J.; Simpson, G. J. *J. Phys. Chem. C* **2009**, *113*, 10158–10165.

(288) Begue, N. J.; Everly, R. M.; Hall, V. J.; Haupert, L.; Simpson, G. J. *J. Phys. Chem. C* **2009**, *113*, 10166–10175.

(289) Stiopkin, I. V; Jayathilake, H. D.; Weeraman, C.; Benderskii, A. V. *J. Chem. Phys.* **2010**, *132*, 234503–234509.

(290) Curtis, A. D.; Burt, S. R.; Calchera, A. R.; Patterson, J. E. *J. Phys. Chem. C* **2011**, *115*, 11550–11559.

(291) Curtis, A. D.; Asplund, M. C.; Patterson, J. E. *J. Phys. Chem. C* **2011**, *115*, 19303–19310.

(292) Laaser, J. E.; Xiong, W.; Zanni, M. T. *J. Phys. Chem. B* **2011**, *115*, 2536–2546.

(293) Rustagi, K. C.; Ducuing, J. *Opt. Commun.* **1974**, *10*, 258–261.

(294) Sauteret, C.; Hermann, J.-P.; Frey, R.; Pradère, F.; Ducuing, J.; Baughman, R. H.; Chance, R. R. *Phys. Rev. Lett.* **1976**, *36*, 956–959.

(295) Cojan, C.; Agrawal, G. P.; Flytzanis, C. *Phys. Rev. B* **1977**, *15*, 909–925.

(296) Agrawal, G. P.; Cojan, C.; Flytzanis, C. *Phys. Rev. B* **1978**, *17*, 776–789.

(297) Kajzar, F.; Messier, J.; Zyss, J.; Ledoux, I. *Opt. Commun.* **1983**, *45*, 133–137.

(298) Kajzar, F.; Messier, J.; Rosilio, C. *J. Appl. Phys.* **1986**, *60*, 3040–3044.

(299) Enoch, S.; Akhouayri, H. *J. Opt. Soc. Am. B* **1998**, *15*, 1030–1041.

(300) Chemla, D. S. *Reports Prog. Phys.* **1980**, *43*, 1191.

(301) Sipe, J. E. *Phys. Rev. B* **1980**, *22*, 1589–1599.

(302) Weber, W. H.; Ford, G. W. *Phys. Rev. Lett.* **1980**, *44*, 1774–1777.

(303) Lukosz, W. *Phys. Rev. B* **1980**, *22*, 3030–3038.

(304) Sipe, J. E. *Surf. Sci.* **1981**, *105*, 489–504.

(305) Ford, G. W.; Weber, W. H. *Surf. Sci.* **1981**, *109*, 451–481.

(306) Lukosz, W. *J. Opt. Soc. Am.* **1981**, *71*, 744–754.

(307) Sipe, J. E.; Young, J. F.; Preston, J. S.; van Driel, H. M. *Phys. Rev. B* **1983**, *27*, 1141–1154.

(308) Ford, G. W.; Weber, W. H. *Phys. Rep.* **1984**, *113*, 195–287.

(309) Litwin, J. A.; Sipe, J. E.; van Driel, H. M. *Phys. Rev. B* **1985**, *31*, 5543–5546.

(310) Werner, L.; Hill, W.; Marlow, F.; Glismann, A.; Hertz, O. *Thin Solid Films* **1991**, *205*, 58–63.

(311) Wang, X. K.; Zhang, T. G.; Lin, W. P.; Liu, S. Z.; Wong, G. K.; Kappes, M. M.; Chang, R. P. H.; Ketterson, J. B. *Appl. Phys. Lett.* **1992**, *60*, 810–812.

(312) Koopmans, B.; Janner, A.-M.; Jonkman, H. T.; Sawatzky, G. A.; van der Woude, F. *Phys. Rev. Lett.* **1993**, *71*, 3569–3572.

(313) Koopmans, B.; Anema, A.; Jonkman, H. T.; Sawatzky, G. A.; van der Woude, F. *Phys. Rev. B* **1993**, *48*, 2759–2764.

(314) Brudny, V. L.; Mochán, W. L. *Phys. Status Solidi A* **1999**, *175*, 183–188.

(315) Wu, Y. Z.; Vollmer, R.; Regensburger, H.; Jin, X.-F.; Kirschner, J. *Phys. Rev. B* **2000**, *63*, 54401.

(316) Briggman, K. A.; Stephenson, J. C.; Wallace, W. E.; Richter, L. J. *J. Phys. Chem. B* **2001**, *105*, 2785–2791.

(317) Cattaneo, S.; Kauranen, M. *Opt. Lett.* **2003**, *28*, 1445–1447.

(318) Maymó, M.; Martorell, J.; Molinos-Gómez, A.; López-Calahorra, F. *Opt. Express* **2006**, *14*, 2864.

(319) Schmid, J. H.; Delâge, A.; Lamontagne, B.; Lapointe, J.; Janz, S.; Cheben, P.; Densmore, A.; Waldron, P.; Xu, D.-X.; Yap, K. P. *Opt. Lett.* **2008**, *33*, 1479.

(320) Pedersen, K.; Pedersen, T. G. *J. Opt. Soc. Am. B* **2009**, *26*, 917–922.

(321) Mullin, C. S.; Guyot-Sionnest, P.; Shen, Y. R. *Phys. Rev. A* **1989**, *39*, 3745–3747.

(322) Hines, M. A.; Todd, J. A.; Guyot-Sionnest, P. *Langmuir* **1995**, *11*, 493–497.

(323) Boyd, R. W. *Nonlinear optics*; Academic Press: San Diego, CA, 2003.

(324) Gautam, K. S.; Schwab, A. D.; Dhinojwala, A.; Zhang, D.; Dougal, S. M.; Yeganeh, M. S. *Phys. Rev. Lett.* **2000**, *85*, 3854–3857.

(325) Wang, J.; Chen, C.; Buck, S. M.; Chen, Z. *J. Phys. Chem. B* **2001**, *105*, 12118–12125.

(326) Wang, J.; Woodcock, S. E.; Buck, S. M.; Chen, C.; Chen, Z. *J. Am. Chem. Soc.* **2001**, *123*, 9470–9471.

(327) Dreesen, L.; Humbert, C.; Hollander, P.; Mani, A. A.; Ataka, K.; Thiry, P. A.; Peremans, A. *Chem. Phys. Lett.* **2001**, *333*, 327–331.

(328) Harp, G. P.; Gautam, K. S.; Dhinojwala, A. *J. Am. Chem. Soc.* **2002**, *124*, 7908–7909.

(329) Wang, J.; Paszti, Z.; Even, M. A.; Chen, Z. *J. Am. Chem. Soc.* **2002**, *124*, 7016–7023.

(330) Ye, S.; Morita, S.; Li, G.; Noda, H.; Tanaka, M.; Uosaki, K.; Osawa, M. *Macromolecules* **2003**, *36*, 5694–5703.

(331) Rangwalla, H.; Schwab, A. D.; Yurdumakan, B.; Yablon, D. G.; Yeganeh, M. S.; Dhinojwala, A. *Langmuir* **2004**, *20*, 8625–8633.

(332) Chen, C.; Clarke, M. L.; Wang, J.; Chen, Z. *Phys. Chem. Chem. Phys.* **2005**, *7*, 2357–2363.

(333) Lu, X.; Xue, G.; Wang, X.; Han, J.; Han, X.; Hankett, J.; Li, D.; Chen, Z. *Macromolecules* **2012**, *45*, 6087–6094.

(334) Buck, M.; Dressler, C.; Grunze, M.; Träger, F. *J. Adhes.* **1996**, *58*, 227–241.

(335) Wei, X.; Hong, S.-C.; Zhuang, X.; Goto, T.; Shen, Y. R. *Phys. Rev. E* **2000**, *62*, 5160–5172.

(336) Gautam, K. S.; Dhinojwala, A. *Macromolecules* **2001**, *34*, 1137–1139.

(337) Chen, Q.; Zhang, D.; Somorjai, G.; Bertozzi, C. R. *J. Am. Chem. Soc.* **1998**, *121*, 446–447.

(338) Kim, D.; Shen, Y. R. *Appl. Phys. Lett.* **1999**, *74*, 3314–3316.

(339) Wei, X.; Zhuang, X.; Hong, S.-C.; Goto, T.; Shen, Y. R. *Phys. Rev. Lett.* **1999**, *82*, 4256–4259.

(340) Zhang, D.; Dougal, S. M.; Yeganeh, M. S. *Langmuir* **2000**, *16*, 4528–4532.

(341) Ye, H.; Abu-Akeel, A.; Huang, J.; Katz, H. E.; Gracias, D. H. *J. Am. Chem. Soc.* **2006**, *128*, 6528–6529.

(342) Wei, Q.; Tajima, K.; Tong, Y.; Ye, S.; Hashimoto, K. *J. Am. Chem. Soc.* **2009**, *131*, 17597–17604.

(343) Anglin, T. C.; Speros, J. C.; Massari, A. M. *J. Phys. Chem. C* **2011**, *115*, 16027–16036.

(344) Miyamae, T.; Takada, N.; Tsutsui, T. *Appl. Phys. Lett.* **2012**, *101*, 73304.

(345) Zhang, D.; Ward, R. S.; Shen, Y. R.; Somorjai, G. A. *J. Phys. Chem. B* **1997**, *101*, 9060–9064.

(346) Oh-e, M.; Lvovsky, A. I.; Wei, X.; Shen, Y. R. *J. Chem. Phys.* **2000**, *113*, 8827–8832.

(347) Jayathilake, H. D.; Zhu, M. H.; Rosenblatt, C.; Bordenyuk, A. N.; Weeraman, C.; Benderskii, A. V. *J. Chem. Phys.* **2006**, *125*, 64706–64709.

(348) Ye, H.; Huang, J.; Park, J.-R.; Katz, H. E.; Gracias, D. H. *J. Phys. Chem. C* **2007**, *111*, 13250–13255.

(349) Zhang, D.; Shen, Y. R.; Somorjai, G. A. *Chem. Phys. Lett.* **1997**, *281*, 394–400.

(350) Gracias, D. H.; Zhang, D.; Lianos, L.; Ibach, W.; Shen, Y. R.; Somorjai, G. A. *Chem. Phys.* **1999**, *245*, 277–284.

(351) Wei, X.; Hong, S.-C.; Lvovsky, A. I.; Held, H.; Shen, Y. R. *J. Phys. Chem. B* **2000**, *104*, 3349–3354.

(352) Li, Q.; Hua, R.; Chou, K. C. *J. Phys. Chem. B* **2008**, *112*, 2315–2318.

(353) Li, G.; Dhinojwala, A.; Yeganeh, M. S. *J. Phys. Chem. B* **2009**, *113*, 2739–2747.

(354) Wilk, D.; Johannsmann, D.; Stanners, C.; Shen, Y. R. *Phys. Rev. B* **1995**, *51*, 10057–10067.

(355) Ishida, H.; Iwatsu, K.; Kubota, J.; Wada, A.; Domen, K.; Hirose, C. *J. Chem. Phys.* **1998**, *108*, 5957–5964.

(356) Hirose, C.; Ishida, H.; Iwatsu, K.; Watanabe, N.; Kubota, J.; Wada, A.; Domen, K. *J. Chem. Phys.* **1998**, *108*, 5948–5956.

(357) Lu, X.; Shephard, N.; Han, J.; Xue, G.; Chen, Z. *Macromolecules* **2008**, *41*, 8770–8777.

(358) Lu, X.; Li, D.; Kristalyn, C. B.; Han, J.; Shephard, N.; Rhodes, S.; Xue, G.; Chen, Z. *Macromolecules* **2009**, *42*, 9052–9057.

(359) Tong, Y.; Zhao, Y.; Li, N.; Osawa, M.; Davies, P. B.; Ye, S. *J. Chem. Phys.* **2010**, *133*, 034704.

(360) Tong, Y.; Zhao, Y.; Li, N.; Ma, Y.; Osawa, M.; Davies, P. B.; Ye, S. *J. Chem. Phys.* **2010**, *133*, 034705.

(361) Lu, X.; Clarke, M. L.; Li, D.; Wang, X.; Xue, G.; Chen, Z. *J. Phys. Chem. C* **2011**, *115*, 13759–13767.

(362) Backus, E. H. G.; Garcia-Araez, N.; Bonn, M.; Bakker, H. J. *J. Phys. Chem. C* **2012**.

(363) Lambert, A. G.; Neivandt, D. J.; Briggs, A. M.; Usadi, E. W.; Davies, P. B. *J. Phys. Chem. B* **2002**, *106*, 5461–5469.

(364) McGall, S. J.; Davies, P. B.; Neivandt, D. J. *J. Phys. Chem. B* **2004**, *108*, 16030–16039.

(365) Hsiung, H.; Shen, Y. R. *Phys. Rev. A* **1986**, *34*, 4303–4309.

(366) Li, G.; Dhinojwala, A.; Yeganeh, M. S. *J. Phys. Chem. C* **2011**, *115*, 7554–7561.

(367) Knittl, Z. *Optics of Thin Films*; John Wiley & Sons: London, England, 1976.

(368) Abelès, F. *Ann. Phys. (Paris).* **1948**, *3*, 504–520.

(369) Abelès, F. *Ann. Phys. (Paris).* **1950**, *5*, 596–640.

(370) Abelès, F. *Ann. Phys. (Paris).* **1950**, *5*, 707–782.

(371) Yeh, P. *Optical Waves in Layered Media*; Wiley Series in Pure and Applied Optics; Wiley: New York, NY, 1988.

(372) O'Brien, D. B.; Massari, A. M. *J. Opt. Soc. Am. B* **2013**, *30*, 1503.

(373) Shen, Y. R. *J. Phys. Chem. C* **2012**, *116*, 15505–15509.

(374) Held, H.; Lvovsky, A. I.; Wei, X.; Shen, Y. R. *Phys. Rev. B* **2002**, *66*, 205110.

(375) Shen, Y. R. *Appl. Phys. B* **1999**, *68*, 295–300.

(376) Morita, A. *Chem. Phys. Lett.* **2004**, *398*, 361–366.

(377) Ishiyama, T.; Morita, A. *J. Phys. Chem. C* **2006**, *111*, 721–737.

(378) Ishiyama, T.; Morita, A. *J. Chem. Phys.* **2009**, *131*, 244714–244717.

(379) Ishiyama, T.; Sokolov, V. V; Morita, A. *J. Chem. Phys.* **2011**, *134*.

(380) Ishiyama, T.; Sokolov, V. V; Morita, A. *J. Chem. Phys.* **2011**, *134*.

(381) Kawaguchi, T.; Shiratori, K.; Henmi, Y.; Ishiyama, T.; Morita, A. *J. Phys. Chem. C* **2012**, *116*, 13169–13182.

(382) Born, M.; Wolf, E.; Bhatia, A. *Principles of optics : electromagnetic theory of propagation, interference, and diffraction of light*; Pergamon Press: New York, NY, 1999.

(383) Bloembergen, N. *Nonlinear optics : a lecture note and reprint volume*; Benjamin Cummings: Reading, MA, 1982.

(384) Butcher, P. N.; Cotter, D. *The elements of nonlinear optics*; Cotter, D. (David), Ed.; Cambridge University Press: New York, NY, 1990.

(385) Hecht, E. *Optics*; Addison-Wesley: Reading,MA, 2002.

(386) Tonouchi, M. *Nat Phot.* **2007**, *1*, 97–105.

(387) Lorentz, H. A. *The theory of electrons and its applications to the phenomena of light and radiant heat*; Dover Publications: New York, NY, 1952.

(388) Raab, R. E.; De Lange, O. L. *Multipole theory in electromagnetism : classical, quantum, and symmetry aspects, with applications*; Oxford: New York, NY, 2005.

(389) Ginzburg, V. L. *Sov. Phys. JETP-USSR* **1958**, *7*, 1096–1103.

(390) Flytzanis, C. In *Quantum electronics : a treatise Vol. I Pt. A*; Rabin, H.; Tang, C. L., Eds.; Academic Press: New York, NY, 1975; pp. 9–207.

(391) Byrnes, S. J.; Geissler, P. L.; Shen, Y. R. *Chem. Phys. Lett.* **2011**, *516*, 115–124.

(392) Harris, D. C.; Bertolucci, M. D. *Symmetry and Spectroscopy: An Introduction to Vibrational and Electronic Spectroscopy*; Dover Books on Chemistry Series; Dover: New York, NY, 1978.

(393) Albright, T. A.; Burdett, J. K.; Whangbo, M. H. *Orbital interactions in chemistry*; A Wiley Interscience publication; Wiley: New York, NY, 1985.

(394) Nye, J. F. *Physical properties of crystals : their representation by tensors and matrices*; Clarendon Press: Oxford, England, 1957.

(395) Lambert, A. G.; Davies, P. B.; Neivandt, D. J. *Appl. Spectrosc. Rev.* **2005**, *40*, 103–145.

(396) Moad, A. J.; Simpson, G. J. *J. Phys. Chem. B* **2004**, *108*, 3548–3562.

(397) O'Brien, D. B.; Massari, A. M. *J. Chem. Phys.* **2013**, *138*, 154708.

(398) Koch, N. *Chemphyschem* **2007**, *8*, 1438–1455.

(399) Facchetti, A.; Yoon, M.-H.; Marks, T. J. *Adv. Mater.* **2005**, *17*, 1705–1725.

(400) Chen, Z.; Shen, Y. R.; Somorjai, G. A. *Annu. Rev. Phys. Chem.* **2002**, *53*, 437–465.

(401) Shen, Y. R. *Appl. Phys. A-Mater.* **1994**, *59*, 541–543.

(402) Han, S.; Lee, K.; Lee, S.; Jang, J. *J. Non. Cryst. Solids* **2008**, *354*, 2870–2874.

(403) Jones, B. A.; Facchetti, A.; Wasielewski, M. R.; Marks, T. J. *Adv. Funct. Mater.* **2008**, *18*, 1329–1339.

(404) Karak, S.; Reddy, V. S.; Ray, S. K.; Dhar, A. *Org. Electron.* **2009**, *10*, 1006–1010.

(405) Zahn, D. R. T.; Gavrila, G. N.; Salvan, G. *Chem. Rev.* **2007**, *107*, 1161–1232.

(406) Sadowski, J. T.; Nagao, T.; Yaginuma, S.; Fujikawa, Y.; Al-Mahboob, A.; Nakajima, K.; Sakurai, T.; Thayer, G. E.; Tromp, R. M. *Appl. Phys. Lett.* **2005**, *86*, 73109.

(407) Hiroshiba, N.; Hayakawa, R.; Petit, M.; Chikyow, T.; Matsuishi, K.; Wakayama, Y. *Org. Electron.* **2009**, *10*, 1032–1036.

(408) Anttila, O. J.; Tilli, M. V. *J. Electrochem. Soc.* **1992**, *139* , 1751–1756.

(409) *Handbook of silicon wafer cleaning technology*; Reinhardt, K. A.; Kern, W., Eds.; William Andrew: Norwich, NY, 2008.

(410) *Handbook of ellipsometry*; Tompkins, H. G.; Irene, E. A., Eds.; William Andrew: Norwich, NY, 2005.

(411) Forget, S.; Balembois, F.; Georges, P.; Devilder, P.-J. *Appl. Phys. B* **2002**, *75*, 481–485.

(412) Liu, Y.; Wolf, L. K.; Messmer, M. C. *Langmuir* **2001**, *17*, 4329–4335.

(413) Antunes, P. A.; Constantino, C. J. L.; Aroca, R.; Duff, J. *Appl. Spectrosc.* **2001**, *55*, 1341–1346.

(414) Guhathakurta-Ghosh, U.; Aroca, R. *J. Phys. Chem.* **1989**, *93*, 6125–6128.

(415) Holman, J.; Davies, P. B.; Neivandt, D. J. *J. Phys. Chem. B* **2004**, *108*, 1396–1404.

(416) Simpson, G. J.; Rowlen, K. L. *Acc. Chem. Res.* **2000**, *33*, 781–789.

(417) Hall, S. A.; Jena, K. C.; Trudeau, T. G.; Hore, D. K. *J. Phys. Chem. C* **2011**, *115*, 11216–11225.

(418) Chen; Wang, J.; Even, M. A.; ChenChen, Z. *Macromolecules* **2002**, *35*, 8093–8097.

(419) Gautam, K. S.; Dhinojwala, A. *Phys. Rev. Lett.* **2002**, *88*, 145501.

(420) Liptay, W. *Angew. Chemie Int. Ed. English* **1969**, *8*, 177–188.

(421) Cho, M. *J. Chem. Phys.* **2009**, *130*, 94505.

(422) Pensack, R. D.; Banyas, K. M.; Asbury, J. B. *Phys. Chem. Chem. Phys.* **2010**, *12*, 14144–14152.

(423) Horowitz, G.; Hajlaoui, R.; Bouchriha, H.; Bourguiga, R.; Hajlaoui, M. *Adv. Mater.* **1998**, *10*, 923–927.

(424) Vidal, F.; Tadjeddine, A. *Reports Prog. Phys.* **2005**, *68*, 1095–1127.

(425) Ghosh, A.; Smits, M.; Sovago, M.; Bredenbeck, J.; Muller, M.; Bonn, M. *Chem. Phys.* **2008**, *350*, 23–30.

(426) Hashizume, N.; Ohashi, M.; Kondo, T.; Ito, R. *J. Opt. Soc. Am. B* **1995**, *12*, 1894.

(427) Wang, H.-F.; Gan, W.; Lu, R.; Rao, Y.; Wu, B.-H. *Int. Rev. Phys. Chem.* **2005**, *24*, 191–256.

(428) Zhuang, X.; Miranda, P.; Kim, D.; Shen, Y. *Phys. Rev. B* **1999**, *59*, 12632–12640.

(429) Zheng, D.-S.; Wang, Y.; Liu, A.-A.; Wang, H.-F. *Int. Rev. Phys. Chem.* **2008**, *27*, 629–664.

(430) Loch, C. L.; Ahn, D.; Chen, Z. *J. Phys. Chem. B* **2005**, *110 (2)*, 914–918.

(431) Ye, S.; Nihonyanagi, S.; Uosaki, K. *Phys. Chem. Chem. Phys.* **2001**, *3*, 3463–3469.

(432) Hirose, C.; Ishida, H.; Iwatsu, K.; Watanabe, N.; Kubota, J. *Chem. Phys.* **1998**, *108*, 5948–5956.

(433) Wang, Y.; Acton, O.; Ting, G.; Weidner, T.; Shamberge, P. J.; Ma, H.; Ohuchi, F. S.; Castner, D. G.; Jen, A. K.-Y. *Org. Electron.* **2010**, *11*, 1066–1073.

(434) Malitson, I. H. *J. Opt. Soc. Am.* **1965**, *55*, 1205.

(435) Tan, C. Z. *J. Non. Cryst. Solids* **1998**, *223*, 158–163.

(436) Kitamura, R.; Pilon, L.; Jonasz, M. *Appl. Opt.* **2007**, *46*, 8118.

(437) *Handbook of Optics, Third Edition Volume IV: Optical Properties of Materials, Nonlinear Optics, Quantum Optics*; Bass, M.; DeCusatis, C.; Mahajan, V.; Li, G.; Enoch, J.; Van Stryland, E., Eds.; Handbook of Optics; McGraw-Hill: New York, NY, 2009.

(438) Herzinger, C. M.; Johs, B.; McGahan, W. A.; Woollam, J. A.; Paulson, W. *J. Appl. Phys.* **1998**, *83*, 3323–3336.

(439) Casson, B. D.; Bain, C. D. *Langmuir* **1997**, *13*, 5465–5469.

(440) Fujiwara, H. *Spectroscopic Ellipsometry*; John Wiley & Sons, Ltd: Chichester, UK, 2007.

(441) Gan, W.; Wu, B.; Zhang, Z.; Guo, Y.; Wang, H. *J. Phys. Chem. C* **2007**, *111*, 8716–8725.

(442) Edgar, R.; Huang, J. Y.; Popovitz-Biro, R.; Kjaer, K.; Bouwman, W. G.; Howes, P. B.; Als-Nielsen, J.; Shen, Y. R.; Lahav, M.; Leiserowitz, L. *J. Phys. Chem. B* **2000**, *104*, 6843–6850.

(443) Wu, H.; Zhang, W.; Gan, W.; Cui, Z.; Wang, H. *J. Chem. Phys.* **2006**, *125*, 133203–133212.

(444) Hore, D. K.; Beaman, D. K.; Parks, D. H.; Richmond, G. L. *J. Phys. Chem. B* **2005**, *109*, 16846–16851.

(445) Rao, Y.; Yi-Sonq Tao, A.; Honq-Fei Wang, A. *J. Chem. Phys.* **2003**, *119*, 5226.

(446) Tao, Y. T.; Lee, M. T.; Chang, S. C. *J. Am. Chem. Soc.* **1993**, *115*, 9547–9555.

(447) Nishi, N.; Hobara, D.; Yamamoto, M.; Kakiuchi, T. *J. Chem. Phys.* **2003**, *118*, 1904.

(448) Shen, Y. R.; Ostroverkhov, V. *Chem. Rev.* **2006**, *106*, 1140–1154.

(449) Hayashi, M.; Lin, S. H.; Raschke, M. B.; Shen, Y. R. *J. Phys. Chem. A* **2002**, *106*, 2271–2282.

(450) Hatch, S. R. *J. Vac. Sci. Technol. A Vacuum, Surfaces, Film.* **1993**, *11*, 2232.

(451) Gan, W.; Wu, B.; Chen, H.; Guo, Y.; Wang, H. *Chem. Phys. Lett.* **2005**, *406*, 467–473.

(452) Salaneck, W. R.; Stafström, S.; Brédas, J.-L. *Conjugated polymer surfaces and interfaces : electronic and chemical structure of interfaces for polymer light emitting devices*; Cambridge University Press: New York, NY, 1996.

(453) Kahn, A.; Koch, N.; Gao, W. *J. Polym. Sci. Part B Polym. Phys.* **2003**, *41*, 2529–2548.

(454) Heeger, A. J. *Curr. Appl. Phys.* **2001**, *1*, 247–267.

(455) Holman, J.; Davies, P. B.; Nishida, T.; Ye, S.; Neivandt, D. J. *J. Phys. Chem. B* **2005**, *109*, 18723–18732.

(456) Anglin, T. C.; Lane, A. P.; Massari, A. M. *J. Mater. Chem. C* **2014**, -.

(457) Vasseur, K.; Rolin, C.; Vandezande, S.; Temst, K.; Froyen, L.; Heremans, P. *J. Phys. Chem. C* **2010**, *114*, 2730–2737.

(458) Tolaieb, B.; Constantino, C. J. L.; Aroca, R. F. *Analyst* **2004**, *129*, 337–341.

(459) Yamaguchi, S.; Shiratori, K.; Morita, A.; Tahara, T. *J. Chem. Phys.* **2011**, *134*, 184705.

(460) Chen, X.; Hua, W.; Huang, Z.; Allen, H. C. *J. Am. Chem. Soc.* **2010**, *132*, 11336.

(461) Hommel, E. L.; Allen, H. C. *Analyst* **2003**, *128*, 750–755.

(462) *Nonlinear optics of organic molecules and polymers*; Nalwa, H. S.; Miyata, S., Eds.; CRC Press: Boca Raton, FL, 1997.

(463) Lagutchev, A.; Hambir, S. A.; Dlott, D. D. *J. Phys. Chem. C* **2007**, *111*, 13645–13647.

(464) Quast, A. D.; Curtis, A. D.; Horn, B. A.; Goates, S. R.; Patterson, J. E. *Anal. Chem.* **2012**, *84*, 1862–1870.

(465) Kaake, L. G.; Zou, Y.; Panzer, M. J.; Frisbie, C. D.; Zhu, X.-Y. *J. Am. Chem. Soc.* **2007**, *129*, 7824–7830.

(466) Bain, C. D.; Troughton, E. B.; Tao, Y. T.; Evall, J.; Whitesides, G. M.; Nuzzo, R. G. *J. Am. Chem. Soc.* **1989**, *111*, 321–335.

(467) Himmelhaus, M.; Eisert, F.; Buck, M.; Grunze, M. *J. Phys. Chem. B* **2000**, *104*, 576–584.

(468) Kudelski, A. *Vib. Spectrosc.* **2005**, *39*, 200–213.

(469) Heeger, A. J.; Kivelson, S.; Schrieffer, J. R.; Su, W.-P. *Rev. Mod. Phys.* **1988**, *60*, 781–850.

(470) Patil, A. O.; Heeger, A. J.; Wudl, F. *Chem. Rev.* **1988**, *88*, 183–200.

(471) Rodgers, J. L.; Nicewander, W. A. *Am. Stat.* **1988**, *42*, pp. 59–66.

(472) Katz, H. E.; Hong, X. M.; Dodabalapur, A.; Sarpeshkar, R. *J. Appl. Phys.* **2002**, *91*, 1572.

(473) Knipp, D.; Street, R. A.; Völkel, A.; Ho, J. *J. Appl. Phys.* **2003**, *93*, 347.

(474) Salleo, A.; Endicott, F.; Street, R. A. *Appl. Phys. Lett.* **2005**, *86*, 263505.

Appendix: Fabrication Procedure for Field-Effect Transistor Substrates

All procedures herein use materials and instruments available in the clean room facilities at the Minnesota Nano Center (MNC, formerly the Nanofabrication Center) in Keller Hall at the University of Minnesota in Minneapolis, MN. Aside from a few small changes, this procedure has remained the primary guide to preparing the electrodes for the oFETs used in this work.

The original silicon wafer specifications for 200 nm thermal oxide are:

- Purchased from Silicon Valley Microelectronics 06-12-2007
  - 100mm Si wafer
  - P-Type (boron doped)
  - Orientation <100>
  - Resistivity 1-100 ohm-cm
  - Thickness 525 ± 25 μm
  - Front Surface: Polished with 200 nm thermal oxide ±5%
  - Back Surface: Etched

A.1 Prepare Gate Electrode

1. Dehydrate polished surface: bake wafers on hotplates 115-120^{o}C ~1 min
2. Protect polished side from etch and metal evaporation:
   - Spin coat Shipley 1818 photoresist on polished side
     - Spin speed: 3500 rpm
     - Ramp rate: 3500 rpm/s
     - Spin for 30 s = ~1.8 μm film

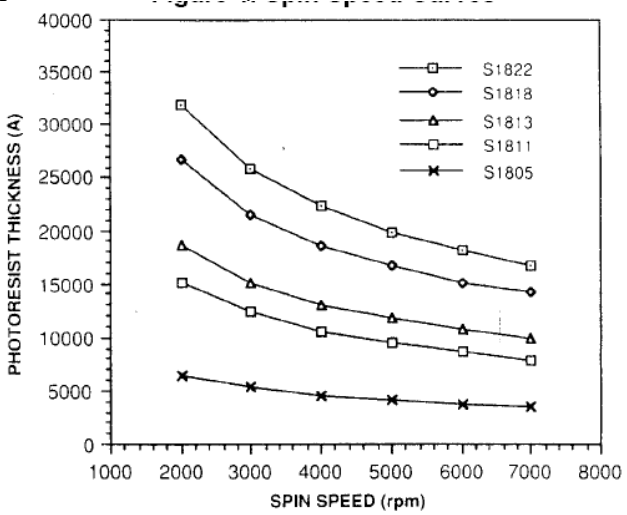

Figure A–1. Photoresist thickness vs. spin speed for various photoresist solutions. http://www.nfc.umn.edu/photolithography/datasheet_s1800.pdf

3. Bake on hotplate 115 ^{o}C 1 min

4. Etch 200 nm SiO_2 for gate contact electrode (back side of wafer)
   - *****Be sure you have access to metal evaporator immediately after etch to minimize native oxide growth*****
   - Buffered oxide etch (BOE) 1:10 solution (bay 1) 5 min. (etch rate ~51.3 nm/min)
   - 3 cycles in DI water dump rinse. (in wet bench)
5. Metal evaporation done on Temescal E-Beam evaporator
   - 50 nm Al (adhesion layer and charge transfer promoter) and 200 nm Au
   - Deposition rates: Al – 4 Å/s
     Au – 3 Å/s
6. Rinse Shipley 1818 off in solvent baths: Acetone→Methanol→IPA ~1–2 min each

A.2 PHOTOLITHOGRAPHY OF FET SOURCE AND DRAIN ELECTRODES

Figure A–2. Schematic cross section of substrate, lift off resist (LOR), and photoresist layers.

Prepare spin coat layers:

1. Clean wafers in 1165 solution ~45 min.
2. Rinse in solvent baths: Acetone→Methanol→IPA ~1-2 min each
3. Dehydrate surface: Hotplate 170 ^{o}C 5 min
4. Prepare metal lift-off resist (LOR) coating
   - Spin on LOR 3A lift-off resist
     - Custom spin program:
       Spin speed 500 rpm ramp rate 500 rpm/s for 2 s followed by spin speed 2900 rpm with ramp rate of 2900 rpm/s for 40 s

****IMPORTANT: Apply LOR 3A <u>FAST</u> and hit start on spinner within a couple seconds. LOR 3A dries quickly, must be spun immediately to get uniform coverage on the wafer.**

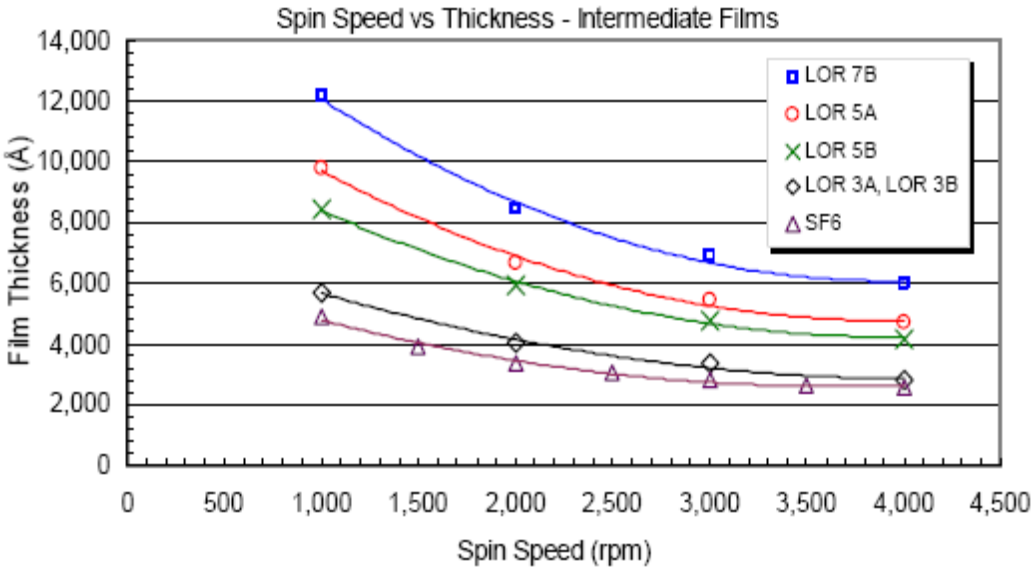

Figure A–3. Spin speed vs. thickness for various lift-off resists (LOR) available at the NFC. http://www.nfc.umn.edu/photolithography/datasheet_lor.pdf

5. Soft bake wafers 170 ^{o}C 3 min each
6. Prepare Shipley 1813 photoresist coating
   - Spin speed 3000 rpm, ramp rate 3000 rpm/s, spin time 30 s → ~1.4 μm film. See Figure A–3 for thickness vs. spin speed plot.
   - **Again, apply photoresist FAST and hit start on the spinner for uniform film coverage**
7. Soft bake on hot plate 105 ^{o}C 2 min

Align mask and expose wafers:

1. Align wafers to mask "SFGOFET2" in maba6 photolithography machine.
   - Expose 8 s
2. Develop wafers in CD-26 solution 45 s
3. 4 cycles in DI water dump rinse
4. Rinse and dry in spin-rinse and dry machine
   - 60 s rinse
   - 260 s dry1
   - 260 s dry2
5. Check features of photoresist under microscope, ensure features are well defined
6. **Note: there is usually an undercut step done; however, the features of this particular mask are large and so undercut is not done here.**
7. Hard bake 125 ^{o}C 5 min

Deposit Source and Drain Electrodes:

1. Source and drain electrodes deposited using Temescal E-Beam evaporator

- 100 nm Al deposited @ 3 Å/s (adhesion layer and facilitates charge transfer). This was the original adhesion layer, in recent procedures a much thinner layer is used, usually ~2 nm chromium, titanium, or aluminum.
- 200 – 300 nm Au deposited @ 3 Å/s

2. Lift off metals:
   - Sonicate or soak in 1165 solution multiple baths. ~20 min if sonicating, overnight if soaking. Use fresh 1165 for final rinse.
     - Sonicating leads to many small metal particles forming and are difficult to remove from wafer surface so that overnight soak should be preferred.
   - Rinse in DI water spray hose and/or 3 cycles DI dump rinse
   - **Verify metal particles do not remain on the FET surface using microscopes, rinse in fresh 1165 if particles are visible**
3. Final rinses in solvent baths Acetone→Methanol→IPA ~1–2 min each
4. Blow dry with house N_2